On the Foundations of the Transmission Line Matrix Method

Jürgen N. Rebel

Lehrstuhl für Hochfrequenztechnik der Technischen Universität München

On the Foundations of the Transmission Line Matrix Method

Jürgen N. Rebel

Vollständiger Abdruck der von der Fakultät für Elektrotechnik und Informationstechnik der Technischen Universität München zur Erlangung des akademischen Grades eines

DOKTOR-INGENIEURS

genehmigten Dissertation.

Vorsitzender:		Univ.-Prof. Dr.-Ing. habil. A. W. Koch
Prüfer der Dissertation:	1.	Univ.-Prof. Dr. techn. P. Russer
	2.	Prof. Dr.-Ing. W. J. R. Hoefer, University of Victoria, Victoria, Canada

Die Dissertation wurde am 16. Dez. 1999 bei der Technischen Universität München eingereicht und durch die Fakultät für Elektrotechnik und Informationstechnik am 14. Feb. 2000 angenommen.

Abstract

The foundations of the TLM method with symmetrical condensed node in the original formulation of JOHNS for the solution of three-dimensional electromagnetic field problems are investigated in this dissertation. It is shown that the mapping between the discretized electromagnetic field components and the TLM wave pulses determines the asymptotic convergence rate of the TLM algorithm. For this, the convergence of the original symmetrical condensed node TLM formulation introduced by JOHNS is proved for the first time. The proof is achieved in three steps. First, the appropriate function spaces providing a suitable norm for proving convergence are constructed. Second, the cell-centred field-mapping is applied at every iteration step yielding a mapping induced finite difference scheme, which is the well known LAX-FRIEDRICHS scheme. Third, it is shown using norm estimations that the difference between the TLM scheme and this mapping induced finite difference scheme approaches zero for Δl approaching zero. It emerges that using a cell-centred field-mapping results in $\mathcal{O}(\sqrt{\Delta t})$ convergence. Other work has shown that using a bijective boundary oriented field-mapping gives second order convergence. This influence of the field-mapping on the asymptotic convergence order is verified in a numerical experiment, where the propagation of a plane wave in a one-dimensional parallel-plate waveguide is studied at various discretizations. Furthermore, the suitability of the recently proposed Alternating Transmission Line Matrix Method for the solution of electromagnetic field problems is discussed. The application's part of this dissertation deals with the characterization of planar microwave components using the TLM method. A TLM algorithm for considering first order dispersive media is derived. The influence of dielectric losses of the adhesive that is used to embed chips into multichip module (MCM) substrates on the transmission properties of MCM interconnects is investigated applying this TLM algorithm. It emerges that a lossy adhesive even slightly improves the transmission properties of such MCM interconnects due to loss impedance matching. Further, the influence of substrate losses on the properties of planar microwave transformers, which are used in mobile communication amplifiers, is investigated. For this, layered absorbers for the truncation of the computational domain have to be implemented. The TLM characterization of a simplified transformer indicates

a potential use of such transformers up to 100 GHz. The lossy substrate has a negligible influence on the transformer characteristics up to 30 GHz.

Acknowledgement

A doctoral thesis can never be prepared without the support and the encouragement of a number of people and organizations.

First of all, I would like to thank cordially my supervisor PROF. RUSSER for initiating this work and giving me his guidance on the scientific work presented in this thesis. He always had an open ear for any kind of problem emerging in the course of this work. The resulting discussions were valuable and stimulating and a great pleasure to me. I am also very grateful that he managed to get financial support for my travelling to several conferences for presenting part of the work presented here.

My special thanks are to my colleagues MARTIN AIDAM and TOBIAS MANGOLD. MARTIN AIDAM never hesitated to enter discussions on theoretical aspects of the TLM algorithm and fundamental questions related to it, which helped me to clarify a number of ideas in my head. Moreover, he was always willing to share his knowledge on the theory, practise, and mathematics of electromagnetism from which I learned a lot. TOBIAS MANGOLD as the architect of the TLM software developed at our institute, taught me how to write proper code. Without his great patience and willingness to help, the code modules that I wrote in the course of this work would not have reached their present mature form. He was also never reluctant to discuss the computational results of our simulator. It was a pleasure and a privilege to work together with both of them. And apart form that, we had a lot of fun together at our work.

I would further like to thank PROF. HOEFER from Vitoria, Canada, for the pleasure I had to work together with him and prepare a collaborated paper. DR. STEFFEN HEIN from Spinner deserves my gratitude for some valuable discussions on the intricacies of the propagator approach to TLM. I am also thankful to DR. LUDWIG TREITINGER, DR. WERNER SIMBÜRGER, HANS-DIETER WOHLMUTH, and PROF. PETER WEGER (now with the IHP at the University of Frankfurt an der Oder) from INFINEON Technologies AG for the fruitful collaboration in this project. Moreover, I thank all colleagues, which have not been mentioned yet, at the Institut für Hochfrequenztechnik for the friendly atmosphere and the friendly and willing collaboration at the institute. I am grateful to all the people who helped me preparing the manuscript.

I am indebted to SIEMENS AG for granting me an ERNST-VON-SIEMENS scholarship. Without this financial support, I would not have been able to prepare the work presented in this thesis.

I would like to mention the support and encouragement of my parents throughout the years of my academic education, which culminates in this thesis.

Especially, I would like to thank my partner INES AIGNER for her patience, moral support, and understanding when I had to work late hours during the preparation of the work for this dissertation.

List of Abbreviations

ABC	absorbing boundary condition
ATLM	Alternating Transmission Line Matrix (Method)
ARTLM	Alternating Rotated Transmission Line Matrix (Method)
BOFM	boundary oriented field-mapping
CFM	cell-centred field-mapping
CPW	coplanar waveguide
FD	finite difference
FDTD	Finite-Difference-Time-Domain
FTCS	forward-in-time-centred-in-space
GSCN	general symmetrical condensed node
HSCN	hybrid symmetrical condensed node
ILGA	integer lattice gas automata
IVP	initial value problem
MCM	multichip module
MoM	method-of-moments
MIFD	mapping induced finite difference scheme
ML	matched layer
PEC	perfectly conducting
PML	perfectly matched layer
PPL	parallel-plate
RF	radio frequency
RTLM	Rotated Transmission Line Matrix (Method)
SCN	symmetrical condensed node
TEM	transverse electromagnetic
TL	transmission line
TLM	Transmission Line Matrix (Method)

List of Symbols

Greek Symbols

$\mathbf{\Gamma}$	connection operator
Γ	reflection coefficient
Γ_m	discrete sum
$\mathbf{\Gamma}_s$	stub connection operator
Δl	discretization step
Δl	length of TLM cell
Δt	time step
Δx	discretization step in x-direction
Δy	discretization step in y-direction
Δz	discretization step in z-direction
Υ	stability matrix
Φ_{LE}	equivalent finite difference scheme LE of ARTLM
Φ_{LO}	equivalent finite difference scheme LO of ARTLM
Φ_{RE}	equivalent finite difference scheme RE of ARTLM
Φ_{RO}	equivalent finite difference scheme RO of ARTLM
Ψ	discrete propagator integral
$\mathbf{\Omega}$	bounded region in $\mathbb{R}^3$
α_0	static molecular polarizability
$\alpha(\omega)$	molecular polarizability
β	constant
γ_μ	coefficient in sum
δ_{ij}	KRONECKER symbol
$\tan\delta$	loss angle
ε	absolute permittivity
$\varepsilon^{'}$	real part of permittivity
$\varepsilon^{''}$	imaginary part of permittivity
ε_0	permittivity of free space
ε_r	relative permittivity
ε_s	static permittivity

ε_∞	permittivity for infinite frequency
ζ	element of discrete LEBESGUE space
η	relative error
θ	time variable
μ	absolute permeability
μ_0	permeability of free space
μ_r	relative permeability
ξ	variable
π	circle constant
$\boldsymbol{\sigma}$	conductivity tensor
σ_e	electric conductivity
σ_m	magnetic conductivity
τ_d	dielectric relaxation time
φ_{ana}	phase of analytical reflection coefficient
φ_n	function of discrete argument
χ_μ	unit pulse function
ω	angular frequency

Bold Symbols: Vectors, Matrices, and Operators

$\boldsymbol{A}$	general finite difference operator
$\boldsymbol{A}$	coefficient matrix
$\boldsymbol{B}$	eigenvector matrix of SCN
$\boldsymbol{B}(\cdot,\cdot)$	submatrices of coefficient matrix of BOFM
$\boldsymbol{C}$	TLM connection matrix
$\boldsymbol{C}(\cdot,\cdot)$	submatrices of coefficient matrix of BOFM
$\vec{\boldsymbol{D}}$	dielectric displacement vector
$\boldsymbol{D}[\cdot]$	deflection operator
$\mathbf{Div}$	generalized divergence operator
$\mathbf{D_R}$	generalized rot operator
$\boldsymbol{D_t}$	generalized temporal differential operator
$\boldsymbol{D}_{\cdot\cdot}$	scalar difference operators
$\vec{\boldsymbol{E}}$	electric field vector
$\boldsymbol{G}$	matrix of discretized known data
$\boldsymbol{G}[\cdot]$	discrete convolution
$\boldsymbol{G}'_E$	coefficient matrix
$\vec{\boldsymbol{H}}$	magnetic field vector
$\boldsymbol{I}$	identity matrix
$\mathcal{L}$	linear differential operator
$\mathcal{O}(\cdot)$	big "O" notation
$\boldsymbol{P}$	cell-centred field-mapping
$\vec{\boldsymbol{P}}$	polarization vector

$\boldsymbol{P}_E$	coefficient matrix of BOFM
$\boldsymbol{P}_H$	coefficient matrix of BOFM
$\mathcal{Q}$	general difference operator
$\boldsymbol{Q}$	nodal excitation field-mapping (CFM)
$\boldsymbol{Q}_\mu$	difference operators
$\boldsymbol{R}$	rotation matrix
$\boldsymbol{R}$	generalized scattering operator
$\boldsymbol{S}$	TLM scattering matrix
$\tilde{\boldsymbol{S}}_0$	rotated free space TLM scattering matrix
$\boldsymbol{S}_D$	deflection matrix
$\boldsymbol{T}$	temporal shift operator
$\boldsymbol{U}$	dielectric relaxation time matrix
$\boldsymbol{V}$	coefficient matrix
$\boldsymbol{V}^i$	vector of incident voltages
$\boldsymbol{V}^r$	vector of reflected voltages
$\boldsymbol{W}(x)$	$Diag(x^{-1}\sinh(x)), Diag(x^{-1}\sinh(x)), Diag(x^{-1}\sinh(x))$
$\boldsymbol{X}$	spatial shift operator
$\boldsymbol{Y}$	spatial shift operator
$\boldsymbol{Z}$	spatial shift operator
$\boldsymbol{a}$	vector of incident TLM wave pulses
$\boldsymbol{a}^l$	vector of incident TLM wave pulses on link lines
$\boldsymbol{b}$	vector of reflected TLM wave pulses
$\boldsymbol{d}$	deflection vector
$d\vec{A}$	infinitesimal area element
$d\vec{s}$	infinitesimal line segment
$\boldsymbol{e}$	electric eigenfield
$\boldsymbol{f}$	vector of nodal field components
$\boldsymbol{g}$	vector of known data
$\boldsymbol{g}_h$	vector of discretized data
$\boldsymbol{h}$	magnetic eigenfield
$\boldsymbol{i}_{pol}$	polarization current
$\boldsymbol{m}$	auxiliary deflection vector
$\boldsymbol{r}$	spatial coordinate vector
$\boldsymbol{u}$	vector of unknown lattice functions
$\boldsymbol{v}$	vector of unknown functions

Scalars and Functions

C	real constant
C	capacitance of symmetrical condensed node
C_0	capacitance per unit length
C_{stub}	capacitance of open stub

D^i	generalized derivative
E	electric field component
F	known data
G	ohmic loss stub
H	magnetic field component
I	current
$Im[.]$	imaginary operator
K	real constant
L_0	inductance per unit length
M	natural number
N	natural number
P	component of electric polarization vector
$Re[.]$	real operator
R	magnetic loss stubs
T	width of GAUSSian pulse
V	voltage
Y_0	admittance of free space
Y_{stub}	admittance of open stub
Y	open circuit stub
Z_0	impedance of free space
Z	short circuit stub
a	incident TLM wave pulse
a	parameter of scattering matrix
a	coefficient of nodal excitation mapping
$a(t)$	time dependent boundary condition
b	parameter of scattering matrix
b	coefficient of nodal excitation mapping
$b(t)$	time dependent boundary condition
c	parameter of scattering matrix
c	coefficient of nodal field-mapping
d	parameter of scattering matrix
d	coefficient of nodal field-mapping
e_1	unity vector
f	parameter of scattering matrix
$f(x)$	initial condition function
g	parameter of scattering matrix
g_l	lattice function
$g(x)$	lattice function
$g_{E\cdot\cdot}$	parameter of TLM-FD scheme
h	parameter of scattering matrix
h	stability factor
i	index

j	index
j	$\sqrt{-1}$, imaginary unit
c_0	speed of light
k	temporal index
l	index
m	index
n	index
p	index
q	index
r	index
$r_{E\cdot\cdot}$	parameter of TLM-FD scheme
$r_{\cdot\cdot}$	stability factor
$s_{E\cdot\cdot}$	parameter of canonical scattering matrix
u_l^k	discrete function
t	time
$v(x,t)$	continuous function
v_t	first derivative of v with respect to time
v_{xx}	second derivative of v with respect to x
u	geometry coefficient of TLM cell
v	geometry coefficient of TLM cell
w	geometry coefficient of TLM cell
x	variable
x	directional index
y	variable
y	directional index
z	directional index

Spaces and Sets

ℓ_2	space of all square summable sequences
ℓ_p	sequence spaces
$\ell_{p,\Delta x}$	discrete LEBESGUE space
$B_{\ell_{2,\Delta t}}$	base of discrete LEBESGUE space $\ell_{2,\Delta t}$
$\mathcal{B}_n$	BANACH spaces
$\mathbb{C}$	set of all complex numbers
$C(\mathbb{R})$	set of all continuous functions $u : \mathbb{R} \longrightarrow \mathbb{R}$
$\mathcal{D}(\cdot)$	domain of operator
$\mathcal{H}$	Lebesgue space $(\mathcal{L}^2(\mathbb{R}^3))^6$
$\mathcal{H}_w$	TLM state space
$\mathbb{I}$	general index set
$I_{k_{ug}}$	set of indices for uniform grid
$I_{k_{ccg}}$	set of indices for cell-centred grid

$\{k\}$	finite set of natural numbers
$\mathcal{L}^2(\mathbb{R})$	space of all LEBESGUE measurable functions
$\mathcal{L}^2(\mathbb{R}^3)$	space of all LEBESGUE measurable functions
$\boldsymbol{L}_p\,(0,T;\mathcal{H})$	LEBESGUE space of vector-valued functions
$\mathbb{N}_0$	set of all natural numbers including 0
$\mathbb{R}$	set of all real numbers
$\mathbb{R}^N$	set of all real N-tuples
$\boldsymbol{V}$	SOBOLEV space
$\boldsymbol{W}_2^1(\mathbb{R}^3)$	SOBOLEV space
$\boldsymbol{W}_2^1\,(0,T;\boldsymbol{V}_0)$	SOBOLEV space of vector-valued functions
$\mathcal{X}$	space of domain
$\mathcal{X}_h$	discrete space of domain
$\mathcal{Y}$	image space
$\mathcal{Y}_h$	discrete image space
$\mathbb{Z}$	set of all integer numbers

Math Symbols

$(\cdot,\cdot)$	inner product
$<\cdot\|$	bra-vector of DIRAC notation
$\|\cdot>$	ket-vector of DIRAC notation
$<\cdot\|\cdot>$	inner product in DIRAC notation
$\|\cdot><\cdot\|$	projection operator in DIRAC notation
$\nabla\cdot$	divergence operator
$\nabla\times$	rot operator
$\times$	CARTESIAN product
$\|\cdot\|$	norm
$\|\cdot\|_{\mathcal{H}}$	norm in space $\mathcal{H}$
$\otimes$	tensor product
$.^T$	matrix transpose
$.^*$	complex conjugate
$.^\dagger$	HERMITIAN conjugate

Suffixes

Superscript suffixes often denote directions. Subscript suffixes are often used to denote directions or the temporal and spatial cell indices. Further, they are used to distinguish parameters of the same type.

Tilde

The $\tilde{}$ Symbol is used to denote transformed TLM quantities and matrices or rotated TLM quantities and matrices. On some occasions it is used to distinguish coefficients of the same type but of different value.

Contents

CHAPTER 1

Introduction

1. Introduction

The recent years have seen an unprecedented boom in mobile communication. For example, in the United States, the number of subscribers to cellular phones has grown exponentially since 1985, which is illustrated in Fig. 1.1 taken from [**83**]. The same development can be recognized in Europe. Nevertheless, there are far more wireless applications coming up. An example is a wireless communication project, known as 'Bluetooth' that aims at linking indoor computer equipment, such as the main unit and peripheral equipment like printers or scanners, without the wiring that is necessary today. However, the more applications are developed, the need for higher bandwidth becomes imminent. This desire can be satisfied by moving to higher frequency bands. However, using higher frequency bands makes it more difficult to find the optimum circuit design of amplifiers, transmitters and the like,

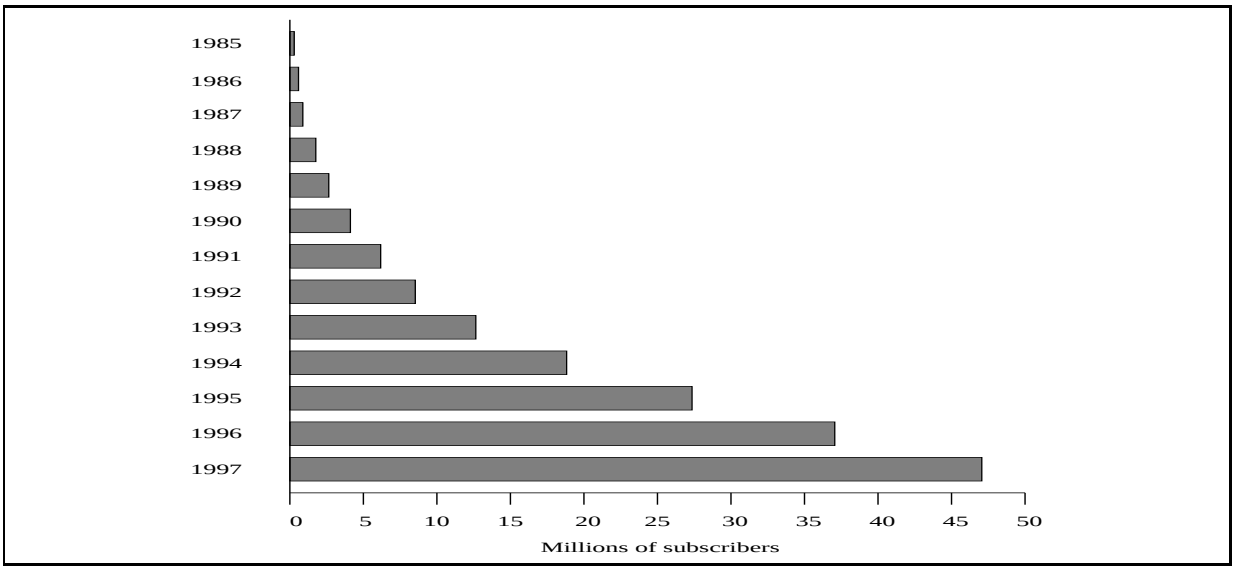

FIGURE 1.1. The exponential growth in communications is illustrated by cellular telephone subscribers in the United States, tabulated as of June in each of the reported years.

as many components cannot be treated as concentrated any more. Appropriate characteristic parameters for describing the components of those circuits at higher frequencies are the so called *scattering parameters* or *S-parameters*. They describe a device in terms of incident and reflected power waves. One can obtain these S-parameters of a device not only by measuring real devices, but also from an electromagnetic full-wave analysis of a discrete model of the device. Once the S-parameters are known, they can be fed into a circuit simulator to see whether the device under consideration meets the specifications of the desired circuit. However, obtaining the S-parameters from a simulation has the advantage of saving the extremely costly actual fabrication of many test devices. Moreover, simulating devices is faster than the fabrication of test devices. For this, the need for reliable and efficient numerical electromagnetic full-wave analysis tools is growing more and more.

2. The Transmission Line Matrix Method

Transmission Line Matrix (TLM) - methods are powerful and versatile algorithms for the numerical full-wave analysis of electromagnetic field problems. They are based on the analogy between the propagation of electromagnetic fields according to HUYGENS principle and the propagation of voltage pulses in transmission line networks [**30**]. Most TLM methods operate in time domain. To obtain S-parameters, the time domain signals need to be transformed to the frequency domain. At first glance, this seems more complicated than a direct field computation in frequency domain. However, one gets the desired parameters for a very large bandwidth, depending on the bandwidth of the input signals, whereas in frequency domain one gets the solution only at certain frequencies. Moreover, the transient electromagnetic field can easily be visualized in time domain, which yields a greater physical insight into the problem under investigation.

Already in the 40ies of this century, physical network models were used to solve electromagnetic field problems. In those days, the propagation of current and voltage waves on a real mesh of interconnected transmission lines, thus modelling the propagation of electromagnetic waves, was analysed by network analysers [**39, 110, 111**].

In 1971, JOHNS and BEUERLE suggested to solve two-dimensional scattering problems by implementing such transmission line methods on a computer [**37**]. Soon, the TLM method was extended for the solution of three-dimensional problems and for the treatment of inhomogeneous, lossy, and anisotropic media. Also, ways to treat curvilinear problems were suggested [**4**]. In 1987, the TLM method with *Symmetrical Condensed Node* (SCN) was introduced by JOHNS [**35**]. It was not long until this method and its generalizations became the most commonly used TLM methods. As the original derivation of the SCN-TLM method by JOHNS was mainly based on analogy, various authors suggested formal derivations. In 1991, CHEN, NEY, and HOEFER presented a Finite Difference scheme that is equivalent

to the SCN-TLM formulation without stubs [**14**]. Although most TLM methods operate in time domain, a TLM method for the frequency domain was presented in 1992, which has also found many applications since then [**33**]. Later, JIN and VAHLDIECK suggested a derivation of the SCN-TLM method with stubs from MAXWELL's equations based on finite differencing and averaging [**34**]. KRUMPHOLZ and RUSSER contributed a *Method-of-Moments* (MoM) derivation of the TLM method without stubs [**44**]. LOVETRI and SIMONS presented a conservation law approach for the derivation of the SCN-TLM method without stubs [**52**]. In 1993, HEIN published a paper that presented a derivation of the SCN parameters from a consistent Finite Difference Scheme approximating MAXWELL's equations [**23**]. In that paper, the issue of consistency of the various formulations of the SCN-TLM methods was hinted at for the first time.

To save memory resources, RUSSER and BADER suggested the ATLM method in 1995 that exploits the inherent redundancy in the usual SCN-TLM algorithm. A further refinement of the ATLM method is the ARTLM method, presented by RUSSER in 1996, which theoretically needs only 25% of the memory resources of the common SCN-TLM method [**85**]. This method appears to be especially interesting for the treatment of thin layers in planar microwave circuits.

3. Objectives

Although the symmetrical condensed node TLM method has been intensively investigated and different views of the basic scattering algorithm have been established, the decisive question of consistency and in-the-end convergence has only been dealt with in special cases, such as [**23**]. However, consistency - and in connection with stability, the convergence - of a difference scheme is by no means guaranteed by the derivation of a difference scheme alone [**100**]. Especially the convergence of JOHNS' original formulation [**35**] has not been proved yet, although it is presumably the most widely used TLM method with condensed node. The rate of convergence is of prominent interest when applying mathematical approximation methods. The faster a method converges, the lesser computational resources are required. As the TLM method has a somewhat larger computational effort than the popular *Finite-Difference-Time-Domain* (FDTD) method [**113, 115**], this issue is of strong interest.

4. Original Contributions

The work presented in this thesis contributes the following original ideas to the subject:

1. The TLM algorithm is considered as a mathematical approximation scheme of MAXWELL's equations in a rigorous functional analytical setting and not in terms of equivalent lumped element models.

2. The convergence of Johns' original TLM formulation with cell-centred field-mapping against solutions of MAXWELL's equations is formally proved for the first time.
3. It is shown that the field-mapping between the discretized electromagnetic field and the TLM wave pulses determines the type of approximation of MAXWELL's approximation and consequently the asymptotic convergence rate.
4. All theoretical predictions are verified in a numerical experiment.
5. It is shown that the field-mapping also determines the type of approximation in the recently proposed Alternating Rotated Transmission Line Matrix Method. A proof of the non-existence of a consistent mapping is given.
6. A novel approach for the simulation of dispersive media with the TLM method is presented. It is based on the propagator approach to TLM.
7. A comprehensive study on the optimum parameter combination of matched layer absorbers for truncating the computational domain in open problems with inhomogeneous planar substrates is performed. It is shown that the performance of these absorbing boundary conditions is mainly determined by the differences in dispersion due to different media parameters in neighbouring regions. The numerical reflections play a minor role.
8. Challenging state-of-the-art field problems are solved using the TLM method. An example is the determination of the influence of conductive substrate losses on the electrical properties of planar microwave transformers.

5. Outline

In the first part of this work, various commonly used SCN-TLM formulations are analysed and compared with respect to their convergence both analytically and numerically. The second part of this work describes the application of the TLM method with symmetrical condensed node to the solution of some challenging state-of-the art problems in the area of planar microwave circuits. The outline of this thesis is as follows.

In Chapter 2, the principles of the TLM method with symmetrical condensed node are explained. The discretization of the computational domain using TLM cells and nodes is illustrated. The TLM scattering algorithm is presented and the symmetrical condensed node both with and without stubs is recalled. Various mappings between the TLM wave pulses and the discretized electromagnetic field components are given. Finally, the HILBERT space formulation of the TLM method following [**87**], which will be used throughout this study, is introduced.

Chapter 3 contains an overview of the published theoretical work on the symmetrical condensed node. The various derivations of the symmetrical condensed

node are discussed and the dispersion characteristics of the TLM mesh with symmetrical condensed node are also considered. Furthermore, a brief overview of recent applications of the TLM method with symmetrical condensed node to the solution of electromagnetic field problems in planar microwave circuits is given.

In Chapter 4, the terms *consistency*, *stability*, and *convergence* classifying finite difference schemes are introduced and means of analysing them are presented. Moreover, appropriate function spaces for investigating the convergence of the TLM method are constructed. They form the basis of the proof of convergence of the SCN-TLM formulation given by JOHNS in the subsequent chapter.

In Chapter 5, a proof of convergence of the most commonly used formulation of the Transmission Line Matrix method - JOHNS' original formulation - is presented. The convergence of both the SCN-TLM method with and without stubs is given. Furthermore, the asymptotic rate of convergence is estimated.

In Chapter 6, the convergence of the *Alternating Rotated Transmission Line Matrix* (ARTLM) scheme is investigated and its suitability for solving electromagnetic field problems is discussed. The basics of the ARTLM scheme are explained and the four possible ARTLM schemes are distinguished. The consistency of various proposed mappings between rotated TLM wave pulses and the discretized electromagnetic field components is studied. It emerges that no consistent mapping exists and a proof of the non-existence of a consistent mapping is presented.

Chapter 7 contains a numerical study on the convergence of the various discussed formulations of the TLM method with symmetrical condensed node. For this, the propagation of a plane wave with GAUSSian transient in a one-dimensional TLM model of an infinite parallel plate wave guide is studied at various discretization. The asymptotic convergence orders predicted by the convergence analysis of Chapter 5 and of other work for other formulations is verified in this experiment.

A TLM algorithm for treating first order dispersive media, known as DEBYE media, is derived in Chapter 8. This TLM algorithm is based on the propagator approach following [**26**]. The derivation is formulated in terms of the HILBERT space formulation of [**87**]. For deriving the updating relations of a dielectric node, the procedure presented in [**26**] for perturbed TLM processes is applied.

Applications of the TLM method for characterizing planar microwave components for mobile communications and *Multichip Modules* (MCM) are presented in Chapter 9. First, the influence of frequency dependent dielectric losses of the adhesive in MCM embeddings on the performance of a microstrip-to-coplanar transition using the TLM algorithm derived in Chapter 8, is investigated. Finally, the influence of substrate losses on the S-parameters of a planar microwave transformer, used in the driver stage of a microwave power amplifier, is studied.

Chapter 10 concludes this thesis by summarizing and discussing its main results.

CHAPTER 2

Principles of the TLM Method

The basic ideas of the TLM methods with symmetrical condensed nodes for the solution of electromagnetic field problems are presented in this chapter. The discretization of space using TLM cells and nodes and the TLM scattering algorithm are explained. The symmetrical condensed node is introduced. The differences between the TLM methods without stubs and the TLM methods with stubs is shown and various mappings between discretized electromagnetic field components and TLM state variables are presented. Finally, the HILBERT space formulation of the TLM method is introduced.

1. The TLM Scattering Algorithm

In all TLM methods, continuous space is separated into *TLM cells* by defining intersecting planes. This step is called the *discretization of space* and is shown in Fig. 2.1 (a) and Fig. 2.1 (b). Therefore, the TLM method is a member of the 'family' of space-discretizing methods - another very popular member of this family is the *Finite-Difference-Time-Domain* (FDTD) method originating from [**115**]. Ports are defined at the tangential planes between two neighbouring cells and a scattering centre is defined at the centre of each cell as indicated in Fig. 2.1 (c). Transmission lines connect the centre of each cell with the ports (see also Fig. 2.1 (c)). The physical model, comprising the scattering centre at the centre of a cell that is connected via transmission lines with the ports at the tangential planes between neighbouring cells is called a *TLM node*. Consequently, continuous space is approximated by a mesh of TLM nodes interconnected by transmission lines as depicted in Fig. 2.1 (d). TLM pulses propagate on these transmission lines between the nodes of interconnected cells. These pulses are scattered at the nodes and the scattered pulses propagate to the neighbouring nodes where they are scattered again. The propagation of TLM pulses in a TLM mesh is schematically shown in Fig. 2.2. A matrix equation of the form

$$\boldsymbol{b}_{k;l,m,n} = \boldsymbol{S}_{l,m,n}\boldsymbol{a}_{k;l,m,n}, \tag{2.1}$$

is defined in each of these cells, describing the scattering process. The matrix $\boldsymbol{S}_{l,m,n}$ is the scattering matrix of the TLM node (l,m,n). The TLM node (l,m,n)

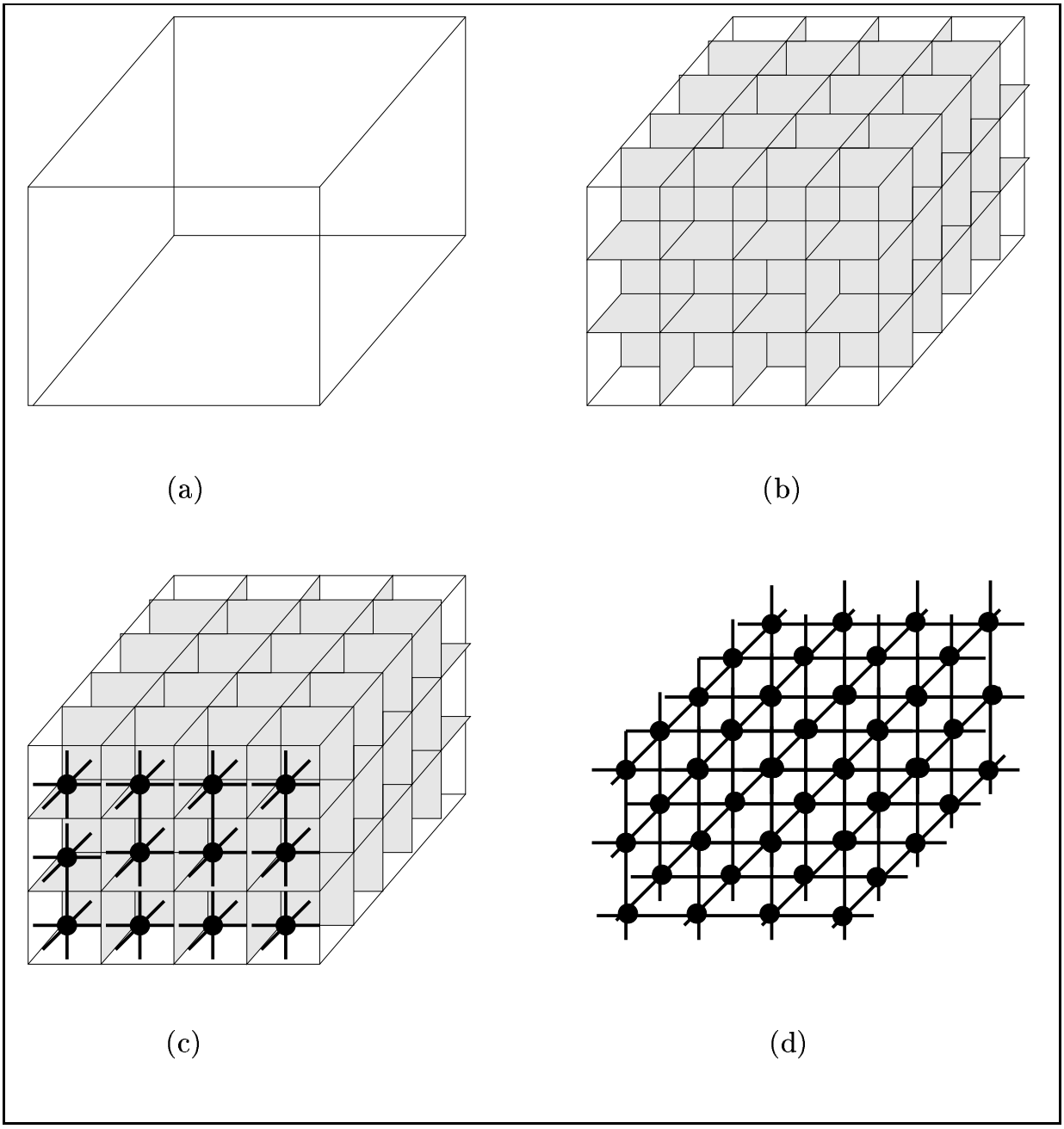

FIGURE 2.1. The approximation of space by an interconnected mesh of TLM nodes in the TLM method. The definition of TLM cells is shown in (a) and (b) and the introduction of interconnected TLM nodes is shown in (c) and (d).

is located at $(l\Delta l, m\Delta l, n\Delta l)$ in a CARTESIAN coordinate system, where Δl constitutes the spacial increment and l, m, n are the spatial indices in $x-, y-$, and $z-$direction of the grid constituted by the location of the TLM nodes. The vectors $\boldsymbol{a}_{k;l,m,n}$ and $\boldsymbol{b}_{k;l,m,n}$ comprise the incident and reflected TLM pulses that

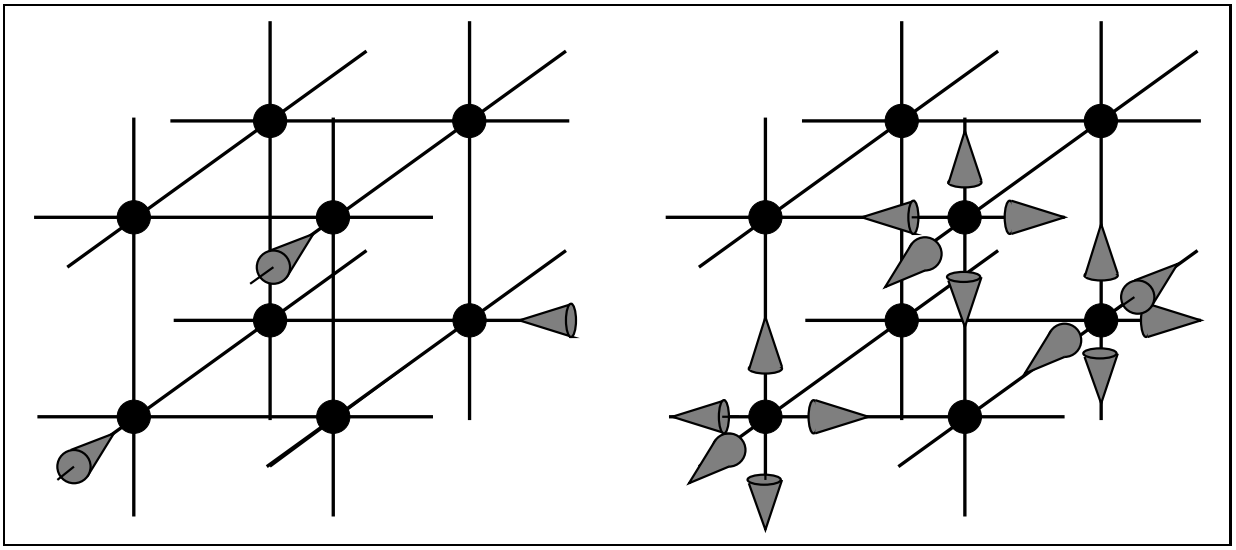

FIGURE 2.2. The propagation of TLM wave pulses in a TLM mesh.

propagate on the transmission lines. They can have different meanings. In many papers $\boldsymbol{a}_{k;l,m,n}$ denote voltage pulses that are incident on the cell, commonly written $\boldsymbol{V}^i_{k;l,m,n}$, whereas the reflected voltages $\boldsymbol{b}_{k;l,m,n}$ are denoted by $\boldsymbol{V}^r_{k;l,m,n}$. The use of voltage pulses has historical reasons, as the TLM-methods originated from real networks, where one could measure physical voltages using network analysers [**39, 110, 111**]. It is equally possible to assign incident and reflected power amplitudes to the vectors $\boldsymbol{a}_{k;l,m,n}$ and $\boldsymbol{b}_{k;l,m,n}$, as done by AIDAM and RUSSER [**2**]. The exchange of pulses between neighbouring cells is achieved by a connection matrix $\boldsymbol{C}$

$$\sum_l \boldsymbol{a}_{k;l,m,n} = \boldsymbol{C} \sum_l \boldsymbol{a}_{k;l,m,n}. \tag{2.2}$$

Iterating equations (2.1) and (2.2), i.e. *scatter* and *connect* in the physical picture, simulates a wave propagation process that closely resembles the propagation of electromagnetic waves in free space or media. An elaborate discussion of the propagation of pulses in TLM meshes with symmetrical condensed nodes can be found in [**28**]. The iteration of equations (2.1) and (2.2) is called the *TLM scattering algorithm*. An excellent review of the principles of the TLM method was given by HOEFER [**30**].

2. The Symmetrical Condensed Node

Today, the commonly used TLM node is the *Symmetrical Condensed Node* (SCN), which was introduced by JOHNS in 1987 [**35**], and its generalizations such

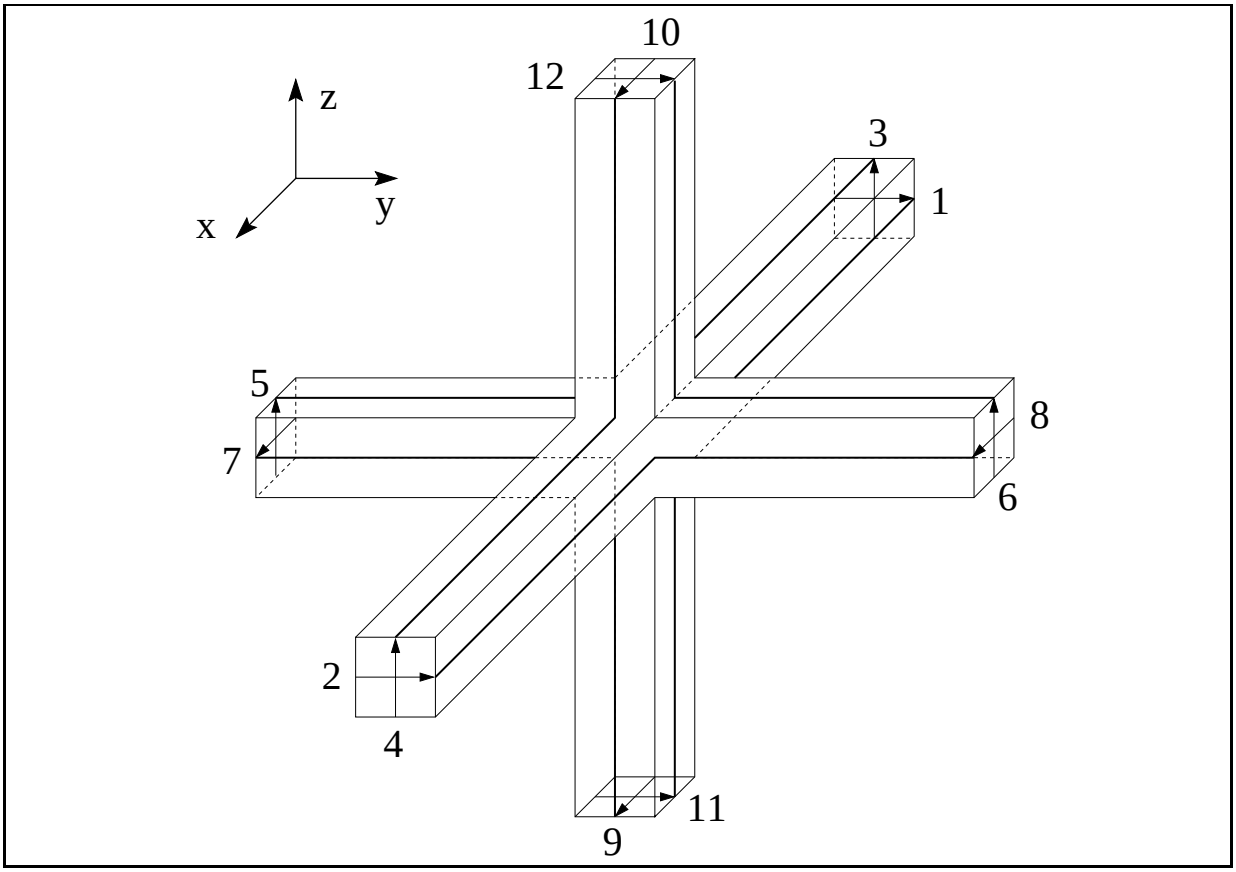

FIGURE 2.3. The symmetrical condensed node.

as the *Hybrid Symmetrical Condensed Node* (HSCN) or *General Symmetrical Condensed Node* (GSCN) [**11, 67, 89, 104, 105, 107**]. The scattering matrix of JOHNS' original node for homogeneous media writes

$$\boldsymbol{S} = \begin{pmatrix} a & c & 0 & 0 & 0 & 0 & d & -d & 0 & 0 & b & b \\ c & a & 0 & 0 & 0 & 0 & -d & d & 0 & 0 & b & b \\ 0 & 0 & a & c & b & b & 0 & 0 & d & -d & 0 & 0 \\ 0 & 0 & c & a & b & b & 0 & 0 & -d & d & 0 & 0 \\ 0 & 0 & b & b & a & c & 0 & 0 & 0 & 0 & d & -d \\ 0 & 0 & b & b & c & a & 0 & 0 & 0 & 0 & -d & d \\ d & -d & 0 & 0 & 0 & 0 & a & c & b & b & 0 & 0 \\ -d & d & 0 & 0 & 0 & 0 & c & a & b & b & 0 & 0 \\ 0 & 0 & d & -d & 0 & 0 & b & b & a & c & 0 & 0 \\ 0 & 0 & -d & d & 0 & 0 & b & b & c & a & 0 & 0 \\ b & b & 0 & 0 & d & -d & 0 & 0 & 0 & 0 & a & c \\ b & b & 0 & 0 & -d & d & 0 & 0 & 0 & 0 & c & a \end{pmatrix}. \tag{2.3}$$

The abstract multi-port that is assigned to it and referred as TLM symmetrical condensed node is depicted in Fig. 2.3. The length of the node in each direction of space is Δl. Each branch that protrudes from the centre in all six directions of space consists of two, with an angle of 90 degrees between them, two-wire transmission lines. Each of them supports one of the two possible polarizations of transverse electromagnetic (TEM) waves on the link lines. The polarization of the TLM pulses follows the direction of the port vectors. Each TLM pulse has an E-field and an H-field component assigned to it. The E-field component is in parallel to the polarization of the TLM pulse, the H-field component perpendicular to it. All six transmission lines of length $\Delta l/2$ have the same characteristic impedance and propagation velocity. The characteristic impedance equals that of free space, i.e. 377 Ω. The drawn connection of the two wire lines in the centre of the node in Fig. 2.3 does not correspond to the actual scattering process. It is simply a mental picture. In brief, JOHNS determined the 12×12 scattering matrix heuristically as follows:

- each incident pulse is according to the field component assigned to it, only connected with some of the other ports. The pulse a^7 for example having an E^x and an H^z field component assigned to it, can according to

$$\varepsilon \frac{\partial E^x}{\partial t} = \frac{\partial H^z}{\partial y} - \frac{\partial H^y}{\partial z} \tag{2.4}$$

  only be scattered into ports 7, 8, 9, and 10, as E^x and H^z are also associated with port 8 on a $y-$directed line, whereas E^x and H^y are associated with ports 7 and 9 on $z-$directed lines,
- by symmetry, there are only four unknown parameters,
- the scattering process must preserve charge,
- the scattering process is supposed to be lossless, so energy must be conserved meaning that the scattering matrix must be unitary

$$\boldsymbol{S}^{\boldsymbol{T}} \boldsymbol{S} = \boldsymbol{I}. \tag{2.5}$$

With this, the unknown parameters a, b, c, and d can be determined as

$$a = 0, \quad b = 0, \quad c = \frac{1}{2}, \quad d = \frac{1}{2}. \tag{2.6}$$

This constitutes one of four possible solutions. The other three solutions are discussed in [**1**].

3. The Symmetrical Condensed Node with Stubs

To account for inhomogeneous media and non-cubic TLM cells, JOHNS added open and short circuited stubs to the node. Each stub has a length according to a propagation time of $\Delta t/2$. The port numbers 13-18 are assigned to the six stubs. The first three stubs couple to E^x, E^y, and E^z. They are open, as to add additional capacitance to the node. The other three stubs are shorted and couple to H^x, H^y, and H^z and add further inductance to the node. As each

Column No.			1	2	3	4	5	6	7	8	9	10	11	12	13	14	15	16	17	18
o/c Stub (Y)			y	y	z	z	z	z	x	x	x	x	y	y	x	y	z			
s/c Stub (Z)			z	z	y	y	x	x	z	z	y	y	x	x				x	y	z
1	y	z	a	c					d	-d			b	b		g				-d
2	y	z	c	a					-d	d			b	b		g				d
3	z	y			a	c	b	b			d	-d					g		d	
4	z	y			c	a	b	b			-d	d					g		-d	
5	z	x			b	b	a	c					d	-d			g	-d		
6	z	x			b	b	c	a					-d	d			g	d		
7	x	z	d	-d					a	c	b	b			g					d
8	x	z	-d	d					c	a	b	b			g					-d
9	x	y			d	-d			b	b	a	c			g				-d	
10	x	y			-d	d			b	b	c	a			g				d	
11	y	x	b	b			d	-d					a	c		g		d		
12	y	x	b	b			-d	d					c	a		g		-d		
13	x								b	b	b	b		0	h					
14	y		b	b									b	b		h				
15	z				b	b	b	b									h			
16		x					-f	f					f	-f				j		
17		y			f	-f					-f	f							j	
18		z	-f	f					f	-f										j
Row (Y) (Z)																				

TABLE 2.1. The scattering matrix with stubs.

stub only couples to one of the field components, it is possible to account for anisotropic material properties, namely permittivity ε_x, ε_y, ε_z, and permeability μ_x, μ_y, μ_z. The scattering matrix of the SCN with stubs can be found in table 2.1. JOHNS obtained the normalized values of the stubs as follows. A field component E^x experiences a total capacitance of $C_x = \varepsilon_x vw\Delta l/u$. The dimensions of a non-cubic TLM cell in $x-$, $y-$, and $z-$direction are $u\Delta l$, $v\Delta l$, and $w\Delta l$. A symmetrical condensed node without stubs has the following capacitance

$$C_{\text{SCN without stubs},x} = \frac{\Delta l \varepsilon_0}{h}, \tag{2.7}$$

where h is a stability factor given by

$$h = \frac{2\Delta l}{c_0 \Delta t} \tag{2.8}$$

and c_0 the speed of light. Consequently, the capacitance of the stub connected with E^x is the difference between total capacitance and capacitance of the symmetrical condensed node without stub, or

$$C_{stub,x} = 2\frac{\varepsilon_x vw\Delta l}{u} - \frac{\Delta l\varepsilon_0}{h}. \tag{2.9}$$

The total capacitance is multiplied by 2 in order to account for the fact that the symmetrical condensed node models a medium of twice the permittivity and permeability of the transmission lines it consists of. The admittance of the stub is calculated using the relation between admittance and low frequency capacitance

$$C_{stub} = Y_0 Y_{stub}\frac{\Delta t}{2} = Y_{stub}\frac{\Delta l\varepsilon_0}{h}, \tag{2.10}$$

where ε_0 is the permittivity of free space. With this and normed to the free space impedance Z_0, the admittances of stubs 13 to 15 are calculated by

$$Y_x = 2\left(\frac{vw}{u}h\varepsilon_{rx} - 2\right), Y_y = 2\left(\frac{uw}{v}h\varepsilon_{ry} - 2\right), Y_z = 2\left(\frac{uv}{w}h\varepsilon_{rz} - 2\right), \tag{2.11}$$

where ε_{rx}, ε_{ry}, and ε_{rz} denote the relative permittivities. The impedances of stubs 16 to 18 are calculated in a similar manner, which results in

$$Z_x = 2\left(\frac{vw}{u}h\mu_{rx} - 2\right), Z_y = 2\left(\frac{uw}{v}h\mu_{ry} - 2\right), Z_z = 2\left(\frac{uv}{w}h\mu_{rz} - 2\right). \tag{2.12}$$

The relative permeabilities are denoted by μ_{rx}, μ_{ry}, and μ_{rz}. If ohmic and magnetic losses have to be considered, six additional stubs are connected to the centre of a node [**67**]. The scattering in these stubs needs not explicitly be considered as the energy dissipated in these lines is lost. The values of the loss stubs for simulating ohmic losses are given by

$$G_x = \frac{vw}{u}\sigma_{ex}\Delta l Z_0, \qquad G_y = \frac{uw}{v}\sigma_{ey}\Delta l Z_0, \qquad G_z = \frac{uv}{w}\sigma_{ez}\Delta l Z_0, \tag{2.13}$$

where σ_{ex}, σ_{ey}, and σ_{ez} stand for the electric conductivities in $x-$, $y-$, and $z-$direction. The loss stubs considering magnetic losses calculate analogously

$$R_x = \frac{vw}{u}\frac{\sigma_{mx}\Delta l}{Z_0}, \qquad R_y = \frac{uw}{v}\frac{\sigma_{my}\Delta l}{Z_0}, \qquad R_z = \frac{uv}{w}\frac{\sigma_{mz}\Delta l}{Z_0}, \tag{2.14}$$

with anisotropic magnetic conductivities σ_{mx}, σ_{my}, and σ_{mz}. Considering the loss stubs, the coefficients of the scattering matrix of the symmetrical condensed node are given as follows

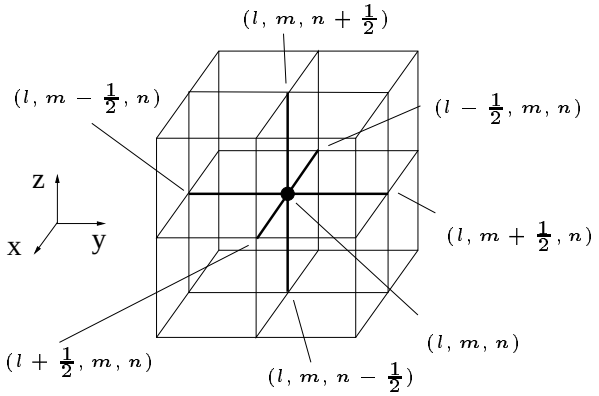

FIGURE 2.4. A TLM cell.

$$
\begin{aligned}
a &= -\frac{G+Y}{2(G+Y+4)} + \frac{R+Z}{2(R+Z+4)}, & b &= \frac{2}{G+Y+4},\\
c &= -\frac{G+Y}{2(G+Y+4)} - \frac{R+Z}{2(R+Z+4)}, & d &= \frac{2}{Z+R+4},\\
f &= \frac{2Z}{R+Z+4}, & g &= \frac{2Y}{G+Y+4},\\
h &= -\frac{G-Y+4}{G+Y+4}, & j &= \frac{4-Z+R}{R+Z+4}.
\end{aligned} \tag{2.15}
$$

The subscripts x, y, and z of the stubs are assigned according to Table 2.1. A lumped equivalent circuit descriptions that can be assigned to the symmetrical condensed node is reported in [**62**]. The scattering given by the modified JOHNS' scattering matrix following Fig. 2.1 can be calculated very efficiently using equivalent node voltages and equivalent loop currents [**66, 101**]. The most efficient algorithm is provided by the representation introduced in [**66**]. The influence of the number of floating point operations of a particular representation of the scattering matrix on the performance of TLM codes was recently investigated in [**5, 55**].

4. Field-Mappings for the Symmetrical Condensed Node

If we consider a TLM cell as depicted in Fig. 2.4, it is possible to define the mapping between the TLM state variables and the electromagnetic field components either at the centre of the cell located at (l, m, n), or at the centre of the tangential planes, i.e. at positions $(l, m, n+\frac{1}{2})$, $(l, m, n-\frac{1}{2})$, $(l, m+\frac{1}{2}, n)$, $(l, m-\frac{1}{2}, n)$, $(l+\frac{1}{2}, m, n)$, and $(l-\frac{1}{2}, m, n)$. The mapping in the centre shall be referred to by *cell-centred field-mapping* (CFM) and the mapping at the boundaries of the TLM cell by *boundary oriented field-mapping* (BOFM).

Originally, the mapping was defined at the centre. Consequently, this mapping is not bijective, as in the TLM algorithm one has twelve or more variables and in MAXWELL's equations, there are only six electromagnetic field components in one point of space. The CFM following JOHNS writes

$$\boldsymbol{f}_{k;l,m,n} = \boldsymbol{P}\boldsymbol{a}_{k;l,m,n}, \tag{2.16}$$

$$\boldsymbol{a}_{k;l,m,n} = \boldsymbol{Q}\boldsymbol{f}_{k;l,m,n}. \tag{2.17}$$

The vector $\boldsymbol{f}_{k;l,m,n}$ comprises the six electromagnetic field components, sampled in the centre of a TLM cell

$$\boldsymbol{f}_{k;l,m,n} = [E^x_{k;l,m,n}, E^y_{k;l,m,n}, E^z_{k;l,m,n}, Z_0 H^x_{k;l,m,n}, Z_0 H^y_{k;l,m,n}, Z_0 H^z_{k;l,m,n}]^T, \tag{2.18}$$

whereas $\boldsymbol{a}_{k;l,m,n}$ is the vector of the incident TLM pulses

$$\boldsymbol{a}_{k;l,m,n} = \left[a^1, a^2, a^3, a^4, a^5, a^6, a^7, a^8, a^9, a^{10}, a^{11}, a^{12}\right]^T_{k;l,m,n}, \tag{2.19}$$

or in case of stubs

$$\boldsymbol{a}_{k;l,m,n} = \left[a^1, a^2, a^3, a^4, a^5, a^6, a^7, a^8, a^9, a^{10}, a^{11}, a^{12}, a^{13}, a^{14}, a^{15}, a^{16}, a^{17}, a^{18}\right]^T_{k;l,m,n}. \tag{2.20}$$

For the symmetrical condensed node without stubs, JOHNS gave the matrices $\boldsymbol{P}$ and $\boldsymbol{Q}$ as

$$\boldsymbol{P} = \boldsymbol{Q}^T = \frac{1}{2}\begin{pmatrix} 0 & 0 & 0 & 0 & 0 & 0 & 1 & 1 & 1 & 1 & 0 & 0 \\ 1 & 1 & 0 & 0 & 0 & 0 & 0 & 0 & 0 & 0 & 1 & 1 \\ 0 & 0 & 1 & 1 & 1 & 1 & 0 & 0 & 0 & 0 & 0 & 0 \\ 0 & 0 & 0 & 0 & 1 & -1 & 0 & 0 & 0 & 0 & -1 & 1 \\ 0 & 0 & -1 & 1 & 0 & 0 & 0 & 0 & 1 & -1 & 0 & 0 \\ 1 & -1 & 0 & 0 & 0 & 0 & -1 & 1 & 0 & 0 & 0 & 0 \end{pmatrix}. \tag{2.21}$$

For the symmetrical condensed node with stubs considering ohmic and magnetic losses, $\boldsymbol{P}$ and $\boldsymbol{Q}$ take the following form

$$\boldsymbol{P} = \begin{pmatrix} 0 & b_y & 0 & 0 & 0 & d_z \\ 0 & b_y & 0 & 0 & 0 & -d_z \\ 0 & 0 & b_z & 0 & -d_y & 0 \\ 0 & 0 & b_z & 0 & d_y & 0 \\ 0 & 0 & b_z & d_x & 0 & 0 \\ 0 & 0 & b_z & -d_x & 0 & 0 \\ b_x & 0 & 0 & 0 & 0 & -d_z \\ b_x & 0 & 0 & 0 & 0 & d_z \\ b_x & 0 & 0 & 0 & d_y & 0 \\ b_x & 0 & 0 & 0 & -d_y & 0 \\ 0 & b_y & 0 & -d_x & 0 & 0 \\ 0 & b_y & 0 & d_x & 0 & 0 \\ b_x Y_x & 0 & 0 & 0 & 0 & 0 \\ 0 & b_y Y_y & 0 & 0 & 0 & 0 \\ 0 & 0 & b_z Y_z & 0 & 0 & 0 \\ 0 & 0 & 0 & -d_x & 0 & 0 \\ 0 & 0 & 0 & 0 & -d_y & 0 \\ 0 & 0 & 0 & 0 & 0 & -d_z \end{pmatrix}^T, \tag{2.22}$$

with the coefficients

$$b_x = \frac{2}{u(Y_x + 4)}, \qquad b_y = \frac{2}{v(Y_y + 4)}, \qquad b_z = \frac{2}{w(Y_z + 4)}, \tag{2.23}$$

$$d_x = \frac{2}{u(Z_x + 4)}, \qquad d_y = \frac{2}{v(Z_y + 4)}, \qquad d_z = \frac{2}{w(Z_z + 4)}. \tag{2.24}$$

The mapping from field components to TLM pulses to excite the TLM mesh is given by

$$\boldsymbol{Q} = \frac{1}{2}\begin{pmatrix} 0 & v & 0 & 0 & 0 & -w \\ 0 & v & 0 & 0 & 0 & w \\ 0 & 0 & w & 0 & v & 0 \\ 0 & 0 & w & 0 & -v & 0 \\ 0 & 0 & w & -u & 0 & 0 \\ 0 & 0 & w & u & 0 & 0 \\ u & 0 & 0 & 0 & 0 & w \\ u & 0 & 0 & 0 & 0 & -w \\ u & 0 & 0 & 0 & -v & 0 \\ u & 0 & 0 & 0 & v & 0 \\ 0 & v & 0 & u & 0 & 0 \\ 0 & v & 0 & -u & 0 & 0 \\ ua_x & 0 & 0 & 0 & 0 & 0 \\ 0 & va_y & 0 & 0 & 0 & 0 \\ 0 & 0 & wa_z & 0 & 0 & 0 \\ 0 & 0 & 0 & -uc_x & 0 & 0 \\ 0 & 0 & 0 & 0 & -vc_y & 0 \\ 0 & 0 & 0 & 0 & 0 & -wc_z \end{pmatrix}, \tag{2.25}$$

with the coefficients

$$a_x = \frac{Y_x + G_x}{Y_x}, \qquad a_y = \frac{Y_y + G_y}{Y_y}, \qquad a_z = \frac{Y_z + G_z}{Y_z}, \tag{2.26}$$

$$c_x = Z_x + R_x, \qquad c_y = Z_y + R_y, \qquad c_z = Z_z + R_z. \tag{2.27}$$

The coefficients a_x, and a_y, and a_z are slightly modified in comparison to [**62**]. This modification originates from an equivalent circuit representation in terms of the total voltage in the centre of a node [**102**]. However, this modification is also nescessary due to a more profound analysis in terms of consistency of mapping induced finite difference schemes of the SCN-TLM scheme, which will become evident in Chapter 5.

Assuming a correspondence between the TLM state variables and the electromagnetic field components at the centre of the tangential planes yields a bijective field-mapping introduced by KRUMPHOLZ and RUSSER [**44, 46**] and independently by HEIN [**23**]. This field-mapping is given by

$$\boldsymbol{E}_{k;l,m,n} = \boldsymbol{P}_E(\boldsymbol{a}^l_{k;l,m,n} + \boldsymbol{b}^l_{k;l,m,n}), \tag{2.28}$$

$$\boldsymbol{H}_{k;l,m,n} = \frac{1}{Z_0}\boldsymbol{P}_H(\boldsymbol{a}^l_{k;l,m,n} - \boldsymbol{b}^l_{k;l,m,n}), \tag{2.29}$$

with the matrices

$$\boldsymbol{P}_E = \begin{pmatrix} \boldsymbol{B}(y,z) & \boldsymbol{0} & \boldsymbol{0} \\ \boldsymbol{0} & \boldsymbol{B}(z,x) & \boldsymbol{0} \\ \boldsymbol{0} & \boldsymbol{0} & \boldsymbol{B}(x,y) \end{pmatrix} \tag{2.30}$$

and

$$\boldsymbol{P}_H = \begin{pmatrix} \boldsymbol{C}(z,y) & \boldsymbol{0} & \boldsymbol{0} \\ \boldsymbol{0} & \boldsymbol{C}(x,z) & \boldsymbol{0} \\ \boldsymbol{0} & \boldsymbol{0} & \boldsymbol{C}(y,x) \end{pmatrix}. \tag{2.31}$$

The submatrices $\boldsymbol{B}(y,z)$ and $\boldsymbol{C}(z,y)$ constituting $\boldsymbol{P}_E$ and $\boldsymbol{P}_H$ write

$$\boldsymbol{B}(y,z) = \begin{pmatrix} \frac{1}{\Delta y} & 0 & 0 & 0 \\ 0 & \frac{1}{\Delta y} & 0 & 0 \\ 0 & 0 & \frac{1}{\Delta z} & 0 \\ 0 & 0 & 0 & \frac{1}{\Delta z} \end{pmatrix} \tag{2.32}$$

and

$$\boldsymbol{C}(z,y) = \begin{pmatrix} \frac{1}{\Delta z} & 0 & 0 & 0 \\ 0 & -\frac{1}{\Delta z} & 0 & 0 \\ 0 & 0 & -\frac{1}{\Delta y} & 0 \\ 0 & 0 & 0 & \frac{1}{\Delta y} \end{pmatrix}. \tag{2.33}$$

The vectors $\boldsymbol{E}_{k;l,m,n}$ and $\boldsymbol{H}_{k;l,m,n}$ comprise the tangential field components on the surface of a TLM cell

$$\boldsymbol{E}_{k;l,m,n} = \begin{bmatrix} E^y_{k;l-\frac{1}{2},m,n} \\ E^y_{k;l+\frac{1}{2},m,n} \\ E^z_{k;l-\frac{1}{2},m,n} \\ E^z_{k;l+\frac{1}{2},m,n} \\ E^z_{k;l,m-\frac{1}{2},n} \\ E^z_{k;l,m+\frac{1}{2},n} \\ E^x_{k;l,m-\frac{1}{2},n} \\ E^x_{k;l,m+\frac{1}{2},n} \\ E^x_{k;l,m,n-\frac{1}{2}} \\ E^x_{k;l,m,n+\frac{1}{2}} \\ E^y_{k;l,m,n-\frac{1}{2}} \\ E^y_{k;l,m,n+\frac{1}{2}} \end{bmatrix}, \qquad \boldsymbol{H}_{k;l,m,n} = \begin{bmatrix} H^z_{k;l-\frac{1}{2},m,n} \\ H^z_{k;l+\frac{1}{2},m,n} \\ H^y_{k;l-\frac{1}{2},m,n} \\ H^y_{k;l+\frac{1}{2},m,n} \\ H^x_{k;l,m-\frac{1}{2},n} \\ H^x_{k;l,m+\frac{1}{2},n} \\ H^z_{k,l,m-\frac{1}{2},n} \\ H^z_{k;l,m+\frac{1}{2},n} \\ H^y_{k;l,m,n-\frac{1}{2}} \\ H^y_{k;l,m,n+\frac{1}{2}} \\ H^x_{k;l,m,n-\frac{1}{2}} \\ H^x_{k,l,m,n+\frac{1}{2}} \end{bmatrix}. \tag{2.34}$$

The vector $\boldsymbol{a}^{l}_{k;l,m,n}$ comprises the incident TLM pulses on the *link* lines (hence the superscript l) as given by eqn. (2.19). The vector of the reflected TLM pulses on link lines is denoted by $\boldsymbol{b}^{l}_{k;l,m,n}$.

5. The TLM Algorithm in Hilbert Space Notation

The set of all state vectors $\boldsymbol{a}$ and $\boldsymbol{b}$ represents the complete state of the discretized electromagnetic field at time k. If we discretize the physical space as described in Section 2.1 we get an enumerable infinite number of TLM cells. The field state of each cell is given by the 12- or 18-dimensional vectors of incident and reflected TLM pulses. The whole set of these vectors comprises an approximate solution of the electromagnetic field problem. As one has not only in space but also in time an enumerable infinite number of intervals, it is possible to define an HILBERT space for describing the discrete field problem [**87**]. The relation to an appropriate function space is shown in Chapter 4. In this abstract HILBERT space, it is possible to investigate the TLM algorithm algebraically, which facilitates the calculation of the dispersion characteristics of TLM meshes [**42**]. A basevector, characterized by the number triple (l, m, n), is assigned to each TLM cell. If the HILBERT space is chosen appropriately, the base vectors fulfil the orthogonality relation

$$<p, q, r|l, m, n> = \delta_{pl}\delta_{qm}\delta_{rn}. \tag{2.35}$$

The HERMITIAN conjugate is denoted by $< p, q, r|$. The CARTESIAN product of the space of base vectors with the space of TLM pulse vectors defines a space for describing the complete field state at time k. The state vector of all incident TLM pulses $|a(k)>$ at time k is given by

$$|a(k)> = \sum_{l=-\infty}^{+\infty} \sum_{m=-\infty}^{+\infty} \sum_{n=-\infty}^{+\infty} \boldsymbol{a}_{k;l,m,n}|l, m, n> . \tag{2.36}$$

Applying the projection operator $|l, m, n><l, m, n|$ yields the vector of the incident wave pulses of TLM cell (l, m, n)

$$|l, m, n><l, m, n|a(k)> = \boldsymbol{a}_{k;l,m,n}|l, m, n> . \tag{2.37}$$

Unitary shift operators $\boldsymbol{X}$, $\boldsymbol{Y}$, $\boldsymbol{Z}$, and their HERMITIAN conjugate $\boldsymbol{X}^{\dagger}$, $\boldsymbol{Y}^{\dagger}$, $\boldsymbol{Z}^{\dagger}$ are defined as

$$\boldsymbol{X}|l,m,n> = |l+1,m,n> , \tag{2.38}$$

$$\boldsymbol{X}^{\dagger}|l,m,n> = |l-1,m,n> , \tag{2.39}$$

$$\boldsymbol{Y}|l,m,n> = |l,m+1,n> , \tag{2.40}$$

$$\boldsymbol{Y}^{\dagger}|l,m,n> = |l,m-1,n> , \tag{2.41}$$

$$\boldsymbol{Z}|l,m,n> = |l,m,n+1> , \tag{2.42}$$

$$\boldsymbol{Z}^{\dagger}|l,m,n> = |l,m,n-1> \ . \tag{2.43}$$

Using these operators, the connection matrix (2.2) can be defined as connection operator $\boldsymbol{\Gamma}$

$$\boldsymbol{\Gamma} = \begin{pmatrix}
0 & \boldsymbol{X} & 0 & 0 & 0 & 0 & 0 & 0 & 0 & 0 & 0 & 0 \\
\boldsymbol{X}^{\dagger} & 0 & 0 & 0 & 0 & 0 & 0 & 0 & 0 & 0 & 0 & 0 \\
0 & 0 & 0 & \boldsymbol{X} & 0 & 0 & 0 & 0 & 0 & 0 & 0 & 0 \\
0 & 0 & \boldsymbol{X}^{\dagger} & 0 & 0 & 0 & 0 & 0 & 0 & 0 & 0 & 0 \\
0 & 0 & 0 & 0 & 0 & \boldsymbol{Y} & 0 & 0 & 0 & 0 & 0 & 0 \\
0 & 0 & 0 & 0 & \boldsymbol{Y}^{\dagger} & 0 & 0 & 0 & 0 & 0 & 0 & 0 \\
0 & 0 & 0 & 0 & 0 & 0 & 0 & \boldsymbol{Y} & 0 & 0 & 0 & 0 \\
0 & 0 & 0 & 0 & 0 & 0 & \boldsymbol{Y}^{\dagger} & 0 & 0 & 0 & 0 & 0 \\
0 & 0 & 0 & 0 & 0 & 0 & 0 & 0 & 0 & \boldsymbol{Z} & 0 & 0 \\
0 & 0 & 0 & 0 & 0 & 0 & 0 & 0 & \boldsymbol{Z}^{\dagger} & 0 & 0 & 0 \\
0 & 0 & 0 & 0 & 0 & 0 & 0 & 0 & 0 & 0 & 0 & \boldsymbol{Z} \\
0 & 0 & 0 & 0 & 0 & 0 & 0 & 0 & 0 & 0 & \boldsymbol{Z}^{\dagger} & 0
\end{pmatrix} . \tag{2.44}$$

The connection operator $\boldsymbol{\Gamma}$ is unitary and HERMITIAN. As the reflected pulses from one TLM cell are the incident TLM pulses of the neighbouring cells, the field state is completely defined by $|a(k)>$ and $|b(k)>$. Hence,

$$|a(k)> = \boldsymbol{\Gamma}|b(k)> \quad \text{and} \quad |b(k)> = \boldsymbol{\Gamma}^{\dagger}|a(k)> . \tag{2.45}$$

A base vector $|k>$ is assigned to each point in time to account for the evolution in time, which also fulfils the orthogonality relation

$$<k|k^{'}> = \delta_{kk'} . \tag{2.46}$$

Building the CARTESIAN product of the HILBERT space of temporal base vectors and the HILBERT space of all state vectors at time k, yields a HILBERT space where all state vectors at all times are defined. In this space the state vector of all incident wave pulses at all times is given by

$$|a> = \sum_{k=-\infty}^{+\infty} |k> \otimes |a(k)> \tag{2.47}$$
$$= \sum_{k,l,m,n} |k> \; \boldsymbol{a}_{k;l,m,n} \otimes |l,m,n>$$
$$= \sum_{k,l,m,n} \boldsymbol{a}_{k;l,m,n} |k;l,m,n> .$$

The vector of all reflected wave pulses at all times is given by

$$|b> = \sum_{k,l,m,n} \boldsymbol{b}_{k;l,m,n} |k;l,m,n> . \tag{2.48}$$

For describing the time evolution, a unitary time shift operator is defined by

$$\boldsymbol{T}|k> = |k+1> \tag{2.49}$$

and its HERMITIAN conjugate by

$$\boldsymbol{T}^{\dagger}|k> = |k-1> . \tag{2.50}$$

With these vectors and operators, the TLM algorithm writes

$$|b> = \boldsymbol{T}\boldsymbol{S}|a>, \tag{2.51}$$
$$|a> = \boldsymbol{\Gamma}|b> . \tag{2.52}$$

The scattering operator $\boldsymbol{S}$ is given by

$$\boldsymbol{S} = \sum_{k;l,m,n} |k;l,m,n> \; \boldsymbol{S}_{k;l,m,n} \; <k;l,m,n|, \tag{2.53}$$

where $\boldsymbol{S}_{k;l,m,n}$ denotes the local scattering matrix of cell (l,m,n), i.e. eqn. (2.3) in case of the symmetrical condensed node without stubs or Fig. 2.1 in case of the symmetrical condensed node with stubs. In the sequel of this study, the indices k,l,m,n indicating local operators are omitted.

CHAPTER 3

State of Research

The historic development of the TLM method with symmetrical condensed node was roughly sketched in Chapter 1. This development can be seen as a succession of different interpretations of the basic TLM scattering algorithm. In this chapter, we classify the various formulations of the SCN-TLM method using the utilized mapping between TLM state variables and electromagnetic field components. Further, an overview of the theoretical work with relevance to convergence and accuracy of the SCN-TLM method is given. Finally, we discuss some recent applications of the SCN-TLM method for the characterisation of planar microwave circuits.

1. Overview of SCN-TLM Formulations

For deriving the symmetrical condensed node, it is necessary to sample the electromagnetic field components at certain points of the TLM cell, as discussed in the previous chapter. This was originally done in the centre of a TLM cell. It is equally possible to define a correspondence between electromagnetic field components and TLM pulses at the tangential planes between neighbouring cells. This was explicitly introduced by KRUMPHOLZ and RUSSER [**44, 46**] and independently by HEIN [**23**]. These authors were the first to discover that the mapping between the TLM wave pulses and the discretized electromagnetic field components has an important influence on the interpretation of the basic scattering algorithm in the sense of different approximation schemes of MAXWELL's equations. Some authors like CHEN, NEY, HOEFER, JIN, and VAHLDIECK, utilized implicitly both mappings for their formulations [**14, 34**]. An overview of the derivations of the SCN-TLM method gives Table 3.1.

For deriving the finite difference scheme that CHEN, NEY, and HOEFER proposed to be equivalent to the symmetrical condensed node, the electromagnetic field was sampled both at the centre of a TLM cell, where all six components are considered, and at the boundaries of a TLM cell, where only the tangential components were taken into account [**14**]. MAXWELL's equations were replaced in each cell by a set of difference equations where the partial derivatives were approximated by centred differences. The energy conservation principle was applied to get updated values of both the $\boldsymbol{E}$- and $\boldsymbol{H}$-field components. Total voltages and

author	year	method	mapping	auxiliary mapping	SCN with stubs
Johns	1987	analogy	CFM	-	yes
Chen, Ney, Hoefer	1991	finite differencing	CFM	BOFM	no
LoVetri, Simons	1993	conservation law and generalized inverse matrices	CFM	-	no
Hein	1993	propagator integral	BOFM	-	yes
Krumpholz, Russer	1994	method of moments	BOFM	-	no
Jin, Vahldieck	1994	finite differencing and averaging	modified CFM	BOFM	yes
Aidam, Russer	1997	finite integration	BOFM	-	no
Tardioli, Hoefer	1998	finite integration and TEM wave propagation	CFM	BOFM	no

TABLE 3.1. Overview of formulations of the symmetrical condensed node.

currents that are the sum or the difference of incoming and reflected pulses were defined at the boundary of a cell. The correspondence between voltages in the TLM mesh and field components is essentially the same as described by the bijective boundary oriented field-mapping, introduced by KRUMPHOLZ and RUSSER. At the node, JOHNS' original mapping was applied to get a correspondence between field components and TLM voltages. A numerical convergence study, where the cutoff frequency of a finned waveguide was calculated using various discretizations, concluded the paper.

LOVETRI and SIMONS started from MAXWELL's curl equations written as a system of hyperbolic conservation laws, to derive the set of constituting equations of the SCN-TLM algorithm [**52, 53**]. These conservation laws were then approximated in each TLM cell as three systems of equations, as it was assumed that propagation along a certain direction (i.e. along the $x-$, $y-$, or $z-$direction), does not involve any variation along the respective transverse directions. Each of these three systems of hyperbolic conservation laws was then uncoupled by diagonalization. New variables called RIEMANN invariants were defined and constitute the propagating pulses in the TLM mesh. They represent the plane wave solutions of these equations corresponding to nonzero eigenvalues or speeds of propagation. These RIEMANN invariants are equivalent to the voltages that JOHNS defined. The mapping between the RIEMANN invariants and the electromagnetic field components was given by JOHNS' original mapping. Considering the propagation of the RIEMANN invariants and defining scattering events at the centre of the TLM cells, scattering matrices could be constructed using MOORE-PENROSE generalized inverses. One of the constructed scattering matrices was the one originally given by JOHNS. Although a mapping induced finite difference scheme was derived and analysed with respect to dispersion and dissipation, the differences to the usual mode of operation of the TLM algorithm when not mapping forth and back between field components and TLM pulses at each time step, were not considered [**53**]. Hence, no estimation of the asymptotic error of SCN-TLM using JOHNS' mapping was given.

The basic idea behind HEIN's approach to TLM was to consider the TLM algorithm as a state system whose response should fulfil a second order FD scheme at every iteration step. From this fulfilment requirement one was led to a procedure to determine the scattering parameters of the scattering matrix from the discretized MAXWELL's equations. MAXWELL's equations were discretized by finite differencing. The stub ports of the scattering matrix were eliminated algebraically leading to a geometrical series representation of the scattering response of a TLM cell. This series representation is formally equivalent to a discrete propagator integral. To decouple the scattering response, the scattering matrix were transformed into its eigensystem. The discretized field components in the finite difference equations were replaced by TLM wave pulses using the bijective boundary oriented mapping. The finite difference scheme was also transformed in the

same manner. For sampling the field at the centre of the TLM cell, the arithmetic mean of the tangential field components was assumed. The decoupled scattering responses were inserted into the transformed finite difference scheme and the scattering parameters of the TLM scattering matrix were calculated. As a consequence of this construction, consistency and second order convergence of the TLM solutions were guaranteed, as the TLM scattering parameters were directly calculated from a consistent second order finite difference scheme approximating MAXWELL's equations. When ohmic and magnetic losses had to be considered, the values of the open and short stubs and thus the matrix elements were calculated slightly differently with this approach, compared to the original scattering matrix with stubs. This approach was extended to non-orthogonal cells and for solving the coupled BLOCH-MAXWELL equations [**24, 26**]. For these applications, MAXWELL's equations are discretized by finite integration. In Chapter 8, this approach is employed to derive a SCN-TLM algorithm for simulating single pole dispersive media.

KRUMPHOLZ and RUSSER applied the Method-of-Moments to MAXWELL's equations to derive the fundamental TLM equations for the symmetrical condensed node without stubs [**44**]. The field components were represented by an expansion in subdomain base functions. Triangle functions in time and a product of two-dimensional triangle functions and rectangular pulse functions with respect to space were used as subdomain base functions. As test functions, delta functions and their derivatives were chosen. The test functions were shifted by half an interval in space and time with respect to the maximum of the base functions. Calculating the inner products, discretized field equations for the electric and magnetic field components were obtained. Applying the bijective cell boundary mapping between field components and TLM variables, the TLM equations were obtained. As in one spatial coordinate a step approximation was assumed and a piecewise linear approximation in the other three coordinates, a second order approximation error was predicted.

JIN and VAHLDIECK introduced a rectangular grid, where the electromagnetic field was sampled both at the centre of the tangential planes between neighbouring TLM cells and at the centre of a TLM cell to get the SCN-TLM scattering equations [**34**]. In the tangential planes, only the tangential field components were considered. Stubs were introduced and a new coordinate system of mixed space-time coordinates was introduced and with the aid of these, the six MAXWELLian equations were transformed. Then, a set of finite difference equations was obtained by centred-differencing with respect to even time steps. A second set of difference equations was obtained by centred-differencing of MAXWELL's equation with respect to half time steps. Both sets of equations were averaged and yielded the scattering equations of the symmetrical condensed node. The boundary oriented field-mapping was implicitly used to sample the electromagnetic field in the tangential planes. A slightly modified JOHNS' field-mapping was introduced for

mapping the nodal field components. As centred differencing was used to get the TLM scattering equations, a second order convergence was assumed. However, the difference between mapping at the tangential planes and mapping at the node was not considered. Excitation of the TLM mesh and sampling the electromagnetic field at the boundaries of the cells yields indeed second order convergence as shown by HEIN's construction [**23**]. This is only assured in the lossless case, as the stubs and matrix elements are calculated slightly differently in case of losses when using the propagator approach.

AIDAM and RUSSER obtained six of the twelve linearly independent TLM equations of the symmetrical condensed node without stubs by finite integration of MAXWELL's equations in integral form and by applying the cell boundary oriented field-mapping [**1, 2**]. The other six equations were obtained by taking the gradient of MAXWELL's equations and integrating over the volume of the cube. This yields eighteen additional equations, where the six non-diagonal elements of the symmetrical part of these tensor equations were taken to get the complete TLM scheme. For the discretization of time, a CRANK-NICOLSON scheme was used, i.e. the time derivative was replaced by forward differences and the remaining terms by the arithmetic mean of the two time steps involved. In terms of accuracy, this suggested second order accuracy, as the CRANK-NICHOLSON scheme is second order accurate in time and second order accurate in space [**100**].

Recently, TARDIOLI and HOEFER presented a derivation of the scattering matrix of the symmetrical condensed node without stubs from the integral formulation of MAXWELL's equations [**99**]. The integral form of MAXWELL's equations, i.e. AMPÈRE's and FARADAY's law, were discretized using finite integration and centred differencing in time. This yielded in connection with the cell boundary oriented field-mapping six difference equations. The second set of equations that is necessary to get the twelve constituting equations of the SCN were obtained by considering plane waves, which propagate through a TLM cell, and applying considerations on energy conservation. However, the authors emphasized that their procedure is only applicable for cubic cells and for a symmetrical condensed node without stubs. The authors did not comment on the presumed order of convergence of their formulation.

2. Properties of the SCN-TLM Mesh

A different way of showing convergence and determining the asymptotic accuracy of finite difference schemes is the investigation of their dispersion characteristics. Generally, one desires that the difference scheme approximating certain partial differential equations has the same dispersion and dissipativity properties as the corresponding partial differential equations [**100**]. For that reason, the dispersion characteristics of the TLM mesh were extensively investigated both numerically and analytically. If the dispersion and dissipativity properties of two

schemes are the same, then the solutions they provide are equivalent. This fact was exploited in synthesizing fourth order TLM models [**95**].

The first complete dispersion analysis of a condensed node TLM mesh was presented by NIELSEN and HOEFER [**70**–**72**]. In these work, the eigenvalue equation was solved numerically. It emerged that the symmetrical condensed node exhibits superior dispersion properties when compared to the popular FDTD scheme, based on the YEE-cell [**115**], and to the expanded node TLM. The reason for this is that the symmetrical condensed node without stubs exhibits no dispersion along the principal axes. Although the symmetrical condensed node has distinct advantages in comparison to other types of nodes such as better dispersion properties, a correct modelling of boundaries, and a collocated field sampling of all field components in one point in space, it was found that an SCN mesh has the undesired feature of supporting propagating unphysical low-frequency modes.

The numerical anisotropy and the dispersion in TLM meshes for different types of nodes, i.e. Johns' SCN and various types of hybrid symmetrical condensed nodes, were investigated by BERINI and WU [**10**]. The study considered also graded meshes and lossy media. For graded meshes, the symmetrical condensed node mesh exhibits more anisotropic dispersion than hybrid symmetrical condensed node meshes. However, when simulating lossy media, the SCN does not introduce anisotropy in contrast to hybrid symmetrical condensed node meshes.

MORENTE et al. derived the dispersion relation for an SCN-TLM mesh with stubs as an implicit function of the wave number, frequency, dielectric permittivity, and magnetic permeability. Group and phase velocities were calculated as a function of frequency for three fundamental directions [**65**]. It was shown that an increase in the permittivity of the modelled medium, which in turn leads to higher stub values, resulted in a decrease in the cutoff frequency for the validity of the numerical results. The analytical expressions of group and phase velocities as a function of frequency in the SCN-TLM mesh without stubs were given by MORENTE et al. in [**64**]. It emerged that the $[1,1,1]-$direction is more dispersive than the $[1,1,0]$ and $[1,0,0]-$directions.

CELUCH-MARCYSIAK and GWAREK observed that when calculating resonant frequencies of structures with inhomogeneous media that exhibited large differences in media parameters, bilateral dispersion can occur [**12**]. This means that the calculated resonant frequencies may be both under- and overestimated. An exact analytic formula evaluating the SCN dispersion errors within arbitrary media was presented and experimentally verified.

The dispersion in irregularly graded TLM and FDTD meshes was investigated by GERMAN et al. [**21**]. The authors of these work found that irregularly graded hybrid symmetrical condensed node meshes show significantly smaller propagation errors than irregularly graded FDTD meshes.

The dispersion of three-dimensional TLM condensed nodes under realistic and practical situations, i.e. an investigation of the velocity and resolution error in the

case of inhomogeneous cavities, was investigated in [**74**]. A structured mesh using variable parallelepipedic cells was used. It emerged that the SCN gave the smallest error of the propagation constant when compared to YEE's FDTD scheme and two generalized symmetrical condensed nodes, the hybrid symmetrical condensed node and the super symmetrical condensed node. The results of this study corroborate the findings of the study presented in [**21**].

DE MENEZES et al. studied the dispersion error and performance of absorbing boundary conditions and also found that SCN-TLM yields a smaller dispersion error when compared to the FDTD method [**59**]. In this study, a plot of the relative error calculated from the analytic dispersion relation versus the number of cells per wavelength, was shown indicating second order accuracy. However, the influence of the mapping between discretized electromagnetic field components and TLM wave pulses was not considered.

Not only numerical dispersion studies were published, but also analytical expressions for dispersion related quantities were derived. A generalized method for the calculation of TLM dispersion relations was presented by KRUMPHOLZ and RUSSER [**42**]. The method was successfully applied to derive the dispersion relations of the scalar TLM node and the symmetrical condensed node without stubs. A detailed presentation of this method can be found in [**45**]. The dispersion characteristics for the TLM scheme with *Symmetrical Super-Condensed Nodes* (SSCN) was presented by KRUMPHOLZ et al. [**41**], using the same method. A comparison of the dispersion characteristics of the stub loaded SCN and SSCN for modelling anisotropic media can be found in [**32**], also applying this general method. Although both meshes support unphysical modes, in SSCN meshes they propagate with the same velocity as the physical solutions. An earlier dispersion analysis of the symmetrical super-condensed node was given in [**103**]. An analytic expression for the dispersion relation of hybrid symmetrical condensed nodes and super symmetrical condensed nodes was presented by TRENKIC et al. [**106**].

The effect of field singularities on the accuracy of SCN-TLM solutions was investigated by SIMONS et al. [**92**]. In this work, the SCN-TLM, FDTD, and *Integer Lattice Gas Automata* (ILGA) solutions for a cavity containing a metallic fin were compared. It emerged that SCN-TLM requires a coarser mesh than FDTD and ILGA to achieve the same accuracy for this type of problem. The FDTD and ILGA meshes must be approximately 1.5 and 3.0 times as fine as the TLM mesh. The curves of the percentage difference of the TLM, FDTD, and ILGA solutions for b/λ (b denoted the width of the cavity and λ the wavelength corresponding to the first resonance of the cavity) from the benchmark solution versus mesh discretization indicated a first order convergence. However, it is known that the asymptotic convergence order is easily reduced by an order in the presence of field singularities and interfaces between different media [**60**]. DE MENEZES and HOEFER investigated the physical origin of the coarseness and dispersion errors influencing TLM solutions of MAXWELL's equations [**60**]. For this, the difference

equations of the numerical method were solved analytically. It was confirmed that the accuracy of the discrete solution is reduced in the vicinity of field singularities. This effect is caused by the finite number of spatial modes supported by the discretized domain. The reduced accuracy in the vicinity of field singularities causes frequency shifts originating from a reduction of the convergence order to first order in the presence of infinitesimally thin walls. Further, it emerged that in inhomogeneous problems not dispersion effects are the main source of error, but interface effects between media of different constitutive parameters. It is pointed out again in that paper that from the dispersion analysis it follows that SCN-TLM has second order convergence. However, in Chapter 5, it will be shown that the process of averaging for the calculation of the nodal fields as proposed by Johns reduces the order of accuracy in contrast to the bijective field-mapping at the cell boundaries, which retains the convergence order predicted by the dispersion relation.

3. Spurious Modes

As a consequence of temporal and spatial sampling of the electromagnetic field, not only dispersion errors are introduced, but also spurious modes that may corrupt the numerical solution [**69, 90**]. A detailed analysis of the unphysical modes that can exist in condensed node TLM meshes was presented in [**32**]. GERMAN et al. pointed out that although these unphysical modes theoretically exist, they do not have a significant influence on practical problems. However, the excitation of these spurious modes can be generally suppressed by applying a special mapping of the field excitation to the wave amplitudes of the TLM algorithm [**50**]. An alternative way of generally suppressing the excitation of spurious modes consists in exploiting the inherent redundancy within the SCN-TLM scheme, which was proposed by RUSSER and BADER [**86**].

4. Summary of Characteristic Features of the SCN-TLM Method

Summarizing the theoretical and numerical investigations of the characteristics of the SCN-TLM method, one is led to the conclusion that the TLM method with symmetrical condensed node exhibits superior dispersion characteristics when compared to the FDTD method. The SCN without stubs shows no dispersion along the principle axes at all. In irregularly graded meshes, the SCN-TLM method introduces significantly smaller propagation errors when compared to irregularly graded FDTD meshes. Analysing the propagation constants of inhomogeneously layered waveguides may show bilateral dispersion effects. In the vicinity of field singularities and media inhomogeneities, the convergence order may be reduced by an order. However, SCN-TLM allows to use a coarser mesh in comparison to the FDTD method for achieving the same accuracy, at least for certain types of problems. The SCN allows a field sampling of all six components of the electromagnetic field in one point of space and the modelling of

boundaries is much simpler when compared to the FDTD method. Although the SCN-TLM mesh supports unphysical static and propagating modes, their practical significance, particularly of the spurious propagating modes, is questionable. The second order convergence of the SCN-TLM method was shown for the SCN in connection with the bijective boundary oriented field-mapping.

However, a proof of convergence of JOHNS' original formulation for a cell-centred field-mapping has not been presented yet, although there have been published a number of derivations of the constituting equations of the symmetrical condensed node. A proof of convergence is of great practical importance, as the formulation of JOHNS' with cell-centred mapping is mostly used in practise and the asymptotic convergence rate influences the overall accuracy of the field computation.

5. Characterization of Planar Microwave Components

Amongst the numerous applications of the TLM method with symmetrical condensed node to electromagnetic field problems, the characterization of planar microwave circuits and components plays a more and more dominant role. The first applications in this field were the computation of the propagation constants of planar transmission lines such as microstrip and coplanar lines. The ATLM method was also applied to study coplanar discontinuities [**7**]. Recently, multigrid meshing techniques for TLM were studied for the example of microstrip impedance steps [**29**]. Multichip-module interconnect-transmission-line crossings were studied in [**57**]. The time domain signals obtained from the TLM simulation were used to generate lumped element equivalent circuits. In [**56**], the TLM modelling of a WILKINSON power divider with design frequency of 4-GHz was described. In [**20**], the analysis of a planar 3dB-stripline-coupler using a nonorthogonal TLM mesh was presented. Planar inductors were investigated by BADER using the ATLM method [**5**]. A variety of planar structures on general anisotropic material were investigated by WU et al. [**114**]. An even more interesting field of research is the investigation of patch antennas. The TLM method was successfully applied in a number of cases. H-shaped patch antennas were investigated by LINDENMEIER et al. using the ATLM method [**48**]. Patch antennas on ferrite substrates were investigated by SOBHY et al. [**97, 98**]. The bandwidth of such antennas can be tuned depending on the magnetization of the ferrite substrate. This is of particular interest for mobile communication applications. DUBARD and POMPEI reported the characterization of microstrip antennas using BERENGER's perfectly matched layers (PML) to truncate the computational domain [**18**]. The TLM simulation of a multi-segment dielectric resonator antenna was compared to solutions obtained by finite integration techniques and FDTD simulations [**94**]. Recently, the TLM method and the integral equation method were hybridized to treat electrically

large problems. This is particularly interesting for the investigation of electromagnetic compatibility problems [**75**]. Using this method, the radiation from microstrip waveguides was analysed [**76**]. The coupling between spiral inductors was also investigated with the aid of this method [**51**].

CHAPTER 4

TLM Formulations and Appropriate Function Spaces

The TLM method with symmetrical condensed node is closely related to difference methods. This is evident when we reconsider the basic equations of the TLM algorithm

$$|b> = \boldsymbol{T}\boldsymbol{S}|a>, \tag{4.1}$$

$$|a> = \boldsymbol{\Gamma}|b> \tag{4.2}$$

and insert (4.1) into (4.2) resulting in

$$|a> = \boldsymbol{T}\boldsymbol{\Gamma}\boldsymbol{S}|a> . \tag{4.3}$$

This equation constitutes a difference scheme with the incident TLM pulses as unknowns. If one wants to investigate the convergence of the SCN-TLM method, the mathematical tools that have been developed to study difference methods are hence appropriate. Therefore, we want to present the necessary tools provided by functional analysis in this chapter. Moreover, not only the symmetrical condensed node TLM scheme is closely related to finite difference methods but also many other TLM methods [**36, 93, 96**]. Approximating a differential equation by a difference equation always means to approximate the function spaces of the continuous problem by function space of finite or enumerable infinite dimension [**88**]. Therefore, we will also construct appropriate function spaces in this chapter for the approximate solution of an *initial value problem* (IVP) given by MAXWELL'S equations using the SCN-TLM scheme.

1. Approximation of Differential Equations by Difference Schemes

Finite difference methods are a universally applicable tool to solve differential equations approximately. The basic idea of all difference methods consists of replacing the differential quotients by difference quotients. A system of partial differential equations can generally be written as a linear operator equation[1] [**22**]

[1] This is of course also true for scalar partial differential equations.

$$\mathcal{L}\boldsymbol{v} = \boldsymbol{g}, \tag{4.4}$$

where $\mathcal{L}$ denotes a linear differential operator, $\boldsymbol{v}$ the vector of unknown functions and $\boldsymbol{g}$ the vector of the known data. Analogously, the approximate system of difference equations can be written as

$$\mathcal{Q}\boldsymbol{u} = \boldsymbol{g}_h, \tag{4.5}$$

where $\mathcal{Q}$ denotes a general difference operator approximating $\mathcal{L}$. The vector $\boldsymbol{u}$ comprises the unknown lattice functions and $\boldsymbol{g}_h$ is the vector of the discretized data. The corresponding approximation scheme may be represented by

$$\begin{array}{ccc} \mathcal{X} & \xrightarrow{\mathcal{L}} & \mathcal{Y} \\ \downarrow & & \downarrow \\ \mathcal{X}_h & \xrightarrow{\mathcal{Q}} & \mathcal{Y}_h \end{array} \tag{4.6}$$

where $\mathcal{X}$ and $\mathcal{Y}$ are the function spaces of the IVP to be approximated and $\mathcal{X}_h$ and $\mathcal{Y}_h$ are the function spaces of the discretized IVP [**117**]. In the case of homogeneous problems one usually has $\mathcal{X} = \mathcal{Y}$ and $\mathcal{X}_h = \mathcal{Y}_h$. Using difference methods, one tries to convert initial value problem (4.4) in the respective initial value problem of difference equations (4.5). The IVP of difference equations is essentially an algebraic system of equations[2]. This means that the discrete problem involves functions of discrete argument, or functions defined on a grid of points instead of functions with continuous argument [**100**]. Therefore, finite difference methods are also called *lattice point methods* or *grid point methods* [**118**]. Hence, the function spaces of the continuous problem are approximated by spaces of finite or enumerable infinite dimension. The following fundamental questions arise, when dealing with finite difference methods (e.g. [**100**]),

- construction of the difference operator $\mathcal{Q}$,
- existence and uniqueness of the boundary- and/or initial value problem of difference equations,
- convergence of the solution of the difference problem to the exact solution of the original problem,
- convergence order or estimation of the error of the method,
- solution of the difference equations.

The construction of a difference operator consists of two steps. First, a discretization of the domain of definition (usually a subdomain of $\mathbb{R}^N \times \mathbb{R}$). This is done by introducing a cubic or locally orthogonal grid. Second, approximation of the

[2]This general procedure applies of course also to boundary value problems and to boundary and initial value problems.

differential operator by appropriate difference operators. There exist a wide variety of methods to derive difference operators, such as PETROV-GALERKIN [**80**], TAYLOR-series expansion (e.g.[**100**]), Finite Volume techniques, conservation law approaches and many more. Some of these or a combination thereof have been applied in attempts to derive the TLM scattering operator directly from MAXWELL's equations. An overview of derivations of the SCN-TLM method was given in the previous chapter. In this work we will not deal with such fundamental questions as existence and uniqueness. The interested reader may refer to the mathematical literature such as [**22**]. However, the most important question when dealing with approximation methods is the question of convergence. There exists a fundamental theorem for difference methods, known as LAX Theorem, stating that *consistency* and *stability* imply convergence [**100, 117**]. This theorem is the 'working horse' of the theoretical analysis of difference schemes. The terms convergence, consistency, and stability will be explained in the next section. The determination of the order of convergence is part of the consistency analysis. The last question, i.e. the solution of the difference equations is not a matter of issue in the TLM method, as the iterative TLM scattering algorithm is solvable by definition, as no matrix inversion is necessary to solve the inherent algebraic system of equations.

In order to be able to answer the question of convergence and accuracy of the TLM method, one needs to specify the discrete function spaces $\mathcal{X}_h$ and $\mathcal{Y}_h$ of the above general approximation scheme. Very important is the relation to the function spaces of the IVP ($\mathcal{X}$ and $\mathcal{Y}$), as the TLM algorithm involves at least twelve unknowns per cell and MAXWELL's equations only six.

2. Consistency, Stability, and Convergence

The terms consistency, stability, and convergence, are illustrated for the example of an initial and boundary value problem of the TELEGRAPHER's equations

$$\frac{\partial V}{\partial t} = -\frac{1}{C_0}\frac{\partial I}{\partial x}, \quad x \in (0,1), t > 0, \tag{4.7}$$

$$\frac{\partial I}{\partial t} = -\frac{1}{L_0}\frac{\partial V}{\partial x}, \quad x \in (0,1), t > 0, \tag{4.8}$$

with initial conditions

$$V(x,0) = f_V(x), \qquad I(x,0) = f_I(x), \quad x \in [0,1] \tag{4.9}$$

and periodic boundary conditions

$$V(0,t) = V(1,t), \qquad I(0,t) = I(1,t). \tag{4.10}$$

The discrete problem writes

$$u_{k+1;l} = u_{k;l} - L_0 \frac{\Delta t}{2\Delta x}(i_{k;l+1} - i_{k;l-1}), \tag{4.11}$$

$$i_{k+1;l} = i_{k;l} - C_0 \frac{\Delta t}{2\Delta x}(u_{k;l+1} - u_{k;l-1}). \tag{4.12}$$

The initial and boundary conditions of the problem are approximated by

$$u_{0;l} = f_u(l\Delta x), \quad i_{0;l} = f_i(l\Delta x), \quad l = 0, ..., M, \tag{4.13}$$

$$u_{k+1;0} = u_{k+1;1}, \quad i_{k+1;0} = i_{k+1;1}, \quad k = 0, ... \tag{4.14}$$

2.1. Consistency. In the course of a consistency analysis, one can see how well a difference scheme approximates the desired partial differential equation [**100**]. For this, the truncated TAYLOR series expansion of the exact continuous solution is inserted into the finite difference equation. From the truncated TAYLOR series exemplified at the voltage on the transmission line

$$V_{k+1;l} = V(l\Delta x, (k+1)\Delta t) = V(l\Delta x, k\Delta t) + \frac{\partial V}{\partial t}\Big|_{l\Delta x, k\Delta t} \frac{\Delta t}{1!} + \frac{\partial V^2}{\partial t^2}\Big|_{l\Delta x, k\Delta t} \frac{\Delta t^2}{2!} \tag{4.15}$$

follows the difference quotient

$$\frac{V_{k+1;l} - V_{k;l}}{\Delta t} = \frac{\partial V}{\partial t}\Big|_{l\Delta x, k\Delta t} + \frac{\Delta t}{2}\frac{\partial V^2}{\partial t^2}\Big|_{l\Delta x, k\Delta t}. \tag{4.16}$$

This can be written in 'big $\mathcal{O}$' notation as

$$\frac{V_{k+1;l} - V_{k;l}}{\Delta t} = \frac{\partial V}{\partial t}\Big|_{l\Delta x, k\Delta t} + \mathcal{O}(\Delta t), \tag{4.17}$$

where it is assumed that the higher order derivatives of V at points $(l\Delta x, k\Delta t)$ are bounded. This means that the error introduced by the finite difference approximation is bounded by $|err| \leq K\,|\Delta t|$, where K is a constant. Using the same argument, one arrives at

$$\frac{V_{k;l+1} - V_{k;l-1}}{2\Delta x} = \frac{\partial V}{\partial x}\Big|_{l\Delta x, k\Delta t} + \mathcal{O}(\Delta x^2) \tag{4.18}$$

for the approximation of the spatial derivative. With this, the following approximation

$$\frac{\partial V}{\partial t}\Big|_{l\Delta x,k\Delta t} + \frac{1}{C_0}\frac{\partial I}{\partial x}\Big|_{l\Delta x,k\Delta t} = \frac{V_{k+1;l} - V_{k;l}}{\Delta t} + \frac{1}{C_0}\frac{I_{k;l+1} - I_{k;l-1}}{2\Delta x} + \mathcal{O}(\Delta t) + \mathcal{O}(\Delta x^2), \tag{4.19}$$

$$\frac{\partial I}{\partial t}\Big|_{l\Delta x,k\Delta t} + \frac{1}{L_0}\frac{\partial V}{\partial x}\Big|_{l\Delta x,k\Delta t} = \frac{I_{k+1;l} - I_{k;l}}{\Delta t} + \frac{1}{L_0}\frac{V_{k;l+1} - V_{k;l-1}}{2\Delta x} + \mathcal{O}(\Delta t) + \mathcal{O}(\Delta x^2) \tag{4.20}$$

follows for the TELEGRAPHER's equations (4.7) and (4.8). Thus, the finite difference scheme (4.11) and (4.12) approximates the TELEGRAPHER's equations (4.7) and (4.8) to the first order in Δt and the second order in Δx. In other words, if the space-time mesh is refined by a factor of two, the approximation error decreases linearly as the lowest order term dominates the error asymptotically.

2.2. Stability. The definition of stability for a two level difference scheme of the form

$$\boldsymbol{u}_{k+1} = \mathcal{Q}\boldsymbol{u}_k, k \geq 0 \tag{4.21}$$

is according to [**100**]: "A difference scheme (4.21) is said to be stable with respect to the norm $\|\cdot\|$ if there exist positive constants Δx_0 and Δt_0, and non-negative constants K and β so that

$$\|\boldsymbol{u}_{k+1}\| \leq Ke^{\beta t}\|\boldsymbol{u}_0\|, \tag{4.22}$$

for $0 \leq (k+1)\Delta t$, $0 < \Delta x < \Delta x_0$, and $0 < \Delta t < \Delta t_0$."

2.3. Convergence. We define the vectors $\boldsymbol{u}_k = (.., u_{k;-1}, u_{k;0}, u_{k;1}, ..)^T$ and $\boldsymbol{v}_k = (.., v_{k;-1}, v_{k;0}, v_{k;1}, ..)^T$. Following Thomas [**100**], "A difference scheme $\mathcal{Q}_{k;l}u_{k;l} = G_{k;l}$ approximating the partial differential equation $\mathcal{L}v = F$ is a convergent scheme of order (p, q) if for any t, as $(n+1)\Delta t$ converges to t,

$$\|\boldsymbol{u}_{k+1} - \boldsymbol{v}_{k+1}\| = \mathcal{O}(\Delta x^p) + \mathcal{O}(\Delta t^q) \tag{4.23}$$

as Δx and Δt converge to 0". We see that the definitions of stability and convergence involve a norm. So before discussing convergence, it is necessary to define an appropriate norm and hence an appropriate function space.

2.4. The Lax Theorem. Convergence, consistency, and stability are connected via the LAX *Equivalence Theorem*, which states [**100, 117**], "A consistent, two level difference scheme for a well-posed linear initial-value problem is convergent if and only if it is stable."
For proving the convergence of TLM, a somewhat restricted version of the above theorem is even more useful [**100**], i.e. "If a two-level difference scheme

$$\boldsymbol{u}_{k+1} = Q\boldsymbol{u}_k + \Delta t \boldsymbol{G}_k \tag{4.24}$$

is accurate of order (p, q) in the norm $\|\cdot\|$ to a well-posed linear initial-value problem and is stable with respect to the norm $\|\cdot\|$, then it is convergent of order (p, q) with respect to the norm $\|\cdot\|$." Using this theorem, the convergence of the SCN-TLM scheme in the formulation of JOHNS will be proven in Chapter 5.

3. Construction of Appropriate Function Spaces

When defining the terms consistency, stability, and convergence in the previous section, it has become evident that proving convergence is not possible without specifying the function spaces comprising those functions that are admissible solutions of the difference problem and the approximated differential. In this section, appropriate function spaces for proving the convergence of the SCN-TLM method are constructed.

3.1. Function Spaces for Maxwell's Equations. Analysing electromagnetic field problems means essentially solving the following IVP involving MAXWELL's equations [**82**]

$$\boldsymbol{\varepsilon}\frac{\partial \vec{\boldsymbol{E}}}{\partial t} = \nabla \times \vec{\boldsymbol{H}}, \tag{4.25}$$

$$\boldsymbol{\mu}\frac{\partial \vec{\boldsymbol{H}}}{\partial t} = -\nabla \times \vec{\boldsymbol{E}}, \tag{4.26}$$

with appropriate initial conditions,

$$\vec{\boldsymbol{E}}(\boldsymbol{r}, t=0), \qquad \vec{\boldsymbol{H}}(\boldsymbol{r}, t=0), \tag{4.27}$$

and auxiliary conditions,

$$\nabla \cdot \vec{\boldsymbol{E}} = 0 \qquad \text{and} \qquad \nabla \cdot \vec{\boldsymbol{H}} = 0. \tag{4.28}$$

Electric or magnetic losses are neglected, as they have no influence on the class of functions. Introducing an operator notation for (4.25) and (4.26) yields the operator equation

$$\boldsymbol{D_t f} = \mathbf{D_R} \boldsymbol{f} \tag{4.29}$$

or

$$\boldsymbol{D_t f} - \mathbf{D_R} \boldsymbol{f} = \boldsymbol{L f} = 0. \tag{4.30}$$

The state of the electromagnetic field is determined by elements $\boldsymbol{f}$ of a function space at every point in space and at any time. The vector $\boldsymbol{f}$ can be regarded as a two-tuple of two vector functions or as a six-tuple or six element vector of six scalar functions

$$\boldsymbol{f} = \left[\vec{\boldsymbol{E}}(\boldsymbol{r}), \vec{\boldsymbol{H}}(\boldsymbol{r})\right]^T = \left[E^x(\boldsymbol{r}), E^y(\boldsymbol{r}), E^z(\boldsymbol{r}), H^x(\boldsymbol{r}), H^y(\boldsymbol{r}), H^z(\boldsymbol{r})\right]^T \tag{4.31}$$

with $\boldsymbol{r} \in \mathbb{R}^3$. The differential operators $\boldsymbol{D_t}$ and $\mathbf{D_R}$ write in matrix representation

$$\boldsymbol{D_t} = \begin{pmatrix} \frac{\partial}{\partial t} & 0 & 0 & 0 & 0 & 0 \\ 0 & \frac{\partial}{\partial t} & 0 & 0 & 0 & 0 \\ 0 & 0 & \frac{\partial}{\partial t} & 0 & 0 & 0 \\ 0 & 0 & 0 & \frac{\partial}{\partial t} & 0 & 0 \\ 0 & 0 & 0 & 0 & \frac{\partial}{\partial t} & 0 \\ 0 & 0 & 0 & 0 & 0 & \frac{\partial}{\partial t} \end{pmatrix}, \tag{4.32}$$

$$\mathbf{D_R} = \begin{pmatrix} 0 & 0 & 0 & 0 & -\frac{\partial}{\partial z} & \frac{\partial}{\partial y} \\ 0 & 0 & 0 & \frac{\partial}{\partial z} & 0 & -\frac{\partial}{\partial x} \\ 0 & 0 & 0 & -\frac{\partial}{\partial y} & \frac{\partial}{\partial x} & 0 \\ 0 & \frac{\partial}{\partial z} & -\frac{\partial}{\partial y} & 0 & 0 & 0 \\ -\frac{\partial}{\partial z} & 0 & \frac{\partial}{\partial x} & 0 & 0 & 0 \\ \frac{\partial}{\partial y} & -\frac{\partial}{\partial x} & 0 & 0 & 0 & 0 \end{pmatrix}. \tag{4.33}$$

Introducing operators only makes sense, if the space on which their elements act is defined. Following (4.31), each scalar component of the electromagnetic field is described by a scalar function on $\mathbb{R}^3$. Hence, it is sensible to admit all square integrable functions of $\mathcal{L}^2(\mathbb{R}^3)$ [3] [**16, 116**]. Consequently, $\boldsymbol{f}$ is an element of the space

$$\mathcal{H}_S = \left\{\mathcal{L}^2(\mathbb{R}^3) \times \mathcal{L}^2(\mathbb{R}^3) \times \mathcal{L}^2(\mathbb{R}^3) \times \mathcal{L}^2(\mathbb{R}^3) \times \mathcal{L}^2(\mathbb{R}^3) \times \mathcal{L}^2(\mathbb{R}^3)\right\}. \tag{4.34}$$

It is necessary to equip this HILBERT space with a scalar product of physical meaning, for example

[3] The HILBERT space $\mathcal{L}^2(\mathbb{R})$ is the space of all LEBESGUE measurable functions $u : \mathbb{R} \longrightarrow \mathbb{R}$, that are summable in the sense of $\int_{\infty}^{\infty} |u(x)|^2 dx < \infty$ with pointwise operations and inner product $(u, v) = \int_{\infty}^{\infty} u(x) v^*(x) dx$.

$$(\boldsymbol{f}_1, \boldsymbol{f}_2) = \iiint_{\infty}^{\infty} \big(\vec{\boldsymbol{E}}_1(\boldsymbol{r})\vec{\boldsymbol{E}}_2^*(\boldsymbol{r}) + \vec{\boldsymbol{H}}_1(\boldsymbol{r})\vec{\boldsymbol{H}}_2^*(\boldsymbol{r})\big) d^3\boldsymbol{r} = \tag{4.35}$$

$$\iiint_{\infty}^{\infty} \big(E_1^x E_2^{x*} + E_1^y E_2^{y*} + E_1^z E_2^{z*} + H_1^x H_2^{x*} + H_1^y H_2^{y*} + H_1^z H_2^{z*}\big) d^3\boldsymbol{r},$$

where $E_j^i = E_j^i(\boldsymbol{r}), H_j^i = H_j^i(\boldsymbol{r})$ with $i = x, y, z; j = 1, 2$. This expression equals the field energy functional. In order to describe an IVP, it is also necessary to describe the time evolution. Usually, time evolution is described in BANACH Spaces, which are complete and equipped with a norm[4] [**82, 117, 119**]. The vector $\boldsymbol{f}(t)$ represents the field state at all times t. Hence, the time evolution is described by vector-valued functions

$$t \longrightarrow \mathcal{H}_S \tag{4.36}$$

that are elements of this BANACH space. The family of LEBESGUE spaces

$$\boldsymbol{L}_p\,(0, T; \mathcal{H}_S) \tag{4.37}$$

with $1 \leq p < \infty$ is an appropriate choice for describing time evolution processes [**82, 117, 119**]. These are the spaces of all measurable (vector-valued) functions $f :]\,0, T\,[\longrightarrow \mathcal{H}_S$ with

$$\|f\|_p = \Big(\int_0^T \|\boldsymbol{f}(t)\|_{\mathcal{H}_S}^p \, dt \Big)^{\frac{1}{p}} < \infty, \tag{4.38}$$

where $\|\cdot\|_{\mathcal{H}_S}$ denotes the norm in $\mathcal{H}_S$, i.e.

$$\|\boldsymbol{f}\|_{\mathcal{H}_S} = \Big(\iiint_{\infty}^{\infty} |E^x(\boldsymbol{r})|^2 + |E^y(\boldsymbol{r})|^2 + |E^z(\boldsymbol{r})|^2 \tag{4.39}$$

$$+ |H^x(\boldsymbol{r})|^2 + |H^y(\boldsymbol{r})|^2 + |H^z(\boldsymbol{r})|^2 \Big)^{\frac{1}{p}}.$$

Again, $p = 2$ is the appropriate choice for specifying the required space. Consequently, the initial value problem constituted by eqn. (4.25) and (4.26) is adequately described in the LEBESGUE space

$$\mathcal{H}_M = \boldsymbol{L}_2\big(0, T; (\boldsymbol{L}_2(\boldsymbol{\Omega}))^6\big), \tag{4.40}$$

[4] Every HILBERT space is also a BANACH space.

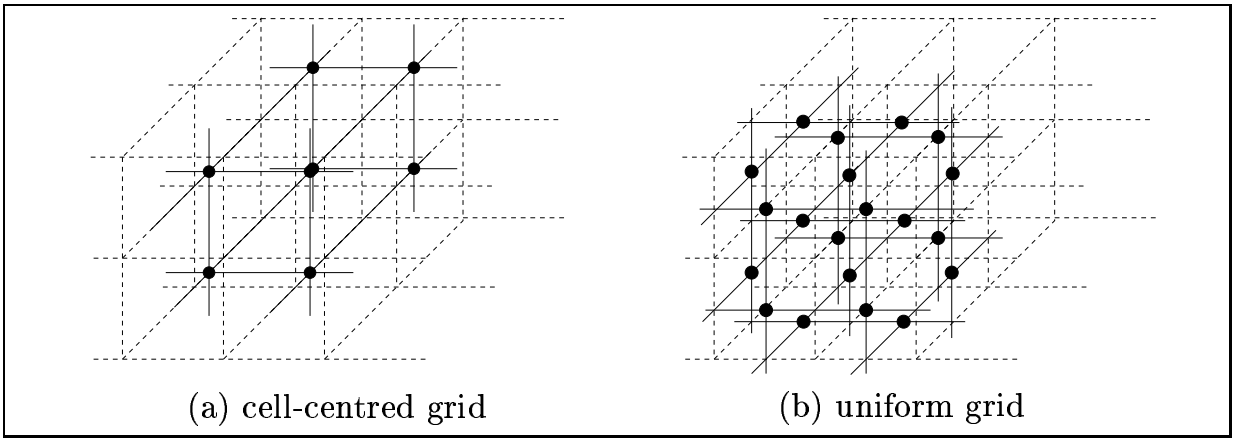

(a) cell-centred grid (b) uniform grid

FIGURE 4.1. Cell-centred and uniform grid corresponding to cell-centred and boundary oriented field-mapping in the SCN-TLM method.

taking the necessary smoothness conditions for the admissible functions solving the problem into account. The restrictions on the admissible functions for solving the IVP of (4.25) and (4.26) are discussed in detail in Appendix A. In the sequel, the required smoothness of the considered solutions is assumed.

3.2. Function Spaces for the Discrete IVP. In this section, the spaces $\mathcal{X}_h$ and $\mathcal{Y}_h$ (refer to the general approximation scheme (4.6)) that are appropriate for investigating the convergence of the TLM method with symmetrical condensed node are constructed. Suitable spaces are discrete LEBESGUE spaces, which are essentially sets of lattice functions with appropriate norms and inner products [**118**].

3.2.1. *The Discretized Domain.* In the TLM-method with symmetrical condensed node, the field-mapping between the discretized electromagnetic field components and the TLM wave pulses defines the grid where the approximate discrete solution of MAXWELL's equations is defined. In Chapter 2, the cell-centred field-mapping and the boundary oriented field-mapping were introduced. Defining the field-mapping at the centre of the TLM cells constitutes a so called *cell-centred grid* as depicted in Fig. 4.1(a). Defining a bijective field-mapping of the tangential field components in the centre of the cell faces constitutes a different grid, which is called *uniform grid* according to [**100**]. This grid is shown in Fig. 4.1(b). The fact that the CFM and the BOFM define two different grids indicates that these two field-mappings also imply different approximations of MAXWELL's equations.

3.2.2. *Discrete* LEBESGUE *Spaces.* The discrete initial value problem can be described appropriately in discrete LEBESGUE spaces. These spaces comprise all admissible lattice functions. Lattice functions are functions, whose continuous values are only known on a grid, i.e. at discrete points (see Appendix C). Discrete LEBESGUE spaces are essentially sequence spaces equipped with a special norm.

For this, the construction of vector-valued sequence spaces is recalled in Appendix B. The only difference between discrete LEBESGUE spaces and sequence spaces is a slightly altered definition of the norm and the inner product. This is due to the fact that the ℓ_p norms diverge for $\Delta x \longrightarrow 0$ [**100**]. As this is a serious drawback when studying convergence, the norms of discrete LEBESGUE spaces are weighted by the spatial increment Δx

$$\|\boldsymbol{x}\|_{p,\Delta x} = \Big(\sum_{n=1}^{\infty} |x_n|^p \, \Delta x \Big)^{\frac{1}{p}}. \tag{4.41}$$

This refers to the one-dimensional case. When more dimensions are considered, the norm is weighted accordingly. This is explicitly shown in Appendix D.

The discrete initial value problem, corresponding to (4.30) can be written as

$$\boldsymbol{f}_{k;l,m,n} = \mathcal{Q} \, \boldsymbol{f}_{k-1;l,m,n}, \tag{4.42}$$

where k denotes the time step and (l, m, n) the cell, where the field components are located at points specified by a cell-centred grid or uniform grid. The operator $\mathcal{Q}$ represents an arbitrary difference operator. In Section 3.1, it was shown that the solutions of the IVP (4.25) and (4.26) are sufficiently smooth functions of

$$\boldsymbol{L}_2 \left(0, T; (\boldsymbol{L}_2(\boldsymbol{\Omega}))^6\right), \tag{4.43}$$

where $\boldsymbol{\Omega}$ denotes a bounded region in $\mathbb{R}^3$. The discrete analogue of this space is the discrete LEBESGUE space

$$\ell_{p,\Delta t} \left(0, T; (\ell_{2,\Delta x \Delta y \Delta z}(\mathbb{I}))^6\right), \tag{4.44}$$

where $\mathbb{I}$ denotes the set of indices, describing the grid according to (C.1) with $\mathbb{I} \in \mathbb{R}^3$, e.g. $\mathbb{I} = \mathbb{Z}^3$. In the TLM algorithm, we have more unknowns than in the continuous problem given by MAXWELL's equations. Hence, a higher dimensional space is required. Therefore,

$$\mathcal{H}_w = \ell_{p,\Delta t} \left(0, T; (\ell_{2,\Delta x \Delta y \Delta z}(I))^{12+n}\right) \tag{4.45}$$

is the appropriate space for solving the discrete initial value problem using the TLM algorithm.

3.2.3. *Definition of the Bases of the TLM State Space $\mathcal{H}_w$.* In order to use the HILBERT space notation introduced in [**87**], we need to choose the appropriate base vectors for the TLM state space $\mathcal{H}_w$, introduced by KRUMPHOLZ [**44**]. Moreover, a suitable norm and inner product need to be defined for this space. The function $\varphi_n = \varphi(x_0 + n \, \Delta x)$ represents a function of discrete argument of $\ell_{2,\Delta x}(D)$. The set

$$B_{\ell_{2,\Delta x}} = \left\{ \varphi_n = (..., 0, 0, 0, x_n = 1, 0, 0, 0, ..), n \in \mathbb{N} \right\} \tag{4.46}$$

represents a base of $\ell_{2,\Delta x}(\mathbb{D})$. With the aid of this one-dimensional base, we can construct a base for the product space $(\ell_{2,\Delta x})^N$

$$\begin{aligned} B_{(\ell_{2,\Delta x})^N} = & \\ \Big\{ & \left\{ \varphi_{l_1,n_1,m_1} = (..., 0, 0, 0, x_{l_1,n_1,m_1} = 1, 0, 0, 0, ..), l_1, n_1, m_1 \in \mathbb{N} \right\} \\ & \times \left\{ \varphi_{l_2,n_2,m_2} = (..., 0, 0, 0, x_{l_2,n_2,m_2} = 1, 0, 0, 0, ..), l_2, n_2, m_2 \in \mathbb{N} \right\} \\ & \times \cdots \\ & \times \left\{ \varphi_{l_N,n_N,m_N} = (..., 0, 0, 0, x_{l_N,n_N,m_N} = 1, 0, 0, 0, ..), l_N, n_N, m_N \in \mathbb{N} \right\} \Big\} \end{aligned} \tag{4.47}$$

An element ζ of $B_{(\ell_{2,\Delta x})^N}$ is an N-fold cross-product of lattice functions whose values are defined at discrete points. The set of indices is enumerable infinite. Therefore, it is possible to reorder it arbitrarily [**82**]. We want to arrange the index set in that way that an element $\zeta_{i,j,k} = \zeta(i\Delta x, j\Delta y, k\Delta z)$ is assigned to the number tuple (i, j, k), i.e. to the location of a TLM cell at $(i\Delta x, j\Delta y, k\Delta z)$. Using bra-ket notation, the base vectors write

$$|l, m, n> := \zeta_{l,m,n}. \tag{4.48}$$

An inner product of $(\ell_{2,\Delta x,\Delta y,\Delta z})^N$ is given by

$$< f|g > := \sum_l \sum_m \sum_n \left(\boldsymbol{x}^*_{l,m,n} \boldsymbol{y}_{l,m,n} \right) \Delta x \Delta y \Delta z \tag{4.49}$$

with the state vectors

$$|f> = \sum_{l,m,n} \boldsymbol{x}_{l,m,n} |l, m, n> \qquad \text{and} \qquad |g> = \sum_{l,m,n} \boldsymbol{y}_{l,m,n} |l, m, n> \ . \tag{4.50}$$

The vectors $\boldsymbol{x}_{l,m,n}$ and $\boldsymbol{y}_{l,m,n}$ comprise the components of the state vectors at point l, m, n. The bases are constructed such that they constitute a complete orthonormal system. Consequently, the relations concerning orthogonality and completeness are fulfilled, which is easily verified

$$< p, q, r|l, m, n> = \delta_{pl}\delta_{qm}\delta_{rn}\Delta x \Delta y \Delta z \ ; \ l, m, n, p, q, r \in \mathbb{Z} \tag{4.51}$$

and

$$\sum_{l,p}\sum_{m,q}\sum_{n,r} = |l,m,n><p,q,r| = \boldsymbol{I}\ ; l,m,n,p,q,r \in \mathbb{Z}. \tag{4.52}$$

Describing the discrete time evolution, one proceeds analogously. The vector-valued functions of $\ell_{2,\Delta t}\left(\{k\};(\ell_{2,\Delta x,\Delta y,\Delta z}(\mathcal{D}))^N\right)$ on domain $\mathcal{D} = \mathbb{Z}^3 \subset \mathbb{R}^3$, are elements of the sequence of LEBESGUE spaces $(\ell_{2,\Delta x\Delta y\Delta z}(\mathbb{I}))_k^N$, indexed by $k \subset \mathbb{N}_0$. In the sequel, k is element of $I_{k_{ug}} = \{k | k \in \mathbb{N}_0\}$, describing a BOFM based approximation with uniform grid and $I_{k_{ccg}} = \{k \pm \frac{1}{2} \mid k \in \mathbb{N}_0\}$, describing a CFM based approximation with cell-centred grid. A base for this space is given by

$$\begin{aligned} B_{\ell_{2,\Delta t}\left((k);(\ell_{2,\Delta x\Delta y\Delta z}(\mathcal{D}))^N\right)} = \\ \Big\{\{ \quad \varphi_k = (...,0,0,0,x_k = \zeta_{l,m,n},0,0,0,..), \\ \varphi_{k\pm\frac{1}{2}} = (...,0,0,0,x_{k\pm\frac{1}{2}} = \zeta_{l,m,n},0,0,0,..)\}; \\ k \subset N_0; l,m,n \in \mathbb{Z}\Big\}. \end{aligned} \tag{4.53}$$

In bra-ket notation the base vectors write

$$|k; l,m,n> \ := \varphi_k, \tag{4.54}$$

$$|k \pm \tfrac{1}{2}; l,m,n> \ := \varphi_{k\pm\frac{1}{2}}. \tag{4.55}$$

The norm of this space is defined by

$$\|u\|_{\mathcal{H}_w} = \sqrt{\sum_{k\in I_{k_{ug}}, I_{k_{ccg}}}^{\infty} \|u_k\|^2_{(\ell_{2,\Delta x\Delta y\Delta z}(\mathcal{D}))_k^N}\ \Delta t} \tag{4.56}$$

with $u_k \in (\ell_{2,\Delta x\Delta y\Delta z}(\mathcal{D}))_k^N$. The inner product in this space is given by

$$<f|g> := \sum_{k\in I_{k_{ug}}, I_{k_{ccg}}} \left(<f_k|g_k>_{\left(\ell_{2,\Delta x\Delta y\Delta z}(\mathbb{I})\right)_k^N}\right)_k \Delta t. \tag{4.57}$$

The base is defined such that it constitutes an orthonormal system. Hence, the orthogonality and completeness relations are fulfilled, i.e.

$$\begin{aligned} <k_1; l_1,m_1,n_1|k_2; l_2,m_2,n_2> = \delta_{k_1k_2}\delta_{l_1l_2}\delta_{m_1m_2}\delta_{n_1n_2}\Delta x\Delta y\Delta z\Delta t \\ \forall \quad l_1,m_1,n_1,l_2,m_2,n_2 \in Z \wedge k_1,k_2 \in I_{k_1}, I_{k_2} \end{aligned} \tag{4.58}$$

and

$$(4.59)\qquad \sum_{k_1,k_2}\sum_{l_1,l_2}\sum_{m_1,m_2}\sum_{n_1,n_2} = |k_1;l_1,m_1,n_1><k_2;l_2,m_2,n_2| = \boldsymbol{I}$$

$$\forall \quad l_1,m_1,n_1,l_2,m_2,n_2 \in Z \wedge k_{ug}, k_{ccg} \in I_{k_{ug}}, I_{k_{ccg}}.$$

The operator $\boldsymbol{I}$ denotes again the identity operator. With the definition of the appropriate function spaces, suitable norms for proving the convergence of the SCN-TLM scheme were introduced. The convergence of the TLM-method using the CFM in these norms will be shown in the following chapter.

CHAPTER 5

The Convergence of the SCN-TLM Formulation of Johns

There has not been given a proof of convergence of the SCN-TLM formulation with cell-centred field-mapping yet, although it is presumably the most widely used TLM method and there have also been presented a number of formal derivations thereof. However, in all these derivations apart from JOHNS' original introduction and LOVETRI and SIMONS' conservation law approach, a boundary oriented field-mapping was additionally employed. In this chapter, the convergence of Johns' original SCN-TLM formulation towards solutions of MAXWELL's equations is proved for the first time. The proof is performed in two steps. First, the convergence of a *mapping induced finite difference scheme* (MIFD) of the SCN-TLM algorithm is shown by using the techniques presented in the previous chapter. The MIFD is derived by mapping between the TLM wave pulses and the electromagnetic field components at *every* time step and not just at the beginning and the end of a simulation. Second, it is shown that the distance between the original SCN-TLM method and this mapping induced finite difference scheme approaches zero in the norm of the previously constructed function spaces when taking the limit.

In order to show the relation between the involved function spaces, the approximation scheme for the classic JOHNS' formulation can be envisaged as

$$
\begin{array}{ccc}
\mathcal{X} & \xrightarrow{\mathcal{L}} & \mathcal{X} \\
\downarrow & & \downarrow \\
\mathcal{X}_h & & \mathcal{X}_h \\
\downarrow \boldsymbol{Q} & & \boldsymbol{P} \uparrow \\
\mathcal{H}_w & \xrightarrow{(\boldsymbol{T}\boldsymbol{\Gamma}\boldsymbol{S})^k} & \mathcal{H}_w
\end{array}
\tag{5.1}
$$

The space $\mathcal{X}$ is the LEBESGUE space

$$\mathcal{X} = \boldsymbol{L}_2\big(0, T; (\boldsymbol{L}_2(\boldsymbol{\Omega}))^6\big) \tag{5.2}$$

of the continuous IVP with MAXWELL's equations, where $\boldsymbol{\Omega}$ denotes a bounded region in $\mathbb{R}^3$. This space was constructed in the previous chapter. The space $\mathcal{X}_h$ is its discrete analogue given by eqn. (4.44)

$$\mathcal{X}_h = \ell_{2,\Delta t}\big(\{k\}; (\ell_{2,\Delta x,\Delta y,\Delta z}(\boldsymbol{G}))^6\big). \tag{5.3}$$

The integer set $\{k\}$ denotes the discrete time interval. The grid of discrete points where the electromagnetic field is sampled is denoted by $\boldsymbol{G} \subset \boldsymbol{\Omega}$, which describes a cell-centred grid as depicted in Fig. 4.1 (a). The TLM state space $\mathcal{H}_w$ of the TLM state vectors $|\boldsymbol{a}>$ and $|\boldsymbol{b}>$ is the space (4.45)

$$\mathcal{H}_w = \ell_{2,\Delta t}\big(\{k\}; (\ell_{2,\Delta x,\Delta y,\Delta z}(\boldsymbol{G}))^q\big), \tag{5.4}$$

with $q = 12$ or 18, depending on the considered TLM-SCN method. The integer set $\{k\}$ denotes the discrete time interval and $\boldsymbol{G} \subset \boldsymbol{\Omega}$ denotes the set of points, where the TLM nodes are located. The norm in the TLM state space is defined by

$$\| |u> \|_{\mathcal{H}_w} = \sqrt{\sum_k \| |u_k> \|^2_{\ell_{2,\Delta x,\Delta y,\Delta z}} \Delta t}, \tag{5.5}$$

with

$$\| |u_k> \|^2_{\ell_{2,\Delta x,\Delta y,\Delta z}} = \sqrt{\sum_{l,m,n,j} |u^j_{l,m,n}|^2 \Delta x \Delta y \Delta z}, \tag{5.6}$$

and

$$|u> = \sum_{k,l,m,n} \boldsymbol{u}_{k;l,m,n} |k; l, m, n>, \tag{5.7}$$

as shown in the previous chapter. The vector $\boldsymbol{u}_{k;l,m,n} = [u^1_{k;l,m,n}, ..., u^j_{k;l,m,n}]^T$ denotes an arbitrary TLM state vector.

1. Proving Convergence via Mapping Induced Finite Difference Schemes

The TLM algorithm is characterized by the two operations scatter and connect

$$|b> \; = \boldsymbol{T}\boldsymbol{S}|a> \, , \tag{5.8}$$

$$|a> \; = \boldsymbol{\Gamma}|b> \, . \tag{5.9}$$

Inserting (5.8) into (5.9) yields a finite difference scheme of the incident TLM wave amplitudes $\boldsymbol{a}_{k;l,m,n}$

$$|a> = \boldsymbol{\Gamma T S}\,|a> . \tag{5.10}$$

The idea of writing the TLM algorithm as an equivalent finite difference scheme involves the mapping of the TLM operator to the equivalent difference operator for each time step. Consequently, the operation conditions are altered such that before each scattering event, the TLM state variables are mapped to the discretized field components and the TLM mesh is re-excited immediately again at every time step. In practical field computations the TLM mesh is excited only at the beginning of the simulation and the field is sampled only at the end. The field and wave amplitudes are related by the cell-centred field-mapping

$$|a> \;= \boldsymbol{Q}|f> , \tag{5.11}$$

$$|f> \;= \boldsymbol{P}|a> . \tag{5.12}$$

Applying the mapping operator $\boldsymbol{P}$ from the left side to (5.10) and substituting (5.12) on the right side of (5.10) results consequently in the mapping induced finite difference scheme

$$|f> = \boldsymbol{P\Gamma T S Q}\,|f>, \tag{5.13}$$

or

$$\sum_k |f_k> = \sum_k \boldsymbol{P\Gamma S Q}\,|f_k>, \tag{5.14}$$

better showing the nature of a finite difference scheme. The approximation scheme of the MIFD scheme is given by

$$\begin{array}{ccc} \mathcal{X} & \xrightarrow{\boldsymbol{L}} & \mathcal{X} \\ \downarrow & & \downarrow \\ \mathcal{X}_h & \xrightarrow{(\boldsymbol{TP\Gamma SQ})^k} & \mathcal{X}_h \end{array} \tag{5.15}$$

As

$$\boldsymbol{QP} \neq \boldsymbol{I} \tag{5.16}$$

holds [**44**] ($\boldsymbol{I}$ denoting the identity operator), one has to consider the differences between the mapping induced finite difference scheme and the classic TLM scheme before one can draw conclusions on the properties of one scheme from the properties of the other scheme. Using LAX's theorem, we can prove the convergence of the mapping induced finite difference scheme via consistency and stability. This means

$$\lim_{\Delta t \to 0} \|(\boldsymbol{PT\Gamma SQ})^k \boldsymbol{f}(0) - \boldsymbol{f}(k\Delta t)\| \longrightarrow 0, \tag{5.17}$$

where $\boldsymbol{f}(0)$ is the discrete initial field distribution and $\boldsymbol{f}(k\Delta t)$ is the discrete field distribution at observation time $k\Delta t$. Convergence of the TLM method means

$$\lim_{\Delta t \to 0} \|\boldsymbol{P}(\boldsymbol{T\Gamma S})^k \boldsymbol{Q}\boldsymbol{f}(0) - \boldsymbol{f}(k\Delta t)\| \longrightarrow 0. \tag{5.18}$$

Consequently, we need to show that

$$\lim_{\Delta t \to 0} \|(\boldsymbol{PT\Gamma SQ})^k - \boldsymbol{P}(\boldsymbol{T\Gamma S})^k \boldsymbol{Q}\| \longrightarrow 0. \tag{5.19}$$

This can be accomplished by exploiting the boundedness of the operator product and operator norm estimations for both the TLM method without stubs and with stubs.

2. Convergence of the TLM Method without Stubs

In this section, the basic considerations for the formulation of the SCN-TLM method without stubs are summarized and the convergence of the scheme is shown using the procedure just described. We will find out that the MIFD scheme is the well known LAX-FRIEDRICHS scheme. Then, it is shown that from the convergence of the mapping induced finite difference scheme the convergence of the TLM method indeed follows.

2.1. Mapping Induced FD Scheme of SCN-TLM without Stubs. Recalling Chapter 2, the scattering matrix of the TLM-SCN algorithm without stubs is given by

(5.20)

$$\boldsymbol{S} = \begin{pmatrix}
0 & 0 & 0 & 0 & 0 & 0 & \frac{1}{2} & -\frac{1}{2} & 0 & 0 & \frac{1}{2} & \frac{1}{2} \\
0 & 0 & 0 & 0 & 0 & 0 & -\frac{1}{2} & \frac{1}{2} & 0 & 0 & \frac{1}{2} & \frac{1}{2} \\
0 & 0 & 0 & 0 & \frac{1}{2} & \frac{1}{2} & 0 & 0 & \frac{1}{2} & -\frac{1}{2} & 0 & 0 \\
0 & 0 & 0 & 0 & \frac{1}{2} & \frac{1}{2} & 0 & 0 & -\frac{1}{2} & \frac{1}{2} & 0 & 0 \\
0 & 0 & \frac{1}{2} & \frac{1}{2} & 0 & 0 & 0 & 0 & 0 & 0 & \frac{1}{2} & -\frac{1}{2} \\
0 & 0 & \frac{1}{2} & \frac{1}{2} & 0 & 0 & 0 & 0 & 0 & 0 & -\frac{1}{2} & \frac{1}{2} \\
\frac{1}{2} & -\frac{1}{2} & 0 & 0 & 0 & 0 & 0 & 0 & \frac{1}{2} & \frac{1}{2} & 0 & 0 \\
-\frac{1}{2} & \frac{1}{2} & 0 & 0 & 0 & 0 & 0 & 0 & \frac{1}{2} & \frac{1}{2} & 0 & 0 \\
0 & 0 & \frac{1}{2} & -\frac{1}{2} & 0 & 0 & \frac{1}{2} & \frac{1}{2} & 0 & 0 & 0 & 0 \\
0 & 0 & -\frac{1}{2} & \frac{1}{2} & 0 & 0 & \frac{1}{2} & \frac{1}{2} & 0 & 0 & 0 & 0 \\
\frac{1}{2} & \frac{1}{2} & 0 & 0 & \frac{1}{2} & -\frac{1}{2} & 0 & 0 & 0 & 0 & 0 & 0 \\
\frac{1}{2} & \frac{1}{2} & 0 & 0 & -\frac{1}{2} & \frac{1}{2} & 0 & 0 & 0 & 0 & 0 & 0
\end{pmatrix}.$$

The connect operator $\boldsymbol{\Gamma}$ writes in matrix representation

$$\boldsymbol{\Gamma} = \begin{pmatrix} 0 & \boldsymbol{X} & 0 & 0 & 0 & 0 & 0 & 0 & 0 & 0 & 0 & 0 \\ \boldsymbol{X}^\dagger & 0 & 0 & 0 & 0 & 0 & 0 & 0 & 0 & 0 & 0 & 0 \\ 0 & 0 & 0 & \boldsymbol{X} & 0 & 0 & 0 & 0 & 0 & 0 & 0 & 0 \\ 0 & 0 & \boldsymbol{X}^\dagger & 0 & 0 & 0 & 0 & 0 & 0 & 0 & 0 & 0 \\ 0 & 0 & 0 & 0 & 0 & \boldsymbol{Y} & 0 & 0 & 0 & 0 & 0 & 0 \\ 0 & 0 & 0 & 0 & \boldsymbol{Y}^\dagger & 0 & 0 & 0 & 0 & 0 & 0 & 0 \\ 0 & 0 & 0 & 0 & 0 & 0 & 0 & \boldsymbol{Y} & 0 & 0 & 0 & 0 \\ 0 & 0 & 0 & 0 & 0 & 0 & \boldsymbol{Y}^\dagger & 0 & 0 & 0 & 0 & 0 \\ 0 & 0 & 0 & 0 & 0 & 0 & 0 & 0 & 0 & \boldsymbol{Z} & 0 & 0 \\ 0 & 0 & 0 & 0 & 0 & 0 & 0 & 0 & \boldsymbol{Z}^\dagger & 0 & 0 & 0 \\ 0 & 0 & 0 & 0 & 0 & 0 & 0 & 0 & 0 & 0 & 0 & \boldsymbol{Z} \\ 0 & 0 & 0 & 0 & 0 & 0 & 0 & 0 & 0 & 0 & \boldsymbol{Z}^\dagger & 0 \end{pmatrix}. \tag{5.21}$$

The cell-centred mapping between electromagnetic field components and TLM wave amplitudes is given by

$$\boldsymbol{P} = \boldsymbol{Q}^T = \frac{1}{2} \begin{pmatrix} 0 & 1 & 0 & 0 & 0 & 1 \\ 0 & 1 & 0 & 0 & 0 & -1 \\ 0 & 0 & 1 & 0 & -1 & 0 \\ 0 & 0 & 1 & 0 & 1 & 0 \\ 0 & 0 & 1 & 1 & 0 & 0 \\ 0 & 0 & 1 & -1 & 0 & 0 \\ 1 & 0 & 0 & 0 & 0 & -1 \\ 1 & 0 & 0 & 0 & 0 & 1 \\ 1 & 0 & 0 & 0 & 1 & 0 \\ 1 & 0 & 0 & 0 & -1 & 0 \\ 0 & 1 & 0 & -1 & 0 & 0 \\ 0 & 1 & 0 & 1 & 0 & 0 \end{pmatrix}^T. \tag{5.22}$$

According to (5.14) and (5.20)-(5.22), we can calculate the mapping induced finite difference operator of the SCN-TLM method without stubs, resulting in

$$\boldsymbol{P}\boldsymbol{\Gamma}\boldsymbol{S}\boldsymbol{Q} = \frac{1}{4} \begin{pmatrix} \boldsymbol{D_{YZ}} & 0 & 0 & 0 & -\boldsymbol{D_Z} & \boldsymbol{D_Y} \\ 0 & \boldsymbol{D_{XZ}} & 0 & \boldsymbol{D_Z} & 0 & -\boldsymbol{D_X} \\ 0 & 0 & \boldsymbol{D_{XY}} & -\boldsymbol{D_Y} & \boldsymbol{D_X} & 0 \\ 0 & \boldsymbol{D_Z} & -\boldsymbol{D_Y} & \boldsymbol{D_{YZ}} & 0 & 0 \\ -\boldsymbol{D_Z} & 0 & \boldsymbol{D_X} & 0 & \boldsymbol{D_{XZ}} & 0 \\ \boldsymbol{D_Y} & -\boldsymbol{D_X} & 0 & 0 & 0 & \boldsymbol{D_{XY}} \end{pmatrix}, \tag{5.23}$$

with the scalar difference operators

$$\begin{aligned} \boldsymbol{D_X} &= \boldsymbol{X}^\dagger - \boldsymbol{X}, & \boldsymbol{D_{XY}} &= \boldsymbol{X}^\dagger + \boldsymbol{X} + \boldsymbol{Y}^\dagger + \boldsymbol{Y}, \\ \boldsymbol{D_Y} &= \boldsymbol{Y}^\dagger - \boldsymbol{Y}, & \boldsymbol{D_{XZ}} &= \boldsymbol{X}^\dagger + \boldsymbol{X} + \boldsymbol{Z}^\dagger + \boldsymbol{Z}, \\ \boldsymbol{D_Z} &= \boldsymbol{Z}^\dagger - \boldsymbol{Z}, & \boldsymbol{D_{YZ}} &= \boldsymbol{Y}^\dagger + \boldsymbol{Y} + \boldsymbol{Z}^\dagger + \boldsymbol{Z}. \end{aligned} \tag{5.24}$$

The operator (5.23) is equivalent with the difference operator of equation (31) given in [**53**].

2.2. Consistency of Mapping Induced FD Scheme. To prove consistency, we expand the sampled exact continuous solution at the point $(k;l,m,n)$ in a TAYLOR series, insert this solution into the finite difference scheme, and let $\Delta t \longrightarrow 0$ and $\Delta l \longrightarrow 0$. After taking the limit, the approximated partial differential equation should remain [**100**]. Written componentwise, this yields the following finite difference scheme. The first three MAXWELL equations are approximated by

$$
\begin{aligned}
(5.25)\quad & E^x_{k+1;l,m,n} = \\
& \frac{1}{4}\left(E^x_{k;l,m+1,n} + E^x_{k;l,m-1,n} + E^x_{k;l,m,n+1} + E^x_{k;l,m,n-1}\right) \\
& -\frac{1}{\varepsilon_0}\frac{\Delta t}{2\Delta l}\left(H^y_{k;l,m,n+1} - H^y_{k;l,m,n-1}\right) + \frac{1}{\varepsilon_0}\frac{\Delta t}{2\Delta l}\left(H^z_{k;l,m+1,n} - H^z_{k;l,m-1,n}\right),
\end{aligned}
$$

$$
\begin{aligned}
(5.26)\quad & E^y_{k+1;l,m,n} = \\
& \frac{1}{4}\left(E^y_{k;l+1,m,n} + E^y_{k;l-1,m,n} + E^y_{k;l,m,n+1} + E^y_{k;l,m,n+1}\right) \\
& +\frac{1}{\varepsilon_0}\frac{\Delta t}{2\Delta l}\left(H^x_{k;l,m,n+1} - H^x_{k;l,m,n-1}\right) - \frac{1}{\varepsilon_0}\frac{\Delta t}{2\Delta l}\left(H^z_{k;l+1,m,n} - H^z_{k;l-1,m,n}\right),
\end{aligned}
$$

$$
\begin{aligned}
(5.27)\quad & E^z_{k+1;l,m,n} = \\
& \frac{1}{4}\left(E^y_{k;l+1,m,n} + E^y_{k;l-1,m,n} + E^y_{k;l,m+1,n} + E^y_{k;l,m-1,n}\right) \\
& -\frac{1}{\varepsilon_0}\frac{\Delta t}{2\Delta l}\left(H^x_{k;l,m+1,n} - H^x_{k;l,m-1,n}\right) + \frac{1}{\varepsilon_0}\frac{\Delta t}{2\Delta l}\left(H^y_{k;l+1,m,n} - H^y_{k;l-1,m,n}\right),
\end{aligned}
$$

and the second three MAXWELL equations are approximated by

$$
\begin{aligned}
(5.28)\quad & H^x_{k+1;l,m,n} = \\
& \frac{1}{4}\left(H^x_{k;l,m+1,n} + H^x_{k;l,m-1,n} + H^x_{k;l,m,n+1} + H^x_{k;l,m,n-1}\right) \\
& +\frac{1}{\mu_0}\frac{\Delta t}{2\Delta l}\left(E^y_{k;l,m,n+1} - E^y_{k;l,m,n-1}\right) - \frac{1}{\mu_0}\frac{\Delta t}{2\Delta l}\left(E^z_{k;l,m+1,n} - E^z_{k;l,m-1,n}\right),
\end{aligned}
$$

$$H^y_{k+1;l,m,n} = \frac{1}{4}\left(H^y_{k;l+1,m,n} + H^y_{k;l-1,m,n} + H^y_{k;l,m,n+1} + H^y_{k;l,m,n+1}\right) - \frac{1}{\mu_0}\frac{\Delta t}{2\Delta l}\left(E^x_{k;l,m,n+1} - E^x_{k;l,m,n-1}\right) + \frac{1}{\mu_0}\frac{\Delta t}{2\Delta l}\left(E^z_{k;l+1,m,n} - E^z_{k;l-1,m,n}\right), \tag{5.29}$$

$$H^z_{k+1;l,m,n} = \frac{1}{4}\left(H^y_{k;l+1,m,n} + H^y_{k;l-1,m,n} + H^y_{k;l,m+1,n} + H^y_{k;l,m-1,n}\right) + \frac{1}{\mu_0}\frac{\Delta t}{2\Delta l}\left(E^x_{k;l,m+1,n} - E^x_{k;l,m-1,n}\right) - \frac{1}{\mu_0}\frac{\Delta t}{2\Delta l}\left(E^y_{k;l+1,m,n} - E^y_{k;l-1,m,n}\right). \tag{5.30}$$

This scheme is exactly the well known LAX-FRIEDRICHS finite difference scheme. A thorough treatment of its properties can be found in [**100**]. For showing that the LAX-FRIEDRICHS scheme is indeed a consistent scheme for approximating MAXWELL's equations, we develop the sampled exact continuous solution E^x, E^y, E^z, H^x, H^y, and H^z in a TAYLOR series. For example, the expansion of the E^x component at point (l, m, n) writes

$$E^x_{k+1;l,m,n} = E^x((k+1)\Delta t; l\Delta x, m\Delta y, n\Delta z) = E^x(k\Delta t; l\Delta x, m\Delta y, n\Delta z) + \frac{\partial E^x}{\partial t}\Big|_{k\Delta t; l\Delta x, m\Delta y, n\Delta z}\frac{\Delta t}{1!} + \frac{\partial^2 E^x}{\partial t^2}\Big|_{k\Delta t; l\Delta x, m\Delta y, n\Delta z}\frac{\Delta t^2}{2!} + \cdots \tag{5.31}$$

The expanded field components are inserted into (5.25) to (5.30). This yields

$$\varepsilon_0\frac{\partial E^x}{\partial t}\Big|_{k\Delta t; l\Delta l, m\Delta l, n\Delta l} + \mathcal{O}(\Delta t) + \mathcal{O}(\frac{\Delta l^2}{\Delta t}) = -\frac{\partial H^y}{\partial z}\Big|_{k\Delta t; l\Delta l, m\Delta l, n\Delta l} + \mathcal{O}(\Delta l^2) + \frac{\partial H^z}{\partial y}\Big|_{k\Delta t; l\Delta l, m\Delta l, n\Delta l} + \mathcal{O}(\Delta l^2), \tag{5.32}$$

$$\varepsilon_0\frac{\partial E^y}{\partial t}\Big|_{k\Delta t; l\Delta l, m\Delta l, n\Delta l} + \mathcal{O}(\Delta t) + \mathcal{O}(\frac{\Delta l^2}{\Delta t}) = \frac{\partial H^x}{\partial z}\Big|_{k\Delta t; l\Delta l, m\Delta l, n\Delta l} + \mathcal{O}(\Delta l^2) - \frac{\partial H^z}{\partial x}\Big|_{k\Delta t; l\Delta l, m\Delta l, n\Delta l} + \mathcal{O}(\Delta l^2), \tag{5.33}$$

$$\varepsilon_0\frac{\partial E^z}{\partial t}\Big|_{k\Delta t; l\Delta l, m\Delta l, n\Delta l;} + \mathcal{O}(\Delta t) + \mathcal{O}(\frac{\Delta l^2}{\Delta t}) = -\frac{\partial H^x}{\partial y}\Big|_{k\Delta t; l\Delta l, m\Delta l, n\Delta l} + \mathcal{O}(\Delta l^2) + \frac{\partial H^y}{\partial x}\Big|_{k\Delta t; l\Delta l, m\Delta l, n\Delta l} + \mathcal{O}(\Delta l^2), \tag{5.34}$$

$$\mu_0 \frac{\partial H^x}{\partial t}\Big|_{k\Delta t;l\Delta l,m\Delta l,n\Delta l} + \mathcal{O}(\Delta t) + \mathcal{O}(\frac{\Delta l^2}{\Delta t}) = \frac{\partial E^y}{\partial z}\Big|_{k\Delta t;l\Delta l,m\Delta l,n\Delta l} + \mathcal{O}(\Delta l^2) - \frac{\partial E^z}{\partial y}\Big|_{k\Delta t;l\Delta l,m\Delta l,n\Delta l} + \mathcal{O}(\Delta l^2), \tag{5.35}$$

$$\mu_0 \frac{\partial H^y}{\partial t}\Big|_{k\Delta t;l\Delta l,m\Delta l,n\Delta l} + \mathcal{O}(\Delta t) + \mathcal{O}(\frac{\Delta l^2}{\Delta t}) = -\frac{\partial E^x}{\partial z}\Big|_{k\Delta t;l\Delta l,m\Delta l,n\Delta l} + \mathcal{O}(\Delta l^2) + \frac{\partial E^z}{\partial x}\Big|_{k\Delta t;l\Delta l,m\Delta l,n\Delta l} + \mathcal{O}(\Delta l^2), \tag{5.36}$$

$$\mu_0 \frac{\partial H^z}{\partial t}\Big|_{k\Delta t;l\Delta l,m\Delta l,n\Delta l} + \mathcal{O}(\Delta t) + \mathcal{O}(\frac{\Delta l^2}{\Delta t}) = \frac{\partial E^x}{\partial y}\Big|_{k\Delta t;l\Delta l,m\Delta l,n\Delta l} + \mathcal{O}(\Delta l^2) - \frac{\partial E^y}{\partial x}\Big|_{k\Delta t;l\Delta l,m\Delta l,n\Delta l} + \mathcal{O}(\Delta l^2). \tag{5.37}$$

As expected from a LAX-FRIEDRICHS scheme, the inherent equivalent finite difference scheme of the classic free space TLM is first order accurate in time and $\mathcal{O}(\frac{\Delta l^2}{\Delta t})$ in space. By taking the limit $\Delta t \longrightarrow 0$ and $\Delta l \longrightarrow 0$, the higher order terms vanish, and MAXWELL's equations remain, i.e.

$$\varepsilon_0 \frac{\partial E^x}{\partial t} = -\frac{\partial H^y}{\partial z} + \frac{\partial H^z}{\partial y}, \tag{5.38}$$

$$\varepsilon_0 \frac{\partial E^y}{\partial t} = \frac{\partial H^x}{\partial z} - \frac{\partial H^z}{\partial x}, \tag{5.39}$$

$$\varepsilon_0 \frac{\partial E^z}{\partial t} = -\frac{\partial H^x}{\partial y} + \frac{\partial H^y}{\partial x}, \tag{5.40}$$

$$\mu_0 \frac{\partial H^x}{\partial t} = \frac{\partial E^y}{\partial z} - \frac{\partial E^z}{\partial y}, \tag{5.41}$$

$$\mu_0 \frac{\partial H^y}{\partial t} = -\frac{\partial E^x}{\partial z} + \frac{\partial E^z}{\partial x}, \tag{5.42}$$

$$\mu_0 \frac{\partial H^z}{\partial t} = \frac{\partial E^x}{\partial y} - \frac{\partial E^y}{\partial x}. \tag{5.43}$$

2.3. Stability of Mapping Induced FD Schemes. LAX's theorem requires that a consistent finite difference scheme is stable for being convergent. The SCN-TLM scheme without stubs is stable by definition as a consequence of its energy conserving nature and the fixed stability factor. As the LAX-FRIEDRICHS scheme is dissipative, the mapping induced finite difference scheme of the SCN without stubs is also stable and hence convergent.

2.4. Convergence of the SCN-TLM Scheme without Stubs. In the previous section, we have shown using the LAX theorem that

$$\lim_{\Delta t \to 0} \|(\boldsymbol{PT\Gamma SQ})^k \boldsymbol{f}(0) - \boldsymbol{f}(k\Delta t)\| \longrightarrow 0. \tag{5.44}$$

In this section, we want to show that this also implies the convergence of SCN-TLM scheme

$$\lim_{\Delta t \to 0} \|\boldsymbol{P}(\boldsymbol{T\Gamma S})^k \boldsymbol{Q}\boldsymbol{f}(0) - \boldsymbol{f}(k\Delta t)\| \longrightarrow 0. \tag{5.45}$$

Consequently, it remains to be shown that the difference between the two difference operators vanishes in the norm of $\mathcal{X}_h$ when $\Delta t \longrightarrow 0$, hence

$$\lim_{\Delta t \to 0} \|(\boldsymbol{PT\Gamma SQ})^k - \boldsymbol{P}(\boldsymbol{T\Gamma S})^k \boldsymbol{Q}\| \longrightarrow 0. \tag{5.46}$$

Exploiting the boundedness of the operator product in (5.46) yields

$$\begin{aligned} &\|(\boldsymbol{PT\Gamma SQ})^k - \boldsymbol{P}(\boldsymbol{T\Gamma S})^k \boldsymbol{Q}\| \\ &= \|\boldsymbol{PT}^k(\boldsymbol{\Gamma SQP} - \boldsymbol{\Gamma S})^{k-1}\boldsymbol{\Gamma SQ}\| \\ &\leq \|\boldsymbol{PT}^{k-1}\|\|(\boldsymbol{\Gamma SQP} - \boldsymbol{\Gamma S})\|^{k-1}\|\boldsymbol{T\Gamma S}\|\|\boldsymbol{Q}\|. \end{aligned} \tag{5.47}$$

Obviously, all norms on the right side of inequality (5.47) are bounded. Now we need to show that one of the terms on the right side of the inequality becomes arbitrarily small and constitutes an upper bound for the distance between the two schemes. The induced norm of an operator is defined by [**100**]

$$\|A\| = \sup_{\|x\| \leq 1} \|Ax\|. \tag{5.48}$$

As this operator norm cannot be calculated directly, we can estimate it by the norm of the sum of the columns

$$\sup_{\|x\| \leq 1} \|Ax\| \leq \sum_j |\lambda_j| \|Ae_j\|, \tag{5.49}$$

as a matrix representation of the operators $\boldsymbol{P}, \boldsymbol{\Gamma}, \boldsymbol{S}, \boldsymbol{Q}$ is given. The λ_j denote constants. We will focus on the factor $\|\boldsymbol{\Gamma SQP} - \boldsymbol{\Gamma S}\|$ on the right hand side of inequality (5.47). For $j = 1$ we get

$$\begin{aligned} &\|(\boldsymbol{\Gamma SQP} - \boldsymbol{\Gamma S})e_1\| \\ &= \sqrt{\frac{(2c_0)^2\Delta t^3}{\Delta l^2}\frac{lmn}{16}\left(|2\boldsymbol{X}|^2 + |\boldsymbol{Y}^2| + |-\boldsymbol{Y}^\dagger|^2 + |-\boldsymbol{Z}|^2 + |-\boldsymbol{Z}^\dagger|^2\right)\Delta x\Delta y\Delta z}. \end{aligned} \tag{5.50}$$

It is only summed over l, m, n (see the definition of the norm in $\mathcal{H}_w$ (5.5), (5.6)), since the operators $\boldsymbol{\Gamma}$, $\boldsymbol{S}$, $\boldsymbol{Q}$, $\boldsymbol{P}$ act on $(\ell_{2,\Delta x,\Delta y,\Delta z}(\boldsymbol{G}))^{12}$. Taking the limit, $l\Delta x$, $m\Delta y$, $n\Delta z$ converge against the width of the domain in directions x, y, z (assuming

a block domain). Exploiting the fixed relation between Δl and Δt, we are left with $\sqrt{\Delta t}\, C_s$. The constant C_s denotes the squared absolute value of the shift operators in (5.50). The same results for all other terms and hence, we have an upper bound of the order $\mathcal{O}(\sqrt{\Delta t})$.

2.5. Order of Accuracy Estimation. In the previous sections, we have shown that for the mapping induced finite difference scheme

$$\|(\boldsymbol{PT\Gamma SQ})^k \boldsymbol{f}(0) - \boldsymbol{f}(k\Delta t)\| \leq \mathcal{O}(\Delta t) \tag{5.51}$$

holds and that the relation

$$\|(\boldsymbol{PT\Gamma SQ})^k \boldsymbol{f}(0) - \boldsymbol{P}(\boldsymbol{T\Gamma S})^k \boldsymbol{Q}\boldsymbol{f}(0)\| \leq \mathcal{O}(\sqrt{\Delta t}) \tag{5.52}$$

is fulfilled for the distance between MIFD and the TLM scheme. With this, we want to estimate the asymptotic convergence order of the SCN-TLM scheme without stubs, yielding

$$\begin{aligned}
&\|\boldsymbol{P}(\boldsymbol{T\Gamma S})^k \boldsymbol{Q}\boldsymbol{f}(0) - \boldsymbol{f}(k\Delta t)\| \\
&\quad = \|\boldsymbol{P}(\boldsymbol{T\Gamma S})^k \boldsymbol{Q}\boldsymbol{f}(0) - (\boldsymbol{PT\Gamma SQ})^k \boldsymbol{f}(0) \\
&\qquad\qquad + (\boldsymbol{PT\Gamma SQ})^k \boldsymbol{f}(0) - \boldsymbol{f}(k\Delta t)\| \\
&\quad \leq \|\boldsymbol{P}(\boldsymbol{T\Gamma S})^k \boldsymbol{Q}\boldsymbol{f}(0) - (\boldsymbol{PT\Gamma SQ})^k \boldsymbol{f}(0)\| \\
&\qquad\qquad + \|(\boldsymbol{PT\Gamma SQ})^k \boldsymbol{f}(0) - \boldsymbol{f}(k\Delta t)\| \\
&\quad \leq \mathcal{O}(\sqrt{\Delta t}).
\end{aligned} \tag{5.53}$$

Surprisingly, the SCN-TLM scheme is asymptotically only of the order of $\mathcal{O}(\sqrt{\Delta t})$, as this term dominates for small Δt! At first sight, this appears to contradict common belief, but from the numerical studies presented in Chapter 7, this asymptotic rate of convergence can be experimentally verified. We can envisage this such that not mapping between the discretized field components and the TLM wave amplitudes at each time step adds an error term with a small constant of the order $\mathcal{O}(\sqrt{\Delta t})$ to the first order equivalent finite difference scheme (5.25) to (5.30) that otherwise cancels.

3. Convergence of the SCN-TLM Method with Stubs

The proof of convergence for the stub-loaded SCN-TLM method runs completely analogously as the one just presented for the SCN-TLM method without stubs. First, the mapping induced finite difference scheme for the SCN with stubs is derived and then its consistency shown. Finally, the convergence of the SCN-TLM method with stubs is shown from the mapping induced finite difference scheme exploiting again the boundedness of the operator product and operator norm estimations. First, we will show the convergence of the SCN-TLM method

without losses and second, the convergence of the SCN-TLM method considering ohmic losses is proved.

3.1. Mapping induced FD Schemes of SCN-TLM with Stubs. When ohmic and magnetic losses are included, we consider the extensions proposed by NAYLOR and DESAI [**67**]. For calculating the mapping induced finite difference operator $\boldsymbol{P\Gamma SQ}$ as in (5.23), the operators $\boldsymbol{P}$, $\boldsymbol{\Gamma}$, $\boldsymbol{S}$, $\boldsymbol{Q}$ for the SCN-TLM method with stubs can be found in Sections 3 and 4 of Chapter 2.

3.2. Consistency of Mapping Induced FD Scheme. Again, to prove the consistency of the MIFD scheme with MAXWELL's equations, we expand the sampled exact solution at point $(k;l,m,n)$ in a TAYLOR series, insert the expanded sampled exact solution into the finite difference scheme, and take the limit $\Delta t \longrightarrow 0$ and $\Delta l \longrightarrow 0$. For simplicity, we set $\Delta x := u\Delta l$, $\Delta y := v\Delta l$, $\Delta z := w\Delta l$ in the sequel.

3.2.1. *Mapping Induced FD Scheme of SCN-TLM without Losses.* Evaluating (5.14) for both $\boldsymbol{\sigma}_e = \mathbf{0}$ and $\boldsymbol{\sigma}_m = \mathbf{0}$, yields the following finite difference scheme in componentwise notation

$$
\begin{aligned}
E^x_{k+1;l,m,n} &= E^x_{k;l,m,n} \\
&+ \frac{u}{w}\frac{r_{xy}}{2Z_0}\left(E^x_{k;l,m+1,n} - 2E^x_{k;l,m,n} + E^x_{k;l,m-1,n}\right) \\
&+ \frac{u}{v}\frac{r_{xz}}{2Z_0}\left(E^x_{k;l,m,n+1} - 2E^x_{k;l,m,n} + E^x_{k;l,m,n-1}\right) \\
&- \frac{r_{xz}}{2}\left(H^y_{k;l,m,n+1} - H^y_{k;l,m,n-1}\right) \\
&+ \frac{r_{xy}}{2}\left(H^z_{k;l,m+1,n} - H^y_{k;l,m-1,n}\right),
\end{aligned}
\tag{5.54}
$$

with the stability factors

$$
r_{xy} = \frac{1}{\varepsilon_0 h_0 \varepsilon_{rx}}\frac{\Delta t}{\Delta y} \qquad \text{and} \qquad r_{xz} = \frac{1}{\varepsilon_0 h_0 \varepsilon_{rx}}\frac{\Delta t}{\Delta z},
\tag{5.55}
$$

$$
\begin{aligned}
E^y_{k+1;l,m,n} &= E^y_{k;l,m,n} \\
&+ \frac{v}{w}\frac{r_{yx}}{2Z_0}\left(E^y_{k;l+1,m,n} - 2E^y_{k;l,m,n} + E^y_{k;l-1,m,n}\right) \\
&+ \frac{v}{u}\frac{r_{yz}}{2Z_0}\left(E^y_{k;l,m,n+1} - 2E^y_{k;l,m,n} + E^y_{k;l,m,n-1}\right) \\
&+ \frac{r_{yz}}{2}\left(H^x_{k;l,m,n+1} - H^x_{k;l,m,n-1}\right) \\
&- \frac{r_{yx}}{2}\left(H^z_{k;l+1,m,n} - H^z_{k;l-1,m,n}\right),
\end{aligned}
\tag{5.56}
$$

with the stability factors

$$r_{yx} = \frac{1}{\varepsilon_0 h_0 \varepsilon_{ry}} \frac{\Delta t}{\Delta x} \qquad \text{and} \qquad r_{yz} = \frac{1}{\varepsilon_0 h_0 \varepsilon_{ry}} \frac{\Delta t}{\Delta z}, \tag{5.57}$$

$$\begin{aligned} E^z_{k+1;l,m,n} &= E^z_{k;l,m,n} \\ &+ \frac{w}{v} \frac{r_{zx}}{2Z_0} \left(E^z_{k;l+1,m,n} - 2E^z_{k;l,m,n} + E^z_{k;l-1,m,n} \right) \\ &+ \frac{w}{u} \frac{r_{zy}}{2Z_0} \left(E^z_{k;l,m+1,n} - 2E^z_{k;l,m,n} + E^z_{k;l,m-1,n} \right) \\ &- \frac{r_{zy}}{2} \left(H^x_{k;l,m+1,n} - H^x_{k;l,m-1,n} \right) \\ &+ \frac{r_{zx}}{2} \left(H^y_{k;l+1,m,n} - H^y_{k;l-1,m,n} \right), \end{aligned} \tag{5.58}$$

with the stability factors

$$r_{zx} = \frac{1}{\varepsilon_0 h_0 \varepsilon_{rz}} \frac{\Delta t}{\Delta x} \qquad \text{and} \qquad r_{zy} = \frac{1}{\varepsilon_0 h_0 \varepsilon_{rz}} \frac{\Delta t}{\Delta y}, \tag{5.59}$$

$$\begin{aligned} H^x_{k+1;l,m,n} &= H^x_{k;l,m,n} \\ &+ \frac{u}{w} \frac{Z_0 r^*_{xy}}{2} \left(H^x_{k;l,m+1,n} - 2H^x_{k;l,m,n} + H^x_{k;l,m-1,n} \right) \\ &+ \frac{u}{v} \frac{Z_0 r^*_{xz}}{2} \left(H^x_{k;l,m,n+1} - 2H^x_{k;l,m,n} + H^x_{k;l,m,n-1} \right) \\ &+ \frac{r^*_{xz}}{2} \left(E^y_{k;l,m,n+1} - E^y_{k;l,m,n-1} \right) \\ &- \frac{r^*_{xy}}{2} \left(E^z_{k;l,m+1,n} - E^y_{k;l,m-1,n} \right), \end{aligned} \tag{5.60}$$

with the stability factors

$$r^*_{xy} = \frac{1}{\mu_0 h_0 \mu_{rx}} \frac{\Delta t}{\Delta y} \qquad \text{and} \qquad r^*_{xz} = \frac{1}{\mu_0 h_0 \mu_{rx}} \frac{\Delta t}{\Delta z}, \tag{5.61}$$

$$\begin{aligned} H^y_{k+1;l,m,n} &= H^y_{k;l,m,n} \\ &+ \frac{v}{w} \frac{Z_0 r^*_{yx}}{2} \left(H^y_{k;l+1,m,n} - 2H^y_{k;l,m,n} + H^y_{k;l-1,m,n} \right) \\ &+ \frac{v}{u} \frac{Z_0 r^*_{yz}}{2} \left(H^y_{k;l,m,n+1} - 2H^y_{k;l,m,n} + H^y_{k;l,m,n-1} \right) \\ &- \frac{r^*_{yz}}{2} \left(E^x_{k;l,m,n+1} - E^x_{k;l,m,n-1} \right) \\ &+ \frac{r^*_{yx}}{2} \left(E^z_{k;l+1,m,n} - E^y_{k;l-1,m,n} \right), \end{aligned} \tag{5.62}$$

with the stability factors

$$r^*_{yx} = \frac{1}{\mu_0 h_0 \mu_{ry}} \frac{\Delta t}{\Delta x} \qquad \text{and} \qquad r^*_{yz} = \frac{1}{\mu_0 h_0 \mu_{ry}} \frac{\Delta t}{\Delta z}, \tag{5.63}$$

and

$$\begin{aligned} H^z_{k+1;l,m,n} &= H^z_{k;l,m,n} \\ &+ \frac{w}{v} \frac{Z_0 r^*_{zx}}{2} \left(H^z_{k;l+1,m,n} - 2H^z_{k;l,m,n} + H^z_{k;l-1,m,n} \right) \\ &+ \frac{w}{u} \frac{Z_0 r^*_{zy}}{2} \left(H^z_{k;l,m,n+1} - 2H^z_{k;l,m,n} + H^z_{k;l,m,n-1} \right) \\ &+ \frac{r^*_{zy}}{2} \left(E^x_{k;l,m+1,n} - E^x_{k;l,m-1,n} \right) \\ &- \frac{r^*_{zx}}{2} \left(E^y_{k;l+1,m,n} - E^y_{k;l-1,m,n} \right), \end{aligned} \tag{5.64}$$

with the stability factors

$$r^*_{zx} = \frac{1}{\mu_0 h_0 \mu_{rz}} \frac{\Delta t}{\Delta x} \qquad \text{and} \qquad r^*_{zy} = \frac{1}{\mu_0 h_0 \mu_{rz}} \frac{\Delta t}{\Delta y}. \tag{5.65}$$

Looking more closely at (5.54) to (5.64), one recognizes a *forward-in-time-centred-in-space* (FTCS) scheme that is stabilized by adding artificial dispersion in form of the $(H^x_{k;l,m+1,n} - 2H^x_{k;l,m,n} + H^x_{k;l,m-1,n})$ and $(E^x_{k;l,m+1,n} - 2E^x_{k;l,m,n} + E^x_{k;l,m-1,n})$ terms [**100**]. Expanding the sampled exact continuous solution in a TAYLOR series, yields for the scheme approximating the first MAXWELL equation

$$\begin{aligned} h_0 \varepsilon_{rx} \varepsilon_0 \frac{\partial E^x}{\partial t}\Big|_{l\Delta x, m\Delta y, n\Delta z; k\Delta t} + \mathcal{O}(\Delta t) = \\ - \frac{\partial H^y}{\partial z}\Big|_{k\Delta t; l\Delta x, m\Delta y, n\Delta z} + \mathcal{O}(\Delta z^2) + \frac{\partial H^z}{\partial y}\Big|_{k\Delta t; l\Delta x, m\Delta y, n\Delta z} + \mathcal{O}(\Delta y^2), \end{aligned} \tag{5.66}$$

$$\begin{aligned} h_0 \varepsilon_{ry} \varepsilon_0 \frac{\partial E^y}{\partial t}\Big|_{k\Delta t; l\Delta x, m\Delta y, n\Delta z} + \mathcal{O}(\Delta t) = \\ \frac{\partial H^x}{\partial z}\Big|_{k\Delta t; l\Delta x, m\Delta y, n\Delta z} + \mathcal{O}(\Delta z^2) - \frac{\partial H^z}{\partial x}\Big|_{k\Delta t; l\Delta x, m\Delta y, n\Delta z} + \mathcal{O}(\Delta x^2), \end{aligned} \tag{5.67}$$

$$\begin{aligned} h_0 \varepsilon_{rz} \varepsilon_0 \frac{\partial E^z}{\partial t}\Big|_{k\Delta t; l\Delta x, m\Delta y, n\Delta z} + \mathcal{O}(\Delta t) = \\ - \frac{\partial H^x}{\partial y}\Big|_{k\Delta t; l\Delta x, m\Delta y, n\Delta z} + \mathcal{O}(\Delta y^2) + \frac{\partial H^y}{\partial x}\Big|_{k\Delta t; l\Delta x, m\Delta y, n\Delta z} + \mathcal{O}(\Delta x^2), \end{aligned} \tag{5.68}$$

and for the scheme approximating the second MAXWELL equation

$$h_0\mu_{rx}\mu_0\frac{\partial H^x}{\partial t}\Big|_{k\Delta t;l\Delta x,m\Delta y,n\Delta z}+\mathcal{O}(\Delta t)= \frac{\partial E^y}{\partial z}\Big|_{k\Delta t;l\Delta x,m\Delta y,n\Delta z}+\mathcal{O}(\Delta z^2)-\frac{\partial E^z}{\partial y}\Big|_{k\Delta t;l\Delta x,m\Delta y,n\Delta z}+\mathcal{O}(\Delta y^2), \tag{5.69}$$

$$h_0\mu_{ry}\mu_0\frac{\partial H^y}{\partial t}\Big|_{k\Delta t;l\Delta x,m\Delta y,n\Delta z}+\mathcal{O}(\Delta t)= -\frac{\partial E^x}{\partial z}\Big|_{k\Delta t;l\Delta x,m\Delta y,n\Delta z}+\mathcal{O}(\Delta z^2)+\frac{\partial E^z}{\partial x}\Big|_{k\Delta t;l\Delta x,m\Delta y,n\Delta z}+\mathcal{O}(\Delta x^2), \tag{5.70}$$

$$h_0\mu_r\mu_0\frac{\partial H^z}{\partial t}\Big|_{k\Delta t;l\Delta x,m\Delta y,n\Delta z}+\mathcal{O}(\Delta t)= \frac{\partial E^x}{\partial y}\Big|_{k\Delta t;l\Delta x,m\Delta y,n\Delta z}+\mathcal{O}(\Delta y^2)-\frac{\partial E^y}{\partial x}\Big|_{k\Delta t;l\Delta x,m\Delta y,n\Delta z}+\mathcal{O}(\Delta x^2). \tag{5.71}$$

Hence, the mapping induced scheme is accurate of the order $\mathcal{O}(\Delta t)$ in time and of the order $\mathcal{O}(\Delta x^2)+\mathcal{O}(\Delta y^2)+\mathcal{O}(\Delta z^2)$ in space. It should be remarked that regardless whether the spatial or the temporal approximation orders are higher, asymptotically the lowest order term will dominate the accuracy of the solution. This was extensively investigated by AIDAM when assessing Wavelet-GALERKIN methods [**3**]. By taking the limit $\Delta t\longrightarrow 0$ and $\Delta l\longrightarrow 0$, the higher order terms vanish, and we are left with

$$h_0\varepsilon_{rx}\varepsilon_0\frac{\partial E^x}{\partial t}=-\frac{\partial H^y}{\partial z}+\frac{\partial H^z}{\partial y}, \tag{5.72}$$

$$h_0\varepsilon_{ry}\varepsilon_0\frac{\partial E^y}{\partial t}=\frac{\partial H^x}{\partial z}-\frac{\partial H^z}{\partial x}, \tag{5.73}$$

$$h_0\varepsilon_{rz}\varepsilon_0\frac{\partial E^z}{\partial t}=-\frac{\partial H^x}{\partial y}+\frac{\partial H^y}{\partial x}, \tag{5.74}$$

and

$$h_0\mu_{rx}\mu_0\frac{\partial H^x}{\partial t}=\frac{\partial E^y}{\partial z}-\frac{\partial E^z}{\partial y}, \tag{5.75}$$

$$h_0\mu_{ry}\mu_0\frac{\partial H^y}{\partial t}=-\frac{\partial E^x}{\partial z}+\frac{\partial E^z}{\partial x}, \tag{5.76}$$

$$h_0\mu_{rz}\mu_0\frac{\partial H^z}{\partial t}=\frac{\partial E^x}{\partial y}-\frac{\partial E^y}{\partial x}. \tag{5.77}$$

As both the permittivities and the permeabilities are scaled by h_0, it is evident that SCN-TLM models a medium with higher permittivity and permeability than

indicated by the values of ε_r and μ_r. Consequently, the relation between modelled media parameters and physical media parameters is given by

$$\varepsilon_{r_{mod}} = h_0 \varepsilon_r, \qquad \mu_{r_{mod}} = h_0 \mu_r. \tag{5.78}$$

The reason for this is that in the TLM mesh we have h_0-times the propagation velocity of the medium to be modelled. In case of TLM without stubs, the higher propagation velocity of the TLM mesh could also be seen as a consequence of the inherent LAX-FRIEDRICHS scheme of the symmetrical condensed node mesh without stubs.

3.2.2. *Mapping Induced FD Scheme of SCN-TLM with Losses.* To illustrate how a mapping induced equivalent scheme following (5.13) and (5.14) looks alike if we include losses, we consider the case with ohmic losses. It is abstained from considering both both ohmic *and* magnetic losses, as this would yield a scheme with a very large number of terms only concealing the main idea. Considering only ohmic losses, the MIFD scheme writes for the three components of the first MAXWELL equation

$$\begin{aligned} E^x_{k+1;l,m,n} = & \frac{2(\varepsilon_0 h_0 \varepsilon_{rx})^2 - \Delta t \sigma_{ex}^2}{2(\varepsilon_0 h_0 \varepsilon_{rx})^2 + 2\varepsilon_0 \varepsilon_{rx} \sigma_{ex} + \Delta t \sigma_{ex}^2} E^x_{k;l,m,n} \\ & + \frac{u}{w} \frac{r_{xy}}{2Z_0} \left(E^x_{k;l,m+1,n} - 2E^x_{k;l,m,n} + E^x_{k;l,m-1,n} \right) \\ & + \frac{u}{v} \frac{r_{xz}}{2Z_0} \left(E^x_{k;l,m,n+1} - 2E^x_{k;l,m,n} + E^x_{k;l,m,n-1} \right) \\ & - \frac{r_{xz}}{2} \left(H^y_{k;l,m,n+1} - H^y_{k;l,m,n-1} \right) \\ & + \frac{r_{xy}}{2} \left(H^z_{k;l,m+1,n} - H^y_{k;l,m-1,n} \right), \end{aligned} \tag{5.79}$$

with the stability factors

$$r_{xy} = \frac{2h_0 \varepsilon_0 \varepsilon_{rx} + \sigma_{ex} \Delta t}{2(\varepsilon_0 h_0 \varepsilon_{rx})^2 + 2\varepsilon_0 \varepsilon_{rx} \sigma_{ex} + \Delta t \sigma_{ex}^2} \frac{\Delta t}{\Delta y}, \tag{5.80}$$

$$r_{xz} = \frac{2h_0 \varepsilon_0 \varepsilon_{rx} + \sigma_{ex} \Delta t}{2(\varepsilon_0 h_0 \varepsilon_{rx})^2 + 2\varepsilon_0 \varepsilon_{rx} \sigma_{ex} + \Delta t \sigma_{ex}^2} \frac{\Delta t}{\Delta z}, \tag{5.81}$$

$$\begin{aligned} E^y_{k+1;l,m,n} = & \frac{2(\varepsilon_0 h_0 \varepsilon_{ry})^2 - \Delta t \sigma_{ey}^2}{2(\varepsilon_0 h_0 \varepsilon_{ry})^2 + 2\varepsilon_0 \varepsilon_{ry} \sigma_{ey} + \Delta t \sigma_{ey}^2} E^y_{k;l,m,n} \\ & + \frac{v}{w} \frac{r_{yx}}{2Z_0} \left(E^y_{k;l+1,m,n} - 2E^y_{k;l,m,n} + E^y_{k;l-1,m,n} \right) \\ & + \frac{v}{u} \frac{r_{yz}}{2Z_0} \left(E^y_{k;l,m,n+1} - 2E^y_{k;l,m,n} + E^y_{k;l,m,n-1} \right) \\ & + \frac{r_{yz}}{2} \left(H^x_{k;l,m,n+1} - H^x_{k;l,m,n-1} \right) \\ & - \frac{r_{yx}}{2} \left(H^z_{k;l+1,m,n} - H^z_{k;l-1,m,n} \right), \end{aligned} \tag{5.82}$$

with the stability factors

$$r_{yx} = \frac{2h_0\varepsilon_0\varepsilon_{ry} + \sigma_{ey}\Delta t}{2(\varepsilon_0 h_0 \varepsilon_{ry})^2 + 2\varepsilon_0\varepsilon_{ry}\sigma_{ey} + \Delta t\sigma_{ey}^2}\frac{\Delta t}{\Delta x}, \tag{5.83}$$

$$r_{yz} = \frac{2h_0\varepsilon_0\varepsilon_{ry} + \sigma_{ey}\Delta t}{2(\varepsilon_0 h_0 \varepsilon_{ry})^2 + 2\varepsilon_0\varepsilon_{ry}\sigma_{ey} + \Delta t\sigma_{ey}^2}\frac{\Delta t}{\Delta z}, \tag{5.84}$$

$$\begin{aligned} E^z_{k+1;l,m,n} = {} & \frac{2(\varepsilon_0 h_0 \varepsilon_{rz})^2 - \Delta t\sigma_{ez}^2}{2(\varepsilon_0 h_0 \varepsilon_{rz})^2 + 2\varepsilon_0\varepsilon_{rz}\sigma_{ez} + \Delta t\sigma_{ez}^2} E^z_{k;l,m,n} \\ & + \frac{w}{v}\frac{r_{zx}}{2Z_0}\left(E^z_{k;l+1,m,n} - 2E^z_{k;l,m,n} + E^z_{k;l-1,m,n}\right) \\ & + \frac{w}{u}\frac{r_{zy}}{2Z_0}\left(E^z_{k;l,m+1,n} - 2E^z_{k;l,m,n} + E^z_{k;l,m-1,n}\right) \\ & - \frac{r_{zy}}{2}\left(H^x_{k;l,m+1,n} - H^x_{k;l,m-1,n}\right) \\ & + \frac{r_{zx}}{2}\left(H^y_{k;l+1,m,n} - H^y_{k;l-1,m,n}\right), \end{aligned} \tag{5.85}$$

with the stability factors

$$r_{zx} = \frac{2h_0\varepsilon_0\varepsilon_{rz} + \sigma_{ez}\Delta t}{2(\varepsilon_0 h_0 \varepsilon_{rz})^2 + 2\varepsilon_0\varepsilon_{rz}\sigma_{ez} + \Delta t\sigma_{ez}^2}\frac{\Delta t}{\Delta x}, \tag{5.86}$$

$$r_{zy} = \frac{2h_0\varepsilon_0\varepsilon_{rz} + \sigma_{ez}\Delta t}{2(\varepsilon_0 h_0 \varepsilon_{rz})^2 + 2\varepsilon_0\varepsilon_{rz}\sigma_{ez} + \Delta t\sigma_{ez}^2}\frac{\Delta t}{\Delta y}. \tag{5.87}$$

For the MIFD for the three components of the second MAXWELL equation, we get the same scheme as in the lossless case

$$\begin{aligned} H^x_{k+1;l,m,n} = {} & H^x_{k;l,m,n} \\ & + \frac{u}{w}\frac{Z_0 r^*_{xy}}{2}\left(H^x_{k;l,m+1,n} - 2H^x_{k;l,m,n} + H^x_{k;l,m-1,n}\right) \\ & + \frac{u}{v}\frac{Z_0 r^*_{xz}}{2}\left(H^x_{k;l,m,n+1} - 2H^x_{k;l,m,n} + H^x_{k;l,m,n-1}\right) \\ & + \frac{r^*_{xz}}{2}\left(E^y_{k;l,m,n+1} - E^y_{k;l,m,n-1}\right) \\ & - \frac{r^*_{xy}}{2}\left(E^z_{k;l,m+1,n} - E^z_{k;l,m-1,n}\right), \end{aligned} \tag{5.88}$$

with the stability factors

$$r^*_{xy} = \frac{1}{\mu_0 h_0 \mu_{rx}}\frac{\Delta t}{\Delta y} \qquad \text{and} \qquad r^*_{xz} = \frac{1}{\mu_0 h_0 \mu_{rx}}\frac{\Delta t}{\Delta z}, \tag{5.89}$$

$$
\begin{aligned}
H^y_{k+1;l,m,n} &= {}_kH^y_{k;l,m,n} \\
&+ \frac{v}{w}\frac{Z_0 r^*_{yx}}{2}\left(H^y_{k;l+1,m,n} - 2H^y_{k;l,m,n} + H^y_{k;l-1,m,n}\right) \\
&+ \frac{v}{u}\frac{Z_0 r^*_{yz}}{2}\left(H^y_{k;l,m,n+1} - 2H^y_{k;l,m,n} + H^y_{k;l,m,n-1}\right) \\
&- \frac{r^*_{yz}}{2}\left(E^x_{k;l,m,n+1} - E^x_{k;l,m,n-1}\right) \\
&+ \frac{r^*_{yx}}{2}\left(E^z_{k;l+1,m,n} - E^z_{k;l-1,m,n}\right),
\end{aligned}
\tag{5.90}
$$

with the stability factors

$$
r^*_{yx} = \frac{1}{\mu_0 h_0 \mu_{ry}}\frac{\Delta t}{\Delta x} \qquad \text{and} \qquad r^*_{yz} = \frac{1}{\mu_0 h_0 \mu_{ry}}\frac{\Delta t}{\Delta z},
\tag{5.91}
$$

and

$$
\begin{aligned}
H^z_{k+1;l,m,n} &= H^z_{k;l,m,n} \\
&+ \frac{w}{v}\frac{Z_0 r^*_{zx}}{2}\left(H^z_{k;l+1,m,n} - 2H^z_{k;l,m,n} + H^z_{k;l-1,m,n}\right) \\
&+ \frac{w}{u}\frac{Z_0 r^*_{zy}}{2}\left(H^z_{k;l,m+1,n} - 2H^z_{k;l,m,n} + H^z_{k;l,m-1,n}\right) \\
&+ \frac{r^*_{zy}}{2}\left(E^x_{k;l,m+1,n} - E^x_{k;l,m-1,n}\right) \\
&- \frac{r^*_{zx}}{2}\left(E^y_{k;l+1,m,n} - E^y_{k;l-1,m,n}\right),
\end{aligned}
\tag{5.92}
$$

with the stability factors

$$
r^*_{zx} = \frac{1}{\mu_0 h_0 \mu_{rz}}\frac{\Delta t}{\Delta x} \qquad \text{and} \qquad r^*_{zy} = \frac{1}{\mu_0 h_0 \mu_{rz}}\frac{\Delta t}{\Delta y}.
\tag{5.93}
$$

In (5.88) to (5.92), we can recognize again the FTCS scheme with added artificial dispersion as in (5.60) to (5.64). The scheme considering ohmic losses (5.79) to (5.85) is of the same type, whereas the forward-in-time term is modified to account for the losses. A Taylor series expansion of the sampled exact solution results for the MIFD approximating the first MAXWELL equation in

$$
\begin{aligned}
(5.94)\quad & h_0\varepsilon_0\varepsilon_{rx}\frac{\partial E^x}{\partial t}\Big|_{k\Delta t;l\Delta x,m\Delta y,n\Delta z}+\mathcal{O}(\Delta t)\\
&+\sigma_{ex}E^x\Big|_{k\Delta t;l\Delta x,m\Delta y,n\Delta z}+\mathcal{O}(\Delta t)=\\
&\qquad -\frac{\partial H^y}{\partial z}\Big|_{k\Delta t;l\Delta x,m\Delta y,n\Delta z}+\mathcal{O}(\Delta t)+\mathcal{O}(\Delta z^2)\\
&\qquad +\frac{\partial H^z}{\partial y}\Big|_{k\Delta t;l\Delta x,m\Delta y,n\Delta z}+\mathcal{O}(\Delta t)+\mathcal{O}(\Delta y^2),
\end{aligned}
$$

$$
\begin{aligned}
(5.95)\quad & h_0\varepsilon_0\varepsilon_{ry}\frac{\partial E^y}{\partial t}\Big|_{k\Delta t;l\Delta x,m\Delta y,n\Delta z}+\mathcal{O}(\Delta t)\\
&+\sigma_{ey}E^y\Big|_{k\Delta t;l\Delta x,m\Delta y,n\Delta z}+\mathcal{O}(\Delta t)=\\
&\qquad \frac{\partial H^x}{\partial z}\Big|_{k\Delta t;l\Delta x,m\Delta y,n\Delta z}+\mathcal{O}(\Delta t)+\mathcal{O}(\Delta z^2)\\
&\qquad -\frac{\partial H^z}{\partial y}\Big|_{k\Delta t;l\Delta x,m\Delta y,n\Delta z}+\mathcal{O}(\Delta t)+\mathcal{O}(\Delta y^2),
\end{aligned}
$$

and

$$
\begin{aligned}
(5.96)\quad & h_0\varepsilon_0\varepsilon_{rz}\frac{\partial E^z}{\partial t}\Big|_{k\Delta t;l\Delta x,m\Delta y,n\Delta z}+\mathcal{O}(\Delta t)\\
&+\sigma_{ez}E^z\Big|_{k\Delta t;l\Delta x,m\Delta y,n\Delta z}+\mathcal{O}(\Delta t)=\\
&\qquad -\frac{\partial H^x}{\partial y}\Big|_{k\Delta t;l\Delta x,m\Delta y,n\Delta z}+\mathcal{O}(\Delta t)+\mathcal{O}(\Delta y^2)\\
&\qquad +\frac{\partial H^y}{\partial x}\Big|_{k\Delta t;l\Delta x,m\Delta y,n\Delta z}+\mathcal{O}(\Delta t)+\mathcal{O}(\Delta x^2),
\end{aligned}
$$

and for the MIFD approximating the three components of the second MAXWELL equation in

$$
\begin{aligned}
(5.97)\quad & h_0\mu_0\mu_{rx}\frac{\partial H^x}{\partial t}\Big|_{k\Delta t;l\Delta x,m\Delta y,n\Delta z}+\mathcal{O}(\Delta t)=\\
&\qquad \frac{\partial E^y}{\partial z}\Big|_{k\Delta t;l\Delta x,m\Delta y,n\Delta z}+\mathcal{O}(\Delta t)+\mathcal{O}(\Delta z^2)\\
&\qquad -\frac{\partial E^z}{\partial y}\Big|_{k\Delta t;l\Delta x,m\Delta y,n\Delta z}+\mathcal{O}(\Delta t)+\mathcal{O}(\Delta y^2),
\end{aligned}
$$

$$
\begin{aligned}
h_0\mu_0\mu_{ry}\frac{\partial H^y}{\partial t}\Big|_{k\Delta t;l\Delta x,m\Delta y,n\Delta z} + \mathcal{O}(\Delta t) = \\
-\frac{\partial E^x}{\partial z}\Big|_{k\Delta t;l\Delta x,m\Delta y,n\Delta z} + \mathcal{O}(\Delta t) + \mathcal{O}(\Delta z^2) \\
+\frac{\partial E^z}{\partial x}\Big|_{k\Delta t;l\Delta x,m\Delta y,n\Delta z} + \mathcal{O}(\Delta t) + \mathcal{O}(\Delta x^2),
\end{aligned} \tag{5.98}
$$

and

$$
\begin{aligned}
h_0\mu_0\mu_{rz}\frac{\partial H^z}{\partial t}\Big|_{k\Delta t;l\Delta x,m\Delta y,n\Delta z} + \mathcal{O}(\Delta t) = \\
\frac{\partial E^x}{\partial y}\Big|_{k\Delta t;l\Delta x,m\Delta y,n\Delta z} + \mathcal{O}(\Delta t) + \mathcal{O}(\Delta y^2) \\
-\frac{\partial E^y}{\partial x}\Big|_{k\Delta t;l\Delta x,m\Delta y,n\Delta z} + \mathcal{O}(\Delta t) + \mathcal{O}(\Delta x^2).
\end{aligned} \tag{5.99}
$$

Hence, the mapping induced finite difference scheme is accurate of the order $\mathcal{O}(\Delta t)$, as the spatial derivatives have also associated with them higher order terms of the order $\mathcal{O}(\Delta t)$. This is a consequence of considering losses. Taking the limit $\Delta t \longrightarrow 0$ and $\Delta l \longrightarrow 0$ the higher order terms vanish and MAXWELL's equation considering ohmic losses remain

$$h_0\varepsilon_{rx}\varepsilon_0\frac{\partial E^x}{\partial t} + \sigma_{ex}E^x = -\frac{\partial H^y}{\partial z} + \frac{\partial H^z}{\partial y}, \tag{5.100}$$

$$h_0\varepsilon_{ry}\varepsilon_0\frac{\partial E^y}{\partial t} + \sigma_{ey}E^y = \frac{\partial H^x}{\partial z} - \frac{\partial H^z}{\partial x}, \tag{5.101}$$

$$h_0\varepsilon_{rz}\varepsilon_0\frac{\partial E^z}{\partial t} + \sigma_{ez}E^z = -\frac{\partial H^x}{\partial y} + \frac{\partial H^y}{\partial x}, \tag{5.102}$$

and

$$h_0\mu_{rx}\mu_0\frac{\partial H^x}{\partial t} = \frac{\partial E^y}{\partial z} - \frac{\partial E^z}{\partial y}, \tag{5.103}$$

$$h_0\mu_{ry}\mu_0\frac{\partial H^y}{\partial t} = -\frac{\partial E^x}{\partial z} + \frac{\partial E^z}{\partial x}, \tag{5.104}$$

$$h_0\mu_{rz}\mu_0\frac{\partial H^z}{\partial t} = \frac{\partial E^x}{\partial y} - \frac{\partial E^y}{\partial x}. \tag{5.105}$$

The scheme models again a medium with h_0-times the indicated physical relative permittivity and permeability as given by eqn. (5.78). Again, this is a consequence of the increased propagation velocity in the TLM mesh.

3.3. Stability of Mapping Induced FD Schemes of SCN-TLM with Stubs. To satisfy LAX's theorem, we need to show that the mapping induced equivalent finite difference scheme of the SCN with stubs is stable. The stability of the SCN-TLM scheme without stubs is given by energy conservation and a

fixed stability factor. In the stub-loaded SCN-TLM scheme, the stability factor directly enters the stubs and hence influences the stability.

One way of showing stability is to apply a discrete Fourier transform in the spatial variables to $\boldsymbol{P\Gamma SQ}$ and show that the eigenvalues are bounded by one [**100**]. As one can only calculate the eigenvalues of square matrices of order greater than five analytically in special cases, we have to follow a different argument. It is a matter of fact that if

$$|Y_x| \geq 0 \quad \wedge \quad |Y_y| \geq 0 \quad \wedge \quad |Y_z| \geq 0, \tag{5.106}$$

$$|Z_x| \geq 0 \quad \wedge \quad |Z_y| \geq 0 \quad \wedge \quad |Z_z| \geq 0, \tag{5.107}$$

is fulfilled, the TLM algorithm is stable. As $\boldsymbol{S}$ is unitary, it is bounded, too [**16**]. $\boldsymbol{\Gamma}$ is a shift operator, therefore it is isometric [**16**] and hence, there exists an upper bound for the operatornorm of $\boldsymbol{\Gamma S}$[1]

$$\|\boldsymbol{\Gamma S}\| \leq C_1. \tag{5.108}$$

We essentially want to show that

$$\|\boldsymbol{\Gamma S}\| \leq C_1 \Longrightarrow \|\boldsymbol{P\Gamma SQ}\| \leq C_2, \tag{5.109}$$

which is equivalent to

$$\|\boldsymbol{P\Gamma SQ}\| \leq \|\boldsymbol{P}\|\|\boldsymbol{\Gamma S}\|\|\boldsymbol{Q}\| \leq C_3. \tag{5.110}$$

All HILBERT spaces of the same dimension are isomorphic and consequently, $\boldsymbol{P}$ and $\boldsymbol{Q}$ can be represented by matrices $\in R^{m\times n}$. All matrices $\in R^{m\times n}$ are continuous. Moreover, the mappings $\boldsymbol{P}$ and $\boldsymbol{Q}$ are both linear. All linear and continuous operators are bounded [**16**], and hence the mapping induced finite difference scheme of the SCN-TLM scheme is stable if the TLM algorithm is stable, which indeed is the fact.

3.4. Convergence of the SCN-TLM Scheme with Stubs. Analogous to the case of SCN-TLM without stubs, we have shown using LAX's theorem that for the MIFD scheme

$$\lim_{\Delta t\to 0} \|(\boldsymbol{PT\Gamma SQ})^k \boldsymbol{f}(0) - \boldsymbol{f}(k\Delta t)\| \longrightarrow 0 \tag{5.111}$$

holds. Now, we want to show that this also implies the convergence of the stub-loaded SCN-TLM scheme

$$\lim_{\Delta t\to 0} \|\boldsymbol{P}(\boldsymbol{T\Gamma S})^k \boldsymbol{Q}\boldsymbol{f}(0) - \boldsymbol{f}(k\Delta t)\| \longrightarrow 0. \tag{5.112}$$

For this, we need to show again that the difference between the two difference operators vanishes in the norm of $\mathcal{X}_h$ when $\Delta t \longrightarrow 0$, i.e.

$$\lim_{\Delta t\to 0} \|(\boldsymbol{PT\Gamma SQ})^k - \boldsymbol{P}(\boldsymbol{T\Gamma S})^k \boldsymbol{Q}\| \longrightarrow 0. \tag{5.113}$$

[1] $\|\boldsymbol{\Gamma S}\| = \|\boldsymbol{\Gamma TS}\|$ as the time shift operator $\boldsymbol{T}$ is also isometric.

Exploiting the boundedness of the operator product in (5.113) yields

$$\|(\boldsymbol{PT\Gamma SQ})^k - \boldsymbol{P}(\boldsymbol{T\Gamma S})^k\boldsymbol{Q}\| \leq \|\boldsymbol{PT}^{k-1}\|\|(\boldsymbol{\Gamma SQP} - \boldsymbol{\Gamma S})\|^{k-1}\|\boldsymbol{T\Gamma S}\|\|\boldsymbol{Q}\|. \tag{5.114}$$

Again, we need to show that one of the terms on the right side of the inequality becomes arbitrarily small and constitutes an upper bound for the distance between the two schemes. Estimating the norm of $\|\boldsymbol{\Gamma SQP}-\boldsymbol{\Gamma S}\|$ by the norm of the sum of the columns, but neglecting ohmic and magnetic losses for simplicity, but without loss of generality, we get for $j = 1$

$$\begin{aligned}\|(\boldsymbol{\Gamma SQP} - \boldsymbol{\Gamma S})e_1\| &= \sqrt{\frac{\Delta t}{h^2u^2v^2}\left(\frac{64huv(4hu\mu_r v - 8w)}{\mu_r} + \frac{16u^4(4u - 2\varepsilon_r hvw)^2}{\varepsilon_r^2 w^2(\varepsilon_r hvw - 2u)^2}\right.} \\ &\quad \sqrt{+\frac{(8u^2\mu_r - 16\varepsilon_r\mu_r huvw + 8\varepsilon_r w^2)^2}{\varepsilon_r^2\mu_r^2 w^2}|\boldsymbol{Y}^\dagger| + \frac{(8\mu_r u^2 - 8\varepsilon_r w^2)^2}{\varepsilon_r^2\mu_r^2 w^2}|\boldsymbol{Y}|} \\ &\quad \left.\sqrt{+\frac{64w^2}{\mu_r^2}(|\boldsymbol{X}|^2 + |\boldsymbol{X}^\dagger|^2) + \frac{64u^4}{\varepsilon_r^2 w^2}(|\boldsymbol{Z}|^2 + |\boldsymbol{Z}^\dagger|^2)}\right) l\Delta x m\Delta y n\Delta z\,.\end{aligned} \tag{5.115}$$

It is only summed over l, m, n (see the definition of the norm (5.5), (5.6)), as the operators $\boldsymbol{\Gamma}$, $\boldsymbol{S}$, $\boldsymbol{Q}$, $\boldsymbol{P}$ act on $(\ell_{2,\Delta x,\Delta y,\Delta z}(\boldsymbol{G}))^{12}$. Taking the limit, $l\Delta x$, $m\Delta y$, $n\Delta z$ converge against the width of the domain in directions x, y, z, assuming again a rectangular domain. Exploiting the fixed relation between Δl and Δt, we are left with $\sqrt{\Delta t}\ C_s$. The constant C_s denotes the squared absolute value of the shift operators in (5.115). The same results for all other terms and hence, we have again an upper bound of the order $\mathcal{O}(\sqrt{\Delta t})$.

3.5. Order of Accuracy Estimation. The estimation of the asymptotic approximation order is completely analogous to the case without stubs. Hence, from

$$\|(\boldsymbol{PT\Gamma SQ})^k\boldsymbol{f}(0) - \boldsymbol{f}(k\Delta t)\| \leq \mathcal{O}(\Delta t) \tag{5.116}$$

and

$$\|(\boldsymbol{PT\Gamma SQ})^k\boldsymbol{f}(0) - \boldsymbol{P}(\boldsymbol{T\Gamma S})^k\boldsymbol{Qf}(0)\| \leq \mathcal{O}(\sqrt{\Delta t}) \tag{5.117}$$

follows again

$$
\begin{aligned}
&\|\boldsymbol{P}(\boldsymbol{T\Gamma S})^k\boldsymbol{Q}\boldsymbol{f}(0) - \boldsymbol{f}(k\Delta t)\| \\
&\quad = \|\boldsymbol{P}(\boldsymbol{T\Gamma S})^k\boldsymbol{Q}\boldsymbol{f}(0) - (\boldsymbol{PT\Gamma SQ})^k\boldsymbol{f}(0) \\
&\qquad\qquad + (\boldsymbol{PT\Gamma SQ})^k\boldsymbol{f}(0) - \boldsymbol{f}(k\Delta t)\| \\
&\quad \leq \|\boldsymbol{P}(\boldsymbol{T\Gamma S})^k\boldsymbol{Q}\boldsymbol{f}(0) - (\boldsymbol{PT\Gamma SQ})^k\boldsymbol{f}(0)\| \\
&\qquad\qquad + \|(\boldsymbol{PT\Gamma SQ})^k\boldsymbol{f}(0) - \boldsymbol{f}(k\Delta t)\| \\
&\quad \leq \mathcal{O}(\sqrt{\Delta t}).
\end{aligned}
\tag{5.118}
$$

Consequently, also the stub-loaded SCN-TLM scheme converges asymptotically only with order $\mathcal{O}(\sqrt{\Delta t})$. The numerical verification is presented in Chapter 7.

CHAPTER 6

The Alternating Rotated Transmission Line Matrix Scheme

1. Introduction to ARTLM

In order to discretize thin layers more accurately, a TLM method is desired that requires less floating point operations for a scattering event and less unknowns, which allows a finer discretization of the structures under consideration. The *Alternating Rotated Transmission Line Matrix* (ARTLM) scheme recently proposed by RUSSER [**85**] requires theoretically only 25 % of the usual number of unknowns in TLM simulations. Also the number of floating point operations and the number of scattering parameters that need to be stored is considerably lower than in usual TLM methods. This makes the ARTLM scheme a promising method for the characterization of planer microwave circuits. However, apart from the original derivation, a detailed analysis of its consistency and convergence has not been given yet. This will be presented in this chapter. We briefly sketch the derivation of the ARTLM scheme in the sequel. The detailed derivation can be found in [**85**]. If one rotates the polarization states of the mesh lines of the SCN-TLM scheme by 45° and combines it with the *Alternating Transmission Line Matrix* (ATLM) scheme, the SCN-TLM scheme degenerates into four independent schemes, known as the ARTLM method. For this, the ATLM scheme is sketched and the RTLM scheme is introduced. Finally, these two schemes are combined, yielding the four possible schemes of the ARTLM method. Various proposed field-mappings between the discretized electromagnetic field components and the rotated TLM pulses are analysed for studying the consistency of the ARTLM method with MAXWELL's equations.

1.1. The ATLM Scheme. The starting point of the alternating transmission line matrix method is the observation that the TLM pulses that propagate through an infinite TLM mesh of symmetrical condensed nodes without stubs can be separated into two independent subsets. In Fig. 6.1 a section of an infinite TLM mesh is shown. The sets of pulses that are assigned to the white and gray nodes are completely independent. This can be exploited to reduce the computational effort by considering only one subset. In principle, one could reduce the storage

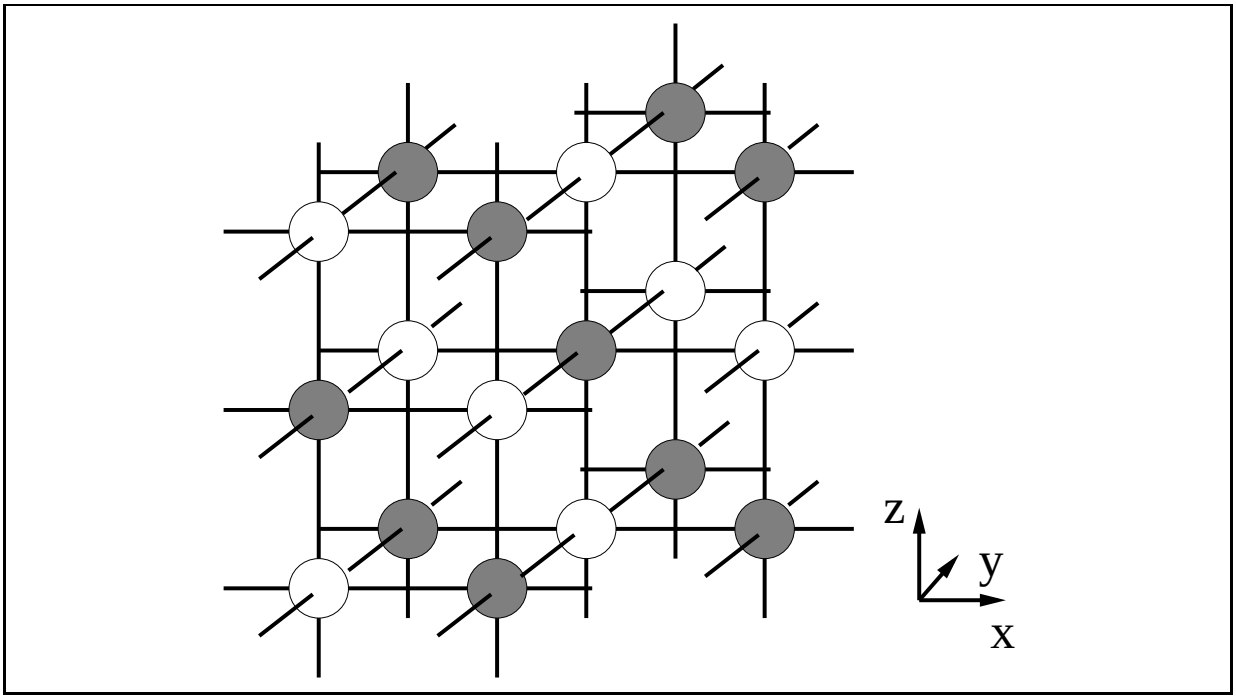

FIGURE 6.1. A section of a condensed node TLM mesh without stubs. The pulses assigned to the white and gray nodes form two completely independent sets.

requirement by 50 % if no medium is required [**86**]. This means no loss of accuracy in the sample points. Only information from the second subset is lost, which has no practical consequences as these field values can be interpolated without loss of accuracy. In comparison to the conventional SCN-TLM method the boundary conditions and the stubs for simulating media need to be modified. This is to avoid that the pulses from the subsets of the two parities are mixed up. The boundaries need to be shifted into the centre of the TLM cells. Consequently, special boundary nodes for all types of walls, edges, and corners have to be designed, which means an additional effort in contrast to conventional TLM [**5**]. To keep the two sets of TLM pulses independent, the length of the open and short circuited stubs needs simply to be doubled in order to double the propagation time of pulses that propagate on them. Practically, when inhomogeneous media have to be considered, the storage savings are of the order of 33 %. A further advantage of the ATLM method is the absence of excitation induced spurious modes, which is illustrated in Fig. 6.2, showing the ATLM dispersion diagram. The dispersion surfaces of constant phase encompassing the origin represent the wave numbers of the physical modes. The dispersion surfaces of constant phase in the upper right corner represent the wave numbers of the spurious modes of the conventional TLM method. They are 'cut away' in the ATLM method by using only one set of the TLM pulses so that the ATLM mesh only supports the physical modes. A detailed

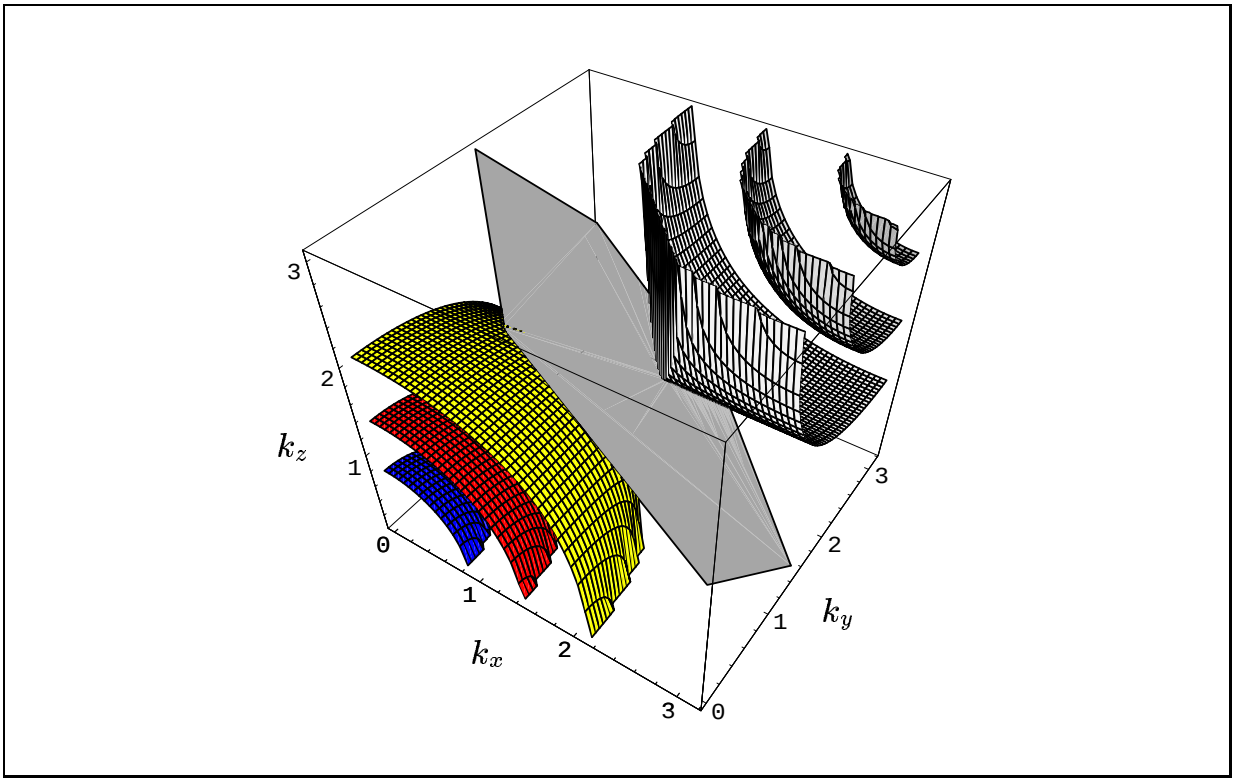

FIGURE 6.2. The ATLM dispersion diagram. The first octant of the three-dimensional $\boldsymbol{k}-$space is shown. The dispersion surfaces of constant phase encompassing the origin represent the wave numbers of the physical modes. The dispersion surfaces of constant phase in the upper right corner represent the wave numbers of the unphysical modes of the conventional TLM method. These are 'cut away' in the ATLM method and only the physical modes are supported in the ATLM mesh.

investigation of the ATLM method can be found in [**5**]. The ATLM method has successfully been applied to simulate coplanar waveguide discontinuities [**7**] and microstrip antennas [**48, 49**].

1.2. The RTLM Scheme. If one rotates the polarization states of the mesh lines of the conventional SCN-TLM scheme by 45°, one gets two independent scattering algorithms with 6×6 scattering matrices. These schemes are called the left- and righthanded *Rotated Transmission Line Matrix* (RTLM) schemes. First, the amplitude vectors $|a>$ and $|b>$ are transformed to rotated amplitude vectors $|\tilde{a}>$ and $|\tilde{b}>$

$$|\tilde{a}> = \boldsymbol{R}|a> \ , \tag{6.1}$$

$$|\tilde{b}> = \boldsymbol{R}|b> \tag{6.2}$$

by using the rotation matrix

$$\boldsymbol{R} = \frac{1}{\sqrt{2}} \begin{pmatrix} 1 & 0 & 1 & 0 & 0 & 0 & 0 & 0 & 0 & 0 & 0 & 0 \\ 0 & 1 & 0 & -1 & 0 & 0 & 0 & 0 & 0 & 0 & 0 & 0 \\ 0 & 0 & 0 & 0 & 1 & 0 & 1 & 0 & 0 & 0 & 0 & 0 \\ 0 & 0 & 0 & 0 & 0 & 1 & 0 & -1 & 0 & 0 & 0 & 0 \\ 0 & 0 & 0 & 0 & 0 & 0 & 0 & 0 & 1 & 0 & 1 & 0 \\ 0 & 0 & 0 & 0 & 0 & 0 & 0 & 0 & 0 & 1 & 0 & -1 \\ 1 & 0 & -1 & 0 & 0 & 0 & 0 & 0 & 0 & 0 & 0 & 0 \\ 0 & 1 & 0 & 1 & 0 & 0 & 0 & 0 & 0 & 0 & 0 & 0 \\ 0 & 0 & 0 & 0 & 1 & 0 & -1 & 0 & 0 & 0 & 0 & 0 \\ 0 & 0 & 0 & 0 & 0 & 1 & 0 & 1 & 0 & 0 & 0 & 0 \\ 0 & 0 & 0 & 0 & 0 & 0 & 0 & 0 & 1 & 0 & -1 & 0 \\ 0 & 0 & 0 & 0 & 0 & 0 & 0 & 0 & 0 & 1 & 0 & 1 \end{pmatrix} . \tag{6.3}$$

This rotates the polarization states of the TLM waves $|a>$ and $|b>$ by 45°, respectively. The scattering matrix $\tilde{\boldsymbol{S}}_0$ relating the rotated wave amplitude vectors $|\tilde{a}>$ and $|\tilde{b}>$ is calculated from the free space SCN-TLM scattering matrix $\boldsymbol{S}_0$ by transformation

$$\tilde{\boldsymbol{S}}_0 = \boldsymbol{R}\boldsymbol{S}_0\boldsymbol{R}^{-1}, \tag{6.4}$$

with $\boldsymbol{S}_0$ given by (5.20). This results in the RTLM scattering matrix

$$\tilde{\boldsymbol{S}}_0 = \begin{pmatrix} \tilde{\boldsymbol{S}}_A & 0 \\ 0 & -\tilde{\boldsymbol{S}}_A \end{pmatrix} \tag{6.5}$$

with the submatrix

$$\tilde{\boldsymbol{S}}_A = \frac{1}{2} \begin{pmatrix} 0 & 0 & 1 & 1 & 1 & -1 \\ 0 & 0 & -1 & -1 & 1 & -1 \\ 1 & -1 & 0 & 0 & 1 & -1 \\ 1 & -1 & 0 & 0 & -1 & -1 \\ 1 & 1 & 1 & -1 & 0 & 0 \\ -1 & -1 & 1 & -1 & 0 & 0 \end{pmatrix} . \tag{6.6}$$

The twelve-port describing the symmetrical condensed TLM node degenerates into two six-port nodes if the polarization state of the TLM waves is rotated by 45°. This is illustrated in Fig. 6.3. The two six-port nodes are called the lefthanded and righthanded rotated TLM nodes or RTLM nodes.

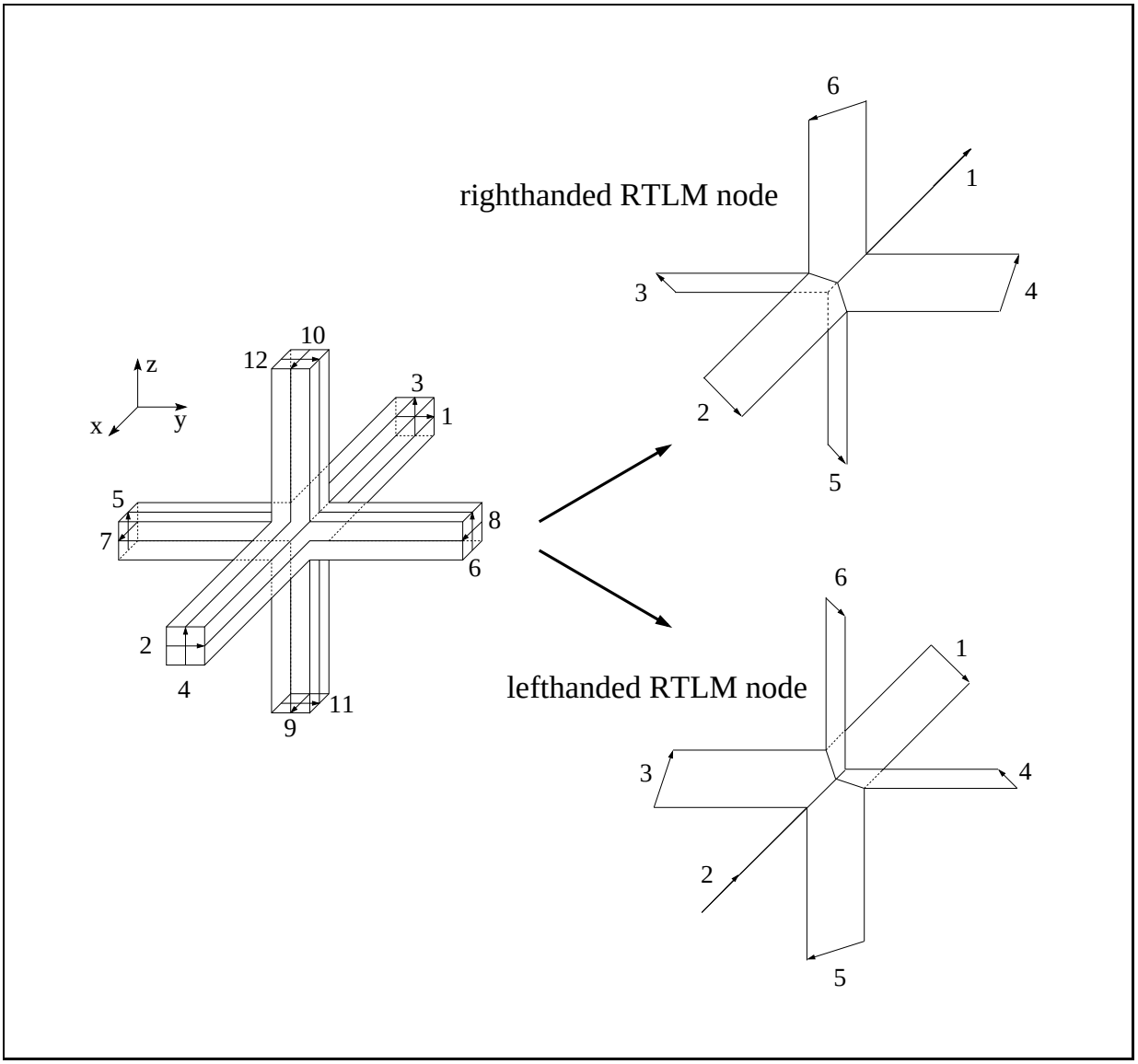

FIGURE 6.3. The twelve-port describing the symmetrical condensed TLM node degenerates into two six-port nodes in the rotated representation.

The connection operator $\tilde{\mathbf{\Gamma}}$ relating the scattered rotated wave amplitude vector $|\tilde{b}>$ to the incident rotated wave amplitude vector $|\tilde{a}>$ calculates

$$\tilde{\mathbf{\Gamma}} = \boldsymbol{R}\mathbf{\Gamma}\boldsymbol{R}^{-1}, \tag{6.7}$$

where $\mathbf{\Gamma}$ is given by eqn. (5.21). From eqn. (6.7) one obtains the rotated connection operator

$$\tilde{\mathbf{\Gamma}} = \begin{pmatrix} 0 & \tilde{\mathbf{\Gamma}}_A \\ \tilde{\mathbf{\Gamma}}_A & 0 \end{pmatrix} \tag{6.8}$$

with

$$\tilde{\mathbf{\Gamma}}_A = \frac{1}{2} \begin{pmatrix} 0 & \boldsymbol{X} & 0 & 0 & 0 & 0 \\ \boldsymbol{X}^\dagger & 0 & 0 & 0 & 0 & 0 \\ 0 & 0 & 0 & \boldsymbol{Y} & 0 & 0 \\ 0 & 0 & \boldsymbol{Y}^\dagger & 0 & 0 & 0 \\ 0 & 0 & 0 & 0 & 0 & \boldsymbol{Z} \\ 0 & 0 & 0 & 0 & \boldsymbol{Z}^\dagger & 0 \end{pmatrix}. \tag{6.9}$$

1.3. The ARTLM Scheme. Combining the ATLM and RTLM schemes results in four independent schemes. A righthanded node is always connected to six lefthanded nodes and vice versa. As a SCN at point (l, m, n) degenerates into one lefthanded RTLM node at (l, m, n) and one righthanded RTLM node at (l, m, n) as indicated in Fig. 6.3, one gets two independent RTLM meshes. The first RTLM mesh has the lefthanded nodes at (l, m, n) with even spatial parity $p_s = l + m + n$, and the other has the righthanded nodes at (l, m, n) with even spatial parity. A section of one of the (A)RTLM mesh is shown in Fig. 6.4. Taking further into account that the pulses that are assigned to the lefthanded and the righthanded node at a certain time step are independent, one gets four independent schemes.

First, let us consider the ARTLM mesh that has the lefthanded nodes at (l, m, n) with even spatial parity. The set of pulses that is assigned to the lefthanded nodes at even time steps shall be called LE and the set of pulses that is assigned to the lefthanded nodes at odd time steps shall be called LO.

In the other mesh, when the righthanded RTLM nodes are located at (l, m, n) with even spatial parity, we get the scheme RE for the set of pulses that is assigned to the righthanded nodes at even time steps and the scheme RO for the set of pulses that is assigned to the righthanded nodes at odd time steps.

For scheme LE, the pulses propagate in the following manner. At the first time step, scattering takes place at lefthanded nodes, whereas the neighbouring righthanded nodes at (l, m, n) with odd spatial parity are not 'visible' during this time for pulses of scheme LE. Then the scattered pulses propagate to their neighbours with odd spatial parity. In the next time step, the pulses of the LE scheme are scattered at righthanded nodes with odd spatial parity and the lefthanded nodes with even spatial parity are invisible to them. After propagating to the neighbouring lefthanded nodes again, the LE pulses are scattered again at lefthanded nodes. This procedure repeats itself further and further.

Scheme LO operates in an analogous way. At odd time steps (considering the same temporal basis), scattering takes place at lefthanded nodes with even spatial parity. Consequently, the righthanded nodes with odd spatial parity are

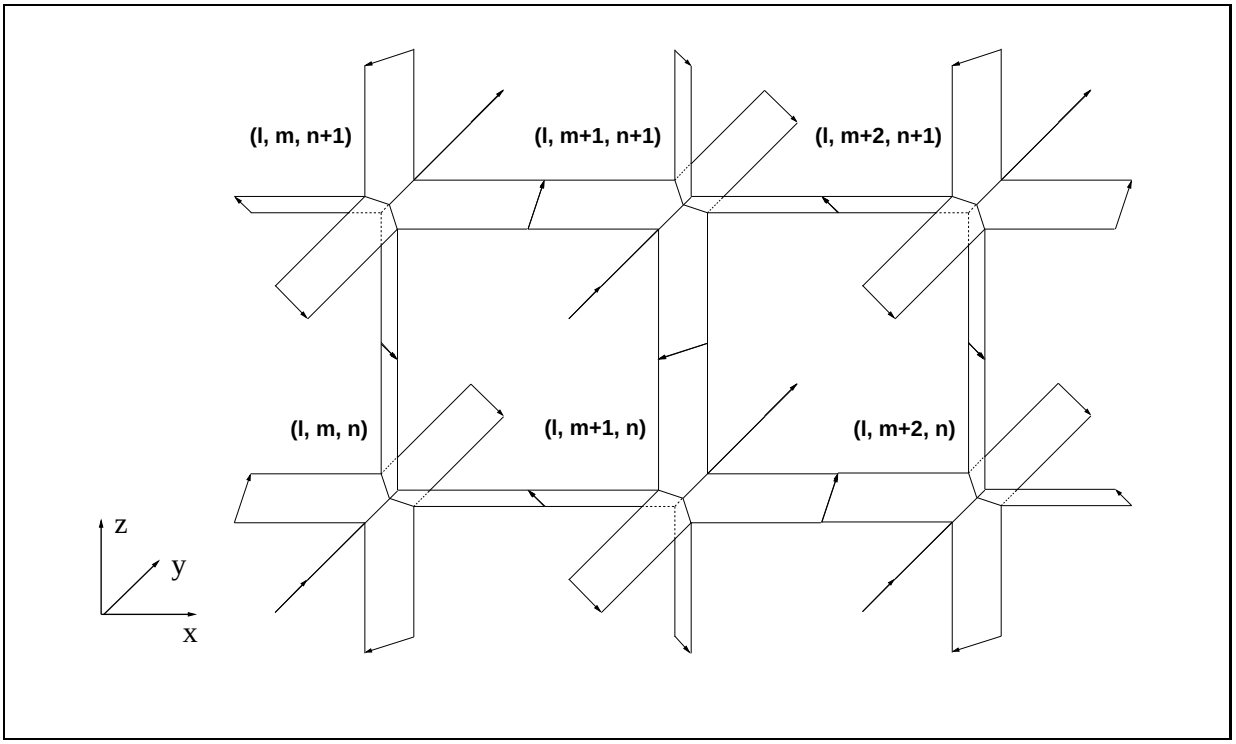

FIGURE 6.4. The RTLM mesh of ARTLM schemes LE and LO, i.e. lefthanded nodes are located at (l, m, n) with even spatial parity. The RTLM mesh of schemes RE and RO is shifted by one spatial index, i.e. righthanded nodes are located at places with even spacial parity, or, at places where in this picture are the lefthanded nodes. Considering even time steps, the set of pulses that is assigned to all lefthanded RTLM nodes at (l, m, n) with even spatial parity is called scheme LE and the set of pulses that is assigned to the righthanded RTLM nodes at (l, m, n) with odd spatial parity is called scheme LO.

not visible to pulses of scheme LO. After the connect operation, the scattering of the LO pulses takes place at the righthanded nodes with odd spatial parity at the next time step.

Schemes RE and RO are iterated analogously. The four schemes can be transformed into each other by shifting one of the two RTLM meshes one increment in space and by shifting time by one temporal increment.

The bijective mapping following [**85**] between the field vector of all field components at all lefthanded nodes $|\tilde{f}_l>$ and the vector of the rotated TLM wave amplitudes assigned to all lefthanded nodes is given by

$$|\tilde{f}_l> = \boldsymbol{Q}_{al}|\tilde{a}_l>, \tag{6.10}$$

with the lefthanded mapping operator

$$\boldsymbol{Q}_{al} = \begin{pmatrix} 0 & 1 & 1 & 0 & -1 & 1 \\ 0 & 1 & -1 & 0 & -1 & -1 \\ 1 & 0 & 1 & 1 & 0 & -1 \\ -1 & 0 & 1 & -1 & 0 & -1 \\ 1 & 1 & 0 & -1 & 1 & 0 \\ 1 & -1 & 0 & -1 & -1 & 0 \end{pmatrix}. \tag{6.11}$$

The relation between incident rotated TLM wave pulses and the electromagnetic field components at the righthanded nodes is given by

$$|\tilde{f}_r> = \boldsymbol{Q}_{ar}|\tilde{a}_r>, \tag{6.12}$$

with the righthanded mapping operator

$$\boldsymbol{Q}_{ar} = \begin{pmatrix} 0 & 1 & -1 & 0 & 1 & 1 \\ 0 & 1 & 1 & 0 & 1 & -1 \\ -1 & 0 & 1 & 1 & 0 & 1 \\ 1 & 0 & 1 & -1 & 0 & 1 \\ 1 & -1 & 0 & 1 & 1 & 0 \\ 1 & 1 & 0 & 1 & -1 & 0 \end{pmatrix}. \tag{6.13}$$

2. Analysis of Consistency of ARTLM Schemes

In order to analyse the consistency of the four ARTLM schemes with MAXWELL's equations, equivalent finite difference schemes are derived by applying the bijective field-mappings at the lefthanded and at the righthanded nodes. The resulting finite difference schemes are then investigated in the known manner by developing the exact solution in a TAYLOR series and taking the limit $\Delta t \longrightarrow 0$ and $\Delta l \longrightarrow 0$, respectively.

2.1. Equivalent Finite Difference Schemes. First, the schemes LE and RE are investigated. The basic scattering equations of these two schemes are written as

$$\begin{bmatrix} |\tilde{b}_{LE}> \\ |\tilde{b}_{RE}> \end{bmatrix} = \begin{pmatrix} \boldsymbol{T}\tilde{\boldsymbol{S}}_A & 0 \\ 0 & -\boldsymbol{T}\tilde{\boldsymbol{S}}_A \end{pmatrix} \begin{bmatrix} |\tilde{a}_{LE}> \\ |\tilde{a}_{RE}> \end{bmatrix}. \tag{6.14}$$

The index LE denotes the state vector whose elements belong to the set of pulses of scheme LE and the index RE indicates that the elements of this state vector belong to the set of pulses of scheme RE. The connection operation is described by the following equation

$$\begin{bmatrix} |\tilde{a}_{LE}> \\ |\tilde{a}_{RE}> \end{bmatrix} = \begin{pmatrix} 0 & \tilde{\boldsymbol{\Gamma}}_{\boldsymbol{A}} \\ \tilde{\boldsymbol{\Gamma}}_{\boldsymbol{A}} & 0 \end{pmatrix} \begin{bmatrix} |\tilde{b}_{LE}> \\ |\tilde{b}_{RE}> \end{bmatrix}. \tag{6.15}$$

Inserting (6.15) into (6.14) yields

$$\begin{bmatrix} |\tilde{a}_{LE}> \\ |\tilde{a}_{RE}> \end{bmatrix} = \begin{pmatrix} 0 & -\tilde{\boldsymbol{\Gamma}}_{\boldsymbol{A}} \boldsymbol{T} \tilde{\boldsymbol{S}}_A \\ \tilde{\boldsymbol{\Gamma}}_{\boldsymbol{A}} \boldsymbol{T} \tilde{\boldsymbol{S}}_A & 0 \end{pmatrix} \begin{bmatrix} |\tilde{a}_{LE}> \\ |\tilde{a}_{RE}> \end{bmatrix}. \tag{6.16}$$

Applying the mapping between electromagnetic field components and the rotated TLM pulses at lefthanded and righthanded RTLM nodes, (6.10) to (6.13), respectively, yields the following schemes written in finite difference operator notation

$$\boldsymbol{f}_{LE;k+1} = -\boldsymbol{Q}_{al}^{-1} \tilde{\boldsymbol{\Gamma}}_{\boldsymbol{A}} \tilde{\boldsymbol{S}}_A \boldsymbol{Q}_{ar} \boldsymbol{f}_{RE;k} = \boldsymbol{\Phi}_{LE} \boldsymbol{f}_{RE;k} \tag{6.17}$$

with the difference operator

$$\boldsymbol{\Phi}_{LE} = \frac{1}{4} \begin{pmatrix} \boldsymbol{D_{YZ}} & -\boldsymbol{D_Z} & -\boldsymbol{D_Y} & \boldsymbol{D^-_{YZ}} & -\boldsymbol{D_Z} & \boldsymbol{D_Y} \\ -\boldsymbol{D_Z} & \boldsymbol{D_{XZ}} & -\boldsymbol{D_X} & \boldsymbol{D_Z} & \boldsymbol{D^-_{ZX}} & -\boldsymbol{D_X} \\ -\boldsymbol{D_Y} & -\boldsymbol{D_X} & \boldsymbol{D_{XY}} & -\boldsymbol{D_Y} & \boldsymbol{D_X} & \boldsymbol{D^-_{XY}} \\ \boldsymbol{D^-_{YZ}} & \boldsymbol{D_Z} & -\boldsymbol{D_Y} & \boldsymbol{D_{YZ}} & \boldsymbol{D_Z} & \boldsymbol{D_Y} \\ -\boldsymbol{D_Z} & \boldsymbol{D^-_{ZX}} & \boldsymbol{D_X} & \boldsymbol{D_Z} & \boldsymbol{D_{XZ}} & \boldsymbol{D_X} \\ \boldsymbol{D_Y} & -\boldsymbol{D_X} & \boldsymbol{D^-_{XY}} & \boldsymbol{D_Y} & \boldsymbol{D_X} & \boldsymbol{D_{XY}} \end{pmatrix}, \tag{6.18}$$

and

$$\boldsymbol{f}_{RE;k+1} = \boldsymbol{Q}_{ar}^{-1} \tilde{\boldsymbol{\Gamma}}_{\boldsymbol{A}} \tilde{\boldsymbol{S}}_A \boldsymbol{Q}_{al} \boldsymbol{f}_{LE;k} = \boldsymbol{\Phi}_{RE} \boldsymbol{f}_{RE;k} \tag{6.19}$$

with the difference operator

$$\boldsymbol{\Phi}_{RE} = \frac{1}{4} \begin{pmatrix} \boldsymbol{D_{YZ}} & \boldsymbol{D_Z} & \boldsymbol{D_Y} & \boldsymbol{D^-_{ZY}} & -\boldsymbol{D_Z} & \boldsymbol{D_Y} \\ \boldsymbol{D_Z} & \boldsymbol{D_{XZ}} & \boldsymbol{D_X} & \boldsymbol{D_Z} & \boldsymbol{D^-_{XZ}} & -\boldsymbol{D_X} \\ \boldsymbol{D_Y} & \boldsymbol{D_X} & \boldsymbol{D_{XY}} & -\boldsymbol{D_Y} & \boldsymbol{D_X} & \boldsymbol{D^-_{YX}} \\ \boldsymbol{D^-_{ZY}} & \boldsymbol{D_Z} & -\boldsymbol{D_Y} & \boldsymbol{D_{YZ}} & -\boldsymbol{D_Z} & -\boldsymbol{D_Y} \\ -\boldsymbol{D_Z} & \boldsymbol{D^-_{XZ}} & \boldsymbol{D_X} & -\boldsymbol{D_Z} & \boldsymbol{D_{XZ}} & -\boldsymbol{D_X} \\ \boldsymbol{D_Y} & -\boldsymbol{D_X} & \boldsymbol{D^-_{YX}} & -\boldsymbol{D_Y} & -\boldsymbol{D_X} & \boldsymbol{D_{XY}} \end{pmatrix}. \tag{6.20}$$

The scalar difference operators of (6.18) and (6.20) are given as follows

$$\boldsymbol{D_X} = \boldsymbol{X}^\dagger - \boldsymbol{X} \tag{6.21}$$

$$\boldsymbol{D_{XY}} = \boldsymbol{X}^\dagger + \boldsymbol{X} + \boldsymbol{Y}^\dagger + \boldsymbol{Y},$$

$$\boldsymbol{D^-_{YX}} = (\boldsymbol{Y}^\dagger + \boldsymbol{Y}) - (\boldsymbol{X}^\dagger + \boldsymbol{X}). \tag{6.22}$$

Analogously, the scattering of the remaining schemes LO and RO is given by

$$\begin{bmatrix} |\tilde{b}_{LO}> \\ |\tilde{b}_{RO}> \end{bmatrix} = \begin{pmatrix} \boldsymbol{T}\tilde{\boldsymbol{S}}_A & 0 \\ 0 & -\boldsymbol{T}\tilde{\boldsymbol{S}}_A \end{pmatrix} \begin{bmatrix} |\tilde{a}_{LO}> \\ |\tilde{a}_{RO}> \end{bmatrix}. \tag{6.23}$$

The connection process is again described by

$$\begin{bmatrix} |\tilde{a}_{LO}> \\ |\tilde{a}_{RO}> \end{bmatrix} = \begin{pmatrix} 0 & \tilde{\boldsymbol{\Gamma}}_{\boldsymbol{A}} \\ \tilde{\boldsymbol{\Gamma}}_{\boldsymbol{A}} & 0 \end{pmatrix} \begin{bmatrix} |\tilde{b}_{LO}> \\ |\tilde{b}_{RO}> \end{bmatrix}. \tag{6.24}$$

Inserting (6.24) into (6.23) yields

$$\begin{bmatrix} |\tilde{a}_{LO}> \\ |\tilde{a}_{RO}> \end{bmatrix} = \begin{pmatrix} 0 & -\tilde{\boldsymbol{\Gamma}}_{\boldsymbol{A}}\boldsymbol{T}\tilde{\boldsymbol{S}}_A \\ \tilde{\boldsymbol{\Gamma}}_{\boldsymbol{A}}\boldsymbol{T}\tilde{\boldsymbol{S}}_A & 0 \end{pmatrix} \begin{bmatrix} |\tilde{a}_{LO}> \\ |\tilde{a}_{RO}> \end{bmatrix}. \tag{6.25}$$

Applying the mapping between electromagnetic field components and the rotated TLM pulses (6.10) to (6.13) yields the following schemes

$$\boldsymbol{f}_{LO;k+1} = -\boldsymbol{Q}_{al}^{-1}\tilde{\boldsymbol{\Gamma}}_{\boldsymbol{A}}\tilde{\boldsymbol{S}}_A\boldsymbol{Q}_{ar}\boldsymbol{f}_{RO;k} = \boldsymbol{\Phi}_{LO}\boldsymbol{f}_{RO;k}, \tag{6.26}$$

with

$$\boldsymbol{\Phi}_{LO} = \boldsymbol{\Phi}_{LE} \tag{6.27}$$

and

$$\boldsymbol{f}_{RO;k+1} = \boldsymbol{Q}_{ar}^{-1}\tilde{\boldsymbol{\Gamma}}_{\boldsymbol{A}}\tilde{\boldsymbol{S}}_A\boldsymbol{Q}_{al}\boldsymbol{f}_{LO;k} = \boldsymbol{\Phi}_{RO}\boldsymbol{f}_{LO;k} \tag{6.28}$$

with

$$\boldsymbol{\Phi}_{RO} = \boldsymbol{\Phi}_{RE}. \tag{6.29}$$

2.2. Consistency of ARTLM Schemes. In this section, we want to investigate whether all four ARTLM schemes $\boldsymbol{\Phi}_{LE}$, $\boldsymbol{\Phi}_{LO}$, $\boldsymbol{\Phi}_{RE}$, and $\boldsymbol{\Phi}_{RO}$ converge to solutions of MAXWELL's equations. For this, we perform a consistency analysis of the equivalent finite difference schemes, analogously to the one presented in Chapter 5. Only the first component of the ARTLM equivalent finite difference operators is considered, as the other components follow by symmetry and duality. Written componentwise, the first component of difference operator (6.18) writes

(6.30)

$$
\begin{aligned}
E^x_{k+1;l,m,n} = & \\
\frac{1}{4}\left(E^x_{k;l,m+1,n} + {}_k E^x_{l,m-1,n} + E^x_{k;l,m,n+1} + E^x_{k;l,m,n-1}\right) & \\
- \frac{1}{4}\left(E^y_{k;l,m,n+1} - E^y_{k;l,m,n-1}\right) - \frac{1}{4}\left(E^z_{k;l,m+1,n} - E^z_{k;l,m-1,n}\right) & \\
+ \frac{1}{\varepsilon_0}\frac{\Delta t}{2\Delta l}\left(H^x_{k;l,m+1,n} + H^x_{k;l,m-1,n} - H^x_{k;l,m,n+1} - H^x_{k;l,m,n-1}\right) & \\
- \frac{1}{\varepsilon_0}\frac{\Delta t}{2\Delta l}\left(H^y_{k;l,m,n+1} - H^y_{k;l,m,n-1}\right) & \\
+ \frac{1}{\varepsilon_0}\frac{\Delta t}{2\Delta l}\left(H^z_{k;l,m+1,n} - H^z_{k;l,m-1,n}\right), &
\end{aligned}
$$

Expanding the exact continuous solution E^x, E^y, E^z, H^x, H^y, and H^z in a TAYLOR series up to second order, i.e.

$$
\begin{aligned}
E^x_{k+1,l,m,n} = E^x((k+1)\Delta t; l\Delta x, m\Delta y, n\Delta z) = E^x(k\Delta t; l\Delta x, m\Delta y, n\Delta z) & \\
+ \frac{\partial E^x}{\partial t}\Big|_{k\Delta t; l\Delta x, m\Delta y, n\Delta z}\frac{\Delta t}{1!} + \frac{\partial^2 E^x}{\partial t^2}\Big|_{k\Delta t; l\Delta x, m\Delta y, n\Delta z}\frac{\Delta t^2}{2!} &
\end{aligned} \tag{6.31}
$$

and inserting these expressions into (6.30), yields

$$
\begin{aligned}
\varepsilon_0\frac{\partial E^x}{\partial t}\Big|_{k\Delta t; l\Delta l, m\Delta l, n\Delta l} + \mathcal{O}(\Delta t) + \mathcal{O}(\frac{\Delta l^2}{\Delta t}) = & \\
- \frac{\partial H^y}{\partial z}\Big|_{k\Delta t; l\Delta l, m\Delta l, n\Delta l} + \mathcal{O}(\Delta l^2) & \\
+ \frac{\partial H^z}{\partial y}\Big|_{k\Delta t; l\Delta l, m\Delta l, n\Delta l} + \mathcal{O}(\Delta l^2) & \\
- \frac{1}{2}c_0\frac{\partial E^y}{\partial z}\Big|_{k\Delta t; l\Delta l, m\Delta l, n\Delta l} + \mathcal{O}(\Delta l^2) & \\
- \frac{1}{2}c_0\frac{\partial E^z}{\partial y}\Big|_{k\Delta t; l\Delta l, m\Delta l, n\Delta l} + \mathcal{O}(\Delta l^2). &
\end{aligned} \tag{6.32}
$$

Taking the limit, i.e. $\Delta l \longrightarrow 0$ and $\Delta t \longrightarrow 0$, results in

$$
\varepsilon_0\frac{\partial E^x}{\partial t} = -\frac{\partial H^y}{\partial z} + \frac{\partial H^z}{\partial y} - \frac{1}{2}c_0\frac{\partial E^y}{\partial z} - \frac{1}{2}c_0\frac{\partial E^z}{\partial y}. \tag{6.33}
$$

However, this is not the first component of the AMPÈRE-MAXWELL equation. Consequently, ARTLM schemes LE and LO do *not* approximate MAXWELL's equations. Considering the first component of difference operator $\mathbf{\Phi}_{RE}$, i.e. eqn. (6.20), yields in componentwise notation

(6.34)

$$
\begin{aligned}
E^x_{k+1;l,m,n} = \\
\frac{1}{4}\left(E^x_{k;l,m+1,n} + E^x_{k;l,m-1,n} + E^x_{k;l,m,n+1} + E^x_{k;l,m,n-1}\right) \\
+ \frac{1}{4}\left(E^y_{k;l,m,n+1} - E^y_{k;l,m,n-1}\right) + \frac{1}{4}\left(E^z_{k;l,m+1,n} - E^z_{k;l,m-1,n}\right) \\
+ \frac{1}{\varepsilon_0}\frac{\Delta t}{2\Delta l}\left(H^x_{k;l,m,n+1} + H^x_{k;l,m,n-1} - H^x_{k;l,m+1,n} - H^x_{k;l,m-1,n}\right) \\
- \frac{1}{\varepsilon_0}\frac{\Delta t}{2\Delta l}\left(H^y_{k;l,m,n+1} - H^y_{k;l,m,n-1}\right) \\
+ \frac{1}{\varepsilon_0}\frac{\Delta t}{2\Delta l}\left(H^z_{k;l,m+1,n} - H^z_{k;l,m-1,n}\right).
\end{aligned}
$$

Inserting the expanded exact continuous solution into (6.34) yields

(6.35)

$$
\begin{aligned}
\varepsilon_0 \frac{\partial E^x}{\partial t}\Big|_{k\Delta t;l\Delta l,m\Delta l,n\Delta l} + \mathcal{O}(\Delta t) + \mathcal{O}(\frac{\Delta l^2}{\Delta t}) = \\
-\frac{\partial H^y}{\partial z}\Big|_{k\Delta t;l\Delta l,m\Delta l,n\Delta l} + \mathcal{O}(\Delta l^2) \\
+\frac{\partial H^z}{\partial y}\Big|_{k\Delta t;l\Delta l,m\Delta l,n\Delta l} + \mathcal{O}(\Delta l^2) \\
+\frac{1}{2}c_0\frac{\partial E^y}{\partial z}\Big|_{k\Delta t;l\Delta l,m\Delta l,n\Delta l} + \mathcal{O}(\Delta l^2) \\
+\frac{1}{2}c_0\frac{\partial E^z}{\partial y}\Big|_{k\Delta t;l\Delta l,m\Delta l,n\Delta l} + \mathcal{O}(\Delta l^2).
\end{aligned}
$$

Taking again the limit, i.e. $\Delta l \longrightarrow 0$ and $\Delta t \longrightarrow 0$ results in

(6.36)

$$
\varepsilon_0 \frac{\partial E^x}{\partial t} = -\frac{\partial H^y}{\partial z} + \frac{\partial H^z}{\partial y} + \frac{1}{2}c_0\frac{\partial E^y}{\partial z} + \frac{1}{2}c_0\frac{\partial E^z}{\partial y}.
$$

This is also not the first component of the AMPÈRE-MAXWELL equation. Hence, also ARTLM schemes RE and RO do not model MAXWELL's equations. Consequently, the ARTLM scheme with the mapping between field components and rotated TLM pulses proposed in [**85**] does not approximate MAXWELL's equations. For this reason, alternative mappings have been proposed that will be dealt with in the following section. It was pointed out that all four ARTLM schemes should contain the full information [**85**]. As a consequence, the operators $\mathbf{\Phi}_{LE}$, $\mathbf{\Phi}_{RE}$, $\mathbf{\Phi}_{LO}$, and $\mathbf{\Phi}_{RO}$ would have to be equal, which they are obviously not. In view of eqns. (6.18) and (6.20), this must be denied for this field-mapping.

Interestingly, adding difference operators $\boldsymbol{\Phi}_{LE}$ and $\boldsymbol{\Phi}_{RE}$ results in the mapping induced difference operator (5.23) of the SCN-TLM method with stubs derived in Chapter 5.

(6.37)
$$\boldsymbol{\Phi}_{LE}+\boldsymbol{\Phi}_{RE}=\boldsymbol{P\Gamma SQ}=\frac{1}{4}\begin{pmatrix} \boldsymbol{D_{YZ}} & 0 & 0 & 0 & -\boldsymbol{D_Z} & \boldsymbol{D_Y} \\ 0 & \boldsymbol{D_{XZ}} & 0 & \boldsymbol{D_Z} & 0 & -\boldsymbol{D_X} \\ 0 & 0 & \boldsymbol{D_{XY}} & -\boldsymbol{D_Y} & \boldsymbol{D_X} & 0 \\ 0 & \boldsymbol{D_Z} & -\boldsymbol{D_Y} & \boldsymbol{D_{YZ}} & 0 & 0 \\ -\boldsymbol{D_Z} & 0 & \boldsymbol{D_X} & 0 & \boldsymbol{D_{XZ}} & 0 \\ \boldsymbol{D_Y} & -\boldsymbol{D_X} & 0 & 0 & 0 & \boldsymbol{D_{XY}} \end{pmatrix}.$$

This corroborates the view that the full information on the field evolution is not contained in each of the four ARTLM schemes.
This means, without applying an alternative mapping between (rotated) TLM pulses and electromagnetic field components a separation of the two RTLM meshes is not allowed.

2.3. Equivalent Finite Difference Schemes Using Alternative Mappings. LINDENMEIER suggested the following mapping between the rotated TLM wave pulses and the discretized electromagnetic field components [**47**]

(6.38)
$$\boldsymbol{Q}_{al,Li}=\frac{1}{2}\begin{pmatrix} 0 & 1 & 0 & 0 & 0 & 1 \\ 0 & 1 & 0 & 0 & 0 & -1 \\ 0 & 0 & 1 & 1 & 0 & 0 \\ 0 & 0 & 1 & -1 & 0 & 0 \\ 1 & 0 & 0 & 0 & 1 & 0 \\ 1 & 0 & 0 & 0 & -1 & 0 \end{pmatrix}$$

and

(6.39)
$$\boldsymbol{Q}_{ar,Li}=\frac{1}{2}\begin{pmatrix} 0 & 0 & 1 & 0 & 1 & 0 \\ 0 & 0 & -1 & 0 & 1 & 0 \\ 1 & 0 & 0 & 0 & 0 & 1 \\ -1 & 0 & 0 & 0 & 0 & 1 \\ 0 & 1 & 0 & 1 & 0 & 0 \\ 0 & -1 & 0 & 1 & 0 & 0 \end{pmatrix}.$$

The equivalent finite difference schemes using this mapping calculate

(6.40)
$$\boldsymbol{\Phi}_{LE,Li}=\boldsymbol{\Phi}_{LO,Li}=-\boldsymbol{Q}_{al,Li}^{-1}\tilde{\boldsymbol{\Gamma}}_{\boldsymbol{A}}\tilde{\boldsymbol{S}}_{A}\boldsymbol{Q}_{ar,Li}$$

with

(6.41)

$$\boldsymbol{\Phi}_{LE,Li} = \boldsymbol{\Phi}_{LO,Li} = \frac{1}{2}\begin{pmatrix} -\boldsymbol{D}_{\boldsymbol{Z}}^{+} & 0 & 0 & 0 & -\boldsymbol{D}_{\boldsymbol{Z}} & 0 \\ 0 & -\boldsymbol{D}_{\boldsymbol{X}}^{+} & 0 & 0 & 0 & -\boldsymbol{D}_{\boldsymbol{X}} \\ 0 & 0 & -\boldsymbol{D}_{\boldsymbol{Y}}^{+} & -\boldsymbol{D}_{\boldsymbol{Y}} & 0 & 0 \\ 0 & 0 & \boldsymbol{D}_{\boldsymbol{Y}} & \boldsymbol{D}_{\boldsymbol{Y}}^{+} & 0 & 0 \\ -\boldsymbol{D}_{\boldsymbol{Z}} & 0 & 0 & 0 & \boldsymbol{D}_{\boldsymbol{Z}}^{+} & 0 \\ 0 & \boldsymbol{D}_{\boldsymbol{X}} & 0 & 0 & 0 & \boldsymbol{D}_{\boldsymbol{X}}^{+} \end{pmatrix}$$

where

$$\boldsymbol{D}_{\boldsymbol{X}}^{+} = \boldsymbol{X}^{\dagger} + \boldsymbol{X}, \tag{6.42}$$

and

$$\boldsymbol{\Phi}_{RO,Li} = \boldsymbol{\Phi}_{RE,Li} = \boldsymbol{Q}_{ar,Li}^{-1}\tilde{\boldsymbol{\Gamma}}_{\boldsymbol{A}}\tilde{\boldsymbol{S}}_{A}\boldsymbol{Q}_{al,Li} \tag{6.43}$$

with

(6.44)

$$\boldsymbol{\Phi}_{RE,Li} = \boldsymbol{\Phi}_{RO,Li} = \frac{1}{2}\begin{pmatrix} -\boldsymbol{D}_{\boldsymbol{Y}}^{+} & 0 & 0 & 0 & 0 & -\boldsymbol{D}_{\boldsymbol{Y}} \\ 0 & -\boldsymbol{D}_{\boldsymbol{Z}}^{+} & 0 & -\boldsymbol{D}_{\boldsymbol{Z}} & 0 & 0 \\ 0 & 0 & -\boldsymbol{D}_{\boldsymbol{X}}^{+} & 0 & -\boldsymbol{D}_{\boldsymbol{X}} & 0 \\ 0 & \boldsymbol{D}_{\boldsymbol{Z}} & 0 & \boldsymbol{D}_{\boldsymbol{Z}}^{+} & 0 & 0 \\ 0 & 0 & \boldsymbol{D}_{\boldsymbol{X}} & 0 & \boldsymbol{D}_{\boldsymbol{X}}^{+} & 0 \\ \boldsymbol{D}_{\boldsymbol{Y}} & 0 & 0 & 0 & 0 & \boldsymbol{D}_{\boldsymbol{Y}}^{+} \end{pmatrix}.$$

The first equation of (6.41) writes componentwise

$$E^{x}_{k+1;l,m,n} = \frac{1}{4}\left(E^{x}_{k;l,m,n+1} + E^{x}_{k;l,m,n-1}\right) - \frac{1}{\varepsilon_0}\frac{\Delta t}{2\Delta l}\left(H^{y}_{k;l,m,n+1} - H^{y}_{k;l,m,n-1}\right). \tag{6.45}$$

The other components of the equivalent finite difference scheme follow again by symmetry and duality.

2.4. Consistency of ARTLM Using Alternative Mappings. Developing the exact continuous solution E^x, E^y, E^z, H^x, H^y, and H^z in a Taylor series and inserting into (6.45) yields

$$\begin{aligned}\varepsilon_0 \frac{\partial E^x}{\partial t}\Big|_{k\Delta t;l\Delta l,m\Delta l,n\Delta l} + \mathcal{O}(\Delta t) = \\ - \frac{\partial H^y}{\partial z}\Big|_{k\Delta t;l\Delta l,m\Delta l,n\Delta l} + \mathcal{O}(\Delta l^2) \\ - \frac{1}{2\Delta l} E^x\Big|_{k\Delta t;l\Delta l,m\Delta l,n\Delta l} + \mathcal{O}(\frac{\Delta l^2}{\Delta t}).\end{aligned} \tag{6.46}$$

With $\Delta l \longrightarrow 0$ and $\Delta t \longrightarrow 0$ the term associated with E^x approaches infinity and the algorithm diverges. Consequently, this scheme also does not model the first component of the first MAXWELL equation. Moreover, there is no approximation of the partial derivative of H^z in scheme (6.45). Similar results are obtained for the remaining three ARTLM schemes *RE*, *LO*, and *RO*.

3. Proof of Non-Existence of a Consistent Mapping

In the previous sections, we have seen that none of the hitherto suggested field-mappings between rotated TLM pulses and electromagnetic field components yields a consistent equivalent finite difference scheme and hence a consistent ARTLM scheme modelling MAXWELL's equations. In this section, we want to deal with the question whether a consistent mapping exists at all and how it would look like. For this, we start by the proposition that all four ARTLM schemes LE, LO, RE, and RO should approximate MAXWELL's equations in the same manner. We assume $\boldsymbol{A}$ is a consistent difference operator, hence

$$\boldsymbol{A} = \boldsymbol{\Phi}_{LE} = \boldsymbol{\Phi}_{LO}, \tag{6.47}$$

$$\boldsymbol{A} = \boldsymbol{\Phi}_{RE} = \boldsymbol{\Phi}_{RO}, \tag{6.48}$$

or

$$\boldsymbol{A} = -\boldsymbol{Q}_{al}^{-1} \tilde{\boldsymbol{\Gamma}}_{\boldsymbol{A}} \tilde{\boldsymbol{S}}_A \boldsymbol{Q}_{ar}, \tag{6.49}$$

$$\boldsymbol{A} = \boldsymbol{Q}_{ar}^{-1} \tilde{\boldsymbol{\Gamma}}_{\boldsymbol{A}} \tilde{\boldsymbol{S}}_A \boldsymbol{Q}_{al}. \tag{6.50}$$

Rearranging (6.49) yields

$$\boldsymbol{Q}_{al} = -\tilde{\boldsymbol{\Gamma}}_{\boldsymbol{A}} \tilde{\boldsymbol{S}}_A \boldsymbol{Q}_{ar} \boldsymbol{A}^{-1} \tag{6.51}$$

and rearranging (6.50) yields

$$\boldsymbol{Q}_{ar} = \tilde{\boldsymbol{\Gamma}}_{\boldsymbol{A}} \tilde{\boldsymbol{S}}_A \boldsymbol{Q}_{al} \boldsymbol{A}^{-1}. \tag{6.52}$$

Inserting (6.52) in (6.49) results in

$$\boldsymbol{A} = -\boldsymbol{Q}_{al}^{-1}(\tilde{\boldsymbol{\Gamma}}_{\boldsymbol{A}}\tilde{\boldsymbol{S}}_A)^2\boldsymbol{Q}_{al}\boldsymbol{A}^{-1} \tag{6.53}$$

or

$$\boldsymbol{Q}_{al}\boldsymbol{A}^2 = -(\tilde{\boldsymbol{\Gamma}}_{\boldsymbol{A}}\tilde{\boldsymbol{S}}_A)^2\boldsymbol{Q}_{al}. \tag{6.54}$$

If we insert (6.51) in (6.50), we get

$$\boldsymbol{A} = -\boldsymbol{Q}_{ar}^{-1}(\tilde{\boldsymbol{\Gamma}}_{\boldsymbol{A}}\tilde{\boldsymbol{S}}_A)^2\boldsymbol{Q}_{ar}\boldsymbol{A}^{-1} \tag{6.55}$$

or

$$\boldsymbol{Q}_{ar}\boldsymbol{A}^2 = -(\tilde{\boldsymbol{\Gamma}}_{\boldsymbol{A}}\tilde{\boldsymbol{S}}_A)^2\boldsymbol{Q}_{ar}. \tag{6.56}$$

Comparing (6.55) and (6.56), one recognizes that the mappings at the lefthanded nodes and at the righthanded nodes must be the same, i.e.

$$\boldsymbol{Q}_{al} = \boldsymbol{Q}_{ar}. \tag{6.57}$$

With this, we can substitute $\boldsymbol{Q}_{ar}$ in (6.49) and (6.50) by $\boldsymbol{Q}_{al}$ resulting in the contradiction

$$\boldsymbol{Q}_{al}^{-1}\tilde{\boldsymbol{\Gamma}}_{\boldsymbol{A}}\tilde{\boldsymbol{S}}_A\boldsymbol{Q}_{al} = -\boldsymbol{A}, \tag{6.58}$$

$$\boldsymbol{Q}_{al}^{-1}\tilde{\boldsymbol{\Gamma}}_{\boldsymbol{A}}\tilde{\boldsymbol{S}}_A\boldsymbol{Q}_{al} = \boldsymbol{A}. \tag{6.59}$$

Consequently, this means that there *does not exist a consistent mapping* between rotated TLM pulses of an ARTLM scheme and discretized electromagnetic field components for arbitrary difference operators modelling MAXWELL's equations! In turn, this means that the separation of the RTLM scheme eqn. (6.5) into two or four independent schemes when considering the independence of sets of different parity in time, is not allowed. Moreover, the TLM and RTLM matrices eqns. (5.20) and (6.5) are of checker board type II with zero diagonal elements. This means that considering the off diagonal block matrices alone as done in deriving the ARTLM schemes, leads to matrices having different eigenvalues than the complete original matrix [**120**]. In view of the analysis presented in this chapter, it remains questionable whether a six-port TLM scheme with symmetrical condensed nodes exists at all.

CHAPTER 7

Numerical Convergence Analysis of TLM Schemes

The proof of convergence of the SCN-TLM method presented in Chapter 5 showed that when the TLM mesh is excited using a nodal field-mapping and the electromagnetic field components are also sampled at the centre of the TLM cell, the SCN-TLM method exhibits an asymptotic convergence order of $\mathcal{O}(\sqrt{\Delta t})$. Thus, the field-mapping determines the convergence order of the SCN-TLM method, as using a TLM formulation with a bijective boundary oriented field-mapping has been shown to be of second order [**23, 44**]. Nevertheless, we want to verify the convergence order of these differing formulation in a numerical experiment. For this, a simple numerical initial value problem is solved using various formulations of the SCN-TLM method at various discretizations. The investigated formulations are compiled in Table 7.1. Formulation A is JOHNS' original formulation of the SCN-TLM method without stubs, where the electromagnetic field components are sampled at the node and the TLM mesh is also excited at the node [**35**]. Formulation B refers to the mapping induced finite difference scheme without stubs introduced in Chapter 5. Formulation C is the SCN-TLM formulation without stubs given by KRUMPHOLZ and RUSSER utilizing a bijective mapping between TLM wave pulses and electromagnetic field components at the tangential planes between neighbouring TLM cells [**44**]. The remaining cases are formulations of the SCN-TLM method with stubs. Formulation D is JOHNS' original formulation with cell-centred field-mapping [**35**]. Formulation E refers to the extensions of the SCN considering ohmic losses given by NAYLOR and DESAI [**67**]. Formulation F denotes the mapping induced finite difference scheme with stubs derived in Chapter 5. Finally, formulation F refers to the formulation of the SCN-TLM method using a discrete propagator integral following Hein [**23**].

1. Numerical Convergence Analysis of Various SCN-TLM Formulations

1.1. The Test Problem. The propagation of a linearly polarized TEM wave in an infinite parallel-plate waveguide with perfectly conducting (PEC) walls

no.	author(s)	mapping	stubs	losses	convergence order
A	JOHNS	CFM	no	-	$\mathcal{O}(\sqrt{\Delta t})$
B	REBEL	CFM	no	-	$\mathcal{O}(\Delta t)$
C	KRUMPHOLZ, RUSSER	BOFM	no	-	$\mathcal{O}(\Delta t^2)$
D	JOHNS	CFM	yes	no	$\mathcal{O}(\sqrt{\Delta t})$
E	NAYLOR, DESAI	CFM	yes	yes	$\mathcal{O}(\sqrt{\Delta t})$
F	REBEL	CFM	yes	yes	$\mathcal{O}(\Delta t)$
G	HEIN	BOFM	yes	yes	$\mathcal{O}(\Delta t^2)$

TABLE 7.1. Overview of investigated formulations of the SCN-TLM method.

is modelled by a linear row of TLM cells, with only a single cell in the transverse directions. The ports of the TLM cells are short-circuited in z-direction and open in y-direction, modelling electric walls in the z-direction and magnetic walls in the y-direction, respectively. Fig. 7.1 shows the TLM model of this infinite parallel-plate waveguide. For a plane wave, linearly polarized in z-direction and propagating in x-direction, a linear row with a single TLM cell in the transverse directions is representative, as the TLM mesh without stubs exhibits no dispersion in axial direction. The parallel plate waveguide was discretized using cubic TLM cells. The size of a TLM cell is Δl. The initial field of GAUSSian shape is distributed across the distance Δx_{ex}. The distance between initial field and observation point is denoted Δx_{ob}. This numerical IVP was solved using various discretizations. The respective simulation parameters can be found in Table 7.2. Fig. 7.2 shows schematically the TLM models for two subsequent discretization steps. It is obvious that with each finer and finer discretization level the real distance between the grid points is filled with twice as many spatial increments as at the previous level. Naturally, the spatial increments are half the length of the previous coarser level. When mapping at the node, i.e. in case of a cell-centred grid, the centres of the TLM-cells of all discretization levels are aligned with each other. Consequently, the cell faces are not aligned. This can be seen in the upper part of Fig. 7.2. Sampling the field components in the tangential planes between two neighbouring cells, the cell faces of all discretization levels are aligned with each others. This refers to a uniform grid. Hence, the cell centres are shifted with respect to different discretization levels. This relation is depicted in the lower part of Fig. 7.2. The initial field distribution, given by the discretized truncated GAUSSian pulse

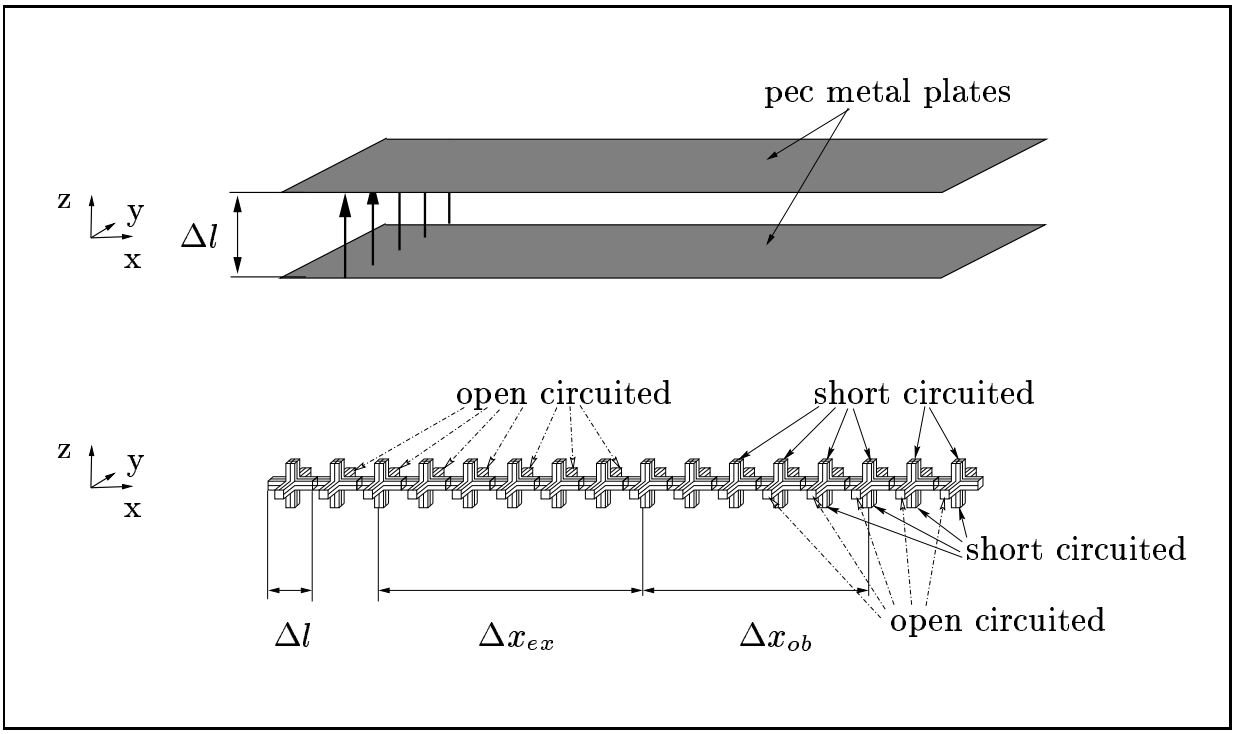

FIGURE 7.1. TLM model of parallel-plate waveguide.

$$E^z_{k=1}(x) = \begin{cases} E_0 e^{-\pi\left(\frac{x-x_0}{\sqrt{2}\sigma}\right)^2} & \text{for} \quad x_1 \le x - x_0 \le x_2 \\ 0 & \text{elsewhere} \end{cases}, \tag{7.1}$$

with $x_1 = \frac{N_{no}}{2}\Delta l_{no}$ and $x_2 = (\frac{N_{no}}{2} + 1)\Delta l_{no}$, is distributed across the distance $\Delta x_{ex} = N_{no}\Delta l_{no}$. The region, where the initial field is given, is marked by the shaded cells in Fig. 7.2. The pulse is centred around $\Delta x_0 = (N_{no}/2 + 1)\Delta l_{no}$ (see the dashed line in Fig. 7.2). The width of the pulse is $\sqrt{2}\sigma = N_{no}\Delta l_{no}/p$, where p was chosen $3\sqrt{2}$. The overall length of the structure was chosen such that in connection with the duration of the simulation no reflections from the terminating walls in the positive and negative x-direction occurred at the observation point. In the case with stubs, a medium with $\varepsilon_r = 2$, and $\mu_r = 1$ was assumed. In the case of a lossy medium, the electric conductivity was chosen isotropically $\sigma_e = 30\ \mathrm{Sm}^{-1}$. The reference solution for calculating the relative error was obtained from a simulation with very small cell size (no. 7 of Table 7.2). The relative error between reference solution and solutions obtained with larger cell sizes is calculated using the norm of the discrete LEBESGUE space (5.3), i.e.

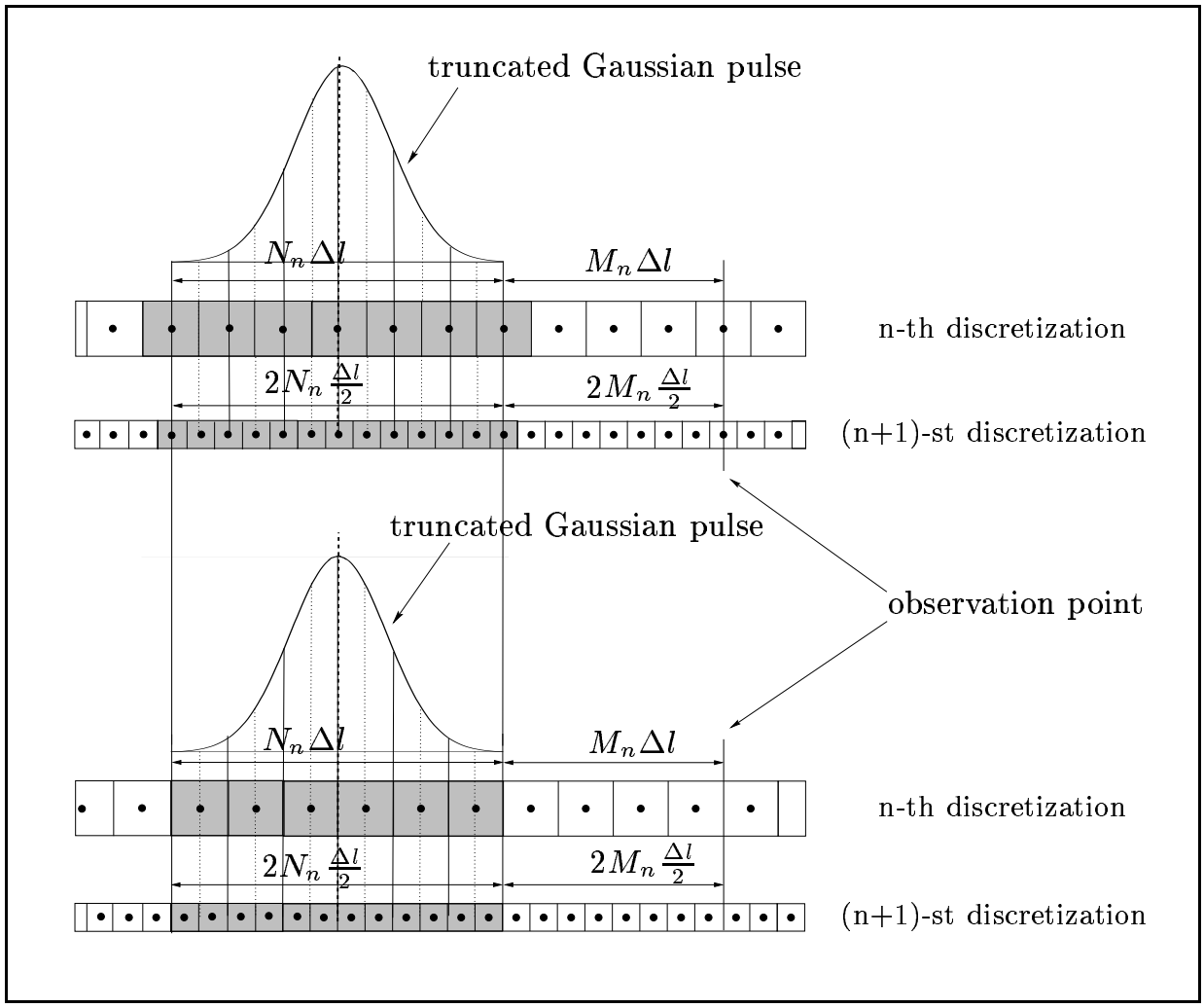

FIGURE 7.2. TLM models of parallel-plate waveguide for two subsequent discretization steps.

no.	Δl_{no} $[\mu m]$	N_{no}	M_{no}
1	1.0	70	6
2	0.5	140	12
3	0.25	280	24
4	0.125	560	48
5	0.0625	1120	96
6	0.03125	2240	192
7	0.015625	4480	384

TABLE 7.2. Parameters of different discretization levels.

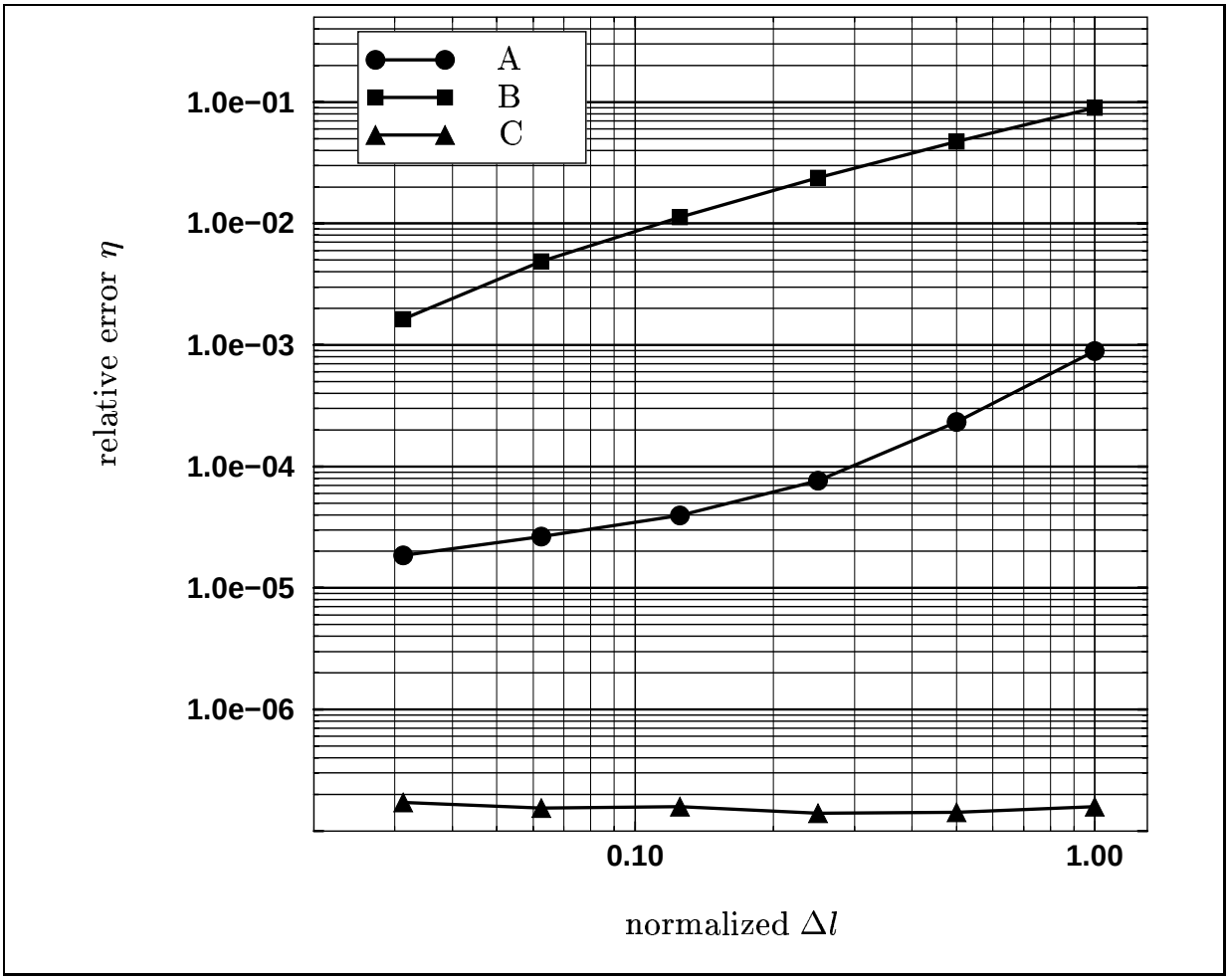

FIGURE 7.3. Relative error between simulated solution and benchmark solution of various SCN-TLM formulations without stubs versus normalized Δl. The normalized Δl is given by $\Delta l_{norm} = (70/3)\Delta l_{no}/\sigma$. Formulation A is JOHNS' original TLM formulation. Formulation B refers to the mapping induced finite difference scheme and formulation C refers to KRUMPHOLZ and RUSSER's TLM formulation.

$$\eta = \sqrt{\frac{\sum_k \left(|u_k|^2\right)}{\left(|E^z_{k,\mathrm{ref}}|^2\right)}}, \tag{7.2}$$

with

$$u_k = E^z_{k,\mathrm{ref}} - E^z_k. \tag{7.3}$$

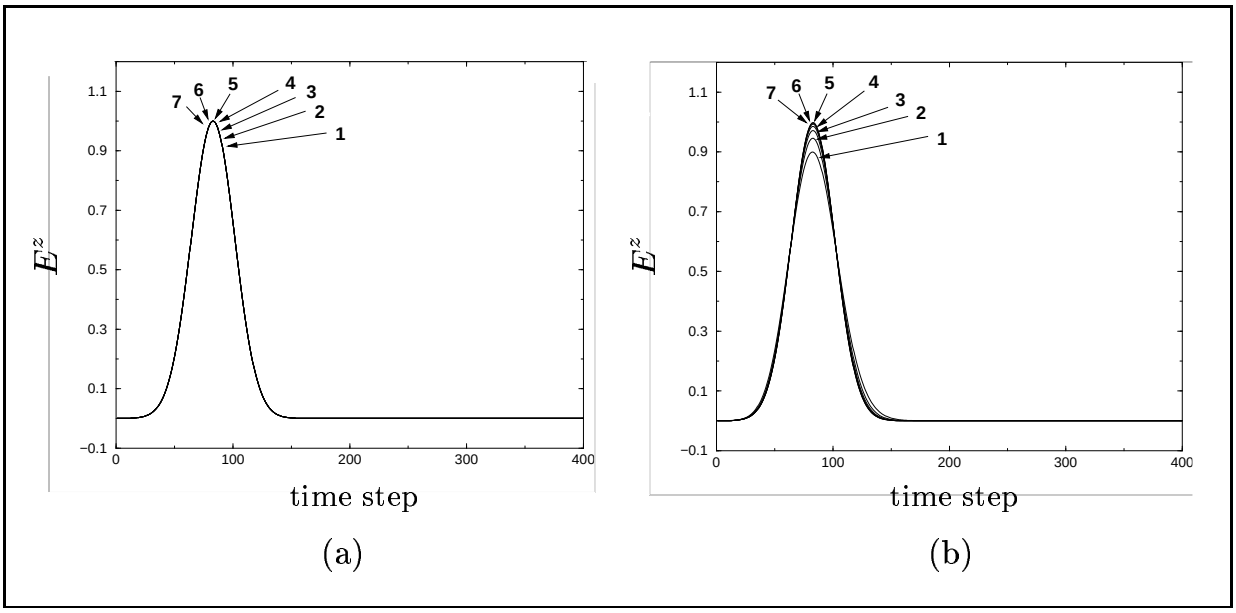

FIGURE 7.4. Propagating pulses in the TLM model of parallel plate waveguide for formulations A and B. Plot (a) was obtained using JOHNS formulation. In plot (b), the dissipative nature of the LAX-FRIEDRICHS scheme is clearly visible.

1.2. Results. In Fig. 7.4, the propagating pulses in the TLM model of the parallel-plate waveguide are shown for formulations A and B. The numbers refer to the respective discretization level of Table 7.2. Clearly, the dissipative nature of the TLM inherent LAX-FRIEDRICHS scheme can be recognized (see Subfigure (a)), whereas in JOHNS' TLM formulation (Subfigure (b)), no loss of energy is evident from the pulse propagation. This is a consequence of the conservation of energy in the SCN scheme [**35**]. The pulses obtained at different discretizations are indistinguishable in this plot.

1.3. SCN-TLM without Stubs. The relative error between simulated solution and reference solution of the SCN-TLM formulations without stubs versus the cell size normalized to the width σ of the initial Gaussian pulse, i.e. $\Delta l_{norm} = (70/3)\Delta l_{no}/\sigma$ is plotted in Fig. 7.3. For JOHNS' original TLM scheme (formulation A of Table 7.1), one observes a second order convergence for coarse discretizations, but the slope of the error curve reduces towards finer discretizations very quickly. Asymptotically, one can deduce a convergence rate of $\sqrt{\Delta t}$ in the $\log - \log$ plot of Fig. 7.3. The slope of the error curve reduces at relatively fine discretization levels, which indicates that only in case of large mesh sizes of about $500 \times 500 \times 500$ cells for three-dimensional problems one can observe any effect. This seems to be the reason, why one has not observed this reduction of the convergence rate before. Moreover, this result clearly shows that the mapping between the discretized fields and the TLM states determines the (asymptotic)

accuracy of the TLM solution, as the SCN mesh without stubs exhibits no dispersion in axial direction and thus should exhibit a constant error independent of the discretization of the order of numerical round-off errors. Looking at the relative error η of the mapping induced finite difference scheme according to (5.25) to (5.30), which is equivalent to a LAX-FRIEDRICHS scheme, one can clearly discern a first order convergence rate. The reason why the slope of the error curve slightly increases towards the finest discretization is that the reference solution and the solution obtained at the previous discretization step are too close together. For formulation C, when the initial data are imposed on the SCN-TLM network at the boundary and the fields are also sampled at the boundary, a much smaller relative error η is observed. As the SCN-TLM scheme without stubs has no dispersion in the axial directions and thus models the propagation of plane waves exactly in axial direction, we only see the numerical round-off error (the code operated with single-precision arithmetic (4 Byte)), as expected. It is noteworthy that the magnitude of the error constant of the mapping induced finite difference scheme (formulation B) is larger than that of the SCN-TLM formulation of JOHNS. This is a consequence of the dissipative nature of the LAX-FRIEDRICHS scheme, which is reflected in the variation of the pulse amplitudes at different discretizations as indicated in the graph on the right side in Fig. 7.4.

1.4. SCN-TLM with Stubs. The relative error η of JOHNS' original formulation is plotted versus the cell size normalized to the width of the initial GAUSSian pulse (see Fig. 7.2). Again, a second order decrease in error can be recognized for coarse discretizations. However, asymptotically the convergence rate reduces to $\sqrt{\Delta t}$, as shown in Chapter 5. Comparing the error curves for TLM without and with stubs, one realizes that in the case of TLM with stubs, the reduction of the convergence rate appears at coarser discretizations in comparison to the TLM scheme without stubs. This is a consequence of the stubs adding additional dispersion to the scheme, which further corrupts the solution, whereas one has no dispersion in axial direction in a TLM mesh without stubs. Again, the error constant of the mapping induced finite difference scheme is larger than that of JOHNS' SCN-TLM formulation, which is a consequence of the dissipative nature of the mapping induced finite difference scheme. For TLM with stubs including losses, i.e. following NAYLOR et al.'s formulation E of Table 7.1, we can observe the same behaviour as for the other formulations with a mapping at the centre of the TLM cell. The error decreases with second order for coarser discretization levels, but we can again recognize a decreasing slope of the error curve towards smaller cell sizes, resulting in asymptotic convergence of $\mathcal{O}(\sqrt{\Delta t})$, as shown in Chapter 5. The error of the mapping MIFD scheme with stubs, i.e. (5.54) to (5.64), decreases again linearly, thus meeting the predictions of Chapter 5. That the slope of the error curve slightly increases towards the finest discretization, is again caused by

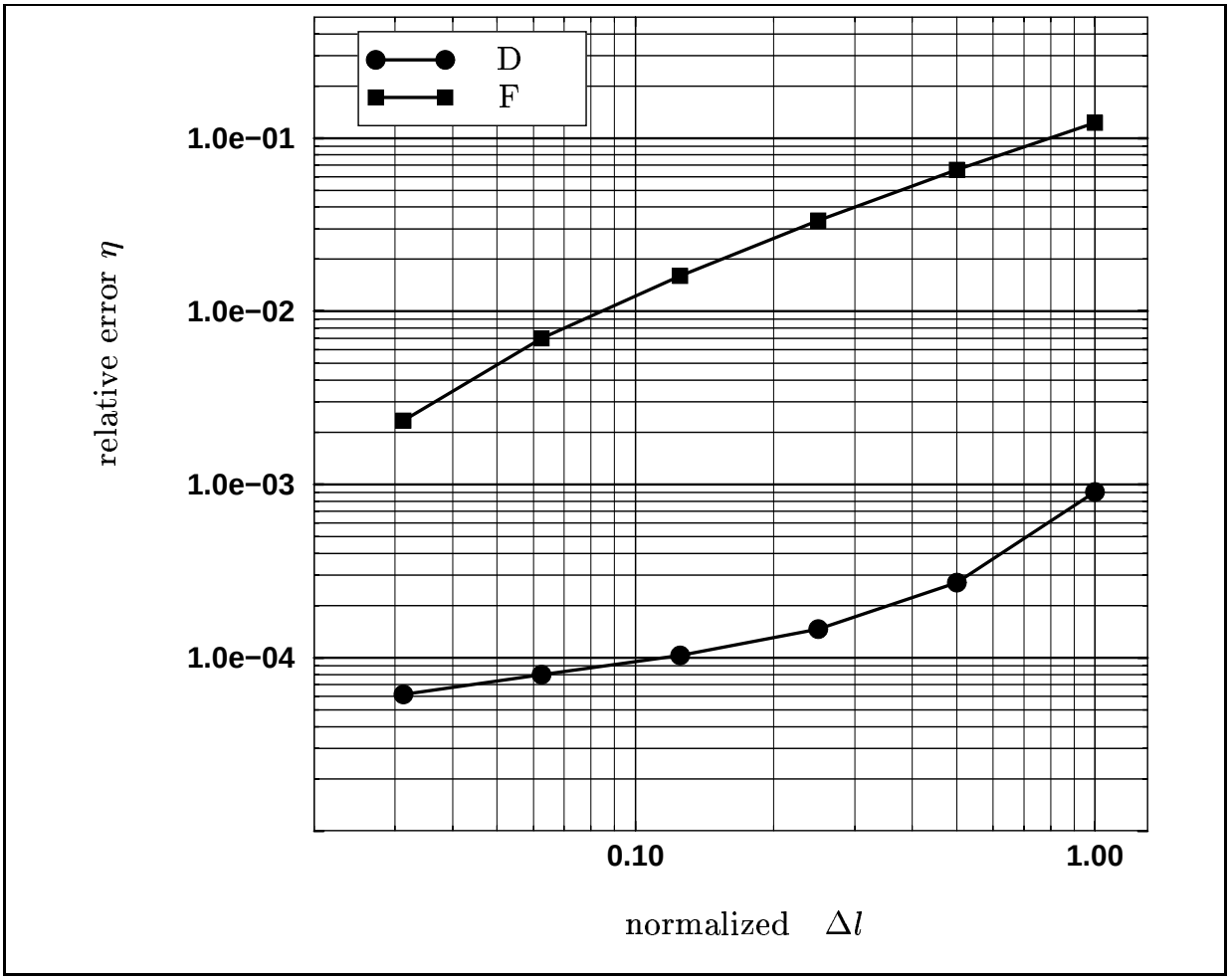

FIGURE 7.5. Relative error between simulated solution and benchmark solution of various SCN-TLM formulations with stubs versus normalized Δl. The normalized Δl is given by $\Delta l_{norm} = (70/3)\Delta l_{no}/\sigma$. Formulation D refers to JOHNS' original SCN-TLM formulation and curve F denotes the case of the mapping induced finite difference scheme with stubs.

the fact that the reference solution and the solution obtained at the previous discretization step are too close together. The same behaviour can be observed in Fig. 7.6 for the MIFD scheme (5.79) to (5.92).

Now we want to have a look what happens when we impose the initial field at the boundaries of the TLM cells in a TLM mesh with stubs. If the field components are mapped at the boundary (formulation G of Table 7.1), one can observe the excitation of spurious modes (see Fig. 7.7). This is caused by a wrong initialization of the stub variables. However, it was emphasized in [**23**] that the initial electric and magnetic fields have to be zero, when the TLM scheme is started. If this condition is neglected, one will inevitably excite spurious modes. The excitation

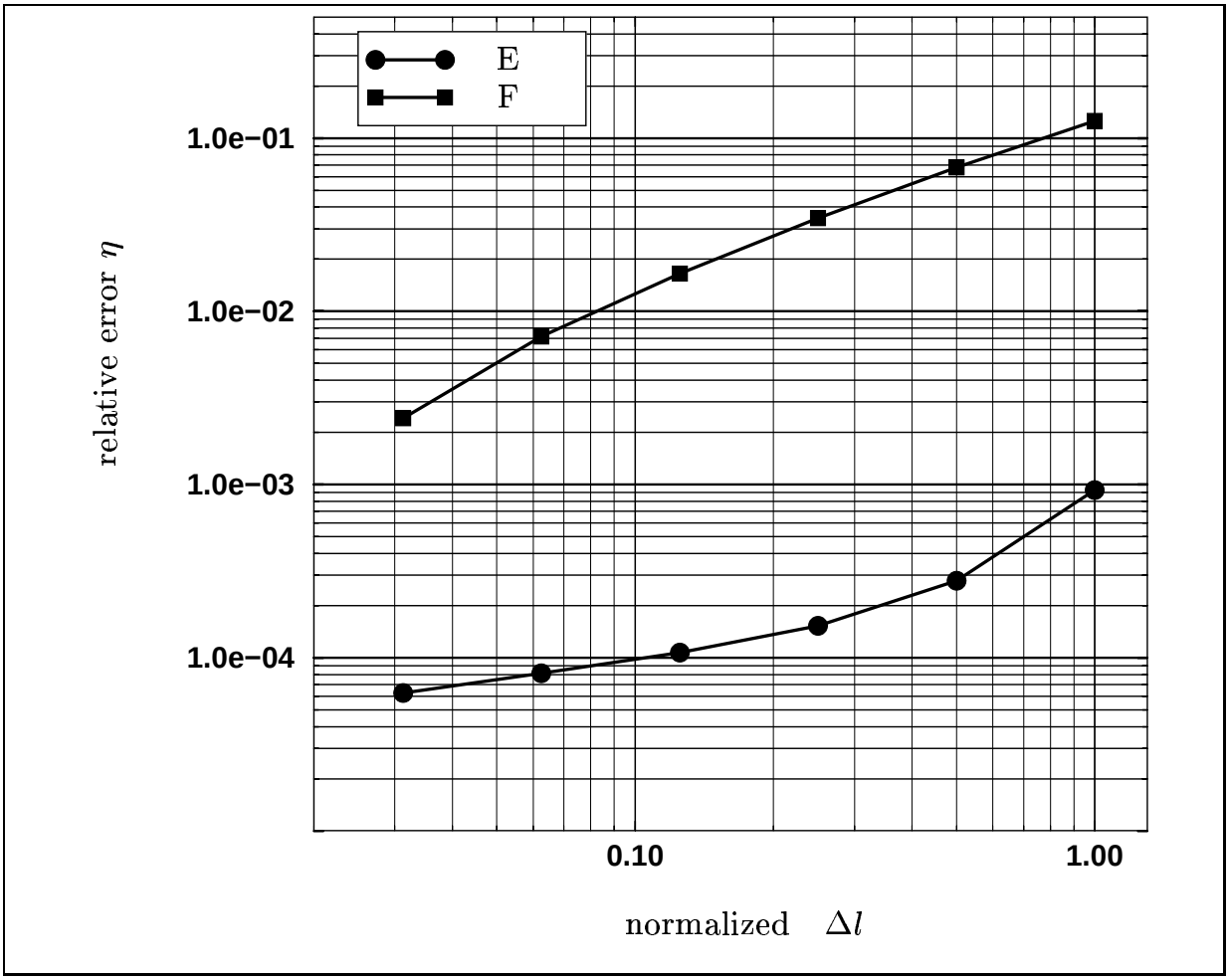

FIGURE 7.6. Relative error between simulated solution and benchmark solution of various SCN-TLM formulations with stubs and ohmic losses versus normalized Δl. The normalized Δl is given by $\Delta l_{norm} = (70/3)\Delta l_{no}/\sigma$. E denotes the error curve for NAYLOR and DESAI's TLM formulation and F refers to the mapping induced finite difference scheme.

of spurious modes when imposing an initial field at the boundary was also observed by others [**20**]. A proper excitation would involve a temporally smooth excitation, e.g. of GAUSSian shape. However, this does not constitute an initial value problem in the sense investigated here. It then constitutes an initial value problem of MAXWELL's equations with current sources where the initial field is zero. How to treat current sources in TLM was shown by BADER et al. [**6**]. As it makes no sense to study the convergence when spurious modes are excited, as they do not present approximate solutions of MAXWELL's equations, no error curves for this case are plotted in Fig. 7.3 and Fig. 7.6. Interestingly, sampling the fields at the node when imposing the initial field at the boundary [**23**], averages out most of

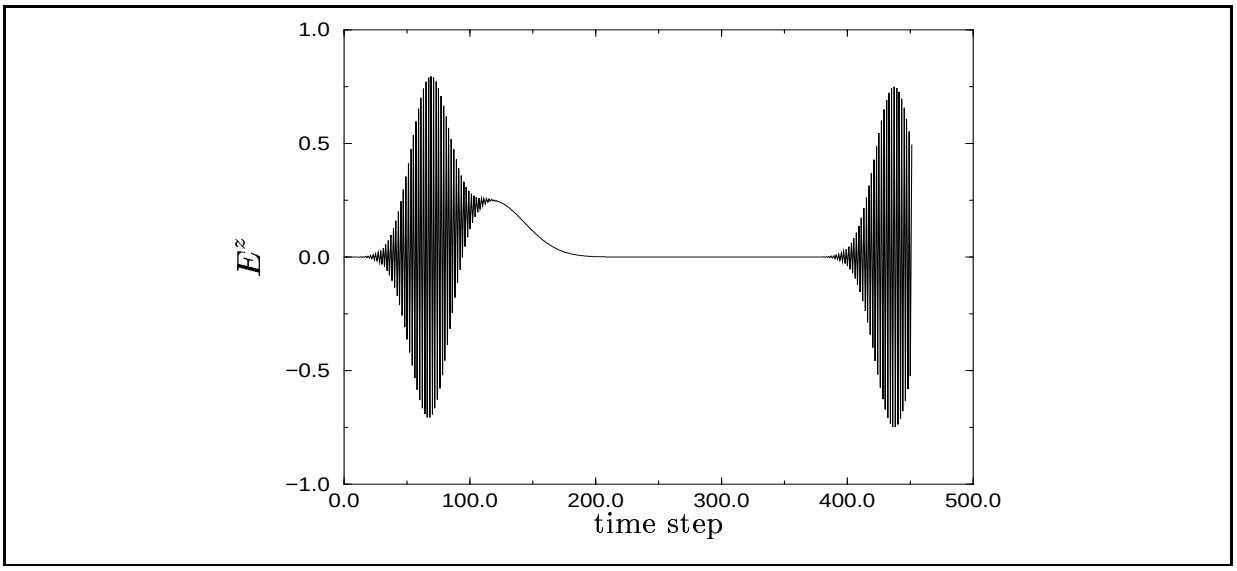

FIGURE 7.7. Excitation of spurious modes, when applying an initial field at $k = 1$ to the cell boundary. The electromagnetic field is also sampled at the cell boundary (formulation G of Table 7.1).

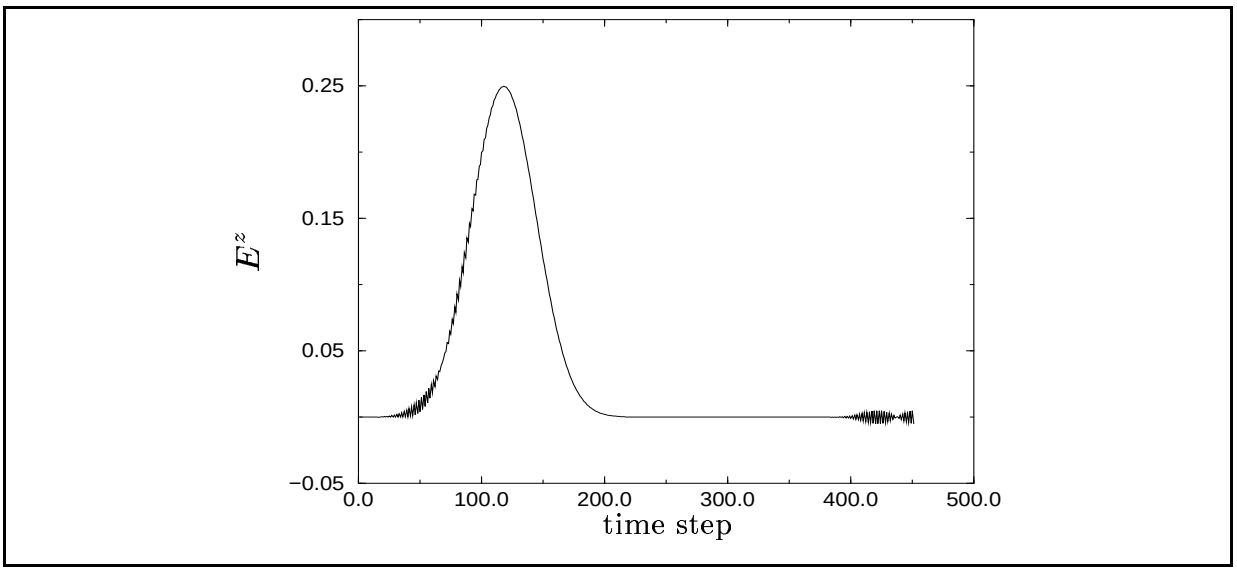

FIGURE 7.8. Excitation with spatial field distribution at $k = 1$ at the cell boundary. Field sampling at the node averages out most of the spurious modes (formulation G of Table 7.1).

the spurious modes (see Fig. 7.8), which is presumably due to the symmetry of the simple field problem considered here.

CHAPTER 8

Modelling Dispersive Media

Many materials exhibit frequency dependent properties. Examples are magnetized ferrites, biological tissues, and dispersive media. Also materials used in planar microwave circuits may be dispersive. Examples are PCB boards, polyimide and many more. The latter are extensively used in multichip modules. These materials contain molecules which possess a permanent electric dipole moment. When they are subject to an electric field, the molecular dipoles will align along the direction of the electric field. If a time harmonic electric field is applied, the molecular dipoles will rotate back and forth up to a certain cut-off frequency. This rotation consumes energy and hence energy is dissipated. This dielectric relaxation mechanism can be described by a so called DEBYE model. Losses influence the characteristics of microwave components. For example, resonant frequencies may be shifted. If one desires accurate modelling of planar microwave structures, also losses due to dielectric relaxation should not be neglected. In this chapter, we derive the updating relations for a SCN-TLM algorithm modelling DEBYE type dielectrics using the propagator approach following [**23, 24**]. This approach allows the analytic derivation of the updating relations of a dielectric TLM node from a finite difference approximation of the polarization current. In published work on SCN-TLM algorithms for dispersive media and magnetized ferrites, usually equivalent voltage and current relations are exploited [**15, 31, 61, 73, 97, 98, 108**]. In view of the results of Chapter 5, this will be an approximation with lower asymptotic convergence and hence accuracy as the formulation derived in the sequel. Besides, the use of controlled voltage sources for modelling of complex media such as DEBYE, LORENTZ, fourth order, and cold plasmas in TLM was reported [**81**].

In the following section, the DEBYE model describing certain types of dispersive media is introduced. Then, the propagator approach is outlined and the algorithm for the dielectric node derived. Finally, the algorithm is validated at a simple parallel-plate waveguide partially filled with a dispersive dielectric.

1. The Debye Model for Dielectric Relaxation

In DEBYE's model, the dielectric relaxation is described by a relaxation time whose reciprocal is the relaxation frequency. When the frequency of an applied field is higher than the relaxation frequency, the molecules will not follow or

respond to the field. DEBYE has found that the orientational part of the polarizability of a material depends on the applied frequency ω as

$$\alpha(\omega) = \frac{\alpha_0}{1 - j\omega\tau_d}, \tag{8.1}$$

where α_0 is the static orientational polarizability and τ_d the relaxation time [**38**]. The polarizability is related to the permittivity of a material via the CLAUSIUS-MOSSOTTI relation [**38**]

$$\frac{\varepsilon - 1}{\varepsilon + 2} = \frac{4\pi}{3} \sum_i N_i \alpha_i. \tag{8.2}$$

The relative permittivity of a dielectric is given by [**84**]

$$\varepsilon_r(\omega) = \varepsilon_\infty + \varepsilon(\omega) = \varepsilon^{'} - j\varepsilon^{''}, \tag{8.3}$$

with

$$\varepsilon(\omega) = \frac{\varepsilon_s - \varepsilon_\infty}{1 + j\omega\tau_d} \tag{8.4}$$

for first order dispersive media. The permittivity ε_s denotes the permittivity when a static field of frequency zero is applied. The real and imaginary part of the permittivity can be written as

$$\varepsilon^{'} = \varepsilon_\infty + \frac{\varepsilon_s - \varepsilon_\infty}{1 + \omega^2\tau_d^2}, \tag{8.5}$$

$$\varepsilon^{''} = (\varepsilon_s - \varepsilon_\infty)\frac{\omega\tau_d}{1 + \omega^2\tau_d^2}. \tag{8.6}$$

In Fig. 8.1, eqns. (8.5) and (8.6) are plotted versus frequency for a model medium with $\varepsilon_s = 10$, $\varepsilon_\infty = 2$, and $\tau_d = 10^{-10}s$ to illustrate the nature of this frequency dependence. A commonly used measure for the losses introduced by the frequency dependency of the material is the *loss tangent* or *loss angle* δ which is given by

$$\tan\delta = \frac{\varepsilon^{''}}{\varepsilon^{'}}. \tag{8.7}$$

The angle δ is the phase angle between the vector of the electric field $\vec{E}$ and the vector of the dielectric displacement $\vec{D}$. The relation between dielectric displacement, the electric field and the polarization is given by

$$\vec{D} = \varepsilon_0\vec{E} + \vec{P}. \tag{8.8}$$

In time domain, dielectric losses can be considered by a polarization current

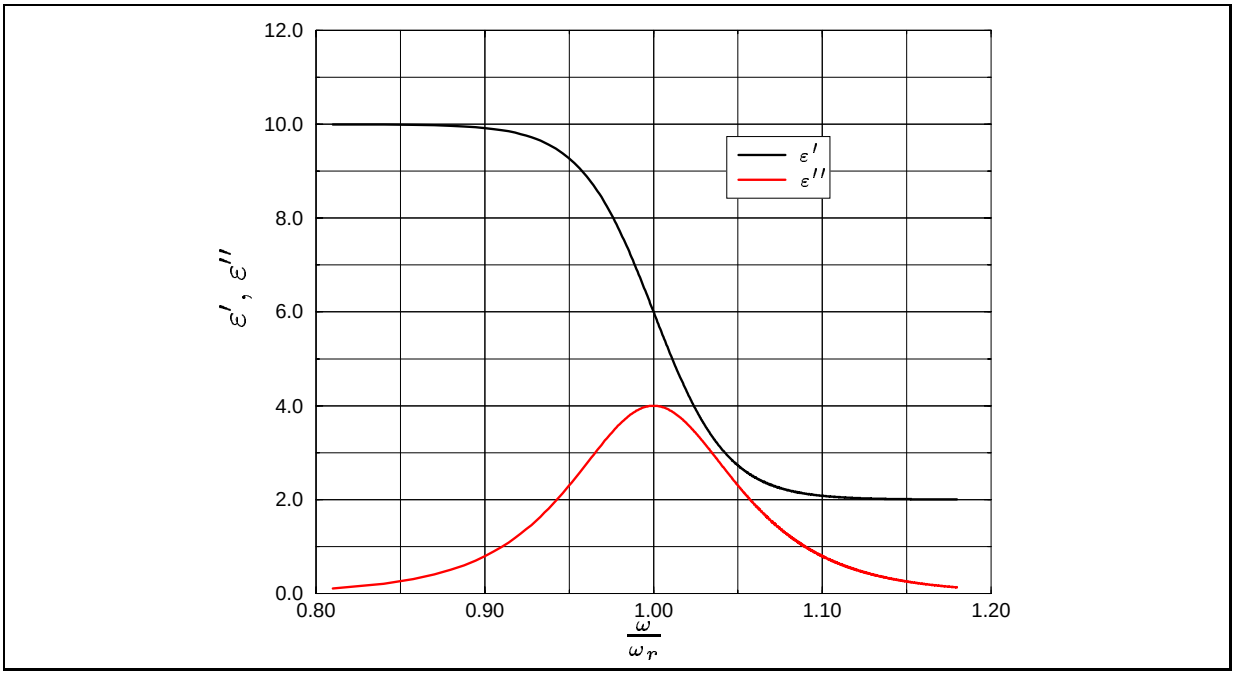

FIGURE 8.1. Graph of $\varepsilon^{'}$ and $\varepsilon^{''}$ versus frequency for $\varepsilon_s = 10$, $\varepsilon_\infty = 2$, and $\tau_d = 10^{-10}s$.

$$\boldsymbol{i}_{pol}(t) = \iint_A \frac{\partial \boldsymbol{P}}{\partial t} \cdot d\vec{A} = f(\boldsymbol{P}, \boldsymbol{E}), \tag{8.9}$$

which adds to ohmic and dielectric currents in the AMPÈRE-MAXWELL equation

$$\int_{\partial A} \vec{H} \cdot d\vec{s} = \boldsymbol{\sigma} \iint_A \vec{E} \cdot d\vec{A} + \varepsilon_0 \boldsymbol{\varepsilon} \iint_A \frac{\partial \vec{E}}{\partial t} \cdot d\vec{A} + \boldsymbol{i}_{pol}. \tag{8.10}$$

For first order dispersive dielectrics, the polarization current density is given by a first order differential equation

$$\frac{\partial \boldsymbol{P}}{\partial t} = \boldsymbol{U}\boldsymbol{P} + \boldsymbol{V}\boldsymbol{E}. \tag{8.11}$$

If we allow anisotropic orientational polarization along the principal axes, $\boldsymbol{U}$ and $\boldsymbol{V}$ take the following form

$$\boldsymbol{U} = \begin{pmatrix} -\frac{1}{\tau_{dx}} & 0 & 0 \\ 0 & -\frac{1}{\tau_{dy}} & 0 \\ 0 & 0 & -\frac{1}{\tau_{dz}} \end{pmatrix} = \begin{pmatrix} U_x & 0 & 0 \\ 0 & U_y & 0 \\ 0 & 0 & U_z \end{pmatrix}, \tag{8.12}$$

$$\boldsymbol{V} = \begin{pmatrix} \frac{\varepsilon_0(\varepsilon_{sx}-\varepsilon_{\infty x})}{\tau_{dx}} & 0 & 0 \\ 0 & \frac{\varepsilon_0(\varepsilon_{sy}-\varepsilon_{\infty y})}{\tau_{dy}} & 0 \\ 0 & 0 & \frac{\varepsilon_0(\varepsilon_{sz}-\varepsilon_{\infty z})}{\tau_{dz}} \end{pmatrix} = \begin{pmatrix} V_x & 0 & 0 \\ 0 & V_y & 0 \\ 0 & 0 & V_z \end{pmatrix}. \tag{8.13}$$

2. Derivation of SCN-TLM Algorithm for Modelling Dispersive Media

The basic idea of the propagator approach to TLM is to consider the SCN-TLM algorithm as a state system whose response fulfils a second order finite difference scheme at every time step. From this condition, one is led to a procedure to determine the scattering parameters of the scattering matrix of the symmetrical condensed node directly from the finite difference equations. Furthermore, the second order convergence of the TLM solution is guaranteed by this construction. The propagator approach can be outlined as follows. MAXWELL's equation are approximated using finite integration yielding a consistent second order finite difference scheme. The cell boundary orientated mapping between the discretized electromagnetic field and the TLM wave pulses is applied to write this finite difference scheme in TLM variables. The stub ports of the scattering matrix are eliminated resulting in a series representation of the scattering response of the SCN. For decoupling the scattering response of the SCN, the scattering matrix is transformed into its eigensystem. The finite difference scheme in TLM variables is also transformed to eigenvariables. Finally, the decoupled scattering response is inserted into the finite difference scheme and the scattering parameters are calculated. To account for dielectric losses according to the DEBYE model, the polarization current in the AMPÈRE-MAXWELL equation is discretized separately. The updating relations are obtained by a perturbation ansatz using the procedure described in [**24**]. Finally, the stability criteria for the algorithm are derived.

2.1. Approximation of Maxwell's Equations. We start from MAXWELL's equations in integral representation for homogeneous and linear media

$$\oint_{\partial A} \vec{H} \cdot d\vec{s} = \boldsymbol{\sigma} \iint_{A} \vec{E} \cdot d\vec{A} + \varepsilon_0 \boldsymbol{\varepsilon} \iint_{A} \frac{\partial \vec{E}}{\partial t} \cdot d\vec{A}, \tag{8.14}$$

$$-\oint_{\partial A} \vec{E} \cdot d\vec{s} = \mu_0 \boldsymbol{\mu} \iint_{A} \frac{\partial \vec{H}}{\partial t} \cdot d\vec{A}. \tag{8.15}$$

The material tensors are given as $\boldsymbol{\sigma} = Diag(\sigma_x, \sigma_y, \sigma_z)$, $\boldsymbol{\varepsilon}_r = Diag(\varepsilon_{rx}, \varepsilon_{ry}, \varepsilon_{rz})$, $\boldsymbol{\mu}_r = Diag(\mu_{rx}, \mu_{ry}, \mu_{rz})$ to account for anisotropic materials. Rectangular TLM

cells of dimension Δx, Δy, Δz, as depicted in Fig. 8.2 are assumed. On the surface of each TLM cell, the tangential field components of the E and H-field are defined in the centre of the cell faces. The line integrals are discretized by applying the midpoint rule. This yields for AMPÈRE's law the approximation

$$\int_{\partial A_x} \vec{H} d\vec{s} \approx - \Delta z \, H^z_{k;l,m-\frac{1}{2},n} + \Delta y \, H^y_{k;l,m,n-\frac{1}{2}} + \Delta z \, H^z_{k;l,m+\frac{1}{2},n} - \Delta y \, H^y_{k;l,m,n+\frac{1}{2}}, \tag{8.16}$$

$$\int_{\partial A_y} \vec{H} d\vec{s} \approx \Delta z \, H^z_{k;l-\frac{1}{2},m,n} + \Delta x \, H^x_{k;l,m,n+\frac{1}{2}} - \Delta z \, H^z_{k;l+\frac{1}{2},m,n} - \Delta x \, H^x_{k;l,m,n-\frac{1}{2}}, \tag{8.17}$$

$$\int_{\partial A_z} \vec{H} d\vec{s} \approx \Delta y \, H^y_{k;l+\frac{1}{2},m,n} - \Delta x \, H^x_{k;l,m+\frac{1}{2},n} - \Delta y \, H^y_{k;l-\frac{1}{2},m,n} + \Delta x \, H^x_{k;l,m-\frac{1}{2},n}. \tag{8.18}$$

For FARADAY's law one gets the following approximation

$$\int_{\partial A_x} \vec{E} d\vec{s} \approx - \Delta z \, E^z_{k;l,m+\frac{1}{2},n} + \Delta y \, E^y_{k;l,m,n+\frac{1}{2}} + \Delta z \, E^z_{k;l,m-\frac{1}{2},n} - \Delta y \, E^y_{k;l,m,n-\frac{1}{2}}, \tag{8.19}$$

$$\int_{\partial A_y} \vec{E} d\vec{s} \approx - \Delta z \, E^z_{k;l-\frac{1}{2},m,n} - \Delta x \, E^x_{k;l,m,n+\frac{1}{2}} + \Delta z \, E^z_{k;l+\frac{1}{2},m,n} + \Delta x \, E^x_{k;l,m,n-\frac{1}{2}}, \tag{8.20}$$

$$\int_{\partial A_z} \vec{E} d\vec{s} \approx \Delta y \, E^y_{k;l-\frac{1}{2},m,n} - \Delta x \, E^x_{k;l,m-\frac{1}{2},n} - \Delta y \, E^y_{k;l+\frac{1}{2},m,n} + \Delta x \, E^x_{k;l,m+\frac{1}{2},n}. \tag{8.21}$$

The area integrals over area A in (8.14) and (8.15) are approximated by multiplying the mean value of the field components at the midpoints of the edges with the area. The shaded area in Fig. 8.2 indicates the area for calculating the area integral A_x. The other integration areas A_y and A_z are defined analogously. This

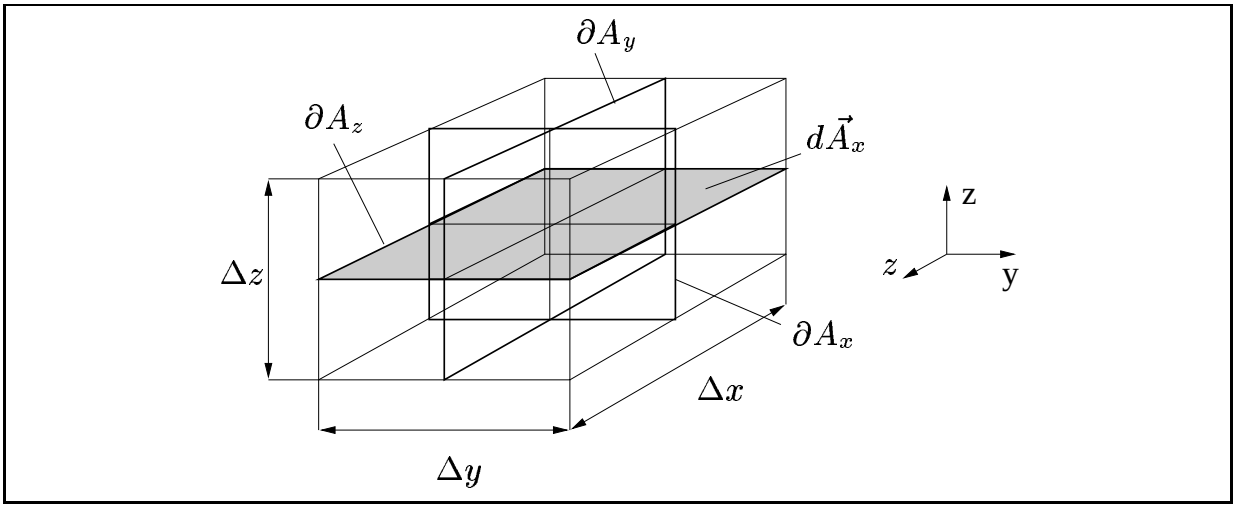

FIGURE 8.2. The three integration paths for finite integration of MAXWELL's equations. The area for approximating the area integral with normal in x-direction is shaded.

yields for the right side of AMPÈRE's law the following approximation

$$(8.22)\quad \sigma_x \iint\limits_{A_x} E_x d\vec{A}_x + \varepsilon_0\varepsilon_{rx} \iint\limits_{A_x} \frac{\partial E_x}{\partial t} d\vec{A}_x \approx$$

$$\sigma_x \frac{\Delta y \Delta z}{2} \left(E^x_{k+\frac{1}{2};l,m,n} + E^x_{k-\frac{1}{2};l,m,n} \right) + \varepsilon_0\varepsilon_{rx} \frac{\Delta y \Delta z}{\Delta t} \left(E^x_{k+\frac{1}{2};l,m,n} - E^x_{k-\frac{1}{2};l,m,n} \right),$$

$$(8.23)\quad \sigma_y \iint\limits_{A_y} E_y d\vec{A}_y + \varepsilon_0\varepsilon_{ry} \iint\limits_{A_y} \frac{\partial E_y}{\partial t} d\vec{A}_y \approx$$

$$\sigma_y \frac{\Delta x \Delta z}{2} \left(E^y_{k+\frac{1}{2};l,m,n} + E^y_{k-\frac{1}{2};l,m,n} \right) + \varepsilon_0\varepsilon_{ry} \frac{\Delta x \Delta z}{\Delta t} \left(E^y_{k+\frac{1}{2};l,m,n} - E^y_{k-\frac{1}{2};l,m,n} \right),$$

$$(8.24)\quad \sigma_z \iint\limits_{A_z} E_z d\vec{A}_z + \varepsilon_0\varepsilon_{rz} \iint\limits_{A_z} \frac{\partial E_z}{\partial t} d\vec{A}_z \approx$$

$$\sigma_z \frac{\Delta x \Delta y}{2} \left(E^z_{k+\frac{1}{2};l,m,n} + E^z_{k-\frac{1}{2};l,m,n} \right) + \varepsilon_0\varepsilon_{rz} \frac{\Delta x \Delta y}{\Delta t} \left(E^z_{k+\frac{1}{2};l,m,n} - E^z_{k-\frac{1}{2};l,m,n} \right),$$

whereas for the right side of FARADAY's law one gets the approximation

$$(8.25)\qquad \mu_0\mu_{rx} \iint\limits_{A_x} \frac{\partial H_x}{\partial t} d\vec{A}_x \approx \mu_0 \frac{\Delta y \Delta z}{\Delta t} \left(H^x_{k+\frac{1}{2};l,m,n} - H^x_{k-\frac{1}{2};l,m,n} \right),$$

$$(8.26)\qquad \mu_0\mu_{ry} \iint\limits_{A_y} \frac{\partial H_y}{\partial t} d\vec{A}_y \approx \mu_0 \frac{\Delta x \Delta z}{\Delta t} \left(H^y_{k+\frac{1}{2};l,m,n} - H^y_{k-\frac{1}{2};l,m,n} \right),$$

$$\mu_0\mu_{rz}\iint\limits_{A_z}\frac{\partial H_z}{\partial t}d\vec{A}_z \approx \mu_0\frac{\Delta x\Delta y}{\Delta t}\left(H^z_{k+\frac{1}{2};l,m,n}-H^z_{k-\frac{1}{2};l,m,n}\right). \tag{8.27}$$

In order to synchronize the updating relations with the operating conditions of the TLM algorithm, the field components in the centre of the cell are expressed as the arithmetic mean of the respective tangential field components, i.e.

$$E^x_{k+\frac{1}{2};l,m,n} \approx \frac{1}{4}\left[E^x_{k+\frac{1}{2};l,m-\frac{1}{2},n}+E^x_{k+\frac{1}{2};l,m+\frac{1}{2},n}+E^x_{k+\frac{1}{2};l,m,n-\frac{1}{2}}+E^x_{k+\frac{1}{2};l,m,n+\frac{1}{2}}\right], \tag{8.28}$$

$$E^y_{k+\frac{1}{2};l,m,n} \approx \frac{1}{4}\left[E^y_{k+\frac{1}{2};l-\frac{1}{2},m,n}+E^y_{k+\frac{1}{2};l+\frac{1}{2},m,n}+E^y_{k+\frac{1}{2};l,m,n-\frac{1}{2}}+E^y_{k+\frac{1}{2};l,m,n+\frac{1}{2}}\right], \tag{8.29}$$

$$E^z_{k+\frac{1}{2};l,m,n} \approx \frac{1}{4}\left[E^z_{k+\frac{1}{2};l,m-\frac{1}{2},n}+E^z_{k+\frac{1}{2};l,m+\frac{1}{2},n}+E^z_{k+\frac{1}{2};l-\frac{1}{2},m,n}+E^z_{k+\frac{1}{2};l+\frac{1}{2},m,n}\right], \tag{8.30}$$

$$H^x_{k+\frac{1}{2};l,m,n} \approx \frac{1}{4}\left[H^x_{k+\frac{1}{2};l,m-\frac{1}{2},n}+H^x_{k+\frac{1}{2};l,m+\frac{1}{2},n}+H^x_{k+\frac{1}{2};l,m,n-\frac{1}{2}}+H^x_{k+\frac{1}{2};l,m,n+\frac{1}{2}}\right], \tag{8.31}$$

$$H^y_{k+\frac{1}{2};l,m,n} \approx \frac{1}{4}\left[H^y_{k+\frac{1}{2};l-\frac{1}{2},m,n}+H^y_{k+\frac{1}{2};l+\frac{1}{2},m,n}+H^y_{k+\frac{1}{2};l,m,n-\frac{1}{2}}+H^y_{k+\frac{1}{2};l,m,n+\frac{1}{2}}\right], \tag{8.32}$$

$$H^z_{k+\frac{1}{2};l,m,n} \approx \frac{1}{4}\left[H^z_{k+\frac{1}{2};l,m-\frac{1}{2},n}+H^z_{k+\frac{1}{2};l,m+\frac{1}{2},n}+H^z_{k+\frac{1}{2};l-\frac{1}{2},m,n}+H^z_{k+\frac{1}{2};l+\frac{1}{2},m,n}\right]. \tag{8.33}$$

Inserting (8.28) into (8.22) and (8.16), one gets the following second order finite difference scheme for the x-component of AMPÈRE's law

$$\begin{aligned}
&-\Delta z\,H^z_{k;l,m-\frac{1}{2},n}+\Delta y\,H^y_{k;l,m,n-\frac{1}{2}}+\Delta z\,H^z_{k;l,m+\frac{1}{2},n}-\Delta y\,H^y_{k;l,m,n+\frac{1}{2}} = \\
&\sigma_x\frac{\Delta y\Delta z}{2}\Big(\frac{1}{4}\left[E^x_{k+\frac{1}{2};l,m-\frac{1}{2},n}+E^x_{k+\frac{1}{2};l,m+\frac{1}{2},n}+E^x_{k+\frac{1}{2};l,m,n-\frac{1}{2}}+E^x_{k+\frac{1}{2};l,m,n+\frac{1}{2}}\right]+ \\
&\quad\frac{1}{4}\left[E^x_{k-\frac{1}{2};l,m-\frac{1}{2},n}+E^x_{k-\frac{1}{2};l,m+\frac{1}{2},n}+E^x_{k-\frac{1}{2};l,m,n-\frac{1}{2}}+E^x_{k-\frac{1}{2};l,m,n+\frac{1}{2}}\right]\Big)+ \\
&\varepsilon_0\varepsilon_{rx}\frac{\Delta y\Delta z}{\Delta t}\Big(\frac{1}{4}\left[E^x_{k+\frac{1}{2};l,m-\frac{1}{2},n}+E^x_{k+\frac{1}{2};l,m+\frac{1}{2},n}+E^x_{k+\frac{1}{2};l,m,n-\frac{1}{2}}+E^x_{k+\frac{1}{2};l,m,n+\frac{1}{2}}\right]- \\
&\quad\frac{1}{4}\left[E^x_{k-\frac{1}{2};l,m-\frac{1}{2},n}+E^x_{k-\frac{1}{2};l,m+\frac{1}{2},n}+E^x_{k-\frac{1}{2};l,m,n-\frac{1}{2}}+E^x_{k-\frac{1}{2};l,m,n+\frac{1}{2}}\right]\Big).
\end{aligned} \tag{8.34}$$

The other five equations of the difference scheme follow accordingly.

2.2. Finite Difference Scheme Written in TLM Variables. Now we insert the one-to-one correspondence between the TLM state variables and the tangential fields on the surface of a TLM cell given by the BOFM

$$\boldsymbol{E}_{k;l,m,n} = \boldsymbol{P}_E(\boldsymbol{a}^l_{k;l,m,n} + \boldsymbol{b}^l_{k;l,m,n}), \tag{8.35}$$

$$\boldsymbol{H}_{k;l,m,n} = \frac{1}{Z_0}\boldsymbol{P}_H(\boldsymbol{a}^l_{k;l,m,n} - \boldsymbol{b}^l_{k;l,m,n}), \tag{8.36}$$

with

$$\boldsymbol{P}_E = \begin{pmatrix} \boldsymbol{B}(y,z) & \mathbf{0} & \mathbf{0} \\ \mathbf{0} & \boldsymbol{B}(z,x) & \mathbf{0} \\ \mathbf{0} & \mathbf{0} & \boldsymbol{B}(x,y) \end{pmatrix}, \tag{8.37}$$

and

$$\boldsymbol{P}_H = \begin{pmatrix} \boldsymbol{C}(z,y) & \mathbf{0} & \mathbf{0} \\ \mathbf{0} & \boldsymbol{C}(x,z) & \mathbf{0} \\ \mathbf{0} & \mathbf{0} & \boldsymbol{C}(y,x) \end{pmatrix}, \tag{8.38}$$

where

$$\boldsymbol{B}(y,z) = \begin{pmatrix} \frac{1}{\Delta y} & 0 & 0 & 0 \\ 0 & \frac{1}{\Delta y} & 0 & 0 \\ 0 & 0 & \frac{1}{\Delta z} & 0 \\ 0 & 0 & 0 & \frac{1}{\Delta z} \end{pmatrix}, \tag{8.39}$$

and

$$\boldsymbol{C}(z,y) = \begin{pmatrix} \frac{1}{\Delta z} & 0 & 0 & 0 \\ 0 & -\frac{1}{\Delta z} & 0 & 0 \\ 0 & 0 & -\frac{1}{\Delta y} & 0 \\ 0 & 0 & 0 & \frac{1}{\Delta y} \end{pmatrix}, \tag{8.40}$$

into the FD scheme (8.34). This yields the following TLM-FD scheme

$$
\begin{aligned}
(8.41)\quad & \Big((a^{7}_{k;l,m-\frac{1}{2},n} - b^{7}_{k;l,m-\frac{1}{2},n}) + (a^{8}_{k;l,m+\frac{1}{2},n} - b^{8}_{k;l,m+\frac{1}{2},n}) \\
& \quad +(a^{9}_{k;l,m,n-\frac{1}{2}} - b^{9}_{k;l,m,n-\frac{1}{2}}) + (a^{10}_{k;l,m,n+\frac{1}{2}} - b^{10}_{k;l,m,n+\frac{1}{2}})\Big) = \\
& \frac{Z_0\varepsilon_0\varepsilon_{rx}}{4}\frac{\Delta y\Delta z}{\Delta t\Delta x}\Big[\Big((a^{7}_{k+\frac{1}{2};l,m,n} + b^{7}_{k+\frac{1}{2};l,m,n}) + (a^{8}_{k+\frac{1}{2};l,m,n} + b^{8}_{k+\frac{1}{2};l,m,n}) + \\
& \quad (a^{9}_{k+\frac{1}{2};l,m,n} + b^{9}_{k+\frac{1}{2};l,m,n}) + (a^{10}_{k+\frac{1}{2};l,m,n} + b^{10}_{k+\frac{1}{2};l,m,n})\Big) - \\
& \quad \Big((a^{7}_{k-\frac{1}{2};l,m,n} + b^{7}_{k-\frac{1}{2};l,m,n}) + (a^{8}_{k-\frac{1}{2};l,m,n} + b^{8}_{k-\frac{1}{2};l,m,n}) + \\
& \quad (a^{9}_{k-\frac{1}{2};l,m,n} + b^{9}_{k-\frac{1}{2};l,m,n}) + (a^{10}_{k-\frac{1}{2};l,m,n} + b^{10}_{k-\frac{1}{2};l,m,n})\Big)\Big] \\
& + \frac{Z_0\sigma_x}{4}\frac{\Delta y\Delta z}{2\Delta x}\Big[\Big((a^{7}_{k+\frac{1}{2};l,m,n} + b^{7}_{k+\frac{1}{2};l,m,n}) + (a^{8}_{k+\frac{1}{2};l,m,n} + b^{8}_{k+\frac{1}{2};l,m,n}) + \\
& \quad (a^{9}_{k+\frac{1}{2};l,m,n} + b^{9}_{k+\frac{1}{2};l,m,n}) + (a^{10}_{k+\frac{1}{2};l,m,n} + b^{10}_{k+\frac{1}{2};l,m,n})\Big) + \\
& \quad \Big((a^{7}_{k-\frac{1}{2};l,m,n} + b^{7}_{k-\frac{1}{2};l,m,n}) + (a^{8}_{k-\frac{1}{2};l,m,n} + b^{8}_{k-\frac{1}{2};l,m,n}) + \\
& \quad\quad (a^{9}_{k-\frac{1}{2};l,m,n} + b^{9}_{k-\frac{1}{2};l,m,n}) + (a^{10}_{k-\frac{1}{2};l,m,n} + b^{10}_{k-\frac{1}{2};l,m,n})\Big)\Big] .
\end{aligned}
$$

The next step is to express the scattering responses $b_{q;r,s,t}$ $(q = k, k+\frac{1}{2}, k-\frac{1}{2}$, $r = l, l+\frac{1}{2}, l-\frac{1}{2}$, $r = m, m+\frac{1}{2}, m-\frac{1}{2}$, $r = n, n+\frac{1}{2}, n-\frac{1}{2})$ in terms of the incident wave pulses $a_{q;r,s,t}$. For this we eliminate the state variables of the stubs.

2.3. Elimination of Stub Variables in Scattering Response. For eliminating the state variables of the stubs, we start from the following state space representation of the TLM algorithm with stubs

$$
(8.42)\qquad \begin{bmatrix} |b^{l}_{cb}> \\ |b^{s}_{cb}> \end{bmatrix} = \boldsymbol{T}\begin{pmatrix} \boldsymbol{S}_{11} & \boldsymbol{S}_{12} \\ \boldsymbol{S}_{21} & \boldsymbol{S}_{22} \end{pmatrix}\begin{bmatrix} |a^{l}_{cb}> \\ |a^{s}_{cb}> \end{bmatrix},
$$

$$
(8.43)\qquad \begin{bmatrix} |a^{l}_{cb}> \\ |a^{s}_{cb}> \end{bmatrix} = \begin{pmatrix} \boldsymbol{\Gamma} & \boldsymbol{0} \\ \boldsymbol{0} & \boldsymbol{\Gamma}_s \end{pmatrix}\begin{bmatrix} |b^{l}_{cb}> \\ |b^{s}_{cb}> \end{bmatrix}.
$$

The superscripts l and s refer to the TLM pulses on link lines and stub lines, respectively. For decoupling the eigenmodes, the scattering matrix in eqn. (8.42) is transformed into its eigensystem using the transformation

$$
(8.44)\qquad \boldsymbol{B} = \begin{pmatrix} \boldsymbol{B}_0 & \boldsymbol{0} \\ \boldsymbol{0} & \boldsymbol{B}_1 \end{pmatrix},
$$

where the submatrices $\boldsymbol{B}_0$ and $\boldsymbol{B}_1$ are given as

$$\boldsymbol{B}_0 = \begin{pmatrix} 0 & 0 & 0 & 0 & 0 & 0 & 1 & 1 & 1 & 1 & 0 & 0 \\ 1 & 1 & 0 & 0 & 0 & 0 & 0 & 0 & 0 & 0 & 1 & 1 \\ 0 & 0 & 1 & 1 & 1 & 1 & 0 & 0 & 0 & 0 & 0 & 0 \\ 0 & 0 & 0 & 0 & 0 & 0 & 1 & 1 & -1 & -1 & 0 & 0 \\ -1 & -1 & 0 & 0 & 0 & 0 & 0 & 0 & 0 & 0 & 1 & 1 \\ 0 & 0 & 1 & 1 & -1 & -1 & 0 & 0 & 0 & 0 & 0 & 0 \\ 0 & 0 & 0 & 0 & 1 & -1 & 0 & 0 & 0 & 0 & -1 & 1 \\ 0 & 0 & -1 & 1 & 0 & 0 & 0 & 0 & 1 & -1 & 0 & 0 \\ 1 & -1 & 0 & 0 & 0 & 0 & -1 & 1 & 0 & 0 & 0 & 0 \\ 0 & 0 & 0 & 0 & -1 & 1 & 0 & 0 & 0 & 0 & -1 & 1 \\ 0 & 0 & -1 & 1 & 0 & 0 & 0 & 0 & -1 & 1 & 0 & 0 \\ -1 & 1 & 0 & 0 & 0 & 0 & -1 & 1 & 0 & 0 & 0 & 0 \end{pmatrix}, \tag{8.45}$$

$$\boldsymbol{B}_1 = \begin{pmatrix} 2 & 0 & 0 & 0 & 0 & 0 \\ 0 & 2 & 0 & 0 & 0 & 0 \\ 0 & 0 & 2 & 0 & 0 & 0 \\ 0 & 0 & 0 & 2 & 0 & 0 \\ 0 & 0 & 0 & 0 & 2 & 0 \\ 0 & 0 & 0 & 0 & 0 & 2 \end{pmatrix}. \tag{8.46}$$

The submatrix $\boldsymbol{B}_0$ constitutes the eigenvector matrix of the SCN without stubs. Applying this orthogonal transformation yields JOHNS' scattering matrix in canonical representation

$$\tilde{\boldsymbol{S}} = \boldsymbol{B}\boldsymbol{S}\boldsymbol{B}^{-1} = \begin{pmatrix} \tilde{\boldsymbol{S}}_{11} & \tilde{\boldsymbol{S}}_{12} \\ \tilde{\boldsymbol{S}}_{21} & \tilde{\boldsymbol{S}}_{22} \end{pmatrix}. \tag{8.47}$$

The submatrices take the following form

$$\tilde{\boldsymbol{S}}_{11} = Diag(s_{E11}, s_{E22}, s_{E33}, -1, -1, -1, s_{H11}, s_{H22}, s_{H33}, 1, 1, 1), \tag{8.48}$$

$$\tilde{\boldsymbol{S}}_{12} = \begin{pmatrix} s_{E14} & 0 & 0 & 0 & 0 & 0 \\ 0 & s_{E25} & 0 & 0 & 0 & 0 \\ 0 & 0 & s_{E36} & 0 & 0 & 0 \\ 0 & 0 & 0 & 0 & 0 & 0 \\ 0 & 0 & 0 & 0 & 0 & 0 \\ 0 & 0 & 0 & 0 & 0 & 0 \\ 0 & 0 & 0 & s_{H14} & 0 & 0 \\ 0 & 0 & 0 & 0 & s_{H25} & 0 \\ 0 & 0 & 0 & 0 & 0 & s_{H36} \\ 0 & 0 & 0 & 0 & 0 & 0 \\ 0 & 0 & 0 & 0 & 0 & 0 \\ 0 & 0 & 0 & 0 & 0 & 0 \end{pmatrix}, \tag{8.49}$$

(8.50)

$$\tilde{\boldsymbol{S}}_{21} = \begin{pmatrix} s_{E41} & 0 & 0 & 0 & 0 & 0 & 0 & 0 & 0 & 0 & 0 & 0 \\ 0 & s_{E52} & 0 & 0 & 0 & 0 & 0 & 0 & 0 & 0 & 0 & 0 \\ 0 & 0 & s_{E63} & 0 & 0 & 0 & 0 & 0 & 0 & 0 & 0 & 0 \\ 0 & 0 & 0 & 0 & 0 & 0 & s_{H41} & 0 & 0 & 0 & 0 & 0 \\ 0 & 0 & 0 & 0 & 0 & 0 & 0 & s_{H52} & 0 & 0 & 0 & 0 \\ 0 & 0 & 0 & 0 & 0 & 0 & 0 & 0 & s_{H63} & 0 & 0 & 0 \end{pmatrix},$$

and

$$\tilde{\boldsymbol{S}}_{22} = Diag(s_{E44}, s_{E55}, s_{E66}, s_{H44}, s_{H55}, s_{H66}). \tag{8.51}$$

For eliminating the stub variables, we rewrite (8.42) as

$$|\tilde{b}^l_{cb}> = \boldsymbol{T}\tilde{\boldsymbol{S}}_{11}|\tilde{a}^l_{cb}> + \boldsymbol{T}\tilde{\boldsymbol{S}}_{12}|\tilde{a}^s_{cb}>, \tag{8.52}$$

$$|\tilde{b}^s_{cb}> = \boldsymbol{T}\tilde{\boldsymbol{S}}_{21}|\tilde{a}^l_{cb}> + \boldsymbol{T}\tilde{\boldsymbol{S}}_{22}|\tilde{a}^s_{cb}>, \tag{8.53}$$

$$|\tilde{a}^s_{cb}> = \boldsymbol{\Gamma}_s|\tilde{b}^s_{cb}> . \tag{8.54}$$

Inverting (8.54) yields

$$|\tilde{b}^s_{cb}> = \boldsymbol{\Gamma}^\dagger_s|\tilde{a}^s_{cb}> . \tag{8.55}$$

Inserting (8.53) into (8.55) and rearranging yields

$$|\tilde{a}^s_{cb}> = \left(\boldsymbol{\Gamma}^\dagger_s - \boldsymbol{T}\tilde{\boldsymbol{S}}_{22}\right)^{-1}\boldsymbol{T}\tilde{\boldsymbol{S}}_{21}|\tilde{a}^s_{cb}> . \tag{8.56}$$

Inserting eqn. (8.56) into (8.52) and solving for $\tilde{b}^l_{cb}$ yields[1]

[1] $\boldsymbol{T}$ commutes with $\tilde{\boldsymbol{S}}_{12}$ and with $\left(\boldsymbol{\Gamma}^\dagger_s - \boldsymbol{T}\tilde{\boldsymbol{S}}_{22}\right)^{-1}$.

$$|\tilde{b}^l_{cb}> = \boldsymbol{T}\tilde{\boldsymbol{S}}_{11}|\tilde{a}^l_{cb}> \; + \boldsymbol{T}^2\tilde{\boldsymbol{S}}_{12}\left(\boldsymbol{\Gamma}^\dagger_s - \boldsymbol{T}\tilde{\boldsymbol{S}}_{22}\right)^{-1}\tilde{\boldsymbol{S}}_{21}|\tilde{a}^l_{cb}> . \tag{8.57}$$

Inserting the definition of a geometrical series

$$\left(\boldsymbol{\Gamma}^\dagger_s - \boldsymbol{T}\tilde{\boldsymbol{S}}_{22}\right)^{-1} = \left(\boldsymbol{\Gamma}^{-1}_s - \boldsymbol{T}\tilde{\boldsymbol{S}}_{22}\right)^{-1} = \boldsymbol{\Gamma}_s\frac{1}{\boldsymbol{I} - \boldsymbol{\Gamma}_s\boldsymbol{T}\tilde{\boldsymbol{S}}_{22}} = \boldsymbol{\Gamma}_s\sum_{\mu=0}^{\infty}\left(\boldsymbol{\Gamma}_s\boldsymbol{T}\tilde{\boldsymbol{S}}_{22}\right)^{\mu}, \tag{8.58}$$

into eqn. (8.57) results in the following series representation of the scattering response of the TLM process

$$|\tilde{b}^l_{cb}> = \boldsymbol{T}\tilde{\boldsymbol{S}}_{11}|\tilde{a}^l_{cb}> \; + \boldsymbol{T}^2\tilde{\boldsymbol{S}}_{12}\boldsymbol{\Gamma}_s\sum_{\mu=0}^{\infty}\left(\boldsymbol{\Gamma}_s\boldsymbol{T}\tilde{\boldsymbol{S}}_{22}\right)^{\mu}\tilde{\boldsymbol{S}}_{21}|\tilde{a}^l_{cb}> . \tag{8.59}$$

This expression is formally equivalent with a discrete propagator integral. Therefore, this method of determining the scattering coefficients of JOHNS' scattering matrix is called *Propagator Approach* or *Propagator Integral Approach* [**9, 25**].

2.4. The Transformed TLM-FD Scheme. For establishing the connection between the decoupled scattering response of the SCN-TLM scattering process and the consistent finite difference scheme, it is necessary to write the finite difference scheme in transformed TLM state variables. The spatial indices l, m, n are omitted in the sequel for clarity. Rearranging the quantities in the TLM-FD scheme (8.41) yields

$$
\begin{aligned}
(8.60)\qquad & \left((a_k^7 + a_k^8 + a_k^9 + a_k^{10}) - (b_k^7 + b_k^8 + b_k^9 + b_k^{10})\right) = \\
& \frac{Z_0 \varepsilon_0 \varepsilon_{rx}}{4} \frac{\Delta y \Delta z}{\Delta t \Delta x} \Big[\Big((a_{k+\frac{1}{2}}^7 + a_{k+\frac{1}{2}}^8 + a_{k+\frac{1}{2}}^9 + a_{k+\frac{1}{2}}^{10}) \\
& \qquad + (b_{k+\frac{1}{2}}^7 + b_{k+\frac{1}{2}}^8 + b_{k+\frac{1}{2}}^9 + b_{k+\frac{1}{2}}^{10}) \Big) \\
& \quad - \Big((a_{k-\frac{1}{2}}^7 + a_{k-\frac{1}{2}}^8 + a_{k-\frac{1}{2}}^9 + a_{k-\frac{1}{2}}^{10}) \\
& \qquad + (b_{k-\frac{1}{2}}^7 + b_{k-\frac{1}{2}}^8 + b_{k-\frac{1}{2}}^9 + b_{k-\frac{1}{2}}^{10}) \Big) \Big] \\
& + \frac{Z_0 \sigma_x}{4} \frac{\Delta y \Delta z}{2 \Delta x} \Big[\Big((a_{k+\frac{1}{2}}^7 + a_{k+\frac{1}{2}}^8 + a_{k+\frac{1}{2}}^9 + a_{k+\frac{1}{2}}^{10}) \\
& \qquad + (b_{k+\frac{1}{2}}^7 + b_{k+\frac{1}{2}}^8 + b_{k+\frac{1}{2}}^9 + b_{k+\frac{1}{2}}^{10}) \Big) \\
& \quad + \Big((a_{k-\frac{1}{2}}^7 + a_{k-\frac{1}{2}}^8 + a_{k-\frac{1}{2}}^9 + a_{k-\frac{1}{2}}^{10}) \\
(8.61)\qquad & \qquad + (b_{k-\frac{1}{2}}^7 + b_{k-\frac{1}{2}}^8 + b_{k-\frac{1}{2}}^9 + b_{k-\frac{1}{2}}^{10}) \Big) \Big].
\end{aligned}
$$

Obviously, one can substitute for the transformed TLM state variables (see eqn. (8.44)) resulting in

$$
\begin{aligned}
(8.62)\qquad (\tilde{a}_k^1 - \tilde{b}_k^1) = & \frac{Z_0 \varepsilon_0 \varepsilon_{rx}}{4} \frac{\Delta y \Delta z}{\Delta t \Delta x} \left[(\tilde{a}_{k+\frac{1}{2}}^1 + \tilde{b}_{k+\frac{1}{2}}^1) - (\tilde{a}_{k-\frac{1}{2}}^1 + \tilde{b}_{k-\frac{1}{2}}^1) \right] \\
& + \frac{Z_0 \sigma_x}{4} \frac{\Delta y \Delta z}{2 \Delta x} \left[(\tilde{a}_{k+\frac{1}{2}}^1 + \tilde{b}_{k+\frac{1}{2}}^1) + (\tilde{a}_{k-\frac{1}{2}}^1 + \tilde{b}_{k-\frac{1}{2}}^1) \right].
\end{aligned}
$$

Rearranging (8.62) results in the transformed finite difference scheme for the x-component of AMPÈRE's law

$$
\begin{aligned}
(8.63)\qquad (\tilde{a}_k^1 - \tilde{b}_k^1) = & \frac{Z_0 \Delta y \Delta z}{4 \Delta x} \left(\frac{\sigma_x}{2} + \frac{\varepsilon_0 \varepsilon_{rx}}{\Delta t} \right) (\tilde{a}_{k+\frac{1}{2}}^1 + \tilde{b}_{k+\frac{1}{2}}^1) \\
& + \frac{Z_0 \Delta y \Delta z}{4 \Delta x} \left(\frac{\sigma_x}{2} - \frac{\varepsilon_0 \varepsilon_{rx}}{\Delta t} \right) (\tilde{a}_{k-\frac{1}{2}}^1 + \tilde{b}_{k-\frac{1}{2}}^1).
\end{aligned}
$$

Introducing coefficients g_{E11} and $\tilde{g}_{E11}$, results in

$$
(8.64)\qquad (\tilde{a}_k^1 - \tilde{b}_k^1) = g_{E11} (\tilde{a}_{k+\frac{1}{2}}^1 + \tilde{b}_{k+\frac{1}{2}}^1) + \tilde{g}_{E11} (\tilde{a}_{k-\frac{1}{2}}^1 + \tilde{b}_{k-\frac{1}{2}}^1),
$$

where g_{E11} and $\tilde{g}_{E11}$ are given by

$$
(8.65)\qquad g_{E11} = \frac{Z_0 \Delta y \Delta z}{4 \Delta x} \left(\frac{\sigma_x}{2} + \frac{\varepsilon_0 \varepsilon_{rx}}{\Delta t} \right), \qquad \tilde{g}_{E11} = \frac{Z_0 \Delta y \Delta z}{4 \Delta x} \left(\frac{\sigma_x}{2} - \frac{\varepsilon_0 \varepsilon_{rx}}{\Delta t} \right).
$$

A further simplification can be achieved by introducing transformed field components

$$\boldsymbol{e}_{k;l,m,n} = \tilde{\boldsymbol{a}}^{l}_{k;l,m,n} + \tilde{\boldsymbol{b}}^{l}_{k;l,m,n}, \tag{8.66}$$

$$\boldsymbol{h}_{k;l,m,n} = \frac{1}{Z_0}(\tilde{\boldsymbol{a}}^{l}_{k;l,m,n} - \tilde{\boldsymbol{b}}^{l}_{k;l,m,n}). \tag{8.67}$$

With these, the transformed TLM-FD scheme (8.64) writes

$$Z_0 h^1_k = g_{E11} e^1_{k+\frac{1}{2}} + \tilde{g}_{E11} e^1_{k-\frac{1}{2}}. \tag{8.68}$$

The other five equations follow by symmetry and duality as

$$Z_0 h^2_k = g_{E22} e^2_{k+\frac{1}{2}} + \tilde{g}_{E22} e^2_{k-\frac{1}{2}}, \tag{8.69}$$

$$Z_0 h^3_k = g_{E33} e^2_{k+\frac{1}{2}} + \tilde{g}_{E33} e^2_{k-\frac{1}{2}}, \tag{8.70}$$

$$Z_0^{-1} e^7_k = r_{H11} h^7_{k+\frac{1}{2}} + \tilde{r}_{H11} h^7_{k-\frac{1}{2}}, \tag{8.71}$$

$$Z_0^{-1} e^8_k = r_{H22} h^8_{k+\frac{1}{2}} + \tilde{r}_{H22} h^8_{k-\frac{1}{2}}, \tag{8.72}$$

$$Z_0^{-1} e^9_k = r_{H33} h^9_{k+\frac{1}{2}} + \tilde{r}_{H33} h^9_{k-\frac{1}{2}}. \tag{8.73}$$

The coefficients in (8.69) to (8.73) are calculated according to

$$g_{E22} = \frac{Z_0 \Delta x \Delta z}{4\Delta y}\left(\frac{\sigma_y}{2} + \frac{\varepsilon_0 \varepsilon_{ry}}{\Delta t}\right), \qquad \tilde{g}_{E22} = \frac{Z_0 \Delta x \Delta z}{4\Delta y}\left(\frac{\sigma_y}{2} - \frac{\varepsilon_0 \varepsilon_{ry}}{\Delta t}\right), \tag{8.74}$$

$$g_{E33} = \frac{Z_0 \Delta x \Delta y}{4\Delta z}\left(\frac{\sigma_z}{2} + \frac{\varepsilon_0 \varepsilon_{rz}}{\Delta t}\right), \qquad \tilde{g}_{E33} = \frac{Z_0 \Delta x \Delta y}{4\Delta z}\left(\frac{\sigma_z}{2} - \frac{\varepsilon_0 \varepsilon_{rz}}{\Delta t}\right), \tag{8.75}$$

$$r_{H11} = \frac{\Delta y \Delta z}{4 Z_0 \Delta x}\frac{\mu_0 \mu_{rx}}{\Delta t}, \qquad \tilde{r}_{H11} = -\frac{\Delta y \Delta z}{4 Z_0 \Delta x}\frac{\mu_0 \mu_{rx}}{\Delta t}, \tag{8.76}$$

$$r_{H22} = \frac{\Delta x \Delta z}{4 Z_0 \Delta y}\frac{\mu_0 \mu_{ry}}{\Delta t}, \qquad \tilde{r}_{H22} = -\frac{\Delta x \Delta z}{4 Z_0 \Delta y}\frac{\mu_0 \mu_{ry}}{\Delta t}, \tag{8.77}$$

$$r_{H33} = \frac{\Delta x \Delta y}{4 Z_0 \Delta z}\frac{\mu_0 \mu_{rz}}{\Delta t}, \qquad \tilde{r}_{H33} = -\frac{\Delta x \Delta y}{4 Z_0 \Delta z}\frac{\mu_0 \mu_{rz}}{\Delta t}. \tag{8.78}$$

2.5. Calculation of Scattering Parameters. The scattering parameters of the transformed SCN scattering matrix (8.47) are now calculated by inserting the expressions of the scattering response for a fictitious DIRAC excitation at the boundary into the transformed TLM-FD scheme. This results in three independent equations for four unknown parameters for each equation of the $\boldsymbol{S}_E$ and $\boldsymbol{S}_H$ blocks. The remaining degree of freedom is due to the introduction of the stubs, which represent a gauge degree of freedom [**25, 27**], and can be chosen arbitrarily. Finally, the scattering coefficients are calculated choosing the degree of freedom appropriately. From expression (8.59) follows the following response at the cell boundary

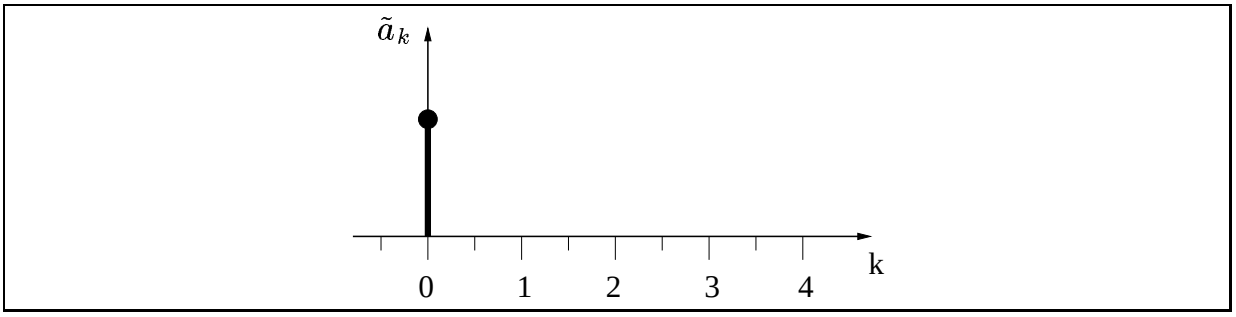

FIGURE 8.3. Dirac excitation at the boundary of a TLM cell for the calculation of the scattering parameters.

$$\tilde{b}^1_k = s_{E11}\tilde{a}^1_{k-1} + s_{E14}\sum_{\mu=0}^{\infty} s^{\mu}_{E44}s_{E41}\tilde{a}^1_{k-2-\mu}. \tag{8.79}$$

The response at the node is given by

$$\tilde{b}^1_{k+\frac{1}{2}} = s_{E11}\tilde{a}^1_{k-\frac{1}{2}} + s_{E14}\sum_{\mu=0}^{\infty} s^{\mu}_{E44}s_{E41}\tilde{a}^1_{k-\frac{3}{2}-\mu}. \tag{8.80}$$

Assuming an excitation at the cell boundary at $k = 0$ with a DIRAC pulse (see Fig. 8.3), one gets the response of a TLM cell at the subsequent time steps according to (8.80) and (8.79). The responses for subsequent time steps are tabulated in Table 8.1.

k	$\tilde{b}^1_k$	$\tilde{b}^1_{k+\frac{1}{2}}$	$\tilde{b}^1_{k-\frac{1}{2}}$
0	0	$s_{E11}\tilde{a}^1_0$	0
1	$s_{E11}\tilde{a}^1_0$	$s_{E14}s_{E41}\tilde{a}^1_0$	$s_{E11}\tilde{a}^1_0$
≥ 2	$s_{E14}s^{k-2}_{E44}s_{E41}\tilde{a}^1_0$	$s_{E14}s^{k-1}_{E44}s_{E41}\tilde{a}^1_0$	$s_{E14}s^{k-2}_{E44}s_{E41}\tilde{a}^1_0$

TABLE 8.1. Response of SCN-TLM cell in eigensystem representation to a Dirac excitation of ports 7-10.

With the response for $k = 0$ from Table 8.1, one gets from (8.64) for $k = 0$

$$\tilde{a}_0^1 = g_{E11}(\tilde{a}_0^1 + s_{E11}\tilde{a}_0^1). \tag{8.81}$$

For $k = 1$, scheme (8.64) writes

$$-s_{E11}\tilde{a}_0^1 = g_{E11}s_{E14}s_{E41}\tilde{a}_0^1 + \tilde{g}_{E11}\tilde{a}_0^1 + s_{E11}\tilde{a}_0^1, \tag{8.82}$$

and for $k = 2$, one gets

$$-s_{E14}s_{E41}\tilde{a}_0^1 = g_{E11}s_{E14}s_{E44}s_{E41}\tilde{a}_0^1 + \tilde{g}_{E11}s_{E14}s_{E41}\tilde{a}_0^1. \tag{8.83}$$

There are now three equations for the four coefficients $s_{E11}, s_{E14}, s_{E41}$, and s_{E41}. As the stubs are internal degrees of freedom, one can choose one of the coefficients. Consequently, it is possible to set $s_{E14} = 1$. After some calculus, the first four scattering coefficients of the transformed scattering matrix of the SCN are given by

$$s_{E11} = g_{E11}^{-1} - 1, \tag{8.84}$$

$$s_{E14} = 1, \tag{8.85}$$

$$s_{E41} = -\frac{1}{s_{E14}}\left(1 + \tilde{g}_{E11} - g_{E11}\right) g_{E11}^{-2}, \tag{8.86}$$

$$s_{E44} = g_{E11}^{-1}\left(\tilde{g}_{E11} - \frac{1}{s_{E14}}\right). \tag{8.87}$$

The remaining coefficients of the canonical scattering matrix are calculated in the same way.

2.6. Discretization of the Polarization Current. The discretization of MAXWELL's equations without the polarization current was presented in the previous sections. Now we derive a finite difference expression for the polarization current that can be solved by a modified TLM scattering algorithm. A special solution of (8.11) is given by the convolution integral

$$\boldsymbol{P} = e^{t\mathbf{U}} \int_0^t e^{-\theta\mathbf{U}}\mathbf{V}\mathbf{E}(\theta)d\theta. \tag{8.88}$$

This convolution writes componentwise

$$P_x = e^{-\frac{t}{\tau_{dx}}} \int_0^t e^{\frac{\theta}{\tau_{dx}}} \frac{\varepsilon_0(\varepsilon_{sx} - \varepsilon_{\infty x})}{\tau_{dx}} E_x(\theta) d\theta, \tag{8.89}$$

$$P_y = e^{-\frac{t}{\tau_{dy}}} \int_0^t e^{\frac{\theta}{\tau_{dy}}} \frac{\varepsilon_0(\varepsilon_{sy} - \varepsilon_{\infty y})}{\tau_{dy}} E_y(\theta) d\theta, \tag{8.90}$$

$$P_z = e^{-\frac{t}{\tau_{dz}}} \int_0^t e^{\frac{\theta}{\tau_{dz}}} \frac{\varepsilon_0(\varepsilon_{sz} - \varepsilon_{\infty z})}{\tau_{dz}} E_z(\theta) d\theta. \tag{8.91}$$

Substituting eqns. (8.89) to (8.91) into expression (8.11) yields the three components of the polarization current density in the following form

$$\frac{\partial P_x}{\partial t} = -\frac{1}{\tau_{dx}} e^{-\frac{t}{\tau}{}_{dx}} \int_0^t e^{\frac{\theta}{\tau_{dx}}} \frac{(\varepsilon_{sx} - \varepsilon_{\infty x})}{\tau_{dx}} E_x(\theta) d\theta + \frac{\varepsilon_0(\varepsilon_{sx} - \varepsilon_{\infty x})}{\tau_{dx}} E_x(t), \tag{8.92}$$

$$\frac{\partial P_y}{\partial t} = -\frac{1}{\tau_{dy}} e^{-\frac{t}{\tau}{}_{dy}} \int_0^t e^{\frac{\theta}{\tau_{dy}}} \frac{(\varepsilon_{sy} - \varepsilon_{\infty y})}{\tau_{dy}} E_y(\theta) d\theta + \frac{\varepsilon_0(\varepsilon_{sy} - \varepsilon_{\infty y})}{\tau_{dx}} E_y(t), \tag{8.93}$$

$$\frac{\partial P_z}{\partial t} = -\frac{1}{\tau_{dz}} e^{-\frac{t}{\tau}{}_{dz}} \int_0^t e^{\frac{\theta}{\tau_{dz}}} \frac{(\varepsilon_{sz} - \varepsilon_{\infty z})}{\tau_{dz}} E_z(\theta) d\theta + \frac{\varepsilon_0(\varepsilon_{sz} - \varepsilon_{\infty z})}{\tau_{dz}} E_z(t). \tag{8.94}$$

For discretizing these convolution integrals, the following step function for the electric field is assumed

$$\boldsymbol{E}(t) \approx \sum_{\mu=0}^{\infty} E_\mu \chi_\mu \left(t - \frac{\Delta t}{2}\right), \tag{8.95}$$

where

$$\chi_\mu = \begin{cases} 1 & \text{for} \quad 0 \le t < 1 \\ 0 & \text{elsewhere} \end{cases}. \tag{8.96}$$

The pulses are delayed by $\Delta t/2$, as the centre of a TLM cell experiences the electric field applied at the cell boundary with a delay of $\Delta t/2$ due to the propagation of the TLM pulses with finite velocity.
Inserting (8.95) into (8.88) results in the following expression for the polarization vector

$$\boldsymbol{P} \approx e^{t\mathbf{U}} \int_0^t e^{-\theta \boldsymbol{U}} \boldsymbol{V} \sum_{\mu=0}^{\infty} \boldsymbol{E}_\mu \chi_\mu \left(t - \frac{\theta}{2}\right) d\theta. \tag{8.97}$$

In the centre of a cell, the electric field is a step function of time as depicted in Fig. 8.4. For the time interval $[t_m, t_{m+1})$ we have to distinguish the two cases $t < t_{m+1/2}$ and $t > t_{m+1/2}$. In *case 1*, $t < t_{m+1/2}$, (8.97) evaluates to

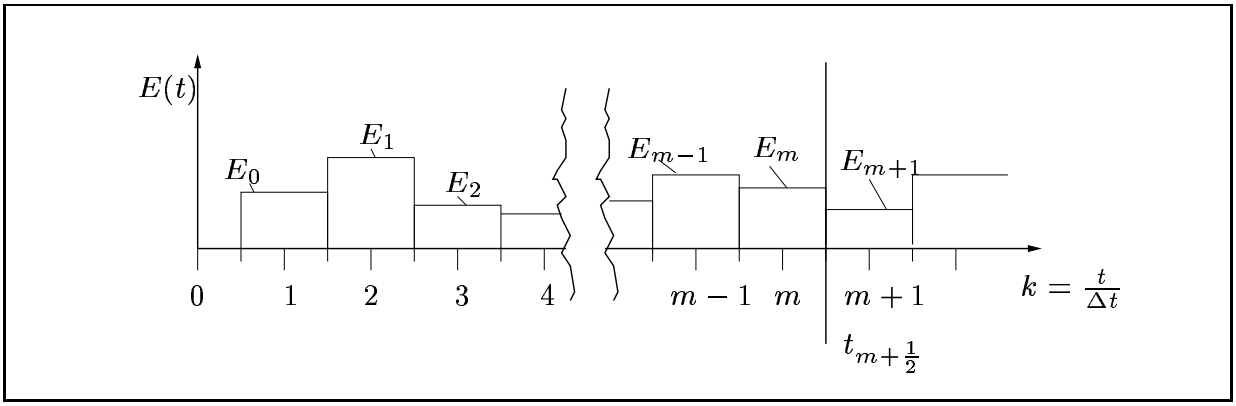

FIGURE 8.4. Electric field variation in the centre of a TLM cell.

(8.98)

$$\boldsymbol{P}(t < t_{m+1/2}) \approx e^{(t-t_{m+1/2})\boldsymbol{U}} \left[\sum_{\mu=0}^{m-1} \boldsymbol{V} e^{(m-\mu)\Delta t \boldsymbol{U}} (\boldsymbol{E}_\mu - \boldsymbol{E}_{\mu-1}) \right] - \boldsymbol{V}\boldsymbol{E}_{m-1}.$$

For *case 2*, $t > t_{m-1/2}$, one gets

(8.99)

$$\boldsymbol{P}(t > t_{m+1/2}) \approx e^{(t-t_{m+1/2})\boldsymbol{U}} \left[e^{-\Delta t \boldsymbol{U}} \left(\sum_{\mu=0}^{m} \boldsymbol{V} e^{(m+1-\mu)\Delta t \boldsymbol{U}} (\boldsymbol{E}_\mu - \boldsymbol{E}_{\mu-1}) \right) \right] - \boldsymbol{V}\boldsymbol{E}_m.$$

Consequently, one gets the following approximation for the polarization current density

(8.100)

$$\frac{\partial \boldsymbol{P}}{\partial t} \approx e^{(t-t_{m+1/2})\boldsymbol{U}} \begin{cases} \Gamma_{m-1} & \text{for} \quad t < t_{m+1/2} \\ e^{-\Delta t \boldsymbol{U}} \Gamma_m & \text{for} \quad t > t_{m+1/2} \end{cases},$$

where

(8.101)

$$\Gamma_m = \sum_{\mu=0}^{m} \boldsymbol{V} e^{(m+1-\mu)\Delta t \boldsymbol{U}} (\boldsymbol{E}_\mu - \boldsymbol{E}_{\mu-1}).$$

As $\partial \boldsymbol{P}/\partial t$ is discontinuous at times $t = \Delta t(m + 1/2)$, we consider the mean value of $\partial \boldsymbol{P}/\partial t$ for a time interval $[t_m, t_{m+1})$

$$\left.\frac{\Delta \boldsymbol{P}}{\Delta t}\right|_{t_{m+1/2}} \approx \tag{8.102}$$

$$\frac{1}{\Delta t}\int_{t_m}^{t_{m+1}} \frac{\partial \boldsymbol{P}}{\partial t} dt = \frac{1}{\Delta t}\int_{t_m}^{t_{m+1/2}} \Gamma_{m-1} dt + \frac{1}{\Delta t}\int_{t_{m+1/2}}^{t_{m+1}} \Gamma_m dt$$

$$= \frac{1}{2}\boldsymbol{W}\Big(\frac{\Delta t \boldsymbol{U}}{4}\Big) e^{\frac{\Delta t \boldsymbol{U}}{4}} \boldsymbol{V}(\boldsymbol{E}_\mu - \boldsymbol{E}_{\mu-1}) + \boldsymbol{W}\Big(\frac{\Delta t \boldsymbol{U}}{2}\Big)\Gamma_{m-1},$$

with

$$\boldsymbol{W}(x) = x^{-1}\mathbf{sinh}(x). \tag{8.103}$$

The sum Γ_m can be written as

$$\Gamma_m = \sum_{\mu=0}^{m} \gamma_\mu \boldsymbol{E}_{m-\mu} \tag{8.104}$$

with

$$\gamma_\mu = \begin{cases} e^{\Delta t \boldsymbol{U}} \boldsymbol{V} & \text{for} \quad \mu = 0 \\ e^{\mu \Delta t \boldsymbol{U}}(e^{\Delta t \boldsymbol{U}} - 1)\boldsymbol{V} & \text{for} \quad \mu > 0 \end{cases}. \tag{8.105}$$

If we sample the electromagnetic field at times $t = \Delta t(k+1/2)$, $k = 0, 1, 2, ...$ at the centres of the TLM cells l, m, n, we get a discrete convolution sum approximating the polarization current density

$$\left.\frac{\Delta \boldsymbol{P}}{\Delta t}\right|_{k+\frac{1}{2};l,m,n} \approx \tag{8.106}$$

$$\frac{1}{2}\boldsymbol{W}\Big(\frac{\Delta t \boldsymbol{U}}{4}\Big) e^{\frac{\Delta t \boldsymbol{U}}{4}} \boldsymbol{V}(\boldsymbol{E}_{k+\frac{1}{2};l,m,n} - \boldsymbol{E}_{k-\frac{1}{2};,l,m,n}) + \boldsymbol{W}\Big(\frac{\Delta t \boldsymbol{U}}{2}\Big)\Gamma_{k-1}.$$

The operator Γ_{k-1} is calculated according to the sum expression (8.104). If we again calculate the nodal field components as the average of the respective tangential field components, i.e.

$$E^x_{k+\frac{1}{2};l,m,n} \approx \tag{8.107}$$

$$\frac{1}{4}\left[E^x_{k+\frac{1}{2};l,m-\frac{1}{2},n} + E^x_{k+\frac{1}{2};l,m+\frac{1}{2},n} + E^x_{k+\frac{1}{2};l,m,n-\frac{1}{2}} + E^x_{k+\frac{1}{2};l,m,n+\frac{1}{2}}\right],$$

and apply the BOFM between electromagnetic field components and TLM state variables, we can express the polarization current in terms of canonical TLM state variables. Finally, the components of the polarization current are given as a function of transformed field components by

$$(8.108)\quad i_{pol,x}(k\Delta t) = \iint\limits_A \frac{\partial P_x}{\partial t}\cdot d\vec{A} \approx \frac{\Delta y\Delta z}{4\Delta x}\left[-\frac{2\varepsilon_0(\varepsilon_{sx}-\varepsilon_{\infty x})}{\Delta t}\sinh\Big(\frac{-\Delta t}{4\tau_{dx}}\Big)e^{-\frac{\Delta t}{4\tau_{dx}}}\ (e^1_{k+\frac{1}{2}}-e^1_{k-\frac{1}{2}}) + \frac{-2\tau_{dx}}{\Delta t}\sinh\Big(\frac{-\Delta t}{2\tau_{dx}}\Big)\Gamma_{k-1,x}\right],$$

$$(8.109)\quad i_{pol,y}(k\Delta t) = \iint\limits_A \frac{\partial P_y}{\partial t}\cdot d\vec{A} \approx \frac{\Delta x\Delta z}{4\Delta y}\left[-\frac{2\varepsilon_0(\varepsilon_{sy}-\varepsilon_{\infty y})}{\Delta t}\sinh\Big(\frac{-\Delta t}{4\tau_{dy}}\Big)e^{-\frac{\Delta t}{4\tau_{dy}}}\ (e^1_{k+\frac{1}{2}}-e^1_{k-\frac{1}{2}}) + \frac{-2\tau_{dy}}{\Delta t}\sinh\Big(\frac{-\Delta t}{2\tau_{dy}}\Big)\Gamma_{k-1,y}\right],$$

$$(8.110)\quad i_{pol,z}(k\Delta t) = \iint\limits_A \frac{\partial P_z}{\partial t}\cdot d\vec{A} \approx \frac{\Delta x\Delta y}{4\Delta z}\left[-\frac{2\varepsilon_0(\varepsilon_{sz}-\varepsilon_{\infty z})}{\Delta t}\sinh\Big(\frac{-\Delta t}{4\tau_{dz}}\Big)e^{-\frac{\Delta t}{4\tau_{dz}}}\ (e^1_{k+\frac{1}{2}}-e^1_{k-\frac{1}{2}}) + \frac{-2\tau_{dz}}{\Delta t}\sinh\Big(\frac{-\Delta t}{2\tau_{dz}}\Big)\Gamma_{k-1,z}\right],$$

with

$$(8.111)\quad \Gamma_{k,x} = \sum_{\mu=0}^{k}\gamma_{\mu,x}e^1_{k-\mu+\frac{1}{2}},$$

$$(8.112)\quad \Gamma_{k,y} = \sum_{\mu=0}^{k}\gamma_{\mu,y}e^2_{k-\mu+\frac{1}{2}},$$

$$(8.113)\quad \Gamma_{k,z} = \sum_{\mu=0}^{k}\gamma_{\mu,z}e^3_{k-\mu+\frac{1}{2}},$$

(8.114)

and

$$\gamma_{\mu,x} = \begin{cases} e^{\Delta t U_x} V_x & \text{for} \quad \mu = 0 \\ e^{\mu \Delta t U_x} \left(e^{\Delta t U_x} - 1\right) V_x & \text{for} \quad \mu > 0 \end{cases}, \tag{8.115}$$

$$\gamma_{\mu,y} = \begin{cases} e^{\Delta t U_y} V_y & \text{for} \quad \mu = 0 \\ e^{\mu \Delta t U_y} \left(e^{\Delta t U_y} - 1\right) V_y & \text{for} \quad \mu > 0 \end{cases}, \tag{8.116}$$

$$\gamma_{\mu,z} = \begin{cases} e^{\Delta t U_z} V_z & \text{for} \quad \mu = 0 \\ e^{\mu \Delta t U_z} \left(e^{\Delta t U_z} - 1\right) V_z & \text{for} \quad \mu > 0 \end{cases}. \tag{8.117}$$

Rearranging yields

$$i_{pol,x}(k\Delta t) = g_{p11} e^1_{k+\frac{1}{2}} + \tilde{g}_{p11} e^1_{k-\frac{1}{2}} + G_x\left[\left(e^1_{k-\mu-\frac{1}{2}}\right)_{\mu=0}^{\infty}\right], \tag{8.118}$$

$$i_{pol,y}(k\Delta t) = g_{p22} e^2_{k+\frac{1}{2}} + \tilde{g}_{p22} e^2_{k-\frac{1}{2}} + G_y\left[\left(e^2_{k-\mu-\frac{1}{2}}\right)_{\mu=0}^{\infty}\right], \tag{8.119}$$

$$i_{pol,z}(k\Delta t) = g_{p33} e^3_{k+\frac{1}{2}} + \tilde{g}_{p33} e^3_{k-\frac{1}{2}} + G_z\left[\left(e^3_{k-\mu+\frac{1}{2}}\right)_{\mu=0}^{\infty}\right], \tag{8.120}$$

with

$$g_{p11} = -\frac{\Delta y \Delta z}{4\Delta x} \frac{2\varepsilon_0(\varepsilon_{sx} - \varepsilon_{\infty x})}{\Delta t} \sinh\left(\frac{-\Delta t}{4\tau_{dx}}\right) e^{-\frac{\Delta t}{4\tau_{dx}}}, \tag{8.121}$$

$$\tilde{g}_{p11} = \frac{\Delta y \Delta z}{4\Delta x} \frac{2\varepsilon_0(\varepsilon_{sx} - \varepsilon_{\infty x})}{\Delta t} \sinh\left(\frac{-\Delta t}{4\tau_{dx}}\right) e^{-\frac{\Delta t}{4\tau_{dx}}}, \tag{8.122}$$

$$g_{p22} = -\frac{\Delta x \Delta z}{4\Delta y} \frac{2\varepsilon_0(\varepsilon_{sy} - \varepsilon_{\infty y})}{\Delta t} \sinh\left(\frac{-\Delta t}{4\tau_{dy}}\right) e^{-\frac{\Delta t}{4\tau_{dy}}}, \tag{8.123}$$

$$\tilde{g}_{p22} = \frac{\Delta x \Delta z}{4\Delta y} \frac{2\varepsilon_0(\varepsilon_{sy} - \varepsilon_{\infty y})}{\Delta t} \sinh\left(\frac{-\Delta t}{4\tau_{dy}}\right) e^{-\frac{\Delta t}{4\tau_{dy}}}, \tag{8.124}$$

$$g_{p33} = -\frac{\Delta x \Delta y}{4\Delta z} \frac{2\varepsilon_0(\varepsilon_{sz} - \varepsilon_{\infty z})}{\Delta t} \sinh\left(\frac{-\Delta t}{4\tau_{dz}}\right) e^{-\frac{\Delta t}{4\tau_{dz}}}, \tag{8.125}$$

$$\tilde{g}_{p33} = \frac{\Delta x \Delta y}{4\Delta z} \frac{2\varepsilon_0(\varepsilon_{sz} - \varepsilon_{\infty z})}{\Delta t} \sinh\left(\frac{-\Delta t}{4\tau_{dz}}\right) e^{-\frac{\Delta t}{4\tau_{dz}}}, \tag{8.126}$$

and

$$G_x\left[\left(e^1_{k-\mu+\frac{1}{2}}\right)_{\mu=0}^{\infty}\right] = -\frac{2\tau_{dx}}{\Delta t} \sinh\left(\frac{-\Delta t}{2\tau_{dx}}\right) \frac{\Delta y \Delta z}{4\Delta x} \Gamma_{k-1,x}, \tag{8.127}$$

$$G_y\left[\left(e^2_{k-\mu+\frac{1}{2}}\right)_{\mu=0}^{\infty}\right] = -\frac{2\tau_{dy}}{\Delta t} \sinh\left(\frac{-\Delta t}{2\tau_{dy}}\right) \frac{\Delta x \Delta z}{4\Delta y} \Gamma_{k-1,y}, \tag{8.128}$$

$$G_z\left[\left(e^3_{k-\mu+\frac{1}{2}}\right)_{\mu=0}^{\infty}\right] = -\frac{2\tau_{dz}}{\Delta t} \sinh\left(\frac{-\Delta t}{2\tau_{dz}}\right) \frac{\Delta x \Delta y}{4\Delta z} \Gamma_{k-1,z}. \tag{8.129}$$

2.7. TLM-FD Scheme for First Order Dispersive Media. Considering the polarization current in the transformed TLM-FD eqns. (8.64) to (8.73)

approximating AMPÈRE's law, results in the following modified TLM-FD equations

$$Z_0 h_k^1 = (g_{E11} + g_{p11}) e_{k+\frac{1}{2}}^1 + (\tilde{g}_{E11} + \tilde{g}_{p11}) e_{k-\frac{1}{2}}^1 + G_x \left[\left(e_{k-\mu+\frac{1}{2}}^1 \right)_{\mu=0}^{\infty} \right], \tag{8.130}$$

$$Z_0 h_k^2 = (g_{E22} + g_{p11}) e_{k+\frac{1}{2}}^2 + (\tilde{g}_{E22} + \tilde{g}_{p11}) e_{k-\frac{1}{2}}^2 + G_y \left[\left(e_{k-\mu+\frac{1}{2}}^2 \right)_{\mu=0}^{\infty} \right], \tag{8.131}$$

$$Z_0 h_k^3 = (g_{E33} + g_{p11}) e_{k+\frac{1}{2}}^2 + (\tilde{g}_{E33} + \tilde{g}_{p11}) e_{k-\frac{1}{2}}^2 + G_z \left[\left(e_{k-\mu+\frac{1}{2}}^3 \right)_{\mu=0}^{\infty} \right]. \tag{8.132}$$

Using matrix operator notation, the transformed TLM-FD scheme considering the polarization current thus writes

$$Z_0 \boldsymbol{h}_k = \boldsymbol{G}_E^{'} \boldsymbol{e}_{k+\frac{1}{2}} + \tilde{\boldsymbol{G}}_E^{'} \boldsymbol{e}_{k-\frac{1}{2}} + \boldsymbol{G} \left[\left(\boldsymbol{e}_{k-\mu+\frac{1}{2};l,m,n} \right)_{\mu=0}^{\infty} \right]. \tag{8.133}$$

The coefficient matrices $\boldsymbol{G}_E^{'}$ and $\tilde{\boldsymbol{G}}_E^{'}$ are given by

(8.134)

$$\boldsymbol{G}_E^{'} = \begin{pmatrix} g_{E11}^{'} & 0 & 0 \\ 0 & g_{E22}^{'} & 0 \\ 0 & 0 & g_{E33}^{'} \end{pmatrix} = \begin{pmatrix} g_{E11} + g_{p11} & 0 & 0 \\ 0 & g_{E22} + g_{p22} & 0 \\ 0 & 0 & g_{E33} + g_{p33} \end{pmatrix},$$

(8.135)

$$\tilde{\boldsymbol{G}}_E^{'} = \begin{pmatrix} \tilde{g}_{E11}^{'} & 0 & 0 \\ 0 & \tilde{g}_{E22}^{'} & 0 \\ 0 & 0 & \tilde{g}_{E33}^{'} \end{pmatrix} = \begin{pmatrix} \tilde{g}_{E11} + \tilde{g}_{p11} & 0 & 0 \\ 0 & \tilde{g}_{E22} + \tilde{g}_{p22} & 0 \\ 0 & 0 & \tilde{g}_{E33} + \tilde{g}_{p33} \end{pmatrix},$$

with the coefficients

$$g_{E11}^{'} = \frac{Z_0 \Delta y \Delta z}{4 \Delta x} \left(\frac{\sigma_x}{2} + \frac{\varepsilon_0 \varepsilon_{rx}}{\Delta t} - \frac{2 \varepsilon_0 (\varepsilon_{sx} - \varepsilon_{\infty x})}{\Delta t} \sinh\left(\frac{-\Delta t}{4 \tau_{dx}} \right) e^{-\frac{\Delta t}{4 \tau_{dx}}} \right), \tag{8.136}$$

$$\tilde{g}_{E11}^{'} = \frac{Z_0 \Delta y \Delta z}{4 \Delta x} \left(\frac{\sigma_x}{2} - \frac{\varepsilon_0 \varepsilon_{rx}}{\Delta t} + \frac{2 \varepsilon_0 (\varepsilon_{sx} - \varepsilon_{\infty x})}{\Delta t} \sinh\left(\frac{-\Delta t}{4 \tau_{dx}} \right) e^{-\frac{\Delta t}{4 \tau_{dx}}} \right), \tag{8.137}$$

$$g_{E22}^{'} = \frac{Z_0 \Delta x \Delta z}{4 \Delta y} \left(\frac{\sigma_y}{2} + \frac{\varepsilon_0 \varepsilon_{ry}}{\Delta t} - \frac{2 \varepsilon_0 (\varepsilon_{sy} - \varepsilon_{\infty y})}{\Delta t} \sinh\left(\frac{-\Delta t}{4 \tau_{dy}} \right) e^{-\frac{\Delta t}{4 \tau_{dy}}} \right), \tag{8.138}$$

$$\tilde{g}_{E22}^{'} = \frac{Z_0 \Delta x \Delta z}{4 \Delta y} \left(\frac{\sigma_y}{2} - \frac{\varepsilon_0 \varepsilon_{ry}}{\Delta t} + \frac{2 \varepsilon_0 (\varepsilon_{sy} - \varepsilon_{\infty y})}{\Delta t} \sinh\left(\frac{-\Delta t}{4 \tau_{dy}} \right) e^{-\frac{\Delta t}{4 \tau_{dy}}} \right), \tag{8.139}$$

$$g_{E33}^{'} = \frac{Z_0 \Delta x \Delta y}{4 \Delta z} \left(\frac{\sigma_z}{2} + \frac{\varepsilon_0 \varepsilon_{rz}}{\Delta t} - \frac{2 \varepsilon_0 (\varepsilon_{sz} - \varepsilon_{\infty z})}{\Delta t} \sinh\left(\frac{-\Delta t}{4 \tau_{dz}} \right) e^{-\frac{\Delta t}{4 \tau_{dz}}} \right), \tag{8.140}$$

$$\tilde{g}_{E11}^{'} = \frac{Z_0 \Delta x \Delta y}{4 \Delta z} \left(\frac{\sigma_z}{2} - \frac{\varepsilon_0 \varepsilon_{rz}}{\Delta t} + \frac{2 \varepsilon_0 (\varepsilon_{sz} - \varepsilon_{\infty z})}{\Delta t} \sinh\left(\frac{-\Delta t}{4 \tau_{dz}} \right) e^{-\frac{\Delta t}{4 \tau_{dz}}} \right). \tag{8.141}$$

2.8. Derivation of Recursive TLM Algorithm. How to solve finite difference schemes that include a discrete convolution sum of unknowns of all past time steps with modified SCN-TLM algorithms was proposed in [**24**]. Employing this method, one can derive recursive relations that avoid the storage of all past values of the unknowns and calculate the coefficients for additional stubs which account for the recursion. In Sections 2.1 to 2.5 of this chapter, it was shown that the solutions of the TLM scattering algorithm

$$\tilde{\boldsymbol{a}}_{k+1} = \boldsymbol{B}\boldsymbol{a}_{k+1}, \tag{8.142}$$

$$\tilde{\boldsymbol{b}}_{k+1} = \Psi\tilde{\boldsymbol{a}}_{k}, \tag{8.143}$$

$$\boldsymbol{b}_{k+1} = \boldsymbol{B}^{-1}\tilde{\boldsymbol{b}}_{k+1}, \tag{8.144}$$

$$\boldsymbol{a}_{k+1} = \Gamma\boldsymbol{b}_{k+1} \tag{8.145}$$

fulfil a second order finite difference scheme

$$\boldsymbol{R}\boldsymbol{f}_{k;l,m,n} = \sum_{\mu} \boldsymbol{Q}_{\mu}\boldsymbol{f}_{k-\mu+\frac{1}{2};l,m,n} \tag{8.146}$$

at every time step, if an appropriate mapping between discretized field components and TLM pulses is applied and the scattering coefficients of JOHNS' scattering matrix are derived appropriately. The unknown vector $\boldsymbol{f}_k$ in (8.146) comprises the transformed field components following (8.66) and (8.67) in complex notation, i.e.

$$\boldsymbol{f}_{k;l,m,n} = \boldsymbol{e}_{k;l,m,n} + j\boldsymbol{h}_{k;l,m,n} \tag{8.147}$$

$$= (\tilde{\boldsymbol{a}}^{l}_{k;l,m,n} + \tilde{\boldsymbol{b}}^{l}_{k;l,m,n}) + j\frac{1}{Z_0}(\tilde{\boldsymbol{a}}^{l}_{k;l,m,n} - \tilde{\boldsymbol{b}}^{l}_{k;l,m,n}), \tag{8.148}$$

$$= \underbrace{(\boldsymbol{I} + jZ_0{}^{-1}\boldsymbol{I})}_{=:\alpha}\boldsymbol{a}^{l}_{k;l,m,n} + \underbrace{(\boldsymbol{I} - jZ_0{}^{-1}\boldsymbol{I})}_{=:\alpha^*}\boldsymbol{b}^{l}_{k;l,m,n}. \tag{8.149}$$

Considering dielectric losses in time domain using a discrete convolution, one has a finite difference scheme (in transformed field components) of the form

$$\boldsymbol{R}\boldsymbol{f}'_{k;l,m,n} = \sum_{\mu} \boldsymbol{Q}_{\mu}\boldsymbol{f}'_{k-\mu+\frac{1}{2};l,m,n} + \boldsymbol{G}\big[(\boldsymbol{f}'_{k-\mu+\frac{1}{2};l,m,n})^{\infty}_{\mu=0}\big]. \tag{8.150}$$

In order to generate solutions for (8.150), we assume a TLM algorithm

$$\tilde{\boldsymbol{a}}'_{k+1} = \boldsymbol{B}\boldsymbol{a}'_{k+1}, \tag{8.151}$$

$$\tilde{\boldsymbol{b}}'_{k+1} = \Psi' \tilde{\boldsymbol{a}}'_{k}, \tag{8.152}$$

$$\boldsymbol{b}'_{k+1} = \boldsymbol{B}^{-1}\tilde{\boldsymbol{b}}'_{k+1}, \tag{8.153}$$

$$\boldsymbol{a}'_{k+1} = \Gamma \boldsymbol{b}'_{k+1}, \tag{8.154}$$

where the scattering operator Ψ' is given by

$$\Psi' \tilde{\boldsymbol{a}}' = \Psi \tilde{\boldsymbol{a}}' + \boldsymbol{D}\big[\big(\boldsymbol{f}'_{k-\mu-\frac{1}{2};l,m,n}\big)_{\mu=0}^{\infty}\big]. \tag{8.155}$$

This expression can be rearranged such that it constitutes the following recursion

$$\begin{aligned}\alpha^* \boldsymbol{Q}_0 \boldsymbol{D}\big[\big(\boldsymbol{f}'_{k-\mu+\frac{1}{2};l,m,n}\big)_{\mu=0}^{\infty}\big] &= (\boldsymbol{R}-\boldsymbol{Q}_1)\alpha^* \boldsymbol{D}\big[\big(\boldsymbol{f}'_{k-\mu-\frac{1}{2};l,m,n}\big)_{\mu=0}^{\infty}\big] \\ &- \sum_{\nu=1}^{\infty} \boldsymbol{Q}_{\nu+1}\alpha^* \boldsymbol{D}\big[\big(\boldsymbol{f}'_{k-\mu-\frac{1}{2};l,m,n}\big)_{\mu=0}^{\infty}\big] + \boldsymbol{G}\big[\big(\boldsymbol{f}'_{k-\mu+\frac{1}{2};l,m,n}\big)_{\mu=0}^{\infty}\big].\end{aligned} \tag{8.156}$$

To solve for the discrete convolution of eqn. (8.156), we identify the unknown operators of eqn. (8.156) from the transformed TLM-FD scheme (8.133) by inspection, yielding

$$\boldsymbol{R} = Im[.], \tag{8.157}$$

$$\boldsymbol{Q}_0 = \boldsymbol{G}'_E Re[.], \tag{8.158}$$

$$\boldsymbol{Q}_1 = \tilde{\boldsymbol{G}}'_E Re[.], \tag{8.159}$$

$$\boldsymbol{Q}_{2..\infty} = \boldsymbol{0}, \tag{8.160}$$

The operators $\boldsymbol{G}'_E$ and $\tilde{\boldsymbol{G}}'_E$ are given according to (8.134) and (8.135). It follows from (8.156)

$$\boldsymbol{Q}_0 \alpha^* \boldsymbol{d}_{k+\frac{1}{2}} = (\boldsymbol{R}-\boldsymbol{Q}_1)\alpha^* \boldsymbol{d}_{k-\frac{1}{2}} - \boldsymbol{G}\big[\big(\boldsymbol{f}'_{k-\mu+\frac{1}{2};l,m,n}\big)_{\mu=0}^{\infty}\big]. \tag{8.161}$$

Inserting (8.158) and (8.159) yields

$$\boldsymbol{G}_E \boldsymbol{d}_{k+\frac{1}{2}} = -(Z_0{}^{-1}\boldsymbol{I} + \tilde{\boldsymbol{G}}_E)\boldsymbol{d}_{k-\frac{1}{2}} - \boldsymbol{G}\big[\big(\boldsymbol{f}'_{k-\mu+\frac{1}{2};l,m,n}\big)_{\mu=0}^{\infty}\big]. \tag{8.162}$$

Finally, solving for $\boldsymbol{d}_{k+\frac{1}{2}}$ results in

$$\boldsymbol{d}_{k+\frac{1}{2}} = -\boldsymbol{G}_E^{-1}(Z_0{}^{-1}\boldsymbol{I} + \tilde{\boldsymbol{G}}_E)\boldsymbol{d}_{k-\frac{1}{2}} - \boldsymbol{G}_E^{-1}\boldsymbol{G}\big[\big(\boldsymbol{f}'_{k-\mu+\frac{1}{2};l,m,n}\big)_{\mu=0}^{\infty}\big]. \tag{8.163}$$

Looking more closely at the convolution sum $\boldsymbol{G}[.]$, one gets by rearranging and substitution

$$
\begin{aligned}
(8.164)\quad \boldsymbol{G}\big[\big(\boldsymbol{f}'_{k-\mu+\frac{1}{2};l,m,n}\big)_{\mu=0}^{\infty}\big] &= \\
\boldsymbol{G}\big[\big(\boldsymbol{e}'_{k-\mu+\frac{1}{2};l,m,n}\big)_{\mu=0}^{\infty}\big] &= \boldsymbol{A}\Gamma_{k-1,x} \\
= \boldsymbol{A}e^{\Delta t\boldsymbol{U}}\boldsymbol{V}\boldsymbol{e}'_{k+\frac{1}{2}} + \boldsymbol{A}e^{\Delta t\boldsymbol{U}}\big[\big(e^{\Delta t\boldsymbol{U}}-1\big)\boldsymbol{V}\boldsymbol{e}'_{k-\frac{1}{2}} & \\
+ e^{\Delta t\boldsymbol{U}}\big[\big(e^{\Delta t\boldsymbol{U}}-1\big)\boldsymbol{V}\boldsymbol{e}'_{k-\frac{3}{2}} + e^{\Delta t\boldsymbol{U}}[\cdots]\big]\big]. &
\end{aligned}
$$

The coefficient matrix $\boldsymbol{A}$ is given by

$$
(8.165)\qquad \boldsymbol{A} = \begin{pmatrix} -\frac{2\tau_{dx}}{\Delta t}\sinh\left(\frac{-\Delta t}{2\tau_{dx}}\right)\frac{\Delta y\Delta z}{4\Delta x} & 0 & 0 \\ 0 & -\frac{2\tau_{dy}}{\Delta t}\sinh\left(\frac{-\Delta t}{2\tau_{dy}}\right)\frac{\Delta x\Delta z}{4\Delta y} & 0 \\ 0 & 0 & -\frac{2\tau_{dz}}{\Delta t}\sinh\left(\frac{-\Delta t}{2\tau_{dz}}\right)\frac{\Delta x\Delta y}{4\Delta z} \end{pmatrix}.
$$

From (8.164) follows the recursive algorithm for computing the discrete convolution sum $G[.]$

$$
(8.166)\qquad G\big[\big(\boldsymbol{e}'_{k-\mu+\frac{1}{2};l,m,n}\big)_{\mu=0}^{\infty}\big] = \boldsymbol{A}e^{\Delta t\boldsymbol{U}}\boldsymbol{V}e^{1}_{k+\frac{1}{2}} + \boldsymbol{A}e^{\Delta t\boldsymbol{U}}m_{k-\frac{1}{2}},
$$

$$
(8.167)\qquad m_{k+\frac{1}{2}} = \big(e^{\Delta t\boldsymbol{U}}-1\big)\boldsymbol{V}e^{1}_{k+\frac{1}{2}} + e^{\Delta t\boldsymbol{U}} + m_{k-\frac{1}{2}}.
$$

The complete TLM algorithm for first order dispersive media is thus given in general notation as follows (after substituting (8.166) and (8.167) into (8.163))

$$
(8.168)\qquad \tilde{\boldsymbol{a}}'_{k+1} = \boldsymbol{B}\,\boldsymbol{a}'_{k+1},
$$

$$
(8.169)\qquad \tilde{\boldsymbol{b}}'_{k+1} = \Psi\,\tilde{\boldsymbol{a}}' + \boldsymbol{D}\big[\big(\boldsymbol{f}'_{k-\mu-\frac{1}{2};l,m,n}\big)_{\mu=0}^{\infty}\big],
$$

$$
(8.170)\qquad \boldsymbol{b}'_{k+1} = \boldsymbol{B}^{-1}\,\tilde{\boldsymbol{b}}'_{k+1},
$$

$$
(8.171)\qquad \boldsymbol{a}'_{k+1} = \Gamma\,\boldsymbol{b}'_{k+1}.
$$

The updating relations of the dielectric node write

$$\tilde{\boldsymbol{a}}'_{k+1} = \boldsymbol{B}\,\boldsymbol{a}'_{k+1}, \tag{8.172}$$

$$\tilde{\boldsymbol{b}}'_{k+1} = \tilde{\boldsymbol{S}}\,\tilde{\boldsymbol{a}}'_{k} + \boldsymbol{d}_k, \tag{8.173}$$

$$\boldsymbol{e}'_{k+\frac{1}{2}} = \tilde{\boldsymbol{a}}'_{k} + \tilde{\boldsymbol{b}}'_{k+1}, \tag{8.174}$$

$$\boldsymbol{d}_{k+1} = \boldsymbol{S}_{D1}\,d_k + \boldsymbol{S}_{D2}\,e'_{k+\frac{1}{2}} + \boldsymbol{S}_{D3}\,m_k, \tag{8.175}$$

$$\boldsymbol{m}_{k+1} = \boldsymbol{S}_{D4}\,e'_{k+\frac{1}{2}} + \boldsymbol{S}_{D5}\,m_k, \tag{8.176}$$

$$\boldsymbol{b}'_{k+1} = \boldsymbol{B}^{-1}\,\tilde{\boldsymbol{b}}'_{k+1}, \tag{8.177}$$

$$\boldsymbol{a}'_{k+1} = \Gamma\,\boldsymbol{b}'_{k+1}, \tag{8.178}$$

yielding a solution of (8.150) at every time step. The coefficient matrices $\boldsymbol{S}_{Di}$, $i = 1, .., 5$ are given by

$$\boldsymbol{S}_{D1} = -\boldsymbol{G}_E^{-1}({Z_0}^{-1}\boldsymbol{I} + \tilde{\boldsymbol{G}}_E), \tag{8.179}$$

$$\boldsymbol{S}_{D2} = -\boldsymbol{G}_E^{-1}\boldsymbol{A}\,e^{\Delta t\boldsymbol{U}}\boldsymbol{V}, \tag{8.180}$$

$$\boldsymbol{S}_{D3} = -\boldsymbol{G}_E^{-1}\boldsymbol{A}\,e^{\Delta t\boldsymbol{U}}, \tag{8.181}$$

$$\boldsymbol{S}_{D4} = \left(e^{\Delta t\boldsymbol{U}} - \boldsymbol{I}\right)\boldsymbol{V}, \tag{8.182}$$

$$\boldsymbol{S}_{D5} = e^{\Delta t\boldsymbol{U}}. \tag{8.183}$$

These updating relations of the TLM node simulating first order dispersive media can easily be implemented into a computer code.

2.9. Stability of Modified SCN-TLM Algorithm. The modified TLM algorithm is stable for proper initial values, if the spectral norm of the eigenvalues of

$$\Upsilon = \begin{pmatrix} \boldsymbol{S}_{D1} + \boldsymbol{S}_{D2} & \boldsymbol{S}_{D3} \\ \boldsymbol{S}_{D4} & \boldsymbol{S}_{D5} \end{pmatrix} \tag{8.184}$$

is bounded by one [**24**]. Furthermore, this condition provides a simple means of calculating the time step for the TLM simulation using the modified TLM algorithm for first order dispersive media.

3. Validation of Modified SCN-TLM Algorithm

To validate the SCN-TLM algorithm for dispersive media of DEBYE type, the reflection of a plane electromagnetic wave from an air-dielectric interface was studied. An infinite parallel-plate (PPL) waveguide was partially filled with a dispersive model dielectric, as depicted in Fig. 8.5. The static dielectric constant of the model medium was $\varepsilon_s = 65$ (for simplicity, ε_∞ was set to 1), its relaxation

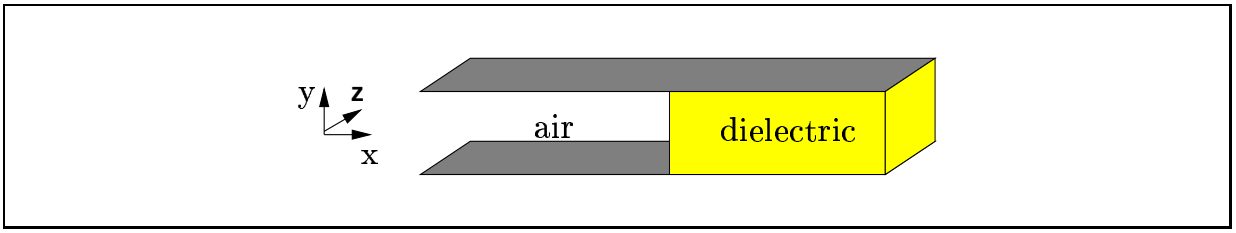

FIGURE 8.5. TEM parallel-plate waveguide, partially filled with dispersive dielectric.

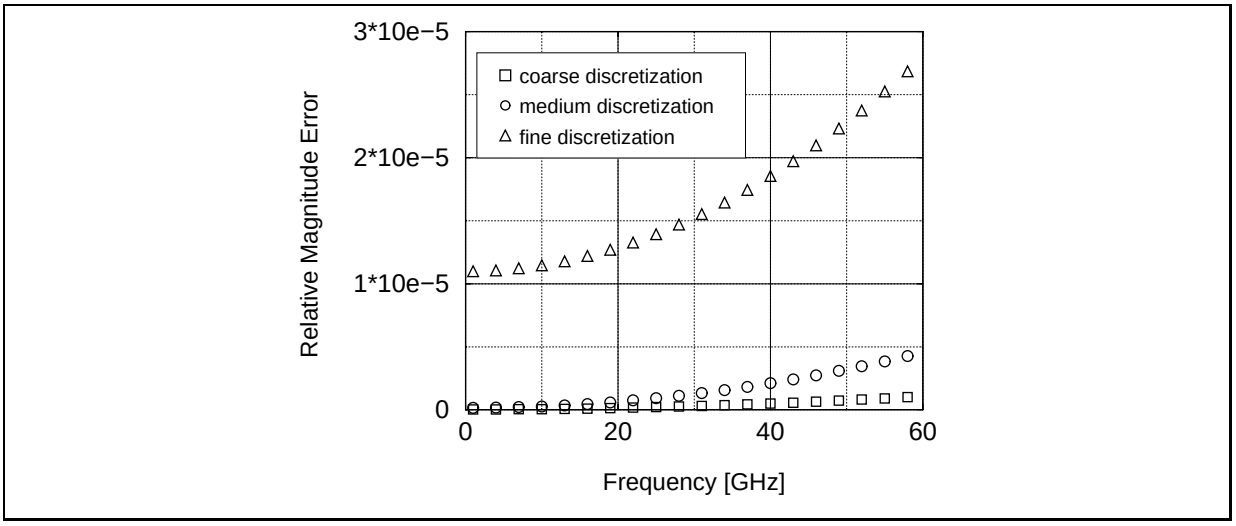

FIGURE 8.6. Relative magnitude error between solution obtained by equation (8.185) and a TLM simulation.

time was $\tau_0 = 1.0 \cdot 10^{-13}$ s. The structure was modelled by a one-dimensional row of TLM nodes, 30 for free space and 70 for the dielectric. A pulse of GAUSSian shape $\boldsymbol{E}_y(k\tau) = \boldsymbol{E}_{y0} \exp(-((k\tau - t_0)^2)/T^2)$ was launched onto the air-dielectric interface and the transient fields calculated. From these data, the complex reflection coefficient was evaluated. Magnitude and phase were then compared to the exact values given by the analytical expressions

$$|\Gamma_{ana}| = \left| \frac{1 - \sqrt{\varepsilon_r(\omega)}}{1 + \sqrt{\varepsilon_r(\omega)}} \right|, \tag{8.185}$$

$$\varphi_{ana} = \frac{\varepsilon''(\omega)}{\varepsilon'(\omega)}. \tag{8.186}$$

In Fig. 8.6 the relative error $||\Gamma_{ana}| - |\Gamma_{sim}|| \,/\, |\Gamma_{ana}|$ between the magnitude of

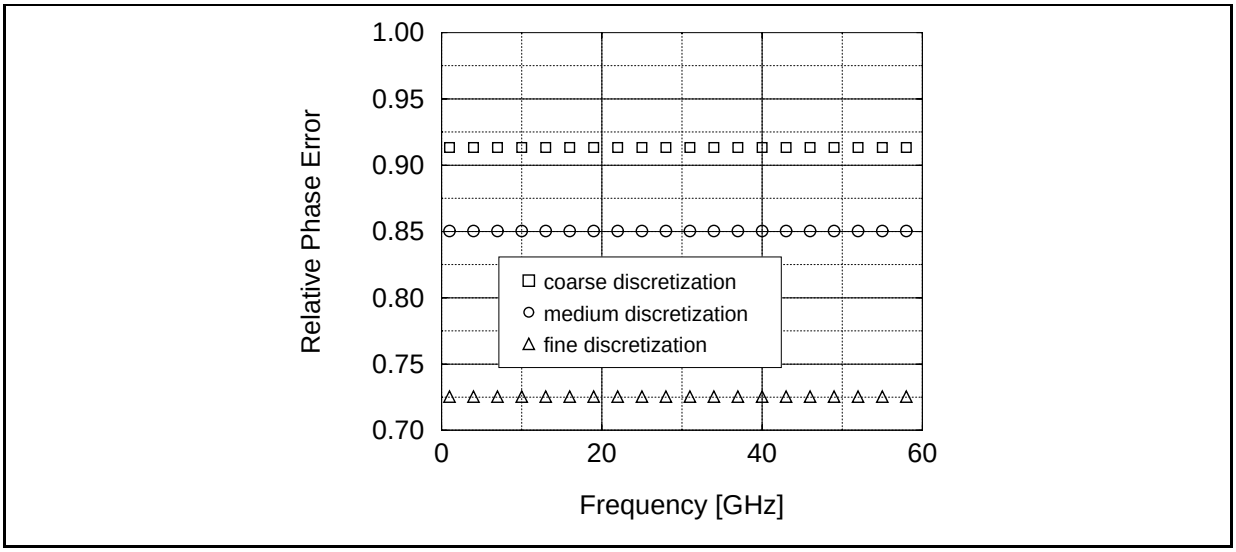

FIGURE 8.7. Relative phase error between solution obtained by equation (8.186) and a TLM simulation.

discretization	Δl [μm]	Δt [s]	T (pulse width) [Δt]
coarse	1.4	$0.2{\cdot}10^{-14}$	25
medium	0.7	$1.0{\cdot}10^{-15}$	50
fine	0.35	$0.5{\cdot}10^{-15}$	100

TABLE 8.2. The simulation parameters.

the reflection coefficient obtained from the TLM simulation, $|\Gamma_{sim}|$, and the exact values calculated using formula (8.185) is shown. Apparently, excellent agreement is found between the analytical and simulated solution, as the magnitude of the relative error is of the order of 10^{-5}. Surprisingly, the error increases with finer discretization. In contrast, Fig. 8.7 indicates that the relative phase error $|\varphi_{ana} - \varphi_{sim}| \,/\, |\varphi_{ana}|$ between the analytical solution given by equation (8.186) and the computed result using TLM, reduces as expected. The deviation of the phase of the TLM solution from the analytical solution is quite significant and can be explained as follows. In the analytical case, the interface between the two media is *exactly* defined. In the TLM mesh, the interface is *supposed* to be at the middle of two nodes. As the dispersion characteristics of the nodes at either side of the interface differ considerably, one does not know where to assume the exact interface plane. That this is indeed the case, can be seen when the relative phase errors for three different discretizations specified in Table 1 are compared. The finer the discretization, the lower is the relative phase error, as the interface

between the two media is better localized in the simulation. The increase of the magnitude error with finer discretization using more and smaller cells can be explained by neglecting the continuity conditions of the normal field components at the air-dielectric interface. In SCN-TLM, only continuity of the tangential field components is enforced at interfaces and boundaries.
Nevertheless, the SCN-TLM algorithm for dispersive media achieves excellent accuracy compared to other ways of implementing algorithms for dispersive media in TLM, such as [**61, 81**]. In none of these work, the error between simulated and exact solution was investigated. Therefore the influence of the normal continuity conditions at air dielectric interfaces on the accuracy of the approximation was not noticed.

CHAPTER 9

Characterization of Planar Microwave Components

1. Layered Absorbers for Mesh Truncation in Open Problems

A prerequisite for simulating planar microwave components in time domain using the SCN-TLM method is truncating the finite computational domain with absorbing boundary conditions. An improper mesh truncation results in back scattering of electromagnetic waves into the computational domain. These back scattered waves interfere with the propagating modes in the simulated structure such that they corrupt the field solution. Hence, the obtained time domain signals at the ports of the device contain artefacts and inhibit a proper calculation of the frequency domain S-parameters of the device under consideration. Eventually, this leads to a misinterpretation of the results of a simulation. For this, a number of different methods have been proposed to absorb electromagnetic waves that impinge on the boundaries of an open space problem [**8, 13, 40, 63, 68**]. Examples are boundary conditions obtained by discretizing one-way analytical conditions derived for the analytical wave equations [**63**] and TAYLOR's expansion of the plane wave solution [**13**]. Another approach is the use of discrete GREEN's functions [**40, 43**]. However, absorbing boundary conditions based on one-way analytical conditions often suffer from instabilities [**8**], which generally limit their applicability. Using GREEN's functions implies using large amounts of memory when regions with different media are to be truncated. Moreover, the calculation of the GREEN's function is not simple in case of inhomogeneous media, which further limit their use with respect to the analysis of planar circuits. However, they have been proved to be efficient in closed waveguide problems. Still, the simplest absorbing boundary condition is a matched load with $\Gamma = 0$, truncating the transmission lines of the TLM mesh that touch the boundary of the computational domain.

The best choice for truncating layered media, as they are encountered in planar microwave circuits appear to be layered absorbers. The principle setup of layered absorbers is shown in Fig. 9.1. The computational domain of the sketched microstrip line shall be truncated by a layered absorber in positive x-direction and negative y-direction. For this, each region of the boundary that truncates a region with different media parameters requires a number of stacked boxes in direction

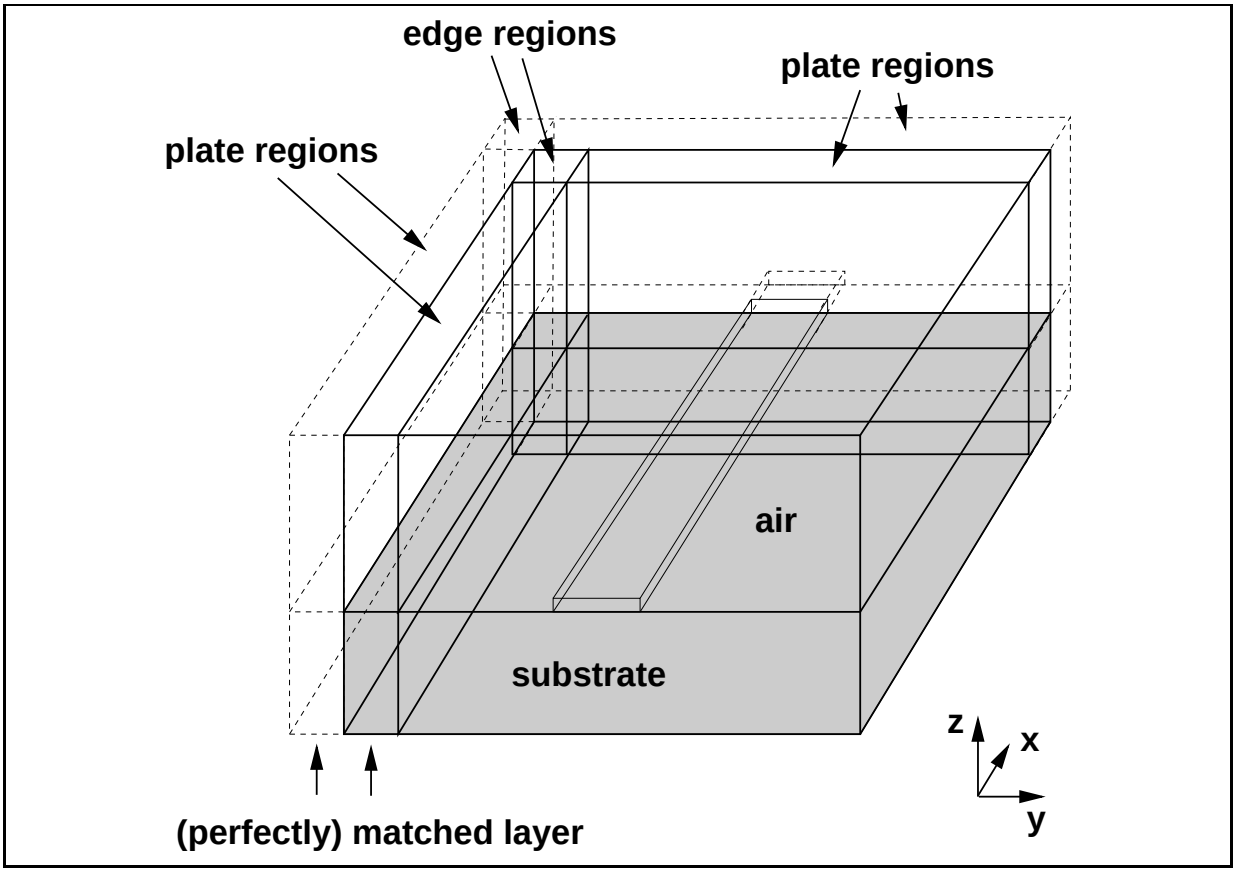

FIGURE 9.1. Principle of layered absorbers such as matched layer and perfectly matched layer.

of the outer normal. This is specified by *plate regions* in Fig. 9.1. At the edges of the computational domain these regions may intersect and require different parameter. Such regions of intersection are denoted as *edge regions*.

The first type of such absorbers are *matched layer* (ML), where the impedance of the absorbing medium matches the impedance of the medium to be truncated. Electric and magnetic losses are introduced to absorb the incident electromagnetic energy, such that this medium represents a MAXWELLian absorber. With respect to Fig. 9.1, the conductivity of the matched layers rise in outward direction normal to the boundary. One can specify isotropic or anisotropic conductivities requiring the specification of edge regions when two plate regions intersect, and corner regions, when three plate regions intersect.

The same principle applies to a second type of layered absorber, which has been introduced by BERENGER [**9**], recently. It constitutes an artificial medium known as *perfectly matched layer* (PML) that achieves a much better absorption than previously suggested absorbing boundary conditions. For the use with the TLM method with symmetrical condensed node, there have been different approaches of implementing the PML. The first reported use of PML in TLM was

given by ESWARAPPA and HOEFER, where a FDTD implementation of PML was interfaced with the TLM computational domain [**19**]. A modified SCN simulating PML media was proposed by DUBARD and POMPEI [**17**]. Although the authors report various applications to three-dimensional antenna problems, it seems that this TLM PML node is numerically extremely critical, which limits its practical use tremendously, especially when the PML layers are supposed to truncated layered inhomogeneous media [**54, 78**]. Very recently, an improved TLM PML node that exhibits much improved stability was proposed by LEMAGUER and NEY. In addition, this PML-SCN is able to absorb also evanescent waves [**54**]. As the implementations of PML in TLM still suffer from instabilities, the use of the unconditionally stable matched layer was preferred.

1.1. Implementation of Matched Layer Generator. Recalling Fig. 9.1, it is obvious that for practical problems, such as characterizing planar structures described in [**57, 112**], the specification of the matched or perfectly matched layer parameters and computational regions has to be automatized. A manual calculation of the required parameters is impracticable, as realistic problems, such as the transformers described in a later section, involve about 3000 different computational regions within a single TLM mesh. For this, an automatic matched and perfectly matched layer generator was implemented in the TLM program. It allows the specification of arbitrary conductivity profiles and theoretical reflection coefficients from the truncated boundary, which in turn automatically calculates the necessary parameters for the SCN of the respective region. This matched layer generator can of course equally be utilized for specifying PML absorbers.

1.2. Optimization of Matched Layer Absorbers. The conductivity profile in the matched layer is given according to

$$\sigma(L) = \sigma_{max}\left(\frac{L}{N}\right)^{p}, \tag{9.1}$$

where σ_{max} denotes the maximum matched layer electric conductivity at the outer layer N of the matched layer, $L \in 1, ..., N$ denotes the index of the matched layer. The maximum conductivity is calculated according to

$$\sigma_{max} = -\frac{a_{red}(p+1)\ln(R_0)}{2N\Delta l Z_0}, \tag{9.2}$$

with R_0 being the theoretical reflection coefficient when the matched layer absorber is terminated by an electric wall and Z_0 being the free space impedance. Using a constant $a_{red} = 1.0$ results in conductivity values that change the dispersion in neighbouring layers with different media parameters such that a worse absorption is achieved in contrast to using lower conductivity values [**78**]. A value of $a_{red} = 0.1$ performs much better thus reducing the differences in dispersion between neighbouring layers. In layered media, the matched condition is as follows

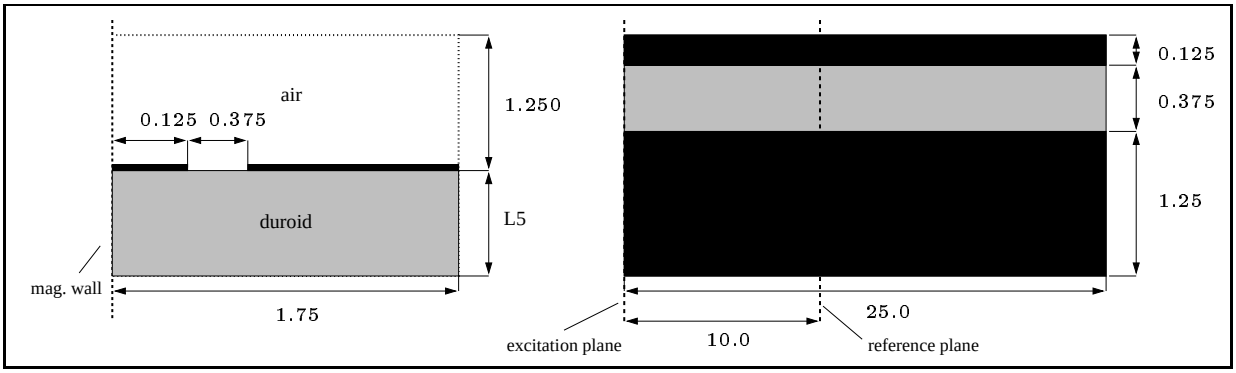

FIGURE 9.2. Details of the test coplanar waveguide used for optimizing the matched layer absorber. All dimensions are in the mm range. Cubic cells with $\Delta l = 0.125$ mm were used. The discretization is analogous to the CPW presented in [**68**].

$$\frac{\sigma_e^i}{\varepsilon^i} = \frac{\sigma_m^i}{\mu^i} = \frac{\sigma_e^{i+1}}{\varepsilon^{i+1}} = \frac{\sigma_m^{i+1}}{\mu^{i+1}} = \cdots. \tag{9.3}$$

Although there are some rules of thumb reported in the literature for choosing the parameters to get optimum absorption from ML absorbers [**68**], no comprehensive investigation on the optimum parameter combination has been presented yet. For this, the return loss of a coplanar waveguide truncated with different number of matched layers for various conductivity profiles and theoretical reflection coefficients is studied. The geometry and the dimensions of the test CPW line is depicted in Fig. 9.2.

It turns out that the optimum conductivity profile depends on the number of matched layers. In the cases of 5 and 10 matched layers, a linear conductivity profile gives the best results in terms of minimum return loss, whereas for 15 matched layers, a steep profile with $p = 2.4$ yields the best results [**78**]. For the optimum parameter combination the theoretical reflection coefficient is found to be $1.0 \cdot 10^{-4}$. A graph of the optimum return loss curves for each layer thickness is shown in Fig. 9.3, where the return loss is compared to that of a simple matched load. The influence of the conductivity profile, expressed by the exponential coefficient p in eqn. (9.1), on the absorption for three different layer thicknesses, i.e. 5, 10, and 15 matched layers is investigated. In each case the profile coefficient is varied from $p = 1.0$ to $p = 1.2, 1.5, 1.8, 2.0, 2.2, 2.4$. The maximum conductivity is in each case varied by setting $R_0 = 1.0^{-2}, 1.0^{-4}, 1.0^{-6}, 1.0^{-8}$. The ML is always terminated with a matched load.

First, we want to compare the return loss curves for the CPW on a substrate with $\varepsilon_r = 9.9$ obtained using 5 matched layers (see Fig. 9.4 to 9.7). Surprisingly, the difference between curves with different profile coefficient is less pronounced

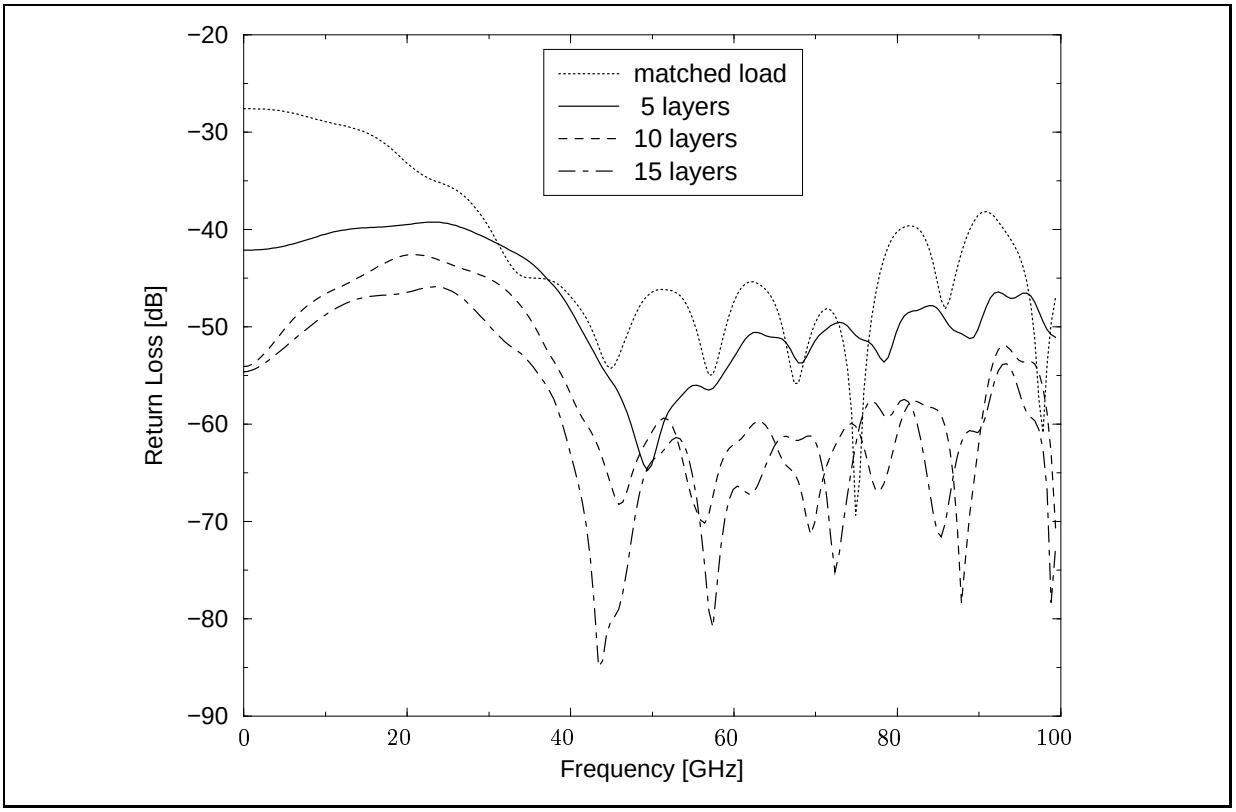

FIGURE 9.3. Minimum return loss curves for 5, 10 and 15 layers ML compared to matched load termination for CPW on substrate with $\varepsilon = 9.9$. For each ML thickness $R_0 = 1.0^{-4}$ yielded the best result. The profile coefficients are $p = 1.0$ for 5 and 10 ML and $p = 2.4$ for 15 ML.

as previously expected. Below 20 GHz, a difference of only ± 1 dB can be recognized for different profiles. Interestingly, if R_0 is chosen too low, i.e. $\sim 1.0^{-2}$, the return loss is only 5 dB less than the one obtained by using only a matched load termination (see Fig.9.4). By inspecting Fig. 9.4 to 9.7, one can find the optimum combination of parameters of the ML with 5 layers as $R_0 = 1.0^{-4}$ and $p = 1.0$ in Fig. 9.5. This parameter combination gives a uniform return loss of at least -40 dB up to 20 GHz.

Increasing the number of ML to 10 results in a return loss of almost -50 dB up to 10 GHz and -43 dB up to 20 GHz for the optimum parameter combination $R_0 = 1.0^{-4}$ and $p = 1.0$, which can be found from Fig. 9.9. Again, if R_0 is chosen too low, as depicted in Fig. 9.8, the return loss is only about 10 dB better then when using a matched load termination. Compared to using 5 matched layers, the influence of the profile coefficient p is more pronounced, which is evident when looking at Fig. 9.9 to 9.11. This is particularly the case when choosing $R_0 = 1.0^{-4}$, where varying p results in a ± 3 dB change in return loss in the 0-10 GHz region.

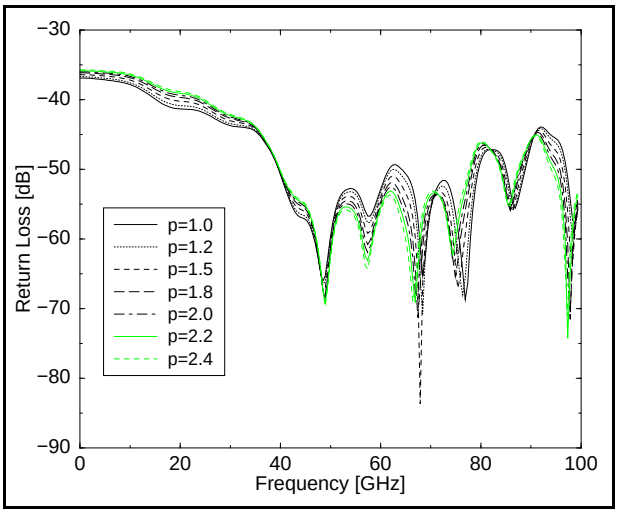

FIGURE 9.4. Return loss for 5 ML with $R_0 = 1.0^{-2}$ for CPW on substrate with $\varepsilon_r = 9.9$.

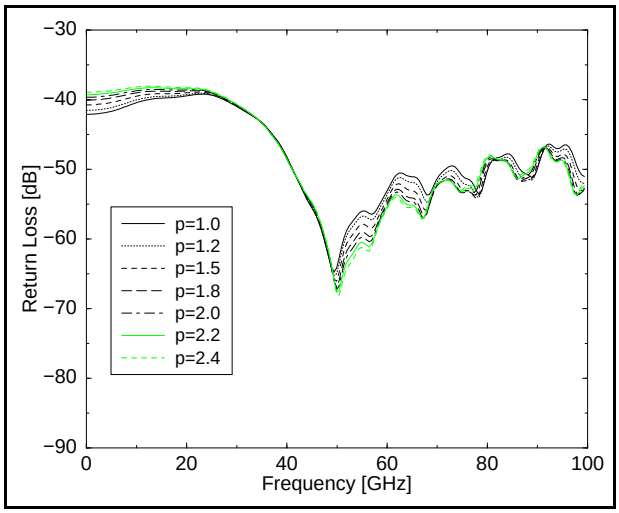

FIGURE 9.5. Return loss for 5 ML with $R_0 = 1.0^{-4}$ for CPW on substrate with $\varepsilon_r = 9.9$.

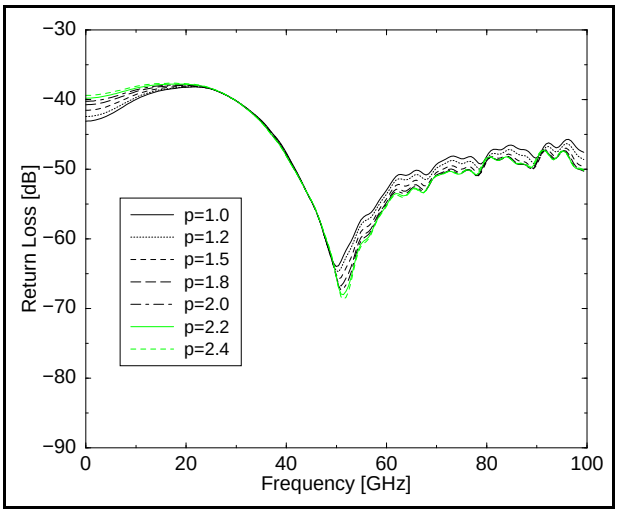

FIGURE 9.6. Return loss for 5 ML with $R_0 = 1.0^{-6}$ for CPW on substrate with $\varepsilon_r = 9.9$.

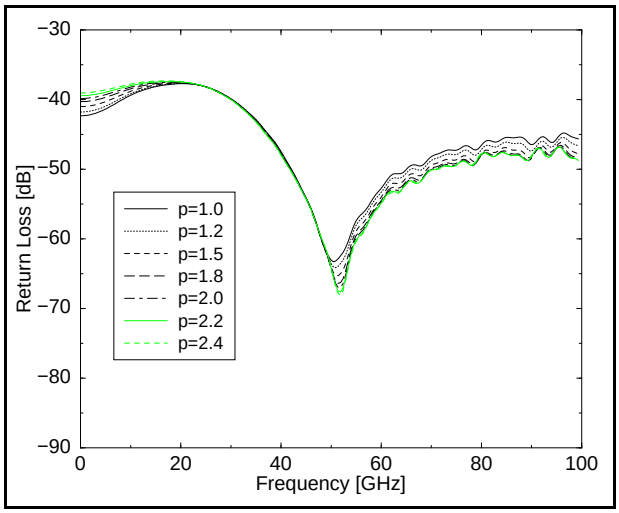

FIGURE 9.7. Return loss for 5 ML with $R_0 = 1.0^{-8}$ for CPW on substrate with $\varepsilon_r = 9.9$.

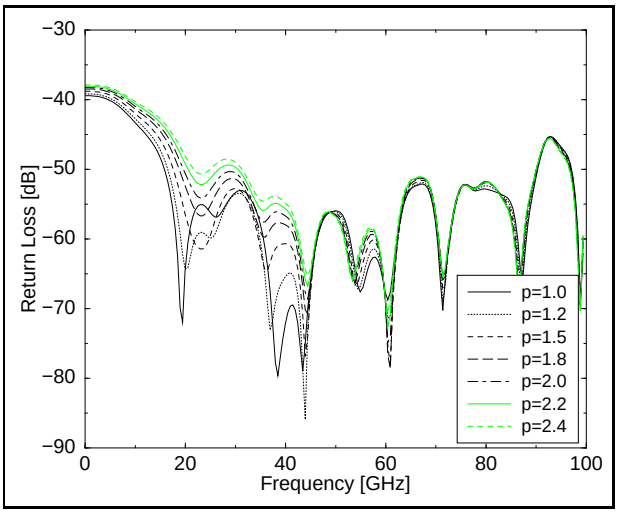

FIGURE 9.8. Return loss for 10 ML with $R_0 = 1.0^{-2}$ for CPW on substrate with $\varepsilon_r = 9.9$.

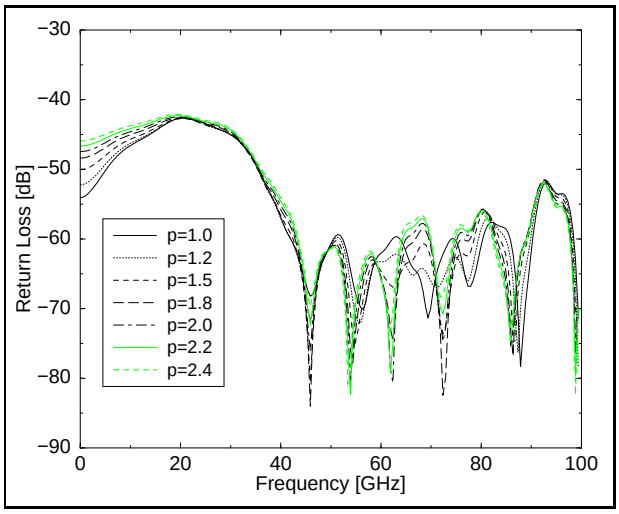

FIGURE 9.9. Return loss for 10 ML with $R_0 = 1.0^{-4}$ for CPW on substrate with $\varepsilon_r = 9.9$.

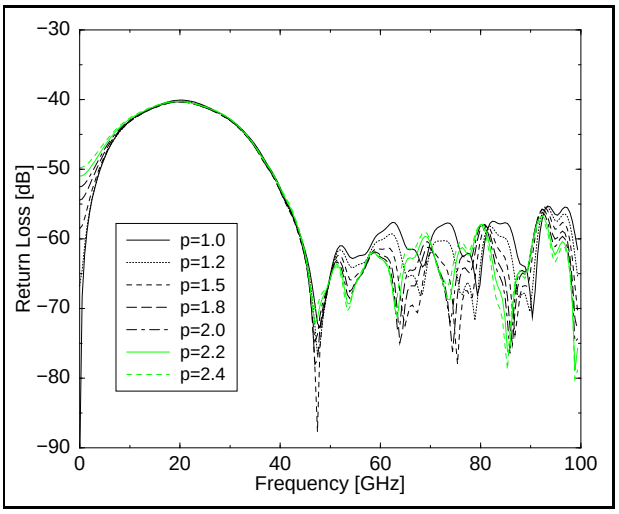

FIGURE 9.10. Return loss for 10 ML with $R_0 = 1.0^{-6}$ for CPW on substrate with $\varepsilon_r = 9.9$.

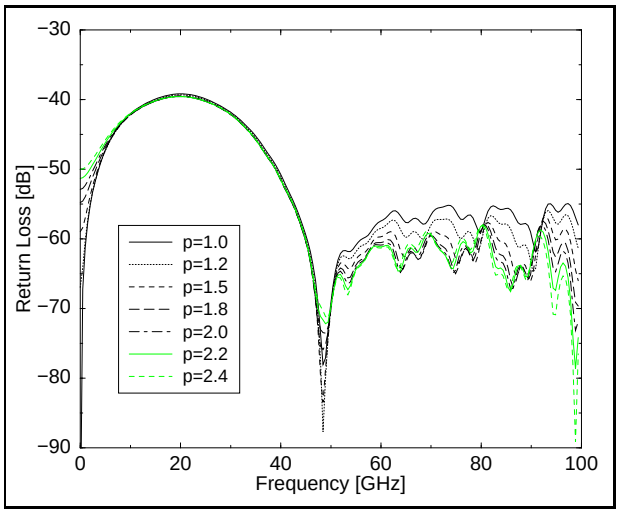

FIGURE 9.11. Return loss for 10 ML with $R_0 = 1.0^{-8}$ for CPW on substrate with $\varepsilon_r = 9.9$.

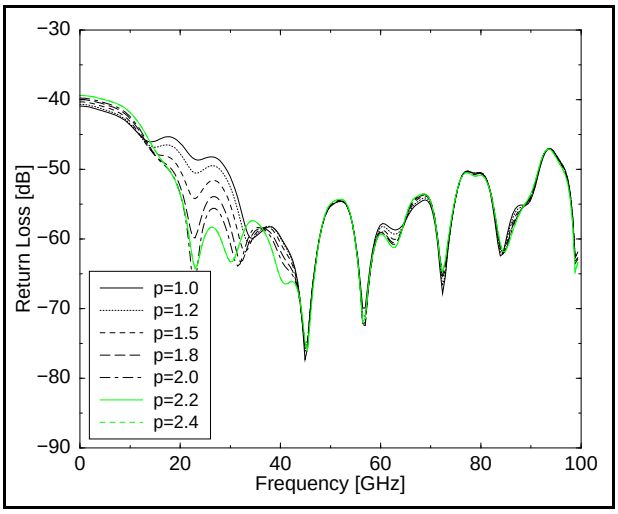

FIGURE 9.12. Return loss for 15 ML with $R_0 = 1.0^{-2}$ for CPW on substrate with $\varepsilon_r = 9.9$.

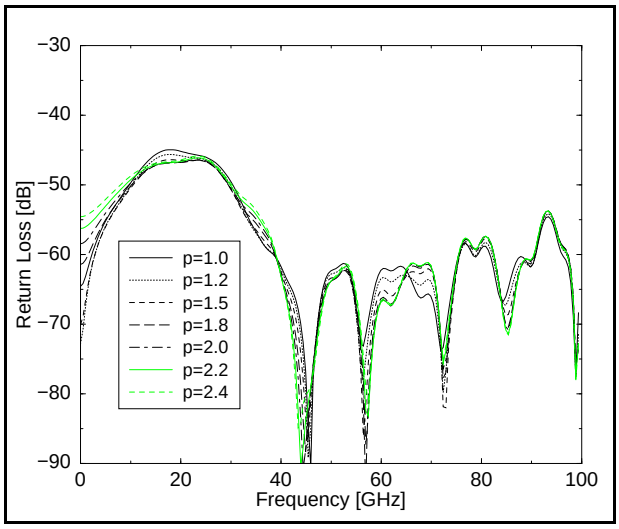

FIGURE 9.13. Return loss for 15 ML with $R_0 = 1.0^{-4}$ for CPW on substrate with $\varepsilon_r = 9.9$.

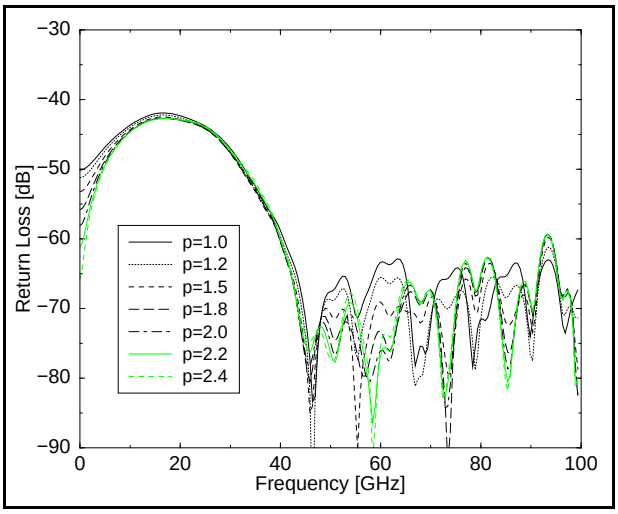

FIGURE 9.14. Return loss for 15 ML with $R_0 = 1.0^{-6}$ for CPW on substrate with $\varepsilon_r = 9.9$.

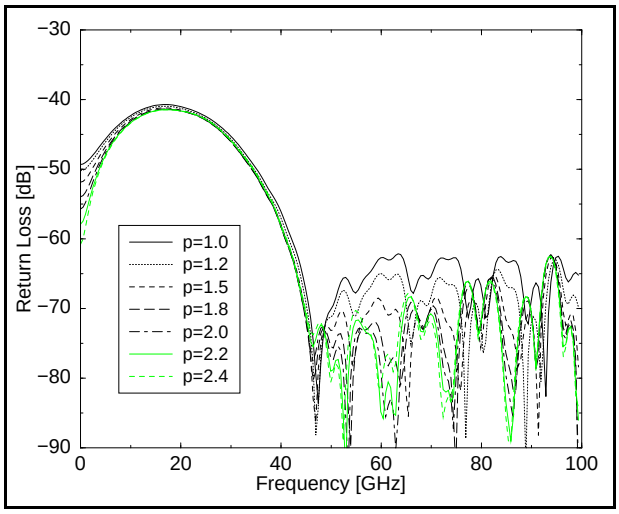

FIGURE 9.15. Return loss for 15 ML with $R_0 = 1.0^{-8}$ for CPW on substrate with $\varepsilon_r = 9.9$.

A similar picture is generated when 15 layers ML are used. Comparing Fig. 9.12 to 9.15 indicates that only for $R_0 = 1.0^{-4}$ the profile coefficient p has a pronounced influence on the return loss in the low frequency region. Again, the 'best' return loss up to 20 GHz is achieved for $R_0 = 1.0^{-4}$. However, using a steeper profile with $p = 2.4$ gives the lowest overall return loss of almost below -57 dB up to 20 GHz.

Looking at the return loss curves for the CPW on a substrate with approximately half the dielectric constant, i.e. $\varepsilon_r = 5.0$ (see Fig. 9.16 to 9.18), one immediately realizes that the more or less uniform low frequency absorption region extends up to approximately 40 GHz. The absorption of the 5, 10, and 15 ML was investigated for $R_0 = 1.0^{-4}$ and the previously mentioned values of p. Interestingly, for 5 and 10 ML a linear profile, i.e. $p = 1.0$, yields the most uniform absorption, whereas in case of 15 ML a profile with $p = 2.4$ yields again the most uniform absorption.

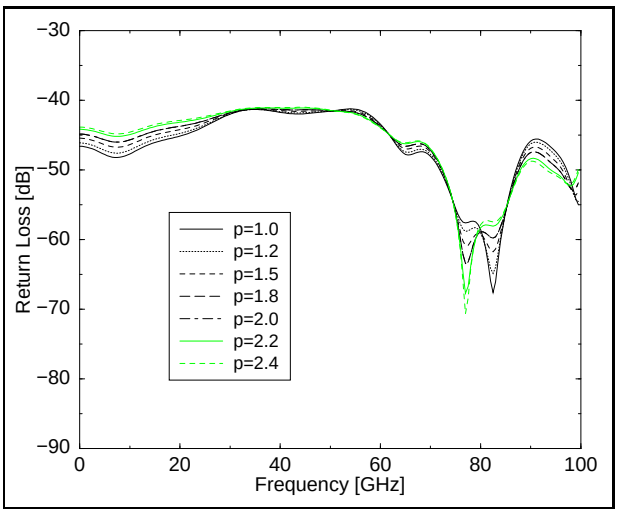

FIGURE 9.16. Return loss for 5 ML with $R_0 = 1.0^{-4}$ for CPW on substrate with $\varepsilon_r = 5.0$.

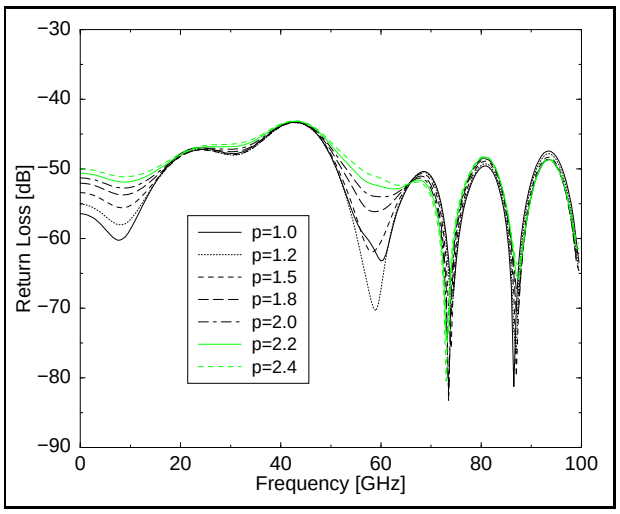

FIGURE 9.17. Return loss for 10 ML with $R_0 = 1.0^{-4}$ for CPW on substrate with $\varepsilon_r = 5.0$.

In Fig. 9.19 to 9.21, the return losses for the CPWs on the two substrates with identical ML parameters are compared. It is evident that the media parameters of the substrate have a distinct influence on the performance of the ML absorber. For the CPW with $\varepsilon_r = 5.0$ substrate, the absorption in the lower frequency region up to 40 GHz is much better when compared to the return loss for the CPW on a substrate with $\varepsilon_r = 9.9$. In the latter case, the absorption in the upper frequency region is better. This shows that the main source of reflection in the matched layer does not originate from parasitic numerical reflections due to the

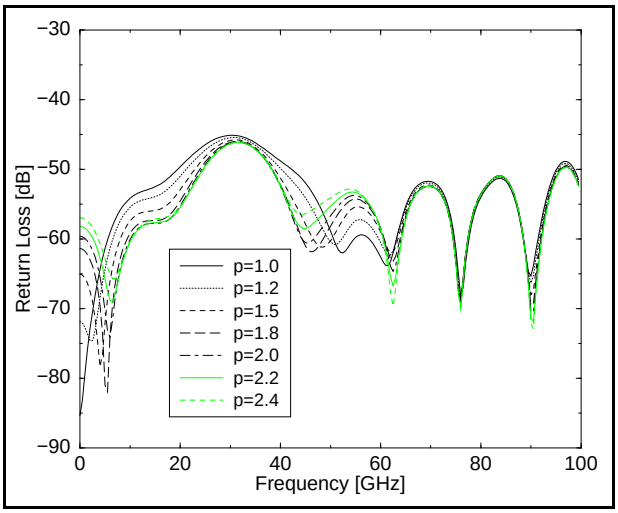

FIGURE 9.18. Return loss for 15 ML with $R_0 = 1.0^{-4}$ for CPW on substrate with $\varepsilon_r = 5.0$.

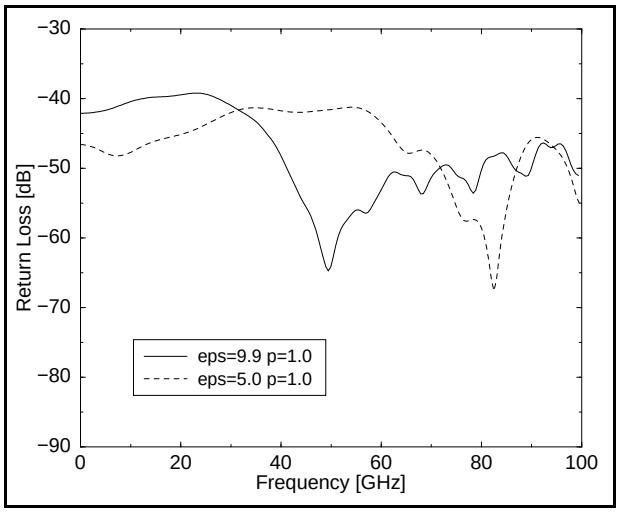

FIGURE 9.19. Comparison of return loss for 5 ML with $R_0 = 1.0^{-4}$ for CPW on substrates of $\varepsilon_r = 5.0$ and $\varepsilon_r = 9.9$.

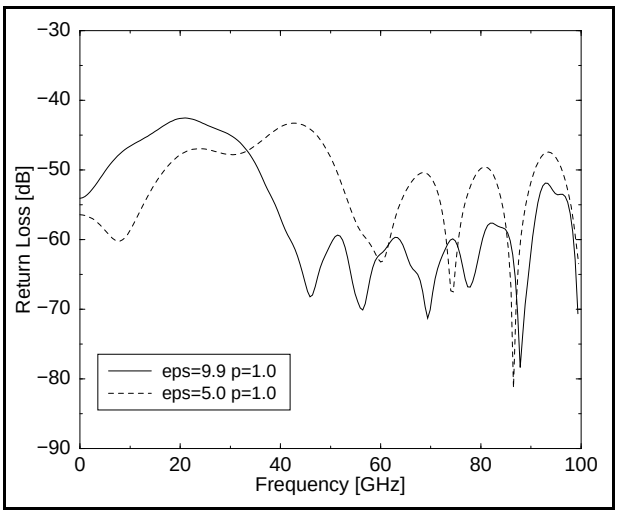

FIGURE 9.20. Comparison of return loss for 10 ML with $R_0 = 1.0^{-4}$ and $p = 1.0$ for CPW on substrates of $\varepsilon_r = 5.0$ and $\varepsilon_r = 9.9$.

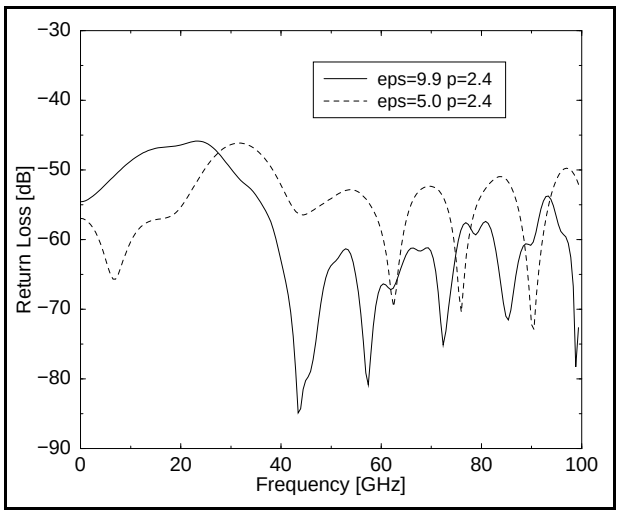

FIGURE 9.21. Comparison of return loss for 15 ML with $R_0 = 1.0^{-4}$ and $p = 2.4$ for CPW on substrates of $\varepsilon_r = 5.0$ and $\varepsilon_r = 9.9$.

abrupt change in conductivity, but from the differing dispersion in neighbouring media with different media parameters.

2. Dielectric Losses in Multichip Module Interconnects

2.1. Multilayer Multichip Modules for Microwave Applications. Multichip modules (MCM) combine several integrated circuits on a specially designed substrate. This allows integrating devices and monolithic integrated subcircuits based on different material systems and from various processing technologies into a single system. Therefore, the MCM technology offers an integration technology for future low-cost mobile communication systems in the millimetre-wave frequency bands that is as reliable, cheap, and small in dimensions as common monolithic integration technology. This is particularly interesting if extremely low noise figures are desired, thus GaAs devices can be incorporated into the system. The highest integration density is achieved by thin film multilayer structures on ceramic, silicon or metal.

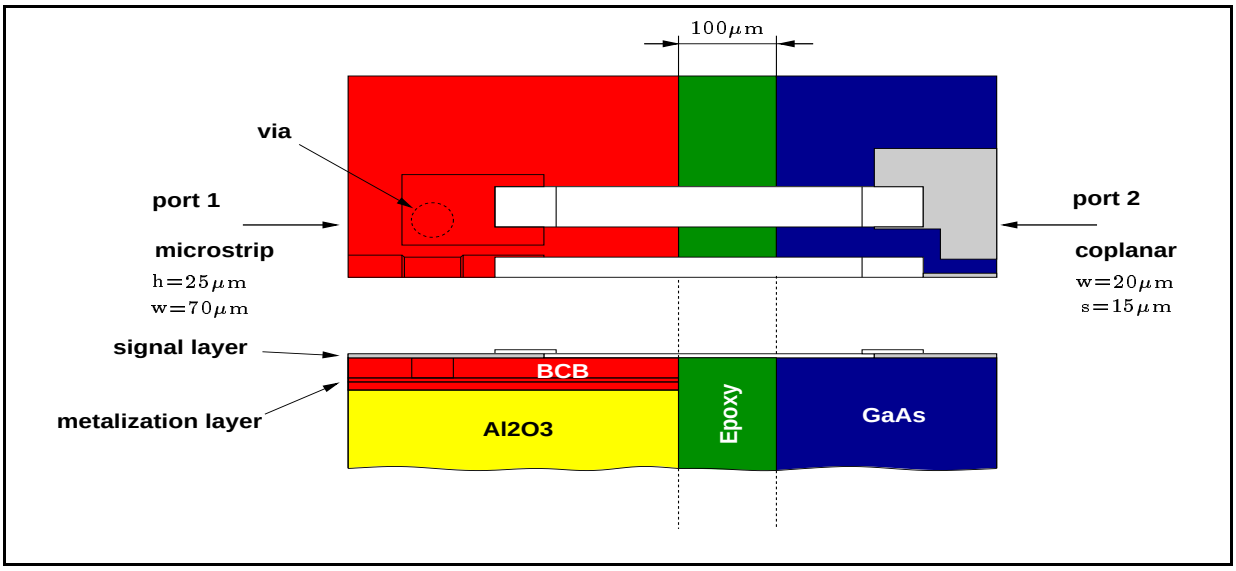

FIGURE 9.22. Schematic layout of microstrip to coplanar MCM substrate chip interconnect in chip-last technology. Only one half of the structure is shown.

A special MCM for high frequency applications was reported in [**58**]. In this technology, bare dice are directly integrated into substrate openings. The interconnection and wiring system is fabricated using thin film technology on the planar chip/substrate surface. This configuration allows short interconnections between chip and substrate, a planar topology, and a high integration density. Furthermore, all transmission lines can be realized with a controlled impedance.

To embed active or passive components in thin film multilayer structures, two mounting principles have been developed [**58**]. In the *chip-first* technology, the chips are mounted into openings in the MCM substrate. The wiring and the interconnects are fabricated by depositing the metalization on top of a first polymer

layer that covers chips and substrate. In order to contact the embedded chips with the first metalization layer, via holes are opened up photolithographically in the photosensitive polymer film. The first metalization layer is deposited by sputtering and electroplating using a photoresist mask. The second polymer layer is deposited with a thickness of 25 micron. Finally, the second metalization layer is sputtered and structured in adjustment to the first metalization layer. In the *chip-last* technology, the thin film wiring is realized on the substrate before the chips are embedded into the substrate. The interconnects from the substrate to the embedded chips are achieved by a final thin film metalization.

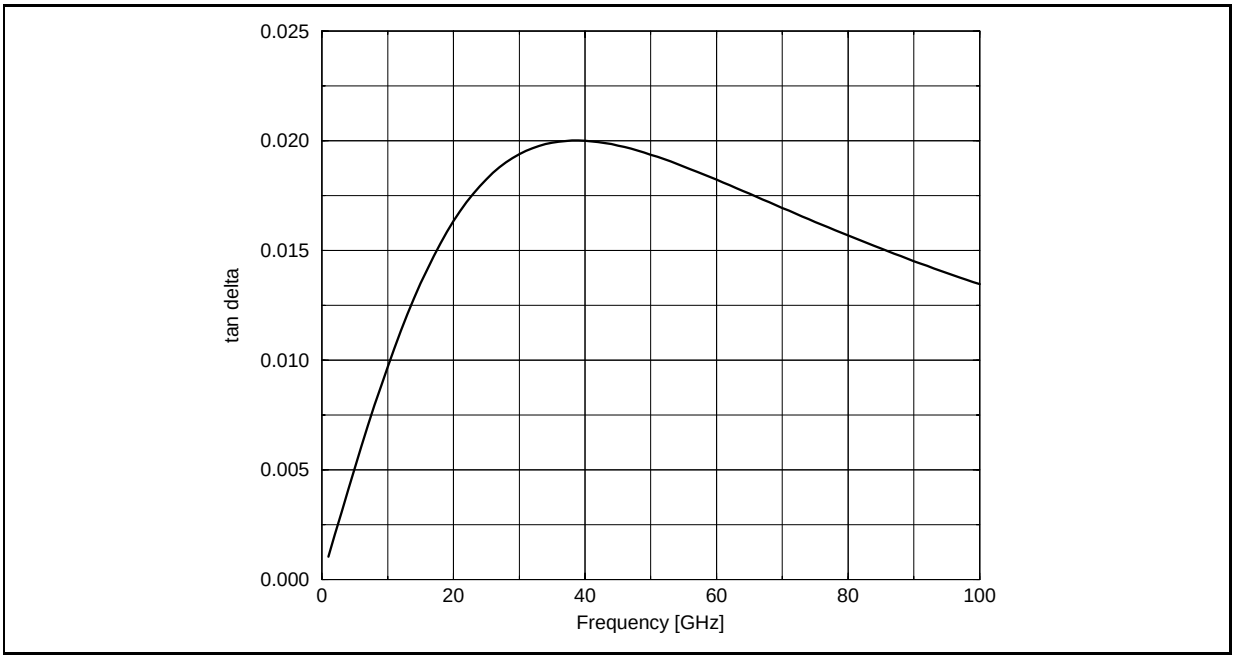

FIGURE 9.23. Graph of tanδ versus frequency for $\tau_d = 4.2 \cdot 10^{-12}$s, $\varepsilon_s = 5.1$, and $\varepsilon_\infty = 4.9$.

The thin film metalization is based on a Ti:W/Cu (100 nm/200 nm) tie layer that is electroplated using a photoresist mask. The metalization is 5 microns thick. To interconnect different chips and passive components on the carrier substrate, microstrip and coplanar waveguides are promising, as they are highly reproducible. Chip connections are preferably realized using coplanar waveguides, whereas microstrip wiring can be used for interconnecting the remaining parts of the MCM. However, reflections at such transmission line discontinuities cannot be neglected at higher frequencies. The adhesive that holds a chip in the substrate lies directly underneath the chip-substrate interconnect. As the employed adhesive has highly dispersive properties, it might influence the transmission properties in an unknown manner. The influence of the dispersive adhesive on the transmission properties

of the microstrip-to-coplanar interconnect are determined in this section. For this, the parameters for describing the dispersive properties of the adhesive system by a DEBYE Model are estimated and the transmission characteristics of an MCM interconnect in chip-last technology are investigated. The interconnect is shown in Fig. 9.22. An exact layout with all dimensions in the μm range can be found in Appendix E. A comparison of the transmission characteristics with and without dispersive losses is presented.

2.2. Parameter Estimation for Dielectric Losses of Adhesive. Although dispersive dielectric materials are frequently used in microwave applications, precise data on their characteristic parameters such as permittivity and loss tangent are not available. Especially for epoxy based adhesives no data are available. Therefore, we estimate parameters for a worst case loss tangent function following a DEBYE model. A loss tangent value of 0.01 at 1 GHz for printed circuit boards consisting mainly of epoxy was given in [**109**]. With this value, we want to estimate parameters for the worst case loss tangent function. Plotting eqn. 8.7 versus frequency for the parameters $\tau_d = 4.2 \cdot 10^{-12}$ s, $\varepsilon_s = 5.1$, and $\varepsilon_\infty = 4.9$ yields a sensible estimation of the true loss tangent curve of pure epoxy. A plot of this estimated loss tangent function can be found in Fig. 9.23.

2.3. Transmission Properties of MCM Interconnects. The TLM simulation of the MCM interconnect involved the following parameters. The irregularly graded mesh comprised 264×79×93 or 1939608 cells and the structure was discretized as follows, written in the number of cells (N) per section in μm (W), as $N_1 : W_1, N_2 : W_2, ..., N_n : W_n$. In x-direction, we have 60:380, 52:260, 25:160, 16:100, 8:50, 34:170, 60:380, 9:57 cells per section, in y-direction 3:10, 6:18, 1:4, 11:33, 4:14, 9:51.5, 8:26, 7:43.5, 30:200 cells per section, and in z-direction 19:129, 2:10, 2:10, 5:1, 8:25, 1:5, 1:5, 20:5, 20:120, 15:100 cells per section. The basic cell size was 3 μm. The simulation was run for 30000 iterations. The interconnect was excited from the MCM-substrate side. For this, the E^z field component was excited in the microstrip line using a GAUSSian transient. Two simulations were performed, one with lossless adhesive and one considering dielectric losses according to a DEBYE model with the parameters estimated in the previous section. For considering these frequency dependent losses of the adhesive, the TLM algorithm derived in the previous chapter was employed. All conductors were treated as ideally conducting. The parameters of the TLM simulation are summarized in Table 9.1.

In Fig. 9.24 the voltage at the input and at the output of the MCM microstrip-to-coplanar waveguide interconnect is shown. The top graph shows the voltage in the microstrip line considered as input and the bottom graph shows the voltage in the coplanar line on the GaAs chip considered as output. The solid line refers to the signals obtained from the simulation with lossless adhesive, and the dashed line refers to the case of considering dielectric losses. From a model simulation of a sole

TLM model of MCM interconnect	
iterations	30000
total mesh size	264×79×93 = 1939608 cells
mesh grading (x)	60:380, 52:260, 25:160, 16:100, 8:50, 34:170, 60:380, 9:57
mesh grading (y)	3:10, 6:18, 1:4, 11:33, 4:14, 9:51.5, 8:26, 7:43.5, 30:200
mesh grading (z)	19:129, 2:10, 2:10, 5:1, 8:25, 1:5, 1:5, 20:5, 20:120, 15:100
basic Δl	3 μm
Δt	$1.92 \cdot 10^{-15}$ s
h (stability factor)	5.2
ABC	matched load
Excitation	E^z beneath microstrip

TABLE 9.1. Parameters of TLM simulation of MCM interconnect.

microstrip line running directly through the gap filled with the epoxy adhesive and through the GaAs chip (which does *not* reflect any physical situation), the nature of the second largest peak in the input voltage could be identified. It originates from the reflection of the microstrip mode at the BCB-epoxy interface, when the open running microstrip is terminated by the epoxy adhesive. Note that in case of dielectric losses, the reflection is lower indicating 'loss impedance matching' to a certain degree, as some of the energy of the incoming pulse is absorbed by the adhesive. The output signal in the coplanar line does show a slightly higher amplitude as a consequence of the loss impedance matching (see bottom graph in Fig. 9.24).

By a reference simulation of the pure input signal on the microstrip line, the S-parameters of the interconnect could be calculated. As the slot of the coplanar output line was only discretized with three cells in transverse direction, the field was not modelled very accurately in the slot. For this, the voltage that was obtained by integrating the transverse E-field was calculated slightly incorrectly. This could be seen in a constant DC-offset in the transmission factor S21. As the input voltage and the output voltage must be the same in the lossless case, a correction factor for the voltage at the output could be calculated. Using this correction, the transmission factor was evaluated and a graph of S21 versus Frequency is shown in Fig. 9.25. The lossy epoxy adhesive seems to have virtually no effect on the transmission properties of the interconnect. Interestingly, the transmission properties are even slightly better in case of the dielectric losses being caused by a better termination of the open microstrip line as a consequence of the lossy adhesive. However, the deviation is very small, at 75 GHz it is about

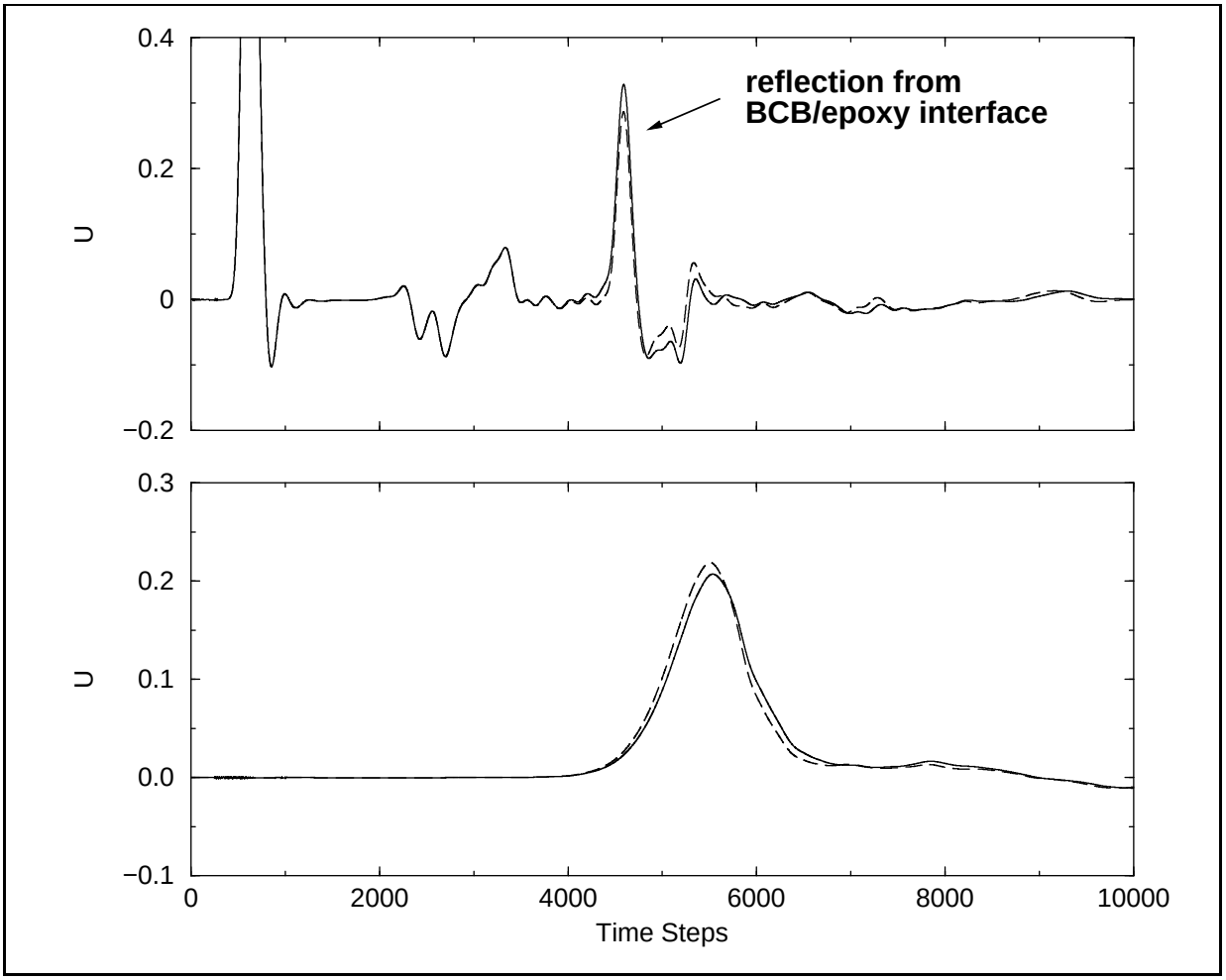

FIGURE 9.24. The voltage in the microstrip line (input) of the MCM microstrip-to-coplanar waveguide interconnect is shown in the graph at the top. The bottom graph shows the voltage at the output in the coplanar line on the GaAs chip.

0.3 dB. To get the complete picture, the return loss is plotted versus frequency up to 200 GHz together with the transmission factor in Fig. 9.26. Comparing the S-parameters for lossless and lossy adhesive, the return loss S11 shows a more pronounced deviation from the lossless case than the S21 curve. The difference is of the order of 2 to 3 dB up to 130 GHz. The return loss is higher in the lossy case clearly indicating that a lossy epoxy adhesive represents a better termination of the open running microstrip.

To illustrate the unsatisfactory termination of the input microstrip line, a three-dimensional field plot of the E^z field is shown for various time steps in Fig. 9.27(a)-(d). In (a), the leading edge of the pulse is just on the brink of hitting the interface. In (b) one can recognize a spherical wave radiating into the gap caused by diffraction at the edge of the finite ground plane of the open microstrip

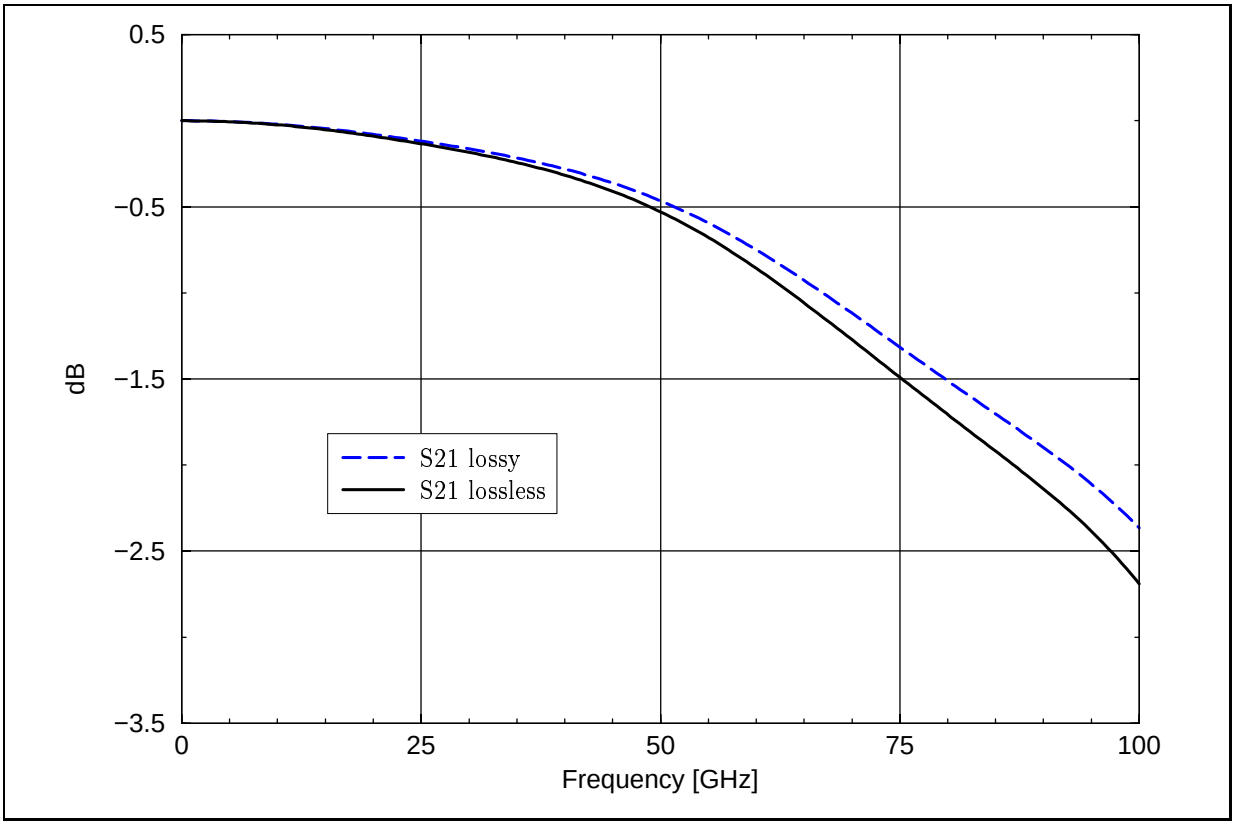

FIGURE 9.25. Transmission factor S21 of the MCM interconnect for lossless and lossy adhesive.

line. Some iterations later, the pulse is already coupling into the coplanar line and the back scattered wave is clearly visible, which can be seen in (c). The final plot (d) shows the pulse travelling in the coplanar line and also the propagation of the reflected wave is clearly discernible.

Summarizing the results of this investigation, it has become evident that the dielectric losses of the epoxy adhesive have very little effect on the transmission characteristics of this MCM interconnect. The presence of losses in the epoxy adhesive even improves the termination of the open running microstrip line as a consequence of loss impedance matching. This investigation has also shown that one can characterize MCM interconnect structures without considering the dispersive losses of the materials constituting such interconnect structures. In turn, neglecting dielectric losses allows using a more efficient TLM code, which produces faster results. Moreover, this study has indicated that the transmission properties of MCM interconnects can be enhanced by optimizing the termination of the open running microstrip line that interfaces the epoxy adhesive.

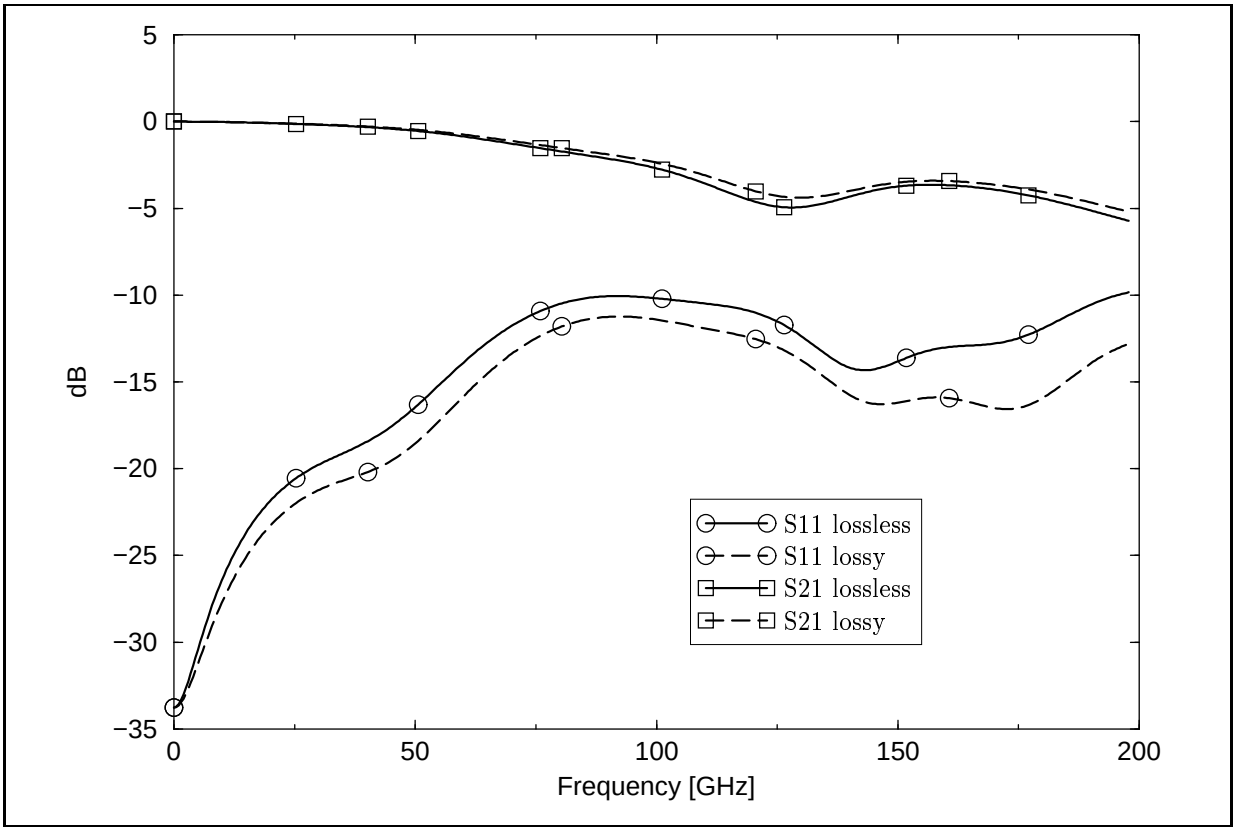

FIGURE 9.26. Return loss and transmission factor of the MCM interconnect for lossless and lossy adhesive.

3. Characterization of Planar Microwave Transformers

Low cost and highly efficient RF power amplifiers with high output power at low supply voltages around 3 V are required in mobile communication applications. Such a monolithic integrated RF power amplifier in silicon technology was presented in [**91**]. It yields 5 W output power at 0.8-1 GHz and achieves 59 % maximum efficiency. It operates at voltages of 2.5-4.5 V. The linear gain is 36 dB. The amplifier is based on the 25 GHz-f_T silicon bipolar technology SIEMENS B6HF. This process uses 0.8 μm lithography and LOCOS isolation and a 3-layer aluminium metalization. A balanced 2-stage circuit design is utilized. The RF part of the balanced 2-stage power amplifier consists of an on-chip transformer as input balun, a driver stage, two transformers as interstage matching network and a power output stage. The input transformer acts as a balun and represents also a matching network. Two further transformers with a turn ratio of N=5:2 act as an interstage matching network. A three-dimensional view of these interstage transformers can be found in Fig. 9.29. They measure 274×274 μm^2. Using transformers in power amplifier design has a number of advantages. For example, using a transformer at the input, allows no restrictions to the external DC potential

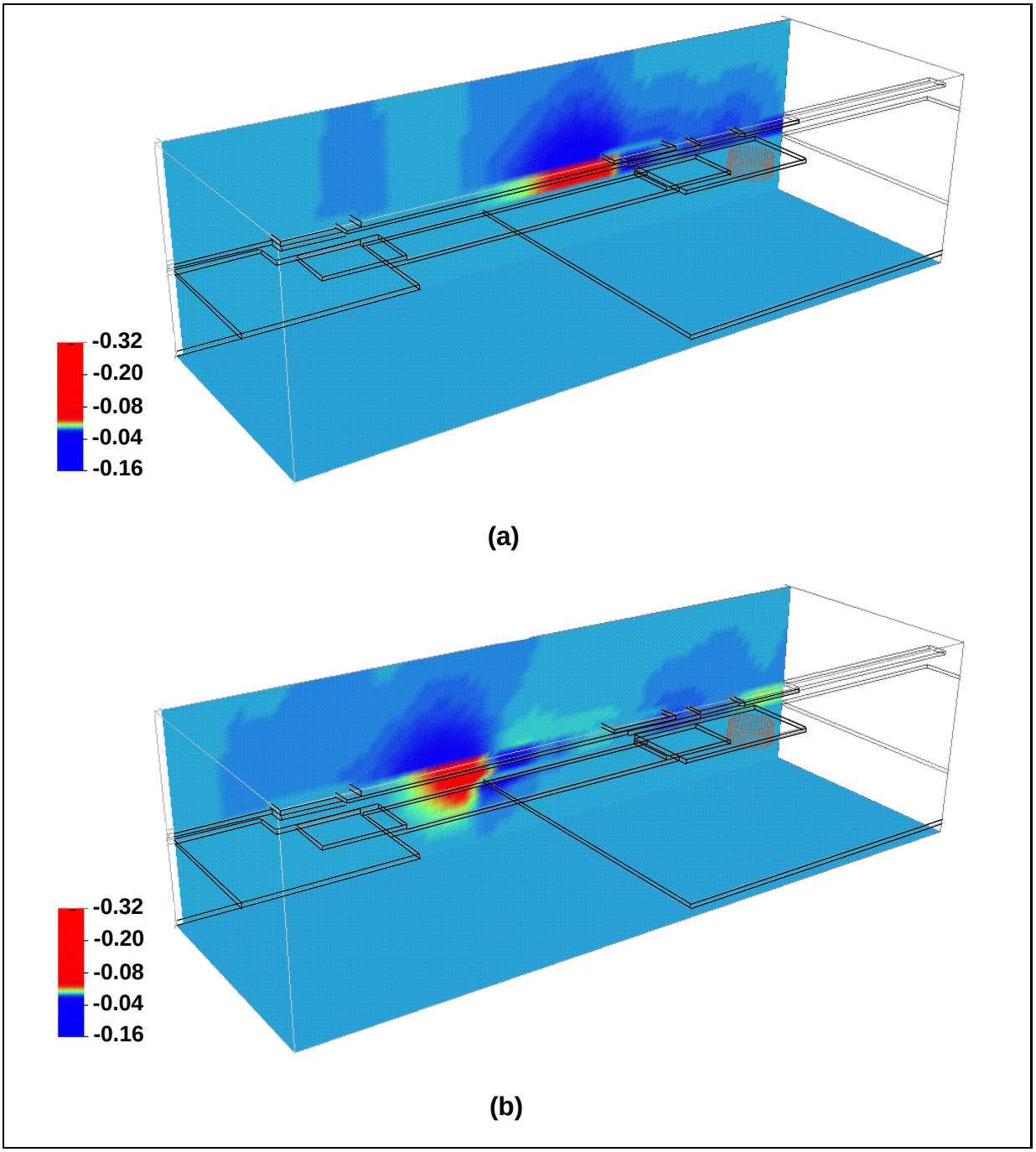

FIGURE 9.27. Reflection at adhesive-substrate interface.

at the input terminals, no external input DC blocking capacitor is required, and the input signal can be applied balanced or single-ended if one input terminal is grounded. For the circuit design, one of the most important objectives is an accurate modelling of these on-chip transformers. In [**91**], the interstage transformers were modelled using relatively simple lumped equivalent circuits that accurately model the low-frequency behaviour of the transformers up to 2 GHz. One of the

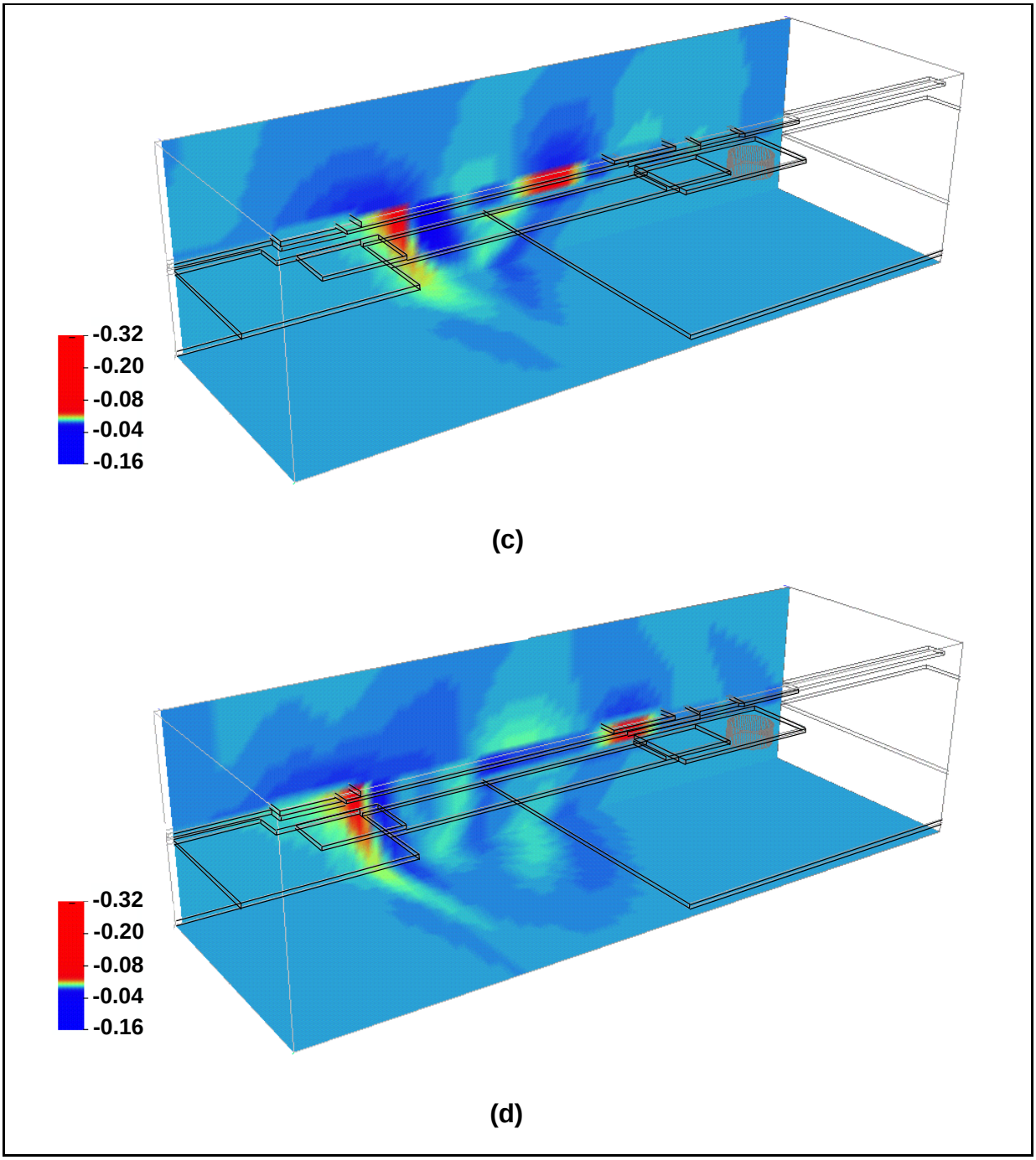

FIGURE 9.28. Reflection at adhesive-substrate interface.

major problems in developing an accurate equivalent lumped circuit model is the precise characterization of the loss mechanisms present in these transformers. Examples are ohmic losses in the conductor material of the windings and substrate losses. To gain further insight into the nature of these loss mechanisms, a profound understanding of the physics of these transformers is necessary. This

understanding also aides in further improving their design. This physical insight can be gained with the aid three-dimensional electromagnetic full-wave analyses in time domain. On the one hand, the propagation of the electromagnetic field can be visualized and on the other hand, the consideration of lossy material is fairly simple in contrast to frequency domain simulation methods.

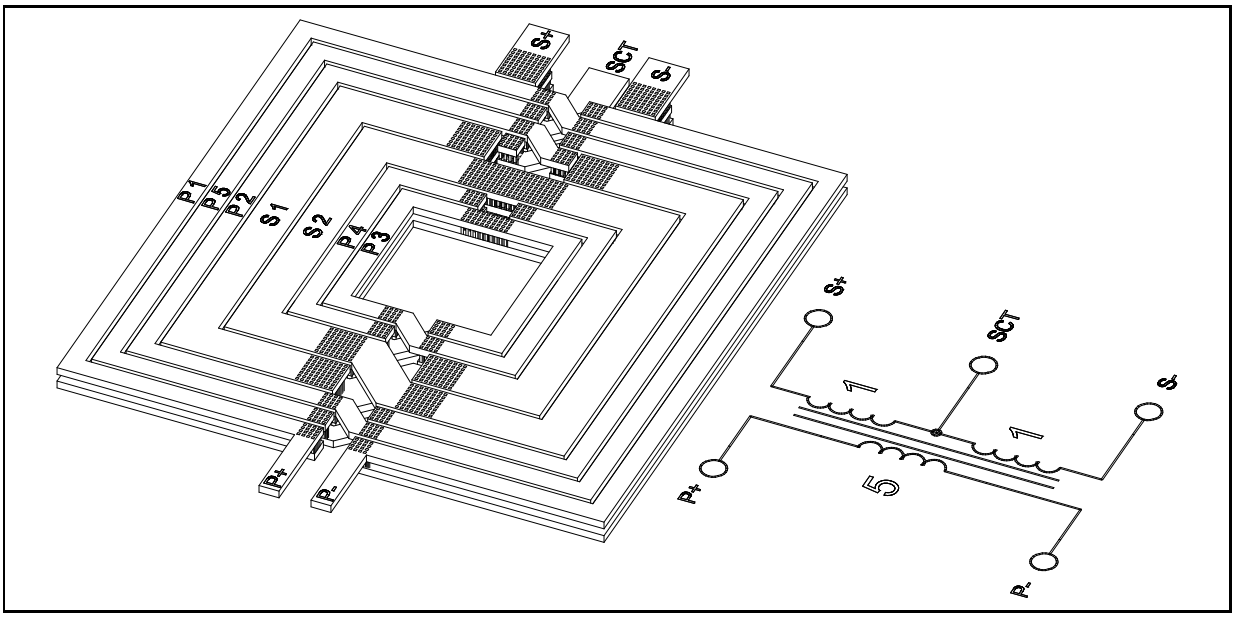

FIGURE 9.29. Interstage transformer with turn ratio N=5:2.

As the characterization of such transformers is a challenging problem for a time domain method, one needs to find reasonable parameters for this type of simulation such as how many cells are sufficient to discretize the gap between the conductor windings, how far away to place the boundaries, where to compute the field integrals, etc. Therefore, the time domain characterization of a simplified planar transformer similar to the interstage transformers in the power amplifier mentioned above, using the SCN-TLM method is presented. As the primary objective of this characterization is to determine the general influence of the lossy silicon substrate on the S-parameters, it does not matter whether the transformers has a turn ratio of 5:2 or 2:1 or the like. Moreover, studying simplified transformers has the advantage of shorter simulation times, as the simulation of such problems takes several days on state-of-the-art workstations. The considered simplified transformer has a turn ratio of N=2:1 using the same conductor widths as the N=5:2 transformer. A three-dimensional view is shown in Fig. 9.30. It measures 166×166 μm^2. The layout of this simplified transformer can be found in Appendix A. The gap between the windings is doubled from 2 to 4 μm. The planar transformers can be characterized in two different modes of operation. First, differential mode excitation with differential output and the centre tap of the secondary winding as common output reference terminal. Second, one input

and one output terminal grounded and the centre tap of the secondary winding floating. The differential mode of operation is considered in the following TLM characterization of the transformers.

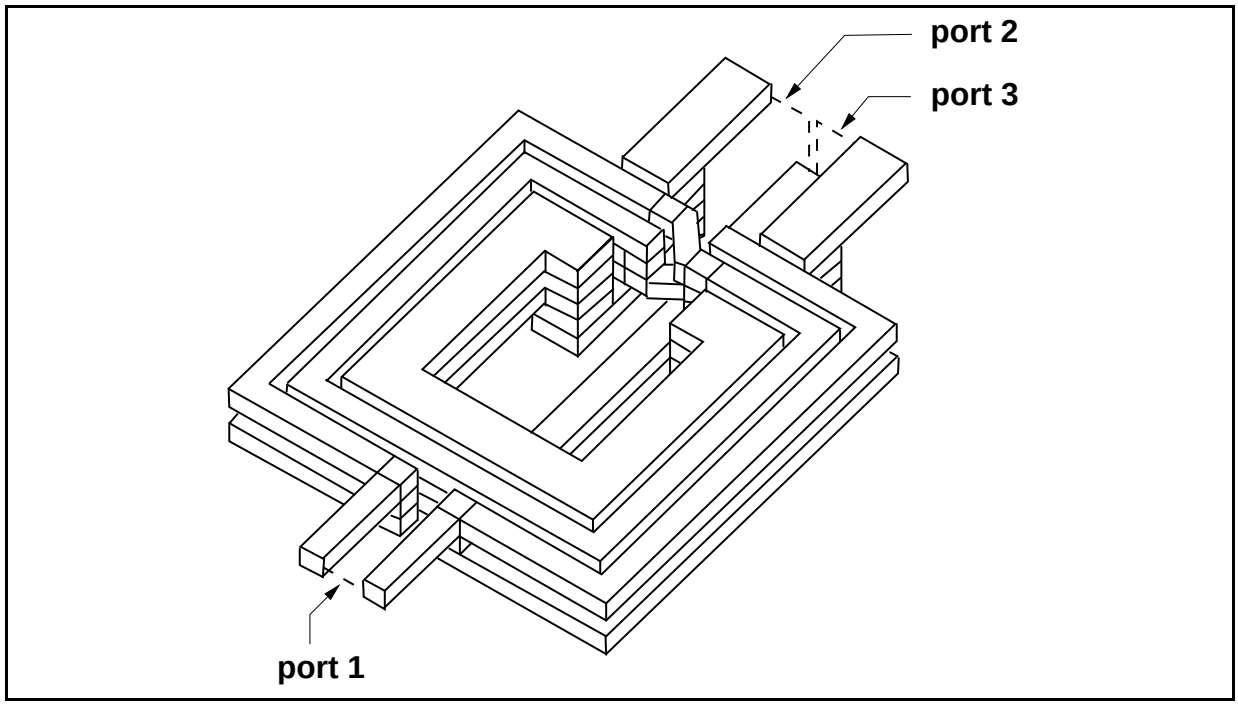

FIGURE 9.30. Simplified interstage transformer with turn ratio N=2:1.

3.1. TLM Simulation of Planar Microwave Transformers. Referring to the top view of the simplified transformer in Appendix F, all dimensions in this top view are in the μm-range. The dashed shaded polygons represent structures on metal plane ALU 1. The dark shaded regions denote vias between the respective metal planes. The vertical location of the metal planes within the substrate is specified in Fig. 9.32. In Fig. 9.31, a cross-section of the transformer design is shown. Metalization planes 1 and 2 (i.e. ALU 1 and ALU 2) are connected through vias in order to reduce the resistance in the windings. At the crossing of the conductors of the primary winding, only one metal layer can be used, as indicated in Fig. 9.30. A cross-section of the substrate of the 25 GHz-f_T silicon bipolar technology SIEMENS B6HF is shown on the left side of Fig. 9.32. The original substrate set-up comprises a number of very thin layers. To achieve a more uniform discretization and a reasonable time step, it is necessary to slightly simplify the substrate set-up for the TLM model as indicated in the sketch on the right of Fig. 9.32. This variation of the layer thicknesses will practically not affect the simulation results. An irregularly graded mesh is used to discretize this transformer. The TLM mesh is schematically shown in Fig. 9.33. The dark regions of the two background planes reflect regions with smaller cells. The irregularly

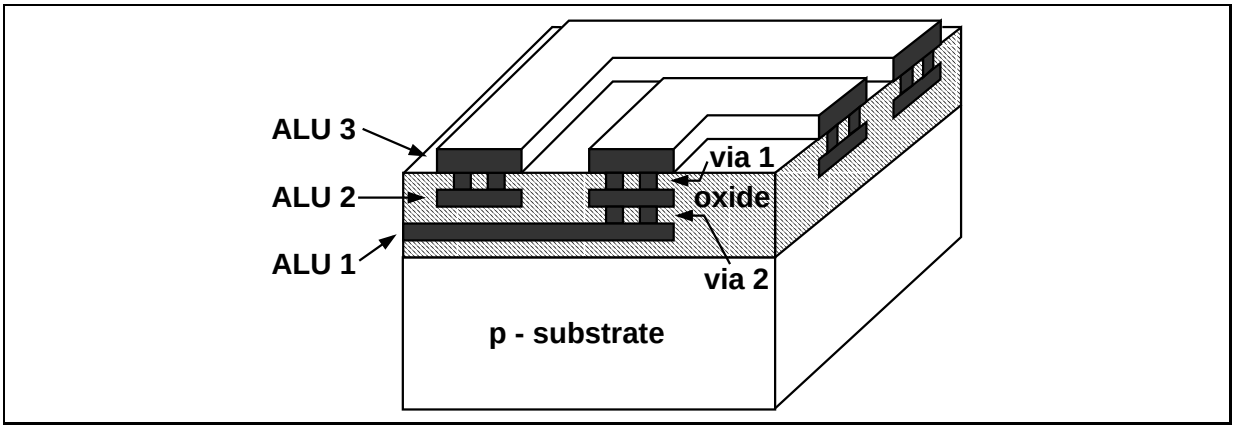

FIGURE 9.31. Schematic cross-section of transformer in B6HF technology.

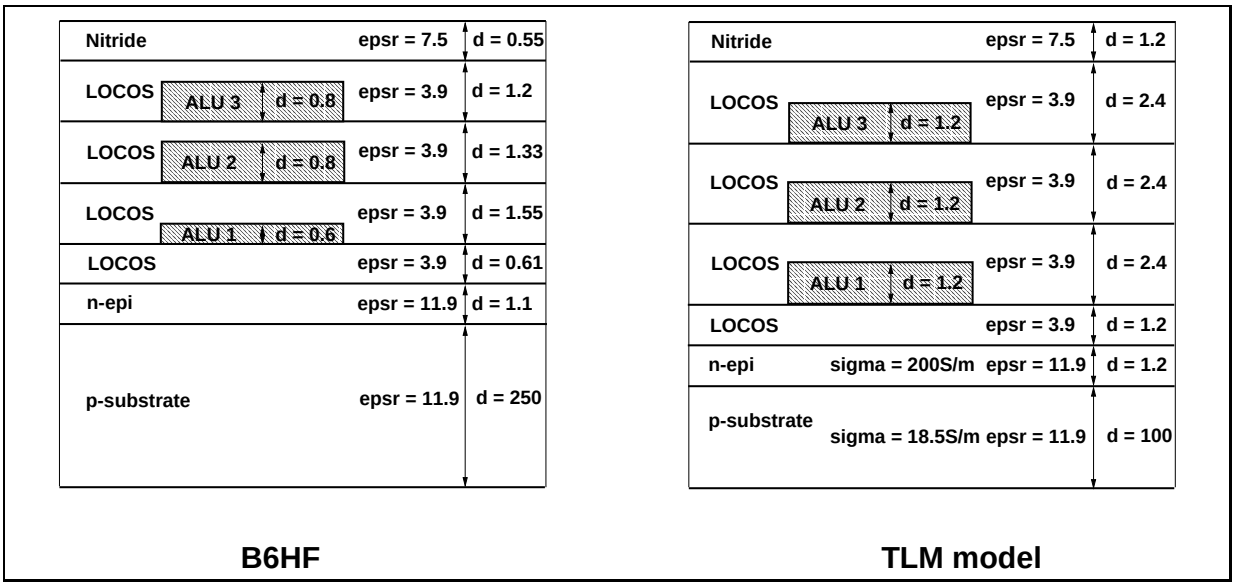

FIGURE 9.32. Schematic cross-section of the SIEMENS B6HF silicon production technology and simplified model substrate used in the TLM simulation.

graded mesh discretization is as follows, written in the number of cells (N) per section in μm (W), as $N_1 : W_1, N_2 : W_2, ..., N_n : W_n$. In x-direction, we have 30:75, 5:10, 4:4, 5:10, 4:4, 10:20, 30:70, 10:20, 4:4, 5:10, 4:4, 5:10, 30:75 cells per section, in y-direction 30:75, 5:10, 4:4, 5:10, 4:4, 10:25, 30:60, 10:25, 4:4, 5:10, 4:4, 5:10, 30:75, and in z-direction 40:100, 7:8.4, 1:1.2, 50:125. In positive and negative x-direction and at bottom of the substrate, a matched layer absorber with 8 cells and a theoretical reflection coefficient of $R_0 = 1.0 \cdot 10^{-4}$ was used. A linear conductivity profile was chosen. This yields a mesh with 162×146×106 cells.

The basic cell size was 1 μm. The simulation was run for 50000 iterations. A precomputed two-dimensional field template was used to excite the TLM mesh of the model transformer. It represents a two-dimensional cross-section of the fundamental propagating field mode in terms of TLM wave amplitudes. This precomputed field template is then superposed on the wave amplitudes in the TLM cells of the excitation plane using a GAUSSian transient. The excitation plane runs through the ends of the conductors of the input terminal. The time-domain signals are

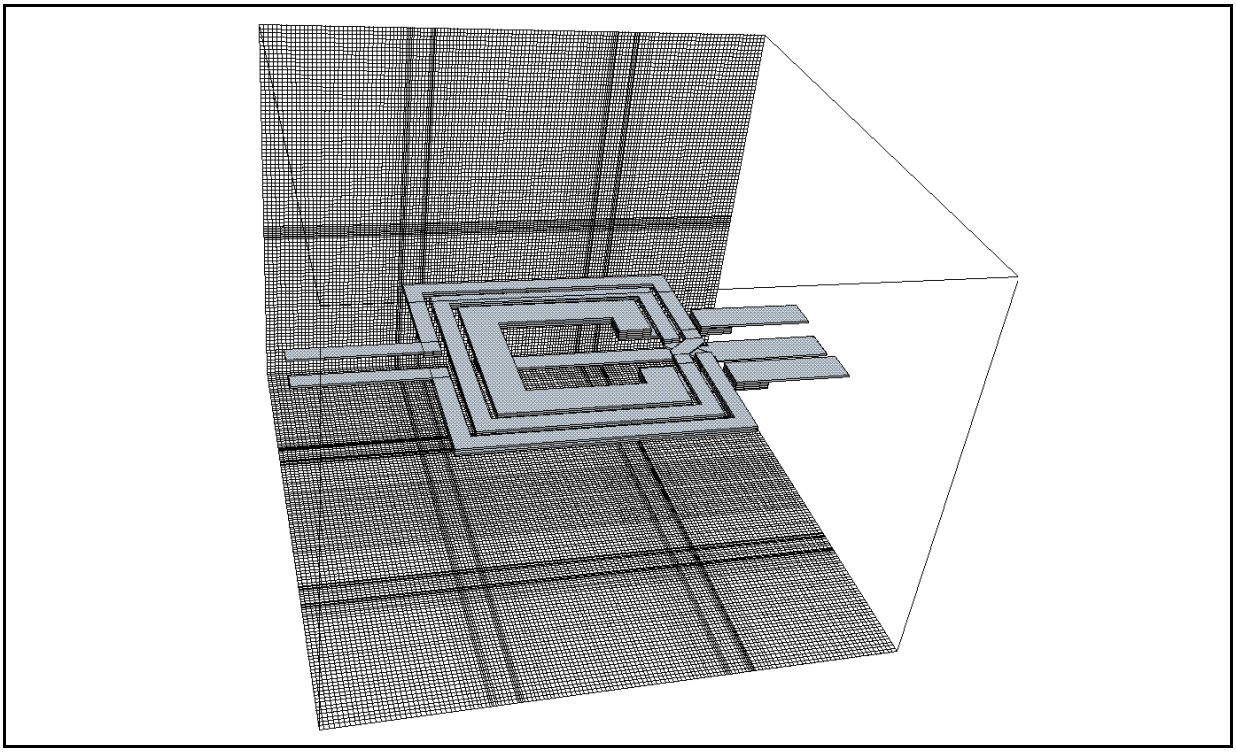

FIGURE 9.33. Three-dimensional view of the metal planes in the TLM mesh describing the topology of the simplified planar transformer. The background planes at the bottom an in the background show the discretization with an irregularly graded mesh. The darker regions indicate regions of smaller cells.

monitored by field integrals. The voltages at the (differential mode) ports that are indicated in Fig. 9.30 is obtained by computing the line integral between the respective conductors at the input and at the output terminal. The voltage at port 1 is calculated by a line integral running from one conductor to the other conductor in the slot. At port 2, the integral runs from the upper conductor on the right side in Fig. 9.30 to the centre tap. At port 3, the line integral runs from the lower conductor on the right side in Fig. 9.30 to the centre tap. The current flowing in the terminals of the transformer is calculated by loop integrals encompassing the respective conductor. The current flowing through port 1 is obtained by a loop

TLM model of N=2:1 transformer	
iterations	50000
total mesh size	162×146×106 = 2507112 cells
mesh grading (x)	30:75, 5:10, 4:4, 5:10, 4:4, 10:20, 30:70, 10:20, 4:4, 5:10, 4:4, 5:10, 30:75
mesh grading (y)	30:75, 5:10, 4:4, 5:10, 4:4, 10:25, 30:60, 10:25, 4:4, 5:10, 4:4, 5:10, 30:75
mesh grading (z)	40:100, 7:8.4, 1:1.2, 50:125
basic Δl	1 μm
Δt	$6.54 \cdot 10^{-16}$ s
h (stability factor)	5.1
ABC	8 ML, p= 1.0, $R_0 = 1.0 \cdot 10^{-4}$ (x-dir./bottom)
Excitation	precomputed field template

TABLE 9.2. Parameters of TLM simulation of simplified N=2:1 transformer.

integral around the upper input conductor in Fig. 9.30. The loop integrals for calculating the current through ports 2 and 3 encompass the upper and the lower conductors indicated in the upper right corner of Fig. 9.30. Both current and voltage integrals of a particular port lie in the same plane, which is indicated by the thick dashed lines in Fig. 9.30. The parameters of the TLM simulation are summarized in Table. 9.2. JOHNS' original formulation in equivalent node voltage and equivalent loop current representation was employed to characterize the planar transformers as this formulation currently represents the fastest TLM algorithm [**5**].

3.2. TLM Simulation Results. The time-domain signals obtained at the ports are shown in Fig. 9.34. The solid line refers to the transformer on a lossless substrate and the dashed curves denote the signals obtained from a simulation where the substrate losses were modelled with $\sigma_e = 18.5\ \mathrm{Sm}^{-1}$ neglecting the conductive epi-layer. The dotted lines stand for the voltages when considering a substrate with both losses with $\sigma_e = 18.5\ \mathrm{Sm}^{-1}$ and a conductive epi-layer with $\sigma_e = 200\ \mathrm{Sm}^{-1}$. The curves represent the voltage obtained at the ports. The graph at the top shows the reference input pulse recorded during a simulation of the input lines alone. The second graph from the top shows the voltage between the input terminals at port 1 of the simplified transformer. The third graph shows the output voltage at port 2 and the graph at the bottom shows the output voltage at port 3 of the simplified transformer.

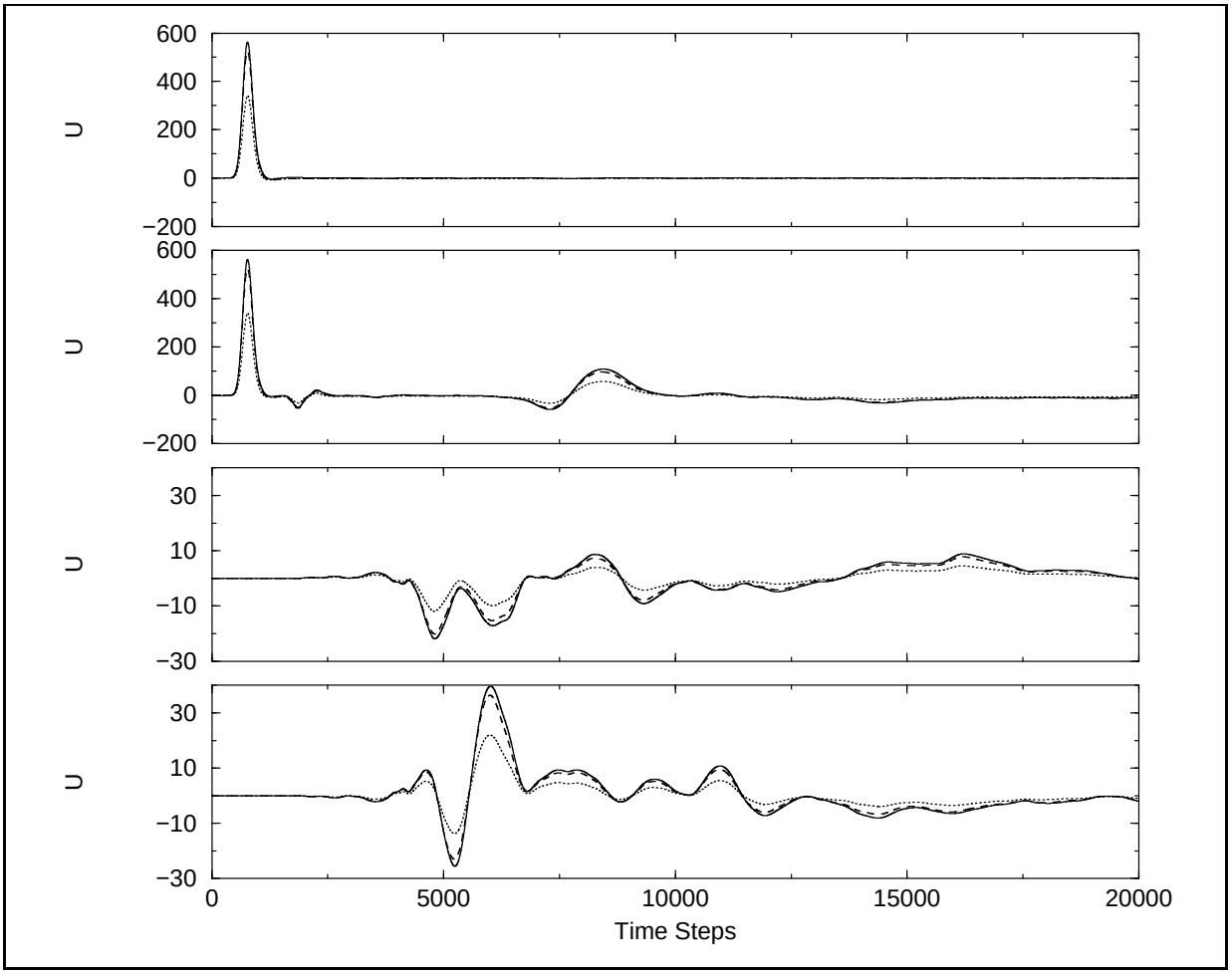

FIGURE 9.34. Excitation and voltage at the ports of the transformer. From top to bottom: temporal GAUSSian excitation, voltage between input terminals (port 1), voltage between first output conductor and centre tap (port 2), and voltage between second output conductor and centre tap (port 3).

Comparing the voltages at port 2 and 3 in the bottom graphs of Fig. 9.34, one notices that the output is not balanced in the simplified transformer. This is caused by the conductors of the primary winding crossing each other only once, whereas in the original design (see Fig. 9.29) there are multiple crossings yielding a fully balanced output. Note that the amplitude of the dashed and dotted signals is always lower. This reflects the dissipation in the lossy substrate. The presence of a relatively highly conductive epi-layer reduces the amplitudes of the signals more significantly. Consequently, the epi-layer acts somehow like a screening to the substrate.

The S-parameters S11, S21, and S31 up to 30 GHz are shown in Fig. 9.35. The solid curves denote the S-parameters of the transformer on the lossless substrate

and the dashed curves refer to the transformer on the lossy substrate with $\sigma_e = 18.5\ \mathrm{Sm}^{-1}$. The dotted lines denote the case of the substrate including both losses and the conductive epi-layer. Looking at the S-parameters, one realizes that the losses in the silicon substrate have virtually no effect on the properties of the transformer in the frequency band of interest up to 5 GHz. Only at very high

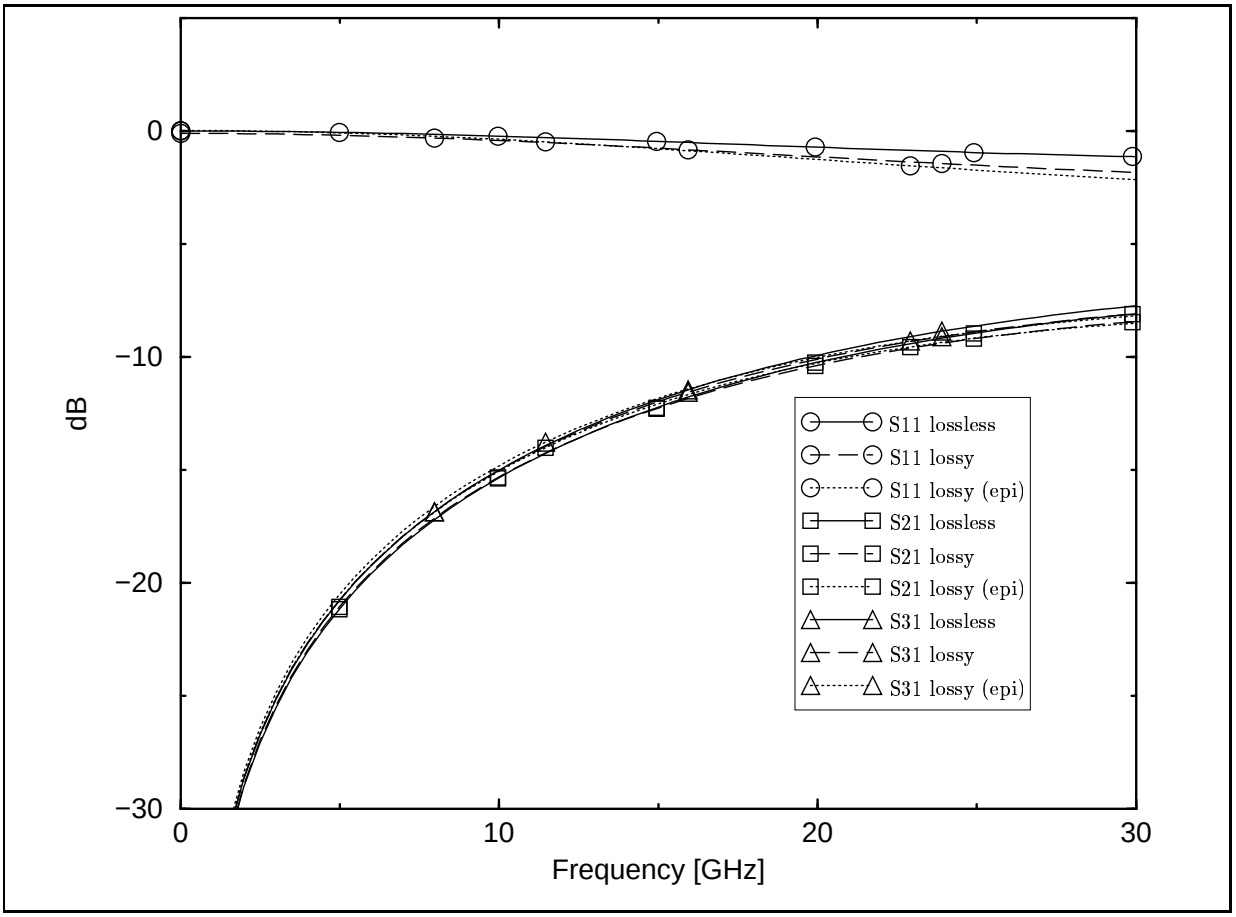

FIGURE 9.35. Comparison of S-parameters of simplified N=2:1 transformer on lossless and lossy substrate. The solid curves refer to the lossless case and the dashed curves to the case with lossy substrate.

frequencies, the substrate losses seem to play a more profound role as indicated in Fig. 9.36. In this graph, the S-parameters are plotted up to 300 GHz. The substrate losses start having a more significant influence on the S-parameters at approximately 25 GHz. The deviation from the curve denoting the lossless case is around 1 dB. Consequently, these simulations suggest that the principle loss mechanism in the planar transformers of the type considered here originates from ohmic losses in the conductors of the transformer windings. The lossy substrate has a less significant influence on their properties. Nevertheless, the negative influence of capacitive coupling to the substrate must not be neglected.

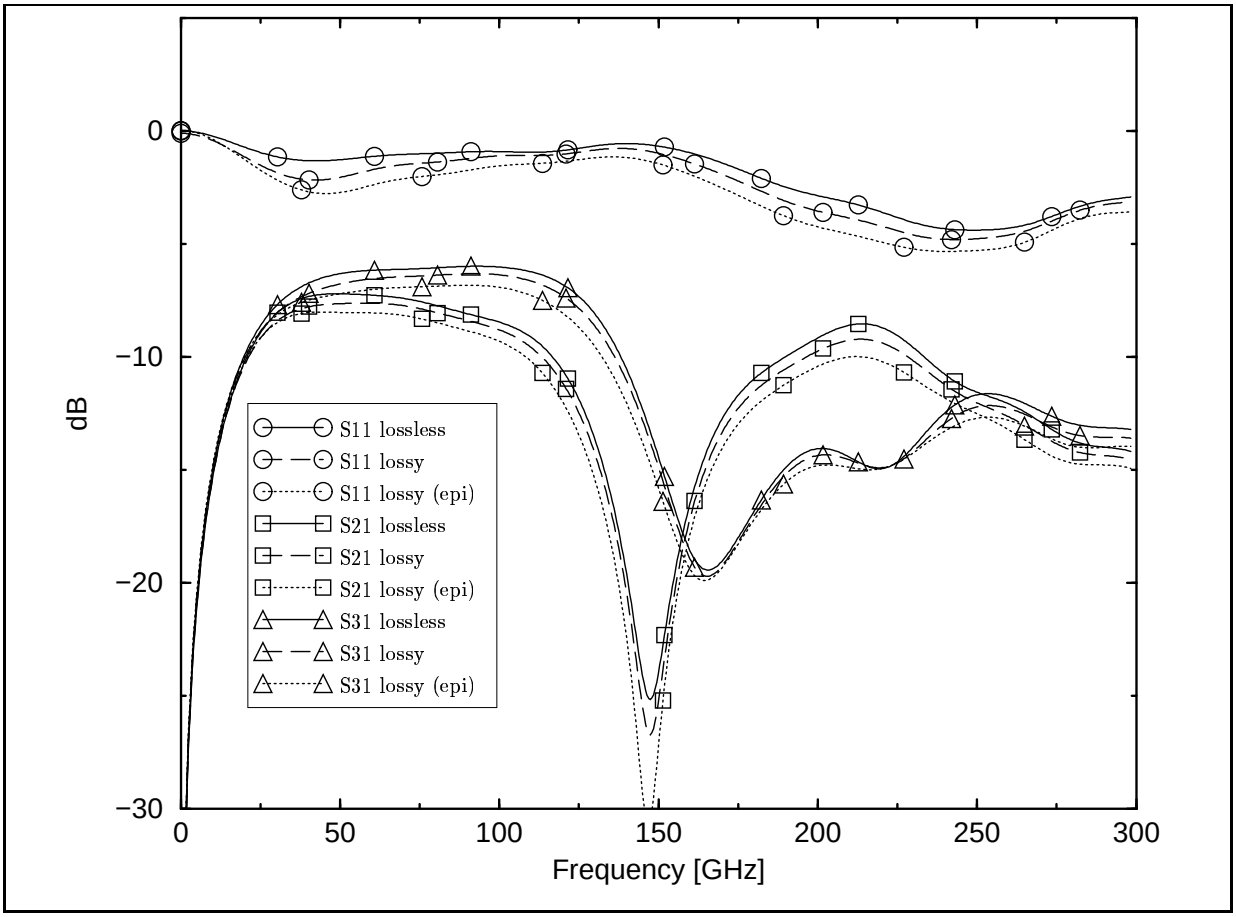

FIGURE 9.36. S-parameters of simplified N=2:1 transformer on lossless and lossy substrate up to 300 GHz. The solid curves refer to the lossless case and the dashed curves to the case with lossy substrate.

By considering the S21 curves in Fig. 9.36, one can locate the first resonance of the simplified transformer at around 150 GHz. This indicates a potential use of such transformers up to nearly 100 GHz, before the transmission (S21, S31) breaks down.

The tangential H-field in a horizontal cross-sectional plane located between ALU 2 and ALU 3 is shown at various times in Fig. 9.37. It reflects the current distribution in the conductors. One can discern two dark regions at the input conductors that represent the incident pulse after 0.73 ps simulation time in Subfigure (a). In Subfigure (b) one can recognize a relatively large reflected current at the top edge of the picture (recorded after 1.203 ps). The currents that flow into the primary winding are also clearly discernible. A radiated spherical wave into the transformer or into the substrate, respectively, can also be recognized. Interestingly, a parallel current is also excited in the second winding of the primary winding. After 1.674 ps simulation time, one can also recognize a current flowing

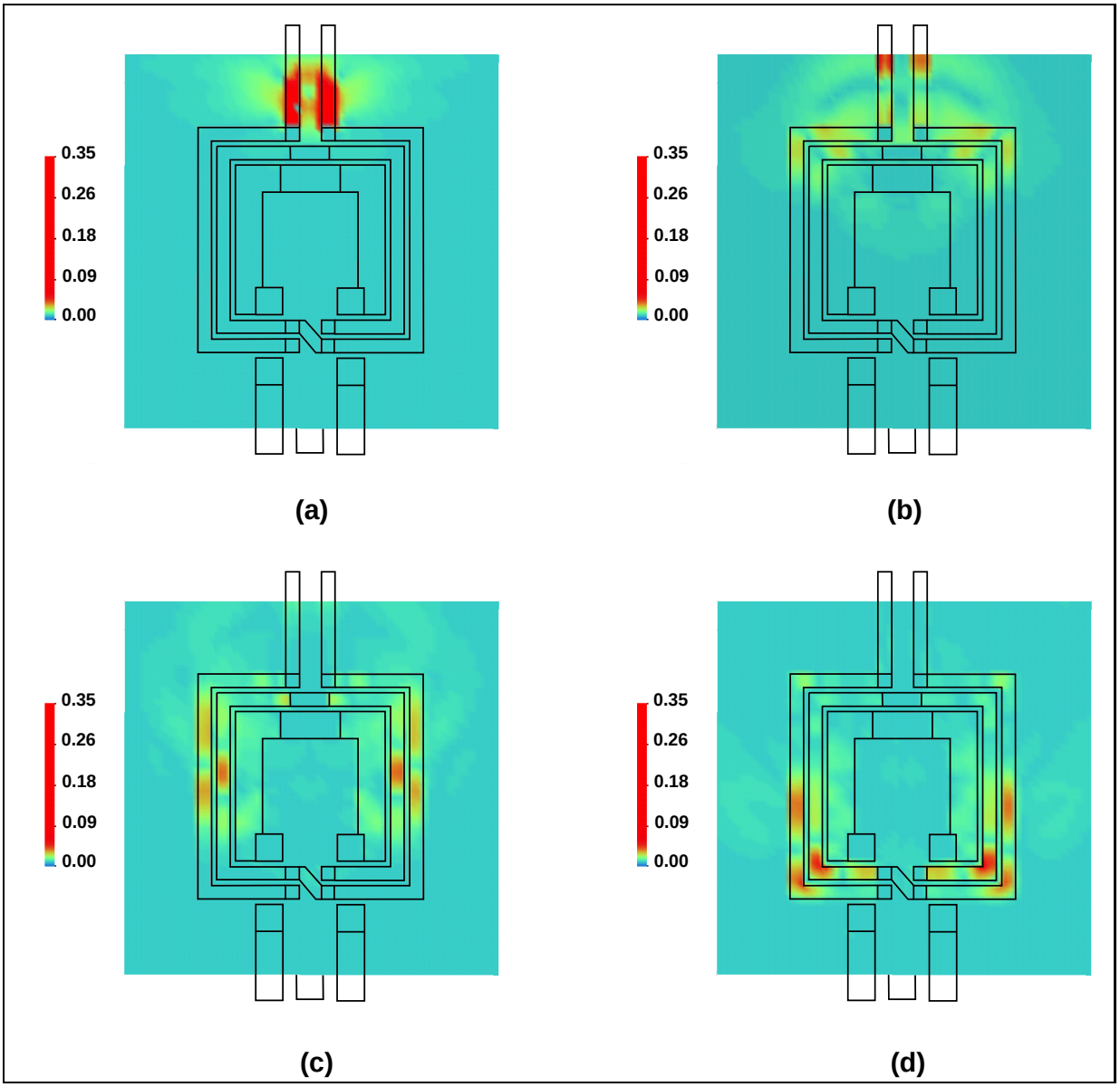

FIGURE 9.37. Tangential H-field in the plane of the transformer between ALU 3 and ALU 2 reflecting the current distribution in the conductors.

in the second winding of the primary winding. Interestingly, when the currents flow around the corners of the conductors, the pulses are better localized. This is shown in Subfigure (d) after 2.145 ps. Comparing Subfigures (c) (H-field after 1.792 ps) and (d), one recognizes that the currents in the second winding flow in the same direction as the ones in the first. When the current pulses reach the vias at the conductor crossing of the primary winding, one can recognize current peaks, which indicate that the vias present a remarkable obstacle for the current to flow (see Subfigure (e) after 2.616 ps). The principle current pulse crosses from

the first to the second winding of the primary winding after 3.21 ps, which can be seen in in Subfigure (f). The current peak at the central via of the secondary winding, which connects the windings on ALU 2 and ALU 3 (Subfigure (g)), can be recognized after 4.028 ps. The current pulses flowing in the primary winding reach again the input terminal after 4.5 ps, which can be seen in Subfigure (h). The outgoing current pulse from the input can be clearly recognized in Subfigure (i) after 5.44 ps. The further current flow is indicated in Subfigure (j), which shows the tangential H-field after 5.91 ps. From the images of the tangential H-field

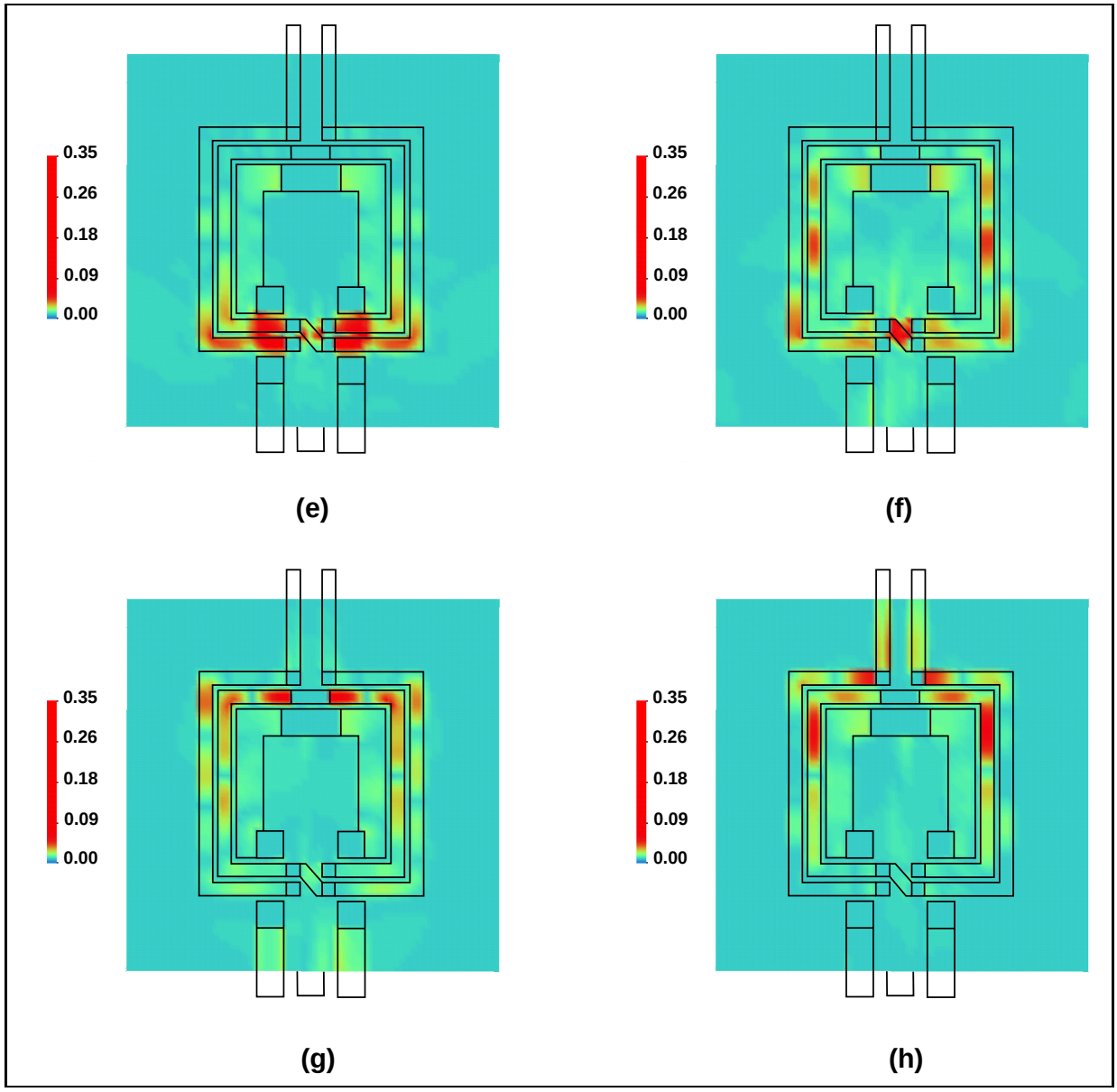

FIGURE 9.37. Tangential H-field in the plane of the transformer between ALU 3 and ALU 2 reflecting the current distribution in the conductors.

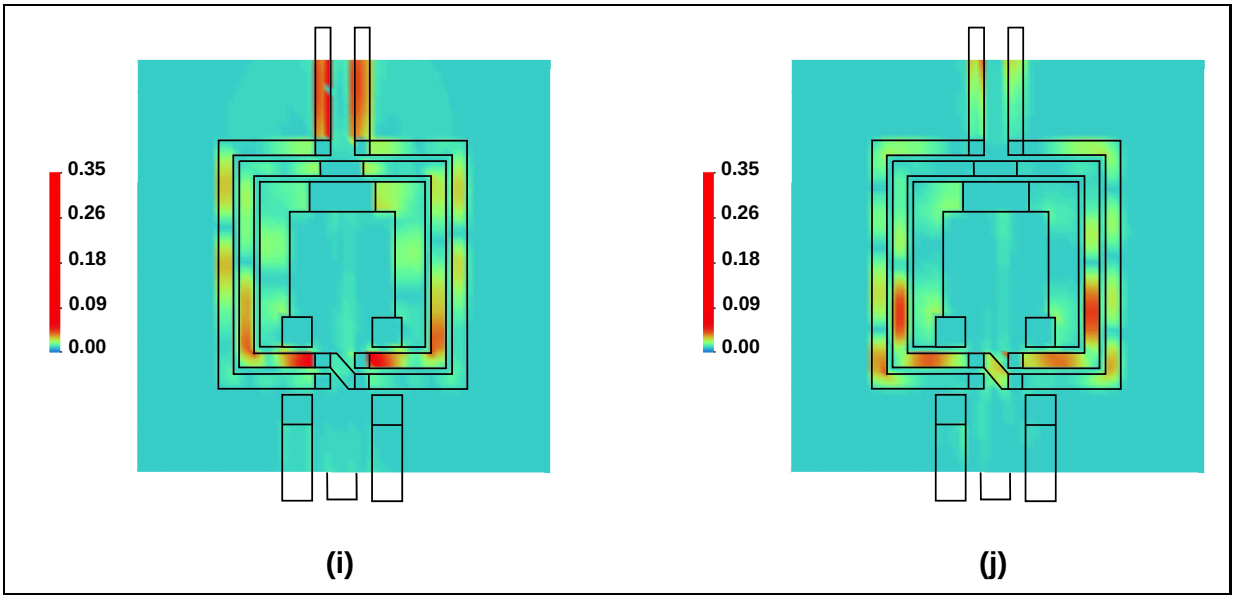

FIGURE 9.37. Tangential H-field in the plane of the transformer between ALU 3 and ALU 2 reflecting the current distribution in the conductors.

in Fig. 9.37 one can identify another loss mechanism in the planar transformer. The interconnection between the ALU 2 and ALU 3 conductors through the vias represent a remarkable obstacle for the current. It might be worth while using vias all along the conductors to reduce the current crowding effects. Furthermore, the field images suggest improving the design of the crossings of the conductors. For example, one could consider a bridge in parallel on metalization layer ALU 1 to reduce the resistance.

3.3. Comparison with HP-Momentum MoM Simulation Results. For comparison, the simplified transformer was also characterized using the commercially available HP-Momentum field solver, based on the method-of-moments. The Momentum solver operates in frequency-domain and therefore considers the steady state. The parameters of the Momentum simulation of the transformer can be found in Table 9.3. As using an infinite substrate layer without ground plane yielded very poor results, a ground plane was specified in the simulations although this does not completely reflect the physical problem. However, considering a ground plane produced much better results.

Although the specification of differential mode ports is available with the HP-Momentum solver, specifying 50 Ohm microstrip ports in connection with grounding the other conductor (i.e. the centre tap of the secondary winding at the output) and using an artificial via to ground, proved much better. The mesh depicted in Fig. 9.38 was automatically generated using the parameters given in Table 9.3 of the Momentum mesh generator.

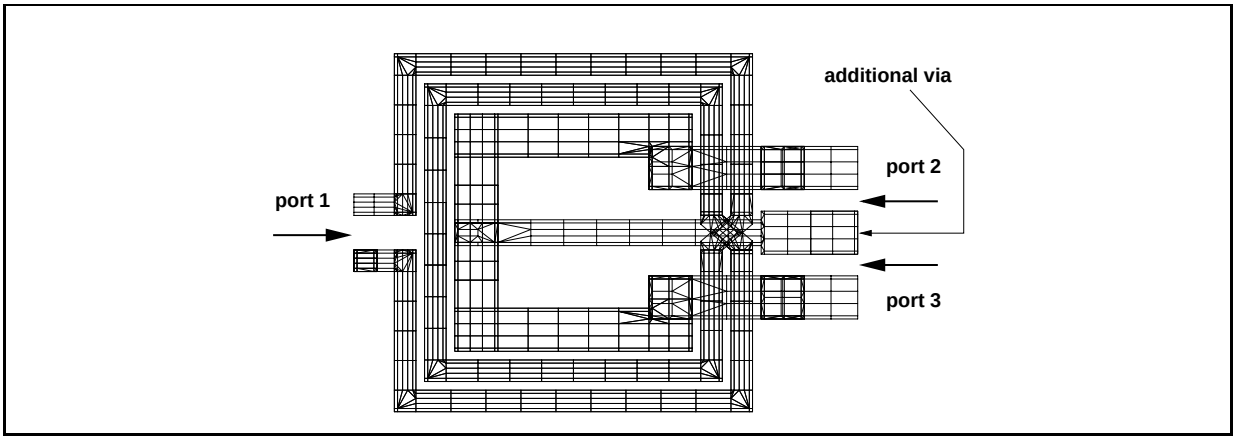

FIGURE 9.38. Automatically generated mesh for HP-Momentum simulation of simplified transformer with turn ratio N=2:1.

Momentum MoM model of N=2:1 transformer	
mesh parameters	
global	60 cells/λ
edge mesh	5 cells
mesh frequency	100 GHz
mesh size	1798 rectangles
	664 triangles
	414 vias
ports	50 Ohm microstrip TL ports

TABLE 9.3. Parameters of Momentum simulation of N=2:1 transformer.

In Fig. 9.39, the S-parameters obtained by the time-domain simulation using SCN-TLM with a lossless substrate and the ones obtained from the HP-Momentum simulation are compared. As the S-parameters from the Momentum simulation are related to 50 Ohm ports, they were transformed to the respective port impedances of the TLM simulation. Port 1 has an impedance of 77 Ohm and Ports 2 and 3 have an impedance of 340 Ohms. When the S-parameters obtained from the two methods are related to the same impedances, one can see a reasonable agreement between the two methods as indicated by the curves in Fig. 9.39. Nevertheless, it seems that the frequency-domain HP-Momentum solver is not suitable for proper simulations of the planar transformers without ground plane.

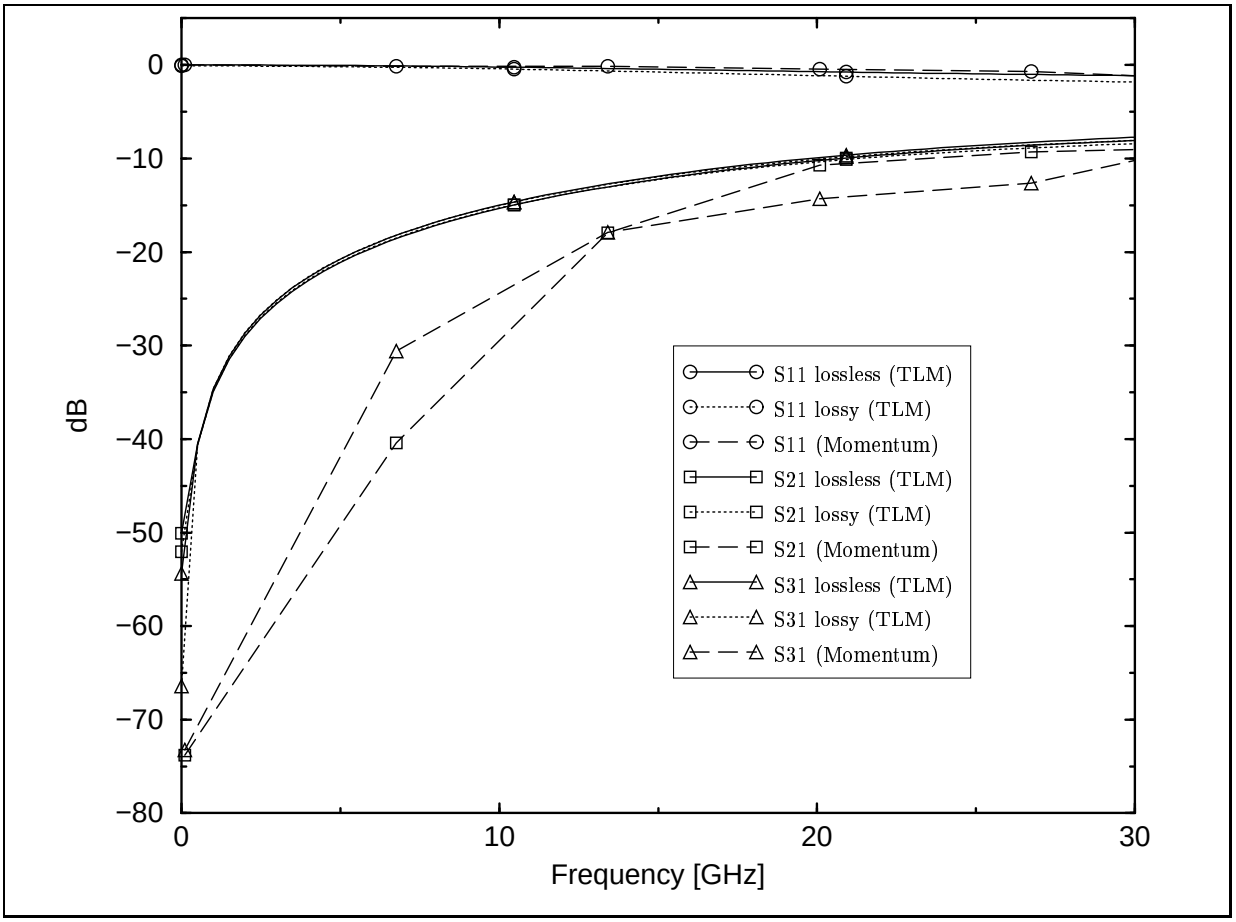

FIGURE 9.39. Comparison of S-parameters for simplified N=2:1 transformer on lossless substrate up to 100 GHz obtained from TLM simulation and HP-Momentum simulation.

Furthermore, it is not possible to consider lossy substrates as the simulation will yield S-parameters greater than one.

CHAPTER 10

Conclusion

The foundations of the TLM method with symmetrical condensed node in the original formulation of JOHNS were investigated in this work. The TLM algorithm was considered as a mathematical approximation scheme of MAXWELL's equations in a rigorous functional analytical setting and not in terms of equivalent lumped element models. It was shown that the field-mapping between the discretized electromagnetic field and the TLM wave pulses determines the asymptotic convergence rate of the TLM algorithm. For this, the convergence of the original SCN-TLM formulation introduced by JOHNS [**35**] was proved for the first time. The proof was achieved for both the SCN-TLM method with and without stubs. As the original field-mapping proposed by JOHNS is not bijective, a proof of convergence is not straightforward. Therefore, the proof was performed in three steps. The first step consisted in constructing the appropriate function spaces providing a suitable norm for proving convergence. In the second step, the cell-centred field-mapping was applied at every iteration step yielding a mapping induced finite difference scheme that was accessible to standard methods for proving convergence. It emerged that the TLM inherent mapping induced finite difference scheme is the well known first order LAX-FRIEDRICHS scheme. In a third step, it was shown using norm estimations that the difference between the TLM scheme and this mapping induced finite difference scheme approaches zero for Δl approaching zero. Using the field-mapping of the original formulation, which defines the electromagnetic field components in the centre of a TLM cell, leads asymptotically to $\mathcal{O}(\sqrt{\Delta t})$ convergence. In view of this, the TLM algorithm can be seen as an energy-conserving LAX-FRIEDRICHS scheme. Energy conservation of the TLM scheme using a cell-centred field-mapping is achieved at the cost of a lower convergence order. However, applying the bijective boundary oriented field-mapping, where the electromagnetic field is sampled at the centre of the cell faces of a TLM cell, will indeed result in second order convergence [**23, 44, 46**]. This influence of the field-mapping on the asymptotic convergence order could be confirmed in a numerical experiment, where the propagation of a plane wave in a one-dimensional parallel-plate waveguide was studied at various discretizations. From the proof of convergence of JOHNS' original formulation follows that the

commonly used picture of the TLM-SCN in terms of equivalent circuits leads to a misinterpretation of the underlying mathematical approximation.

The convergence of the recently proposed ARTLM scheme was also investigated. It is shown that the field-mapping also determines the type of approximation in the ARTLM Method. A proof of the non-existence of a consistent mapping was given. As the ARTLM scheme is based on exploiting the inherent redundancy of the TLM scheme, it follows that fully exploiting this redundancy does not lead to a convergent scheme modelling MAXWELL's equations. Consequently, it is only possible to utilize the redundancy with respect to time, as done in the ATLM method.

Moreover, the SCN-TLM method was applied to challenging problems in characterizing planar microwave circuits. In the course of the characterization of such planar components it emerged that in many practical situations the use of simple absorbing boundaries for truncating the computational domain is not sufficient. Therefore, the matched layer technique was optimized and made applicable by implementing an automatized layer generator into the TLM code. A comprehensive study on the optimum parameter combination of such matched layer absorbers for truncating the computational domain in open problems with inhomogeneous planar substrates was performed. It was shown that the performance of these absorbing boundary conditions is mainly determined by the differences in dispersion due to different media parameters in neighbouring regions. The numerical reflections play a minor role.

One objective was the investigation of the influence of dielectric losses of the adhesive used in multichip module interconnect structures on the transmission properties of these interconnections. The interconnect structure consisted of a microstrip-to-coplanar transition. For this, a novel symmetrical condensed node algorithm for simulating dispersive dielectrics of Debye type was derived using the propagator approach. It offers the advantage of guaranteeing second order convergence, whereas methods based on equivalent circuits may lead to algorithms of lower asymptotic convergence. As no accurate data on the dispersive properties of the epoxy adhesive applied in this interconnect structure are available, worst case parameters of the adhesive were estimated. It could be shown that the frequency dependent losses of the adhesive only have a slight influence on the transmission properties. The lossy adhesive even improves the transmission properties as it presents a loss impedance match to a certain degree to the open running input microstrip line. It follows that MCM interconnects can be modelled neglecting the dielectric losses without a misinterpretation of the simulation results. This leads to shorter simulation times, as more efficient TLM algorithms can be used. Furthermore, it was found that the MCM interconnect structure can be optimized by better matching the impedance of the interfacing media.

The second studied problem consisted of determining the influence of a lossy substrate on the performance of planar microwave transformers. As this problem

involved using a very large mesh, the most efficient TLM algorithm which is based on a special representation of JOHNS' original formulation was utilized to shorten the simulation times. It was found that in the frequency regime of interest up to 5 GHz the losses of the substrate have a negligible influence on the performance of such transformers. Hence the main source of loss stems from the resistance of the conductors. Moreover, the S-parameters obtained from the TLM simulation indicate a possible use of such transformers up to 100 GHz, which is very interesting for next generation mobile communication applications. The field visualization yielded an insight into the operation of such transformers. It could be shown that the via-holes and the conductor crossings represent a bottle neck for the flowing currents. These two substructures should be optimized to reduce the overall losses in the transformers.

The characterization of these planar microwave structures has shown that the TLM method with symmetrical condensed node is a reliable and competitive tool for the analysis and the design of such structures. I expect the contributions presented in this thesis to have the following impact on the future development of the TLM method and its use as an electromagnetic modelling tool:

1. It will be necessary to explicitly show consistency and convergence of a particular TLM algorithm, as deriving TLM algorithms in terms of equivalent lumped element circuits may lead to false conclusions on the chosen approximation of MAXWELL's equations.
2. The question of the existence of a six-port TLM has to be tackled from a different line of thought. A further exploitation of the inherent redundancy of the TLM algorithm appears to be impossible.
3. New types of absorbing boundary conditions for use in open problems involving inhomogeneous layered media need to be developed. The currently used matched layer (this also applies to PML) absorbers are practical but still not perfect.
4. The TLM method seems to be particularly suited for the characterization of arbitrary loss mechanisms in planar microwave circuits. Using the propagator approach has indicated a promising direction with respect to modelling dispersive media, as the asymptotic convergence rate can be guaranteed.

APPENDIX A

Smoothness Conditions for Solutions of Maxwell's Equations

In Chapter 4, the LEBESGUE space

$$\mathcal{H}_M = \boldsymbol{L}_2\big(0,T;(\boldsymbol{L}_2(\boldsymbol{\Omega}))^6\big) \tag{A.1}$$

was specified for solving an initial value problem of MAXWELL's equations. However, not all functions of $(\boldsymbol{L}_2(\boldsymbol{\Omega}))^6$ are a solution of (4.25) and (4.26). The generalized rot-operator $\mathbf{D}_{\mathbf{R}}$ admits only certain functions of $(\boldsymbol{L}_2(\boldsymbol{\Omega}))^6$. Moreover, the time derivative on the left side of (4.25) and (4.26) further restricts the number of admissible functions from $\mathcal{H}_M$. The first restriction can be seen as a condition for the domain of the operator $\mathbf{D}_{\mathbf{R}}$

$$\mathcal{D}(\mathbf{D}_{\mathbf{R}}) = \Big\{ \boldsymbol{f} \in \mathcal{H}_S : \boldsymbol{R}\boldsymbol{f} \in \mathcal{H}_S \Big\}. \tag{A.2}$$

It simply means that the wanted functions are differentiable with respect to space at least once. A LEBESGUE space comprising such functions is called a SOBOLEV space [**16, 117**]. In the case considered here, the SOBOLEV space

$$\boldsymbol{V} = \big(\boldsymbol{W}_2^1(\mathbb{R}^3)\big)^6 . \tag{A.3}$$

would be appropriate to comprise all admissible functions. A scalar product in this space may be defined as

$$\begin{aligned}(\boldsymbol{f}_1,\boldsymbol{f}_2) = \Big(\iiint_{\infty}^{\infty} & (\boldsymbol{E}_1(\boldsymbol{r})\boldsymbol{E}_2^*(\boldsymbol{r}) + \boldsymbol{H}_1(\boldsymbol{r})\boldsymbol{H}_2^*(\boldsymbol{r}) \\ & + D^1\boldsymbol{E}_1(\boldsymbol{r})D^1\boldsymbol{E}_2^*(\boldsymbol{f}r) + D^1\boldsymbol{H}_1(\boldsymbol{r})D^1\boldsymbol{H}_2^*(\boldsymbol{f}r)\big)d^3\boldsymbol{r}. \Big)^{\frac{1}{2}}\end{aligned} \tag{A.4}$$

It should be noted that this scalar product no longer equals the energy functional. D^i denotes following ZEIDLER [**117**], a generalized derivative

$$D^i = \frac{\partial^{|i|}}{\partial \xi_1^{i_1} \cdots \partial \xi_N^{i_N}} \quad \text{with} \quad |i| = |i_1 + \cdots + i_N|, \tag{A.5}$$

where i denotes a 'multiindex' and ξ a general variable. Using the same argument, it is sensible to restrict the domain of functions of $t \longrightarrow \boldsymbol{H}$ or $t \longrightarrow \boldsymbol{V}$ to those, whose partial derivatives up to order one exist. Consequently, all functions of the SOBOLEV space

$$\boldsymbol{W}_p^1(0,T;\boldsymbol{V}) \tag{A.6}$$

are admissible. In case of $p = 2$, the scalar product is defined according to (A.4). Still, the divergence condition of the electromagnetic field needs to be considered. For this we define the extended divergence operator **Div** [**82**]

$$\mathbf{Div} = \begin{pmatrix} \nabla\cdot & 0 \\ 0 & \nabla\cdot \end{pmatrix}. \tag{A.7}$$

This leads finally to the SOBOLEV space

$$\boldsymbol{W}_2^1(0,T;\boldsymbol{V}_0) \qquad \text{with} \qquad \boldsymbol{V}_0 = \Big\{ f \in \boldsymbol{V} | \boldsymbol{Div} f \in \boldsymbol{V} \Big\}. \tag{A.8}$$

for the given initial value problem involving MAXWELL's equations of eqn. (4.25) and (4.26). The additional restrictions on the admissible functions ensure that the considered solutions are sufficiently smooth.

APPENDIX B

Sequence Spaces

Sequence spaces are spaces that are often used as introductory example to the theory of HILBERT spaces. They are very similar to the spaces of lattice functions. The sequence spaces $\ell_p, p \geq 1$ are the spaces of all bounded sequences [**16, 116**]. They are complete and a norm is defined on them. A typical example of this class of spaces is the space ℓ_2, which is a HILBERT space. Each element $\boldsymbol{x}$ is a sequence $(x_n)_{n=1}^{\infty}$ of real or complex numbers, such that $\sum_{n=1}^{\infty} |x_n|^2 < \infty$ is fulfilled. This means that the sequence converges to a finite number. Hence, the space ℓ_2 is given by

$$\ell_2 = \left\{ \boldsymbol{x} = (x_n)_{n=1}^{\infty} : \sum_{n=1}^{\infty} |x_n|^2 < \infty \right\}. \tag{B.1}$$

The norm in this space is given by

$$\|\boldsymbol{x}\|_2 = \|(x_n)_{n=1}^{\infty}\| = \sqrt{\sum_{k=1}^{\infty} |x_n|^2}. \tag{B.2}$$

As ℓ_2 is naturally a linear vector space over $\mathbb{R}$ or $\mathbb{C}$, componentwise addition and multiplication is declared. An inner product is given by

$$(\boldsymbol{x}, \boldsymbol{y}) = \sum_{n=1}^{\infty} x_n y_n^* \tag{B.3}$$

with $\boldsymbol{x} = (x_n), \boldsymbol{y} = (y_n)$ [**82, 116**]. Related spaces are the spaces

$$\ell_p = \left\{ \boldsymbol{x} = (x_n)_{n=1}^{\infty} : \sum_{n=1}^{\infty} |x_n|^p < \infty \right\}, \tag{B.4}$$

which are BANACH spaces but not HILBERT spaces. Their norms are defined as

$$\|\boldsymbol{x}\|_p = \Big(\sum_{k=1}^{\infty} |x_n|^p \Big)^{\frac{1}{p}} \tag{B.5}$$

for $p \geq 1$. These spaces can be generalized in the way that the elements x_n of the sequence $(x_n)_{n=1}^{\infty}$ denote BANACH spaces, indexed n, $(\mathcal{B}_n)$ instead of real or complex numbers as before. The element x_n still denotes an element of the sequence, but it is now an element of $\mathcal{B}_n$. Hence, the space $\ell_p(\mathcal{B}_n)$ denotes a sequence of BANACH spaces indexed n $(n = 1, 2, 3...)$ whose elements $\boldsymbol{x}_n$ are sequences $(x_m)_{m=1}^{\infty}$ of elements of the BANACH spaces $(\mathcal{B}_n)$. The sequence converges in the sense of $\sum_{n=1}^{\infty} \|x_n\|_{\mathcal{B}_n}^p < \infty$. $\|\cdot\|_{\mathcal{B}_n}^p$ denotes the norm of $(\mathcal{B}_n)$. Now, the spaces look as follows

$$\ell_p(\mathcal{B}_n) = \Big\{ \boldsymbol{x} = (x_n)_{n=1}^{\infty} : \sum_{n=1}^{\infty} \|x_n\|_{\mathcal{B}_n}^p < \infty, x_n \in \mathcal{B}_n \Big\}, \tag{B.6}$$

with norms

$$\|\boldsymbol{x}\|_p = \Big(\sum_{k=1}^{\infty} \|x_n\|_{\mathcal{B}_n}^p \Big)^{\frac{1}{p}} \tag{B.7}$$

for $p \geq 1$. An example of such spaces are the FOCK spaces in quantum mechanics with $p = 2$ and $\mathcal{B}_n$ denoting HILBERT spaces [**82**].

APPENDIX C

Lattice Functions

Lattice functions are functions, whose continuous values are only known on a grid, i.e. at discrete points of an interval in the one-dimensional case or at discrete points of a higher dimensional domain in higher dimensional cases. As an example,

$$g = g(x_0 + l\Delta x) \,, \qquad l \in \mathbb{Z} \tag{C.1}$$

is a lattice function, where $g(x) \in C(\mathbb{R})$. This shows that a grid can also be described by a set of numbers $\mathbb{I}$. In example (C.1) the equality $\mathbb{I} = \mathbb{Z}$ would hold. The values of the function g can be written as an enumerable infinite tuple $(..., g_{-2}, g_{-1}, g_0, g_1, g_2, ...)$, which is also a sequence of real or complex numbers of index $l \in \mathbb{I}$. Hence, lattice functions are functions of discrete argument.

APPENDIX D

Discrete Lebesgue Spaces

In Appendix B, the sequence spaces ℓ_2, ℓ_p and $\ell_p(\mathcal{B}_n)$ were considered. Finite difference methods are usually investigated in *discrete* LEBESGUE *spaces* $\ell_{p,\Delta x}$ [**100, 118**]. They represent the discrete analogue to the LEBESGUE spaces introduced when defining the initial value problem for MAXWELL's equations in Chapter 4. The only difference between discrete LEBESGUE spaces and sequence spaces is a slightly altered definition of the norm and the inner product. This is due to the fact that the ℓ_p norms diverge for $\Delta x \longrightarrow 0$ [**100**]. As this is a serious drawback when studying convergence, the norms of the discrete LEBESGUE spaces are weighted by the spatial increment Δx

$$\|\boldsymbol{x}\|_{p,\Delta x} = \Big(\sum_{n=1}^{\infty} |x_n|^p \, \Delta x \Big)^{\frac{1}{p}}. \tag{D.1}$$

In case of $p = 2$ this norm is called *energy norm*. The norms of the spaces $\ell_{p,\Delta x}(\mathcal{B}_n)$ are defined analogously as

$$\|\boldsymbol{x}\|_{p,\Delta x} = \Big(\sum_{n=1}^{\infty} \|x_n\|_{\mathcal{B}_n}^p \, \Delta x \Big)^{\frac{1}{p}}. \tag{D.2}$$

In case of discrete initial and boundary value problems, one has spaces of finite dimension. These spaces are simply $\mathbb{R}^N$ (or $\mathbb{C}^N$) equipped with $\ell_{p,\Delta x}$-norm (or the appropriate inner product in case of $p = 2$), consequently the norms are given by

$$\|\boldsymbol{x}\|_{p,\Delta x} = \Big(\sum_{n=1}^{N} |x_n|^p \, \Delta x \Big)^{\frac{1}{p}}. \tag{D.3}$$

For problems that involve more than one dimension, the norms are defined accordingly [**100, 118**] such as

$$\left\|(x_{nm})_{n,m}^{\infty}\right\|_{p,\Delta x\Delta y} = \Big(\sum_{n=1}^{\infty}\sum_{m=1}^{\infty}|x_{nm}|^{p}\,\Delta x\Delta y\Big)^{\frac{1}{p}}. \tag{D.4}$$

APPENDIX E

Layout of MCM Interconnect

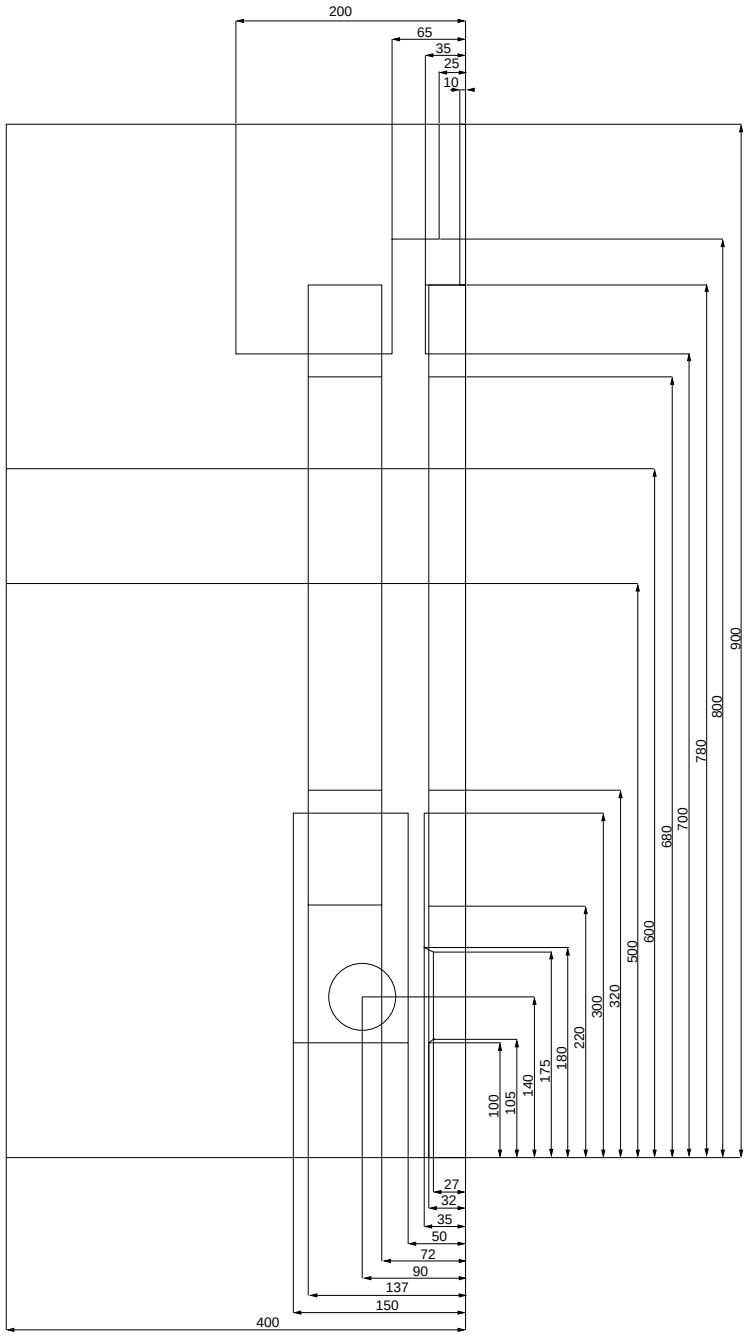

APPENDIX F

Layout of Simplified Transformer

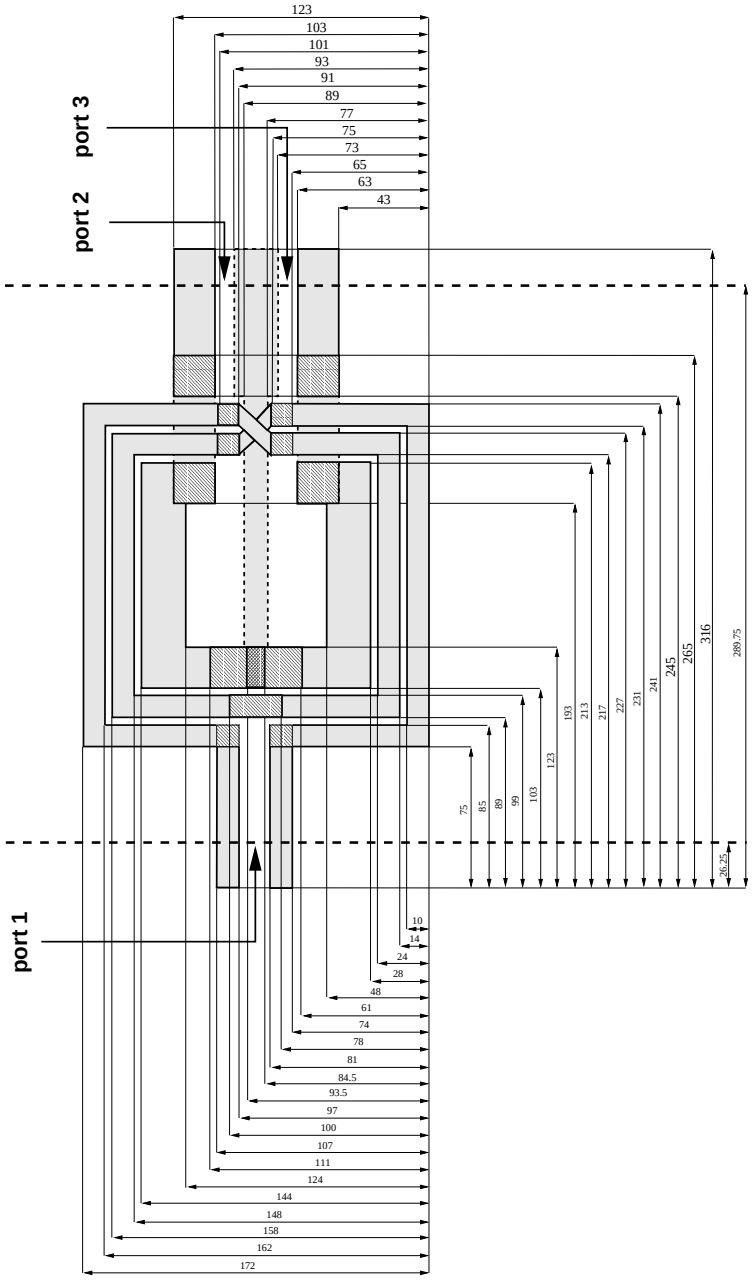

Bibliography

[1] M. Aidam. Grundlagen der TLM-Methode zur Berechnung elektromagnetischer Felder. Diplomarbeit, Technische Universität Berlin, 1995.

[2] M. Aidam and P. Russer. Derivation of the Transmission Line Matrix Method by Finite Integration. *AEÜ Int. J. Electron. Commun.*, 51(1):35–39, January 1997.

[3] M. Aidam and P. Russer. New High Order Time-Stepping Schemes for Finite Differences. In *15th Annual Review of Progress in Applied Computational Electromagnetics Digest*, pages 578–585, Monterey, March 1999.

[4] D.A. Al-Mukhtar and J.E. Sitch. Transmission-Line Matrix Method with Irregularly Graded Space. *Proc. Inst. Elec. Eng.*, 128(6):299–305, December 1981.

[5] B. Bader. *Untersuchung der Alternating-Transmission-Line-Matrix-Methode (ATLM) für die Zeitbereichsanalyse elektromagnetischer Felder.* Doktorarbeit, Lehrstuhl für Hochfrequenztechnik an der Technischen Universität München, 1996.

[6] B. Bader, M. Krumpholz, and P. Russer. Current Sources in TLM. In *IEEE AP-S International Antennas and Propagation Symposium Digest*, pages 1110–1115, June 1994.

[7] B. Bader and P. Russer. Modelling of coplanar waveguide discontinuities using the Alternating Transmission Line Matrix (ATLM) Method. In *12th Annual Review of Progress in Applied Computational Electromagnetics Digest*, pages 310–316, Monterey, March 1996.

[8] A. Banai, F. Farzaneh, F. Ndagijimana, and P. Saguet. An Interpretation of Instabilities in the Absorbing Boundary Conditions in TLM Method and an Improved Matched Termination Wall. *Int. J. Num. Modelling*, 11:243–254, 1998.

[9] J.P. Berenger. Three-dimensional perfectly matched layer for the absorption of electromagnatic waves. *Journal of Computational Physics*, 127:363–379, 1996.

[10] P. Berini. A Comprehensive Study of Numerical Anisotropy and Dispersion in 3-D TLM Meshes. *IEEE Trans. Microwave Theory Tech.*, 43(5):1173–1181, May 1995.

[11] P. Berini and K. Wu. A Pair of Hybrid Symmetrical Condensed TLM Nodes. *IEEE Microwave and Guided Wave Lett.*, 4:244–246, July 1994.

[12] M. Celuch-Marcysiak and W.K. Gwarek. On the Effect of Bilateral Dispersion in Inhomogeneous Symmetrical Condensed Node Modeling. *IEEE Trans. Microwave Theory Tech.*, 42(6):1069–1073, June 1994.

[13] Z. Chen, M. Ney, and W.J.R. Hoefer. Absorbing and Connecting Boundary Conditions for the TLM Method. *IEEE Trans. Microwave Theory Tech.*, 41(11):2016–2024, November 1993.

[14] Z. Chen, M.M. Ney, and W.J.R. Hoefer. A New Finite-Difference Time-Domain Formulation and its Equivalence with the TLM Symmetrical Condensed Node. *IEEE Trans. Microwave Theory Tech.*, 39(12):2160–2169, December 1991.

[15] J.F. Dawson. Improved Magnetic Loss for TLM. *Electron. Lett.*, 29:467–468, February 1993.

[16] L. Debnath and P. Mikusiński. *Introduction to Hilbert Spaces with Applications.* Academic Press, 1990.

[17] J.L. Dubard and D. Pompei. A Modified 3D-TLM Variable Node for the Berenger's Perfectly Matched Layer Implementation. In *13th Annual Review of Progress in Applied Computational Electromagnetics Digest*, pages 661–665, Monterey, March 1997.

[18] J.L. Dubard and D. Pompei. Microstrip Antenna Characterization Using TLM and Berenger's Perfectly Matched Layers (PML). In *13th Annual Review of Progress in Applied Computational Electromagnetics Digest*, pages 1439–1444, Monterey, March 1997.

[19] C. Eswarappa and W.J.R. Hoefer. Implementation of berenger absorbing boundary conditions in tlm by interfacing fdtd perfectly matched layers. *Electron. Lett.*, 31(15):1264–1266, 1995.

[20] R. Gehring. Analyse von Streifenleitungen nach der Transmission-Line-Matrix Methode (TLM). *private communication, Spinner GmbH, 80335 München*, 1998.

[21] F.J. German, J.A. Svigelj, and R. Mittra. A Numerical Comparison of Dispersion in Irregularly Graded TLM and FDTD Meshes. In *12th Annual Review of Progress in Applied Computational Electromagnetics Digest*, pages 270–278, Monterey, March 1996.

[22] K.E. Gustafson. *Introduction to Partial Differential Equations and Hilbert Space Methods*. John Wiley, New York, 1980.

[23] S. Hein. Consistent finite-difference modelling of Maxwell's equations with lossy symmetrical condensed node. *Int. J. Num. Modelling*, 6:207–220, 1993.

[24] S. Hein. Finite-difference time-domain approximation of Maxwell's equations with nonorthogonal condensed TLM mesh. *Int. J. Num. Modelling*, 7:179–188, 1994.

[25] S. Hein. Synthesis of TLM Algorithms in the Propagator Integral Framework. In *2nd Intl. Workshop on Transmission Line Matrix Modeling (TLM) - Theory and Applications*, pages 1–11, Munich, October 1997.

[26] S. Hein. TLM numerical solution of Bloch's equations for magnetized gyrotropic media. *Appl. Math. Modelling*, 21:221–229, 1997.

[27] S. Hein. Gauge techniques in time and frequency domain. In *3rd Intl. Workshop on Transmission Line Matrix Modeling (TLM) - Theory and Applications*, pages 51–72, Nice, October 1999.

[28] J.L. Herring. *Developments in the Transmission-Line Modelling Method for Electromagnetic Compatibility Studies*. Phd thesis, University of Nottingham, 1993.

[29] J.L. Herring and W.J.R. Hoefer. Comparison of 3D TLM Meshing Techniques for Modelling Microwave Components. In *13th Annual Review of Progress in Applied Computational Electromagnetics Digest*, pages 1418–1425, Monterey, March 1997.

[30] W.J.R. Hoefer. The Transmission-Line-Matrix Method - Theory and Applications. *IEEE Trans. Microwave Theory Tech.*, 33(4):882–893, October 1985.

[31] J. Huang and K. Wu. A Unified TLM Model for Wave Propagation of Electrical and Optical Structures Considering Permittivity and Permeability Tensors. *IEEE Trans. Microwave Theory Tech.*, 43(10):2472–2477, October 1995.

[32] C. Huber, M. Krumpholz, and P. Russer. Dispersion in Anisotropic Media Modeled by Three-Dimensional TLM. *IEEE Trans. Microwave Theory Tech.*, 43(8):1923–1934, August 1995.

[33] H. Jin and R. Vahldieck. The Frequency-Domain TLM Method - a New Concept. *IEEE Trans. Microwave Theory Tech.*, 40(12):2207–2218, December 1992.

[34] H. Jin and R. Vahldieck. Direct Derivations of TLM Symmetrical Condensed Node and Hybrid Symmetrical Condensed Node from Maxwell's Equations Using Centered Differencing and Averaging. *IEEE Trans. Microwave Theory Tech.*, 42(12):2554–2561, December 1994.

[35] P.B. Johns. A Symmetrical Condensed Node for the TLM Method. *IEEE Trans. Microwave Theory Tech.*, 35(4):370–377, April 1987.

[36] P.B. Johns. On the Relationship Between TLM and Finite-Difference Methods for Maxwell's Equations. *IEEE Trans. Microwave Theory Tech.*, 35(1):60–61, January 1987.

[37] P.B. Johns and R.L. Beurle. Numerical solution of 2-dimensional scattering problems using a transmission-line matrix. *Proc. Inst. Elec. Eng.*, 118(9):1203–1208, September 1971.

[38] C. Kittel. *Introduction to Solid State Physics*. John Wiley, New York, 1996.

[39] G. Kron. Equivalent Circuit of the Field Equations of Maxwell. *Proc. Inst. Radio Engrs.*, 32:289–299, May 1944.

[40] M. Krumpholz, B. Bader, and P. Russer. On the Theory of Discrete TLM Green's Functions in Three-Dimensional TLM. *IEEE Trans. Microwave Theory Tech.*, 43(7):1472–1483, July 1995.

[41] M. Krumpholz, L. Roselli, and P. Russer. Dispersion Characteristics of the TLM Scheme with Symmetrical Super-Condensed Node. In *IEEE MTT-S International Microwave Symposium Digest*, volume 1, pages 369–372, 1995.

[42] M. Krumpholz and P. Russer. A Generalized Method for the Calculation of TLM Dispersion Relations. In *Proc. of the 23rd Europ. Microwave Conf.*, pages 288–290, September 1993.

[43] M. Krumpholz and P. Russer. Discrete Time-Domain Functions for Three-Dimensional TLM Modelling of the Radiating Boundary Conditions. In *9th Annual Review of Progress in Applied Computational Electromagnetics Digest*, pages 458–466, Monterey, March 1993.

[44] M. Krumpholz and P. Russer. A Field Theoretical Derivation of TLM. *IEEE Trans. Microwave Theory Tech.*, 42(9):1660–1668, September 1994.

[45] M. Krumpholz and P. Russer. On the Dispersion in TLM and FDTD. *IEEE Trans. Microwave Theory Tech.*, 42(7):1275–1279, July 1994.

[46] M. Krumpholz, P. Russer, and H. Zscheile. The Derivation of the Condensed Symmetric TLM Node from Maxwell's Equations. In *Proc. Progress In Electromagnetic Research Symp.–PIERS*, page 150, Pasadena, 1993.

[47] S. Lindenmeier, 1997. private communication.

[48] S. Lindenmeier, B. Bader, and P. Russer. Investigation of various H-shaped Antennas with an ATLM Field-Solver. In *IEEE MTT-S International Microwave Symposium Digest*, volume 3, pages 1365–1368, June 1997.

[49] S. Lindenmeier, B. Bader, and P. Russer. The ATLM Method. In *2nd Intl. Workshop on Transmission Line Matrix Modeling (TLM) - Theory and Applications*, pages 24–35, Munich, October 1997.

[50] S. Lindenmeier, B. Isele, R. Weigel, and P. Russer. A Fast Spatial-Domain Method for the Suppression of Excitation-Induced Spurious Modes SCN TLM. *IEEE Trans. Microwave Theory Tech.*, 45(11):1998–2006, November 1997.

[51] S. Lindenmeier, L. Pierantoni, and P. Russer. Time Domain Modeling of E.M. Coupling Between Microwave Circuit Structures. In *IEEE MTT-S Digest*, volume 3, pages 1569–1572, June 1999.

[52] J. LoVetri and N.R.S. Simons. A Class of Symmetrical Condensed Node TLM Methods Derived Directly from Maxwell's Equations. *IEEE Trans. Microwave Theory Tech.*, 41(8):1419–1428, August 1993.

[53] J. LoVetri and N.R.S. Simons. A Framework to Construct Symmetrical Condensed Node TLM Methods using Generalized Inverses of Matrices. In *1st Intl. Workshop on Transmission Line Matrix Modeling (TLM) - Theory and Applications*, pages 13–22, Victoria, August 1995.

[54] S. Le Maguer and M. Ney. PML-TLM technique: Extension to evanescent waves and to advanced symmetrical condensed nodes.

[55] T. Mangold, J. Rebel, W.J.R. Hoefer, P.P.M. So, and P. Russer. What Determines the Speed of Time-Discrete Algorithms ? In *16th Annual Review of Progress in Applied Computational Electromagnetics Digest*, Monterey, March 2000. submitted for publication.

[56] T. Mangold and P. Russer. A Systematic Approach to the Problem of Equivalent Circuit Model Generation. In *IEEE MTT-S Digest*, volume 3, pages 1409–1412, June 1998.

[57] T. Mangold and P. Russer. Generation of Lumped Element Equivalent Circuits from Time-Domain Scattering Signals. In *14th Annual Review of Progress in Applied Computational Electromagnetics Digest*, pages 351–358, Monterey, March 1998.

[58] T. Mangold, J. Wolff, M. Töpper, H. Reichl, and P. Russer. Multilayer Multichip Modules for Microwave and Millimeterwave Integration. In *Proc. of the 28th Europ. Microwave Conf.*, pages 443–448, 1998.

[59] L. De Menezes, C. Eswarappa, and W.J.R. Hoefer. A Comparative Study of Dispersion Errors and Performance of Absorbing Boundary Conditions in SCN-TLM and FDTD. In *13th Annual Review of Progress in Applied Computational Electromagnetics Digest*, pages 673–678, Monterey, March 1997.

[60] L. De Menezes and W.J.R. Hoefer. Accuracy of TLM Solutions of Maxwell's Equations. *IEEE Trans. Microwave Theory Tech.*, 44(12):2512–2517, December 1996.

[61] L. De Menezes and W.J.R. Hoefer. Modeling of General Constitutive Relationships in SCN TLM. *IEEE Trans. Microwave Theory Tech.*, 44(6):854–861, June 1996.

[62] J. Mlakar. Lumped Circuit Symmetrical TLM Node. *Electron. Lett.*, 28(5):497–498, February 1992.

[63] J. Morente, J. Porti, and M. Khalladi. Absorbing Boundary Conditions for the TLM Method. *IEEE Trans. Microwave Theory Tech.*, 40(11):2095–2099, November 1992.

[64] J.A. Morente, G. Giménez, J.A. Portí, and M. Khalladi. Group and Phase Velocities in the TLM-Symmetrical -Condensed Nodes Mesh. *IEEE Trans. Microwave Theory Tech.*, 42(3):514–517, March 1994.

[65] J.A. Morente, G. Giménez, J.A. Portí, and M. Khalladi. Dispersion Analysis for a TLM Mesh of Symmetrical Condensed Nodes with Stubs. *IEEE Trans. Microwave Theory Tech.*, 43(2):452–456, February 1995.

[66] P. Naylor and A. Ait-Sadi. Simple Method for Determining 3-D TLM Nodal Scattering in Nonscalar Problems. *Electron. Lett.*, 28(25):2353–2354, November 1992.

[67] P. Naylor and R.A. Desai. New three dimensional Symmetrical Condensed Lossy Node for Solution of Electromagnetic Wave Problems by TLM. *Electron. Lett.*, 26(7):492–495, March 1990.

[68] M. Ney, S. Le Maguer, and N. Pena. Modeling of Absorbing Media for the Simulation of Open Boundaries in TLM. In *2nd Intl. Workshop on Transmission Line Matrix Modeling (TLM) - Theory and Applications*, pages 91–102, Munich, October 1997.

[69] J. Nielsen. Spurious Modes of the TLM-Condensed Node Formulation. *IEEE Microwave and Guided Wave Lett.*, 1(8):201–203, August 1991.

[70] J. Nielsen and W.J.R. Hoefer. A Complete Dispersion Analysis of the Condensed Node TLM Mesh. *IEEE Trans. Magn.*, 27(5):3982–3985, September 1991.

[71] J. Nielsen and W.J.R. Hoefer. Effect of Dispersion in the 3-D Condensed TLM Mesh. In *IEEE MTT-S International Microwave Symposium Digest*, pages 853–855, 1992.

[72] J.S. Nielsen. Generalized Dispersion Analysis and Spurious Modes of 2-D and 3-D TLM Formulations. *IEEE Trans. Microwave Theory Tech.*, 41(8):1375–1384, August 1993.

[73] J. Paul, C. Christopoulos, and D.W.P. Thomas. Modelling of Antennas in Close Proximity to Biological Tissues Using the TLM Method. In *14th Annual Review of Progress in Applied Computational Electromagnetics Digest*, pages 490–497, Monterey, March 1998.

[74] N. Pena and M. Ney. Investigation of the Dispersion of 3D-TLM Condensed Nodes: Comparison with the FDTD Yee's Scheme. In *Proc. Progress In Electromagnetic Research Symp.–PIERS*, page 872, Nantes, July 1998.

[75] L. Pierantoni, S. Lindenmeier, and P. Russer. A Combination of Integral Equation Method and FD/TLM Method for Efficient Solution of EMC Problems. In *Proc. of the 27th Europ. Microwave Conf.*, pages 937–942, September 1997.

[76] L. Pierantoni, S. Lindenmeier, and P. Russer. Efficient analysis of microstrip radiation by the tlm integral equation (tlmie) method. In *IEEE MTT-S Digest*, volume 2, pages 1267–1270, June 1998.

[77] J. Rebel, T. Mangold, and P. Russer. On the Performance of TLM-SCN Codes. In *3rd Intl. Workshop on Transmission Line Matrix Modeling (TLM) - Theory and Applications*, pages 43–50, Nice, October 1999.

[78] J. Rebel, T. Mangold, and P. Russer. On the Practical Use of Layered Absorbers for the Simulation of Planar Microwave Circuits using the SCN-TLM Method. In *16th Annual Review of Progress in Applied Computational Electromagnetics Digest*, Monterey, March 2000. submitted for publication.

[79] J. Rebel and P. Russer. Modelling of Dispersive Media in TLM Using the Propagator Approach. In *14th Annual Review of Progress in Applied Computational Electromagnetics Digest*, pages 336–343, Monterey, March 1998.

[80] H.-J. Reinhardt. *Analysis of Approximation Methods for Differential and Integral Equations*. Springer, 1985.

[81] J. Represa, A.C.L. Cabecceira, and I. Barba. The Use of Sources for TLM Modelling of Complex Materials. In *13th Annual Review of Progress in Applied Computational Electromagnetics Digest*, pages 638–648, Monterey, March 1997.

[82] R.D. Richtmyer. *Principles of Advanced Mathematical Physics*. Springer, 1978.

[83] M.J. Riezenman. Technology 1998: Analysis & Forcast - Communications. *IEEE Spectrum*, 35(1):882–893, January 1998.
[84] P. Robert. *Electric and Magnetic Properties of Materials*. Artech House, 1988.
[85] P. Russer. The Alternating Rotated Transmission Line Matrix ARTLM Scheme. *Electromagnetics*, 16(1):537–551, October 1996.
[86] P. Russer and B. Bader. The Alternating Transmission Line Matrix (ATLM) Scheme. In *IEEE MTT-S International Microwave Symposium Digest*, volume 1, pages 19–22, May 1995.
[87] P. Russer and M. Krumpholz. The Hilbert Space Formulation of the TLM Method. *Int. J. Num. Modelling*, 6(1):29–45, February 1993.
[88] A.A. Samarskij. *Numerical Methods for Grid Equations*. Birkhäuser, Basel, 1989.
[89] R. Scaramuzza and A.J. Lowery. Hybrid Symmetrical Condensed Node for the TLM Method. *Electron. Lett.*, 28:1947–1949, July 1990.
[90] W. Schroeder and I. Wolff. The Origin of Spurious Modes in Numerical Solutions of Electromagnetic Field Eigenvalue Problems. *IEEE Trans. Microwave Theory Tech.*, 42(4):644–653, April 1994.
[91] W. Simbürger, H.-D. Wohlmuth, P. Weger, and A. Heinz. A Monolithic Transformer Coupled 5W Silicon Power Amplifier with 59% PAE at 0.9GHz. *IEEE J. Solid-State Circuits, Special Issue on ISSCC'99*, December 1999. accepted for publication.
[92] N. Simons, R. Siushansian, J. Lo Vetri, G. Bridges, and M. Cuhaci. Comparison of Symmetric Condensed TLM, Yee FDTD and Integer Lattice Gas Automata Solutions for a Problem Containing a Sharp Metallic Edge. In *12th Annual Review of Progress in Applied Computational Electromagnetics Digest*, pages 326–330, Monterey, March 1996.
[93] N.R.S. Simons and E. Bridges. Equivalence of Propagation Characteristics for the Transmission-Line Matrix and Finite-Difference Time-Domain Methods in Two Dimensions. *IEEE Trans. Microwave Theory Tech.*, 39(2):354–357, February 1991.
[94] N.R.S. Simons, A. Petosa, M. Cuhaci, A. Ittipiboon, R. Siushansian, J. LoVetri, and S. Gutschling. Validation of Transmission Line Matrix and Finite-Integration Technique, and Finite-Difference Time-Domain Simulations of a Multi-Segment Dielectric Resonator Antenna. In *13th Annual Review of Progress in Applied Computational Electromagnetics Digest*, pages 1433–1438, Monterey, March 1997.
[95] N.R.S. Simons and A. Sebak. A Fourth-Order in Space and Second-Order in Time TLM Model. *IEEE Trans. Microwave Theory Tech.*, 43(2):437–444, February 1995.
[96] N.R.S. Simons and A.A. Sebak. Spatially Weighted Numerical Models for the Two-Dimensional Wave Equation: FD Algorithm and Synthesis of the Equivalent TLM Model. *Int. J. Num. Modelling*, 6:47–65, 1993.
[97] M.I. Sobhy, M.W.R. Ng, R.J. Langley, and J.C. Batchelor. TLM Analysis of Microstrip Patch Antenna on Ferrite Substrate. In *IEEE MTT-S Digest*, volume 3, pages 1297–1300, Anaheim, June 1999.
[98] M.I. Sobhy, R. Ng, R.J. Langley, and J. Batchelor. Using TLM to Simulate Ferrite and Dispersive Media. In *2nd Intl. Workshop on Transmission Line Matrix Modeling (TLM) - Theory and Applications*, pages 246–255, Munich, October 1997.
[99] G. Tardioli and W.J.R. Hoefer. Derivation of the SCN-TLM Node Scattering Matrix from the Integral Formulation of Maxwell's Equations. In *2nd Intl. Workshop on Transmission Line Matrix Modeling (TLM) - Theory and Applications*, pages 36–46, Munich, October 1997.
[100] J.W. Thomas. *Numerical Partial Differential Equations*. Springer, New York, 1995.
[101] C.E. Tong and Y. Fujino. An Efficient Algorithm for Transmission Line Matrix Analysis of Electromagnetic Problems Using the Symmetrical Condensed Node. *IEEE Trans. Microwave Theory Tech.*, 39(8):1420–1424, August 1991.
[102] V. Trenkic. *The Development and Characterization of Advanced Nodes for the TLM Method*. Phd thesis, University of Nottingham, 1995.
[103] V. Trenkic, C. Christopoulos, and T.M. Benson. Dispersion Analysis of the TLM Symmetrical Super-Condensed Node. *Electron. Lett.*, 30(25):2151–2153, December 1994.
[104] V. Trenkic, C. Christopoulos, and T.M. Benson. Generally Graded TLM Mesh Using the Symmetrical Super-Condensed Node. *Electron. Lett.*, 30(10):795–797, May 1994.

[105] V. Trenkic, C. Christopoulos, and T.M. Benson. New Symmetrical Super-Condensed Node for the TLM Method. *Electron. Lett.*, 30(4):329–330, February 1994.

[106] V. Trenkic, C. Christopoulos, and T.M. Benson. Analytical Expressions of the Dispersion Relation for the TLM Condensed Nodes. *IEEE Trans. Microwave Theory Tech.*, 44(12):2223–2230, December 1996.

[107] V. Trenkic, C. Christopoulos, and T.M. Benson. Development of a General Symmetrical Condensed Node for the TLM Method. *IEEE Trans. Microwave Theory Tech.*, 44(12):2129–2135, December 1996.

[108] V. Trenkic, J. Paul, I. Argyri, and C. Christopoulos. Modelling of Ferrite Tiles as Frequency Dependent Boundaries in General Time-Domain TLM Schemes. In *13th Annual Review of Progress in Applied Computational Electromagnetics Digest*, pages 630–637, Monterey, March 1997.

[109] R.H. Voelker, G. Lei, G. Pan, and B. Gilbert. Determination of Complex Permittivity of Low-Loss Dielectrics. *IEEE Trans. Microwave Theory Tech.*, 45(10):1955–1960, October 1997.

[110] J.R. Whinnery, C. Concordic, W. Ridgeway, and G. Kron. Network Analyzer Studies of Electromagneitc Cavity Resonators. *Proc. Inst. Radio Engrs.*, 32:360–367, June 1944.

[111] J.R. Whinnery and S. Ramo. A new Approach to the Solution of High-Frequency Field Problems. *Proc. Inst. Radio Engrs.*, 32:284–288, May 1944.

[112] H.-D. Wohlmuth, W. Simbürger, H. Knapp, and A.L. Scholz. 2GHz Meißner VCO in Si Bipolar Technology. In *Proc. of the 29th Europ. Microwave Conf.*, volume 1, pages 190–193, Munich, October 1999.

[113] I. Wolff. Finite Difference Time-Domain Simulation of Electromagnetic Fields and Microwave Circuits. *Int. J. Num. Modelling*, 5:163–182, February 1992.

[114] K. Wu, Q. Zhang, and J. Huang. Analysis of Planar Structure on General Anisotropic Material: Unified TLM Model in Frequency- and Time-domain and Experimental Verification. In *13th Annual Review of Progress in Applied Computational Electromagnetics Digest*, pages 679–685, Monterey, March 1997.

[115] K.S. Yee. Numerical Solution of Initial Boundary Value Problems Involving Maxwell's Equations in Isotropic Media. *IEEE Trans. Antennas and Propagation*, 14(3):302–307, May 1966.

[116] N. Young. *An introduction to Hilbert space*. Cambridge University Press, 1988.

[117] E. Zeidler. *Nonlinear Functional Analysis and its Applications II/A*. Springer, 1985.

[118] E. Zeidler. *Nonlinear Functional Analysis and its Applications II/B*. Springer, 1985.

[119] E. Zeidler. *Applied Functional Analysis*. Springer, 1995.

[120] R. Zurmühl and S. Falk. *Matrizen und ihre Anwendungen. Teil 1: Grundlagen*. Springer, 1984.

Author's Publications

[1] J. Rebel, H.-D. Wohlmuth, and P. Russer. Time Domain Characterization of Planar Microwave Transformers Using the SCN-TLM Method. In *IEEE MTT-S International Microwave Symposium - IMS 2000*, Boston, Massachusetts, June 2000, submitted for publication.

[2] J. Rebel, T. Mangold, and P. Russer. Time Domain Characterization of Dielectric Losses in Multichip Module Interconnect Structures using the SCN-TLM Method. In *IEEE IEEE MTT-S International Microwave Symposium - IMS 2000*, Boston, Massachusetts, June 2000, submitted for publication.

[3] T. Mangold, J.Rebel, W.J.R. Hoefer, P.P.M. So, and P. Russer. What Determines the Speed of Time-Discrete Algorithms ?. *16th Annual Review of Progress in Applied Computational Electromagnetics Symposium*, Monterey, California, USA, March 2000, accepted for publication.

[4] J. Rebel, T. Mangold, and P. Russer. On the Practical Use of Layered Absorbers for the Simulation of Planar Microwave Circuits using the SCN-TLM Method. *16th Annual Review of Progress in Applied Computational Electromagnetics Symposium* Monterey, California, USA, March 2000, accepted for publication.

[5] J. Rebel, T. Mangold, and P. Russer. On the Performance of TLM-SCN Codes. *Proceedings of Third Int. Workshop on Transmission Line Matrix (TLM) Modelling, Nice*, pages 43–50, October 1999.

[6] J. Rebel, M. Aidam, and P. Russer. On the Convergence of the Classical Symmetrical Condensed Node - TLM Scheme. *IEEE Trans. Microwave Theory Tech.*, submitted for publication.

[7] J. Rebel, M. Aidam, and P. Russer. A Numerical Study on the Accuracy of TLM-SCN Formulations for the Solution of Initial Value Problems. *15th Annual Review of Progress in Applied Computational Electromagnetics Digest*, pages 628–635, March 1999. Awarded the Best Student Paper Prize

[8] J. Rebel and P. Russer. Application of the Propagator Approach to the modelling of dispersive media in TLM. *Proceedings of the Progress in Electromagnetics Research Symposium PIERS 98*, page 871, July 1998.

[9] J. Rebel and P. Russer. Modelling of Dispersive Media in TLM Using the Propagator Approach. *14th Annual Review of Progress in Applied Computational Electromagnetics Digest*, pages 336–343, March 1998.

List of Figures

List of Tables